The Transverse Proximity Effect in Quasar Spectra

Gábor Worseck

Astrophysikalisches Institut Potsdam

Dissertation zur Erlangung des akademischen Grades
doctor rerum naturalium (Dr. rer. nat.)
in der Wissenschaftsdisziplin Astrophysik
Eingereicht an der Mathematisch-Naturwissenschaftlichen Fakultät
der Universität Potsdam

Dezember 2007

Bravado

Have I not walked without an upward look
Of caution under stars that very well
Might not have missed me when they shot and fell?
It was a risk I had to take – and took.

Robert Frost (1946)

ABSTRACT

The intergalactic medium is kept highly photoionised by the intergalactic UV background radiation field generated by the overall population of quasars and star-forming galaxies. In the vicinity of sources of UV photons, such as luminous high-redshift quasars, the UV radiation field is enhanced due to the local source contribution. The higher degree of ionisation is visible as a reduced line density or generally as a decreased level of absorption in the Lyman alpha (Lyα) forest of neutral hydrogen. This so-called proximity effect has been detected with high statistical significance towards luminous quasars. If quasars radiate rather isotropically, background quasar sightlines located near foreground quasars should show a region of decreased Lyα absorption close to the foreground quasar. Despite considerable effort, such a transverse proximity effect has only been detected in a few cases. It is still unclear, whether this effect is a common phenomenon in the Lyα forest.

So far, studies of the transverse proximity effect were mostly limited by the small number of suitable projected pairs or groups of high-redshift quasars. With the aim to substantially increase the number of quasar groups in the vicinity of bright quasars we conduct a targeted survey for faint $V \lesssim 22$ quasars at redshifts $1.7 \lesssim z \lesssim 3.6$ around 18 well-studied quasars at $2.76 < z < 4.69$ employing slitless spectroscopy. Among the reduced and calibrated slitless spectra of $\sim$ 29000 objects on a total area of 4.39 square degrees we discover in total 169 previously unknown quasar candidates based on their prominent emission lines. 81 potential $z > 1.7$ quasars are selected for confirmation by slit spectroscopy at the Very Large Telescope (VLT). We are able to confirm 80 of these as $0.580 \leq z \leq 3.586$ quasars. 64 of the newly discovered quasars reside at $z > 1.7$. Excluding the central quasars in the fields, our survey increases the number of $z > 1.7$ quasars in these fields by a factor $\sim$ 5. The high success rate of the follow-up observations implies that the majority of the remaining candidates are quasars as well.

In 16 of these groups we search for a transverse proximity effect as a systematic underdensity in the intergalactic H i Lyα absorption. We employ a novel technique to characterise the random absorption fluctuations in the Lyα forest in order to estimate the significance of the transverse proximity effect. Neither low-resolution spectra nor high-resolution spectra of background quasars of our groups present evidence for a transverse proximity effect. However, via Monte Carlo simulations the effect should be detectable only at the 1–2σ level near three of the foreground quasars. Thus, we cannot distinguish between the presence or absence of a weak signature of the transverse proximity effect. The systematic effects of quasar variability, quasar anisotopy and intrinsic overdensities near quasars likely explain the apparent lack of the transverse proximity effect. Even in absence of the systematic effects, we show that a statistically significant detection of the transverse proximity effect requires at least $\sim$ 5 medium-resolution quasar spectra of background quasars near foreground quasars whose UV flux exceeds the UV background by a factor $\gtrsim$ 3. Therefore, statistical studies of the transverse proximity effect in the H i Lyα forest require large numbers of suitable pairs.

Two sightlines towards the central quasars of our survey fields show intergalactic He ii Lyα absorption. A comparison of the He ii absorption to the corresponding H i absorption yields an estimate of the spectral shape of the intergalactic UV radiation field, typically parameterised by the He ii/H i column density ratio η. We analyse the fluctuating UV spectral shape on both lines of sight and correlate it with seven foreground quasars. On the line of sight towards Q 0302−003 we find a harder radiation field near 4 foreground quasars. In the direct vicinity of the quasars η is consistent with values of 25–100, whereas at large distances from the quasars $\eta \gtrsim 200$ is required. The second line of sight towards HE 2347−4342 probes lower redshifts where η is directly measurable in the resolved He ii forest. Again we find that the radiation field near the 3 foreground quasars is significantly harder (median $\eta \sim$ 20–50) than in general (median $\eta \sim$ 80–100). While η still shows large fluctuations near the quasars, probably due to radiative transfer, the radiation field is on average harder near the quasars than far away from them.

We interpret these discoveries as the first detections of the transverse proximity effect as a local hardness fluctuation in the UV spectral shape. No significant H i proximity effect is predicted for the 7 foreground quasars. In fact, the H i Lyα absorption near the quasars is close to or slightly above the average, suggesting that the weak signature of the transverse proximity effect is masked by intrinsic overdensities. However, we show that the UV spectral shape traces the transverse proximity effect even in overdense regions or at large distances. Therefore, the spectral hardness is a sensitive physical measure of the transverse proximity effect that is able to break the density degeneracy affecting the traditional searches.

The transverse proximity effect yields a lower limit on the quasar lifetime. From our detections we get values of 10–30 Myr consistent with other more indirect estimates.

ZUSAMMENFASSUNG

Das intergalaktische Medium wird durch das intergalaktische UV-Hintergrundsstrahlungsfeld in einem hochgradig photoionisierten Zustand gehalten. Der UV-Hintergrund stammt von der gesamten Population von Quasaren und sternbildenden Galaxien. In der Nähe von UV-Strahlungsquellen, wie zum Beispiel leuchtkräftigen hochrotverschobenen Quasaren, ist das UV-Strahlungsfeld lokal erhöht durch den Anteil der Quelle. Der höhere Ionisationsgrad ist beobachtbar als eine reduzierte Liniendichte oder allgemein als ein vermindertes Maß an Absorption im Lyman-alpha (Lyα) Wald des neutralen Wasserstoffs. Dieser sogenannte Proximity-Effekt ist bei leuchtkräftigen Quasaren mit hoher statistischer Signifikanz nachgewiesen worden. Falls Quasare fast isotrop strahlen, dann sollten Sichtlinien zu Hintergrundquasaren in der Nähe von Vordergrundquasaren eine Region mit verminderter Lyα-Absorption zeigen. Trotz beträchtlichen Aufwands wurde solch ein transversaler Proximity-Effekt nur in wenigen Fällen entdeckt. Es ist noch unklar, ob dieser Effekt ein generelles Phänomen im Lyα-Wald ist.

Bisher waren Studien des transversalen Proximity-Effekts meist begrenzt durch die kleine Anzahl von geeigneten projizierten Paaren oder Gruppen von hochrotverschobenen Quasaren. Mit dem Ziel die Zahl der Quasargruppen in der Nähe von hellen Quasaren beträchtlich zu erhöhen, führen wir eine gezielte Durchmusterung mittels spaltloser Spekroskopie nach schwachen $V \lesssim 22$ Quasaren bei Rotverschiebungen $1.7 \lesssim z \lesssim 3.6$ um 18 oft studierte Quasare bei $2.76 < z < 4.69$ durch. Unter den reduzierten und kalibrierten spaltlosen Spektren von ~ 29000 Objekten auf einer Gesamtfläche von 4.39 Quadratgrad entdecken wir insgesamt 169 vorher unbekannte Quasarkandidaten anhand ihrer vorstehenden Emissionslinien. 81 potentielle $z > 1.7$ Quasare werden ausgesucht zur Bestätigung mittels Spaltspektroskopie am Very Large Telescope (VLT). Wir können 80 von diesen als $0.580 \leq z \leq 3.586$ Quasare bestätigen. 64 der neu entdeckten Quasare liegen bei $z > 1.7$. Unter Ausschluss der Zentralquasare in den Feldern erhöht unsere Durchmusterung die Zahl der $z > 1.7$ Quasare in diesen Feldern um einen Faktor ~ 5. Die hohe Erfolgsrate der Nachfolgebeobachtungen deutet an, dass die Mehrzahl der verbleibenden Kandidaten ebenfalls Quasare sind.

In 16 dieser Gruppen suchen wir nach dem transversalen Proximity-Effekt als eine systematische Unterdichte in der intergalaktischen H I Lyα-Absorption. Wir nutzen eine neuartige Methode die zufälligen Absorptionsfluktuationen im Lyα-Wald zu charakterisieren, um die Signifikanz des transversalen Proximity-Effekts abschätzen zu können. Weder schwach aufgelöste noch hoch aufgelöste Spektren von Hintergrundquasaren unserer Gruppen zeigen Anzeichen für einen transversalen Proximity-Effekt. Aufgrund von Monte Carlo Simulationen sollte der Effekt jedoch nur auf einem Signifikanzniveau von 1–2σ in der Nähe von 3 Vordergrundquasaren detektierbar sein. Deshalb können wir nicht zwischen An- oder Abwesenheit eines schwachen transversalen Proximity-Effekts unterscheiden. Die systematischen Effekte von Quasarvariabilität, Quasar-Anisotropie oder intrinsischen Überdichten nahe Quasaren erklären wahrscheinlich das scheinbare Fehlen des transversalen Proximity-Effekts. Selbst in Abwesenheit der systematischen Effekte zeigen wir, dass eine statistisch signifikante Detektion des transversalen Proximity-Effekts mindestens ~ 5 Hintergrundquasarspektren bei mittlerer Auflösung nahe Vordergrundquasaren erfordert, deren UV-Fluss den UV-Hintergrund um einen Faktor $\gtrsim 3$ übersteigt. Deshalb erfordern statistische Studien des transversalen Proximity-Effekts im H I Lyα-Wald große Zahlen von geeigneten Quasaren.

Zwei Sichtlinien zu den Zentralquasaren unserer Durchmusterungsfelder zeigen intergalaktische He II Lyα-Absorption. Ein Vergleich der He II-Absorption mit der entsprechenden H I-Absorption liefert eine Abschätzung der Spektralform des intergalaktischen UV-Strahlungsfelds, das typischerweise durch das He II/H I Säulendichteverhältnis η parameterisiert wird. Wir analysieren die fluktuierende spektrale Form des UV-Strahlungsfelds auf beiden Sichtlinien und korrelieren sie mit 7 Vordergrundquasaren. Auf der Sichtlinie zu Q 0302−003 finden wir ein härteres Strahlungsfeld nahe 4 Vordergrundquasaren. In der direkten Umgebung der Quasare ist η konsistent mit Werten von 25–100, wogegen bei großen Entfernungen zu den Quasaren $\eta \gtrsim 200$ erforderlich ist. Die zweite Sichtlinie zu HE 2347−4342 sondiert kleinere Rotverschiebungen, wo η im aufgelösten He II-Wald direkt messbar ist. Wieder finden wir, dass das Strahlungsfeld nahe der 3 Vordergrundquasaren signifikant härter ist (Median η ~20–50) als im allgemeinen (Median η ~80–100). Während η trotzdem große Fluktuationen nahe den Quasaren aufweist, die wahrscheinlich von Strahlungstransport herrühren, ist das Strahlungsfeld in der Nähe der Quasare im Mittel härter als in großer Entfernung.

Wir interpretieren diese Entdeckungen als die ersten Detektionen des transversalen Proximity-Effekts als eine lokale Fluktuation im spektralen Härtegrad. Kein signifikanter H I Proximity-Effekt ist für die 7 Vordergrundquasare vorhergesagt. Tatsächlich ist die H I Lyα-Absorption nahe den Quasaren nahe am oder etwas über dem Mittelwert, was darauf hindeutet, dass die schwache Signatur des transversalen Proximity-Effekts maskiert wird durch intrinsische Überdichten. Jedoch zeigen wir, dass der Härtegrad den transversalen Proximity-Effekt selbst in überdichten Regionen oder auf großen Distanzen sichtbar werden läßt. Deshalb ist der spektrale Härtegrad ein empfindliches physikalisches Maß für den transversalen Proximity-Effekt, der in der Lage ist, die Dichteentartung zu brechen, die die traditionelle Suche behindert.

Der transversale Proximity-Effekt ergibt eine Untergrenze für die Quasar-Lebensdauer. Aus unseren Detektionen bekommen wir Werte von 10–30 Myr, was mit anderen indirekteren Abschätzungen verträglich ist.

Contents

Chapter 1

The Lyman alpha forest and the proximity effect

G. Worseck

ABSTRACT

We present a short introduction to the topic of this work. While this discussion is not meant to be an exhaustive review on the reionisation of the universe, the Lyα forest and the proximity effect, it provides a concise overview focussed on the relevant aspects of this work.

1.1. Intergalactic neutral hydrogen

1.1.1. The hydrogen reionisation epoch

Due to cosmological expansion the fading photon background of the Big Bang ceased to interact with the baryonic plasma that became neutral at a redshift $z \sim 1100$. The perturbations in the matter distribution grew by gravitational collapse to the first gravitationally bound systems that were able to form the first stars and Black Holes. Eventually, the UV radiation generated via nuclear burning in the first stars and via accretion onto the first Black Holes reionised the large amounts of hydrogen present in the intergalactic medium (IGM).

Observationally, the cosmic microwave background (CMB) observed by the Wilkinson Microwave Anisotropy Probe (WMAP) revealed a Thomson scattering optical depth of $\tau_{\mathrm{e}} = 0.09 \pm 0.03$ (Page et al. 2007) that implies a reionisation epoch $z \sim 11$ for models of instantaneous H I reionisation (Spergel et al. 2007). Likewise, absorption spectra of $z \gtrsim 6$ quasars show very high intergalactic H I absorption (see below). Together with the evolving sizes of the H II regions around the background quasars the large absorption suggests that the reionisation epoch ended at $z \sim 6$ as the H II regions of individual sources overlapped (Fan et al. 2006). However, the epoch of H I reionisation is not well defined, because it depends on the evolving population of ionising sources that leads to an extended reionisation plateau (e.g. Wyithe & Cen 2007). A combination of protogalaxies with metal-free Population III (Pop III) stars, early galaxies with Pop II stars and early active galactic nuclei (AGN) are likely responsible for H I reionisation.

Because the quasar space density declines rapidly at $z \gtrsim 2.5$ (e.g. Warren et al. 1994; Schmidt et al. 1995) luminous quasars do not provide enough ionising photons to reionise H I at $z \sim 6$ (e.g. Fan et al. 2001). Although numerous low-luminosity AGN at very high redshift cannot be ruled out (Meiksin 2005), their luminosity function at $z \sim 3$ does not imply a significant contribution (Hunt et al. 2004).

It is still debated whether the number density of observed $z \sim 6$ star-forming galaxies is sufficient to reionise H I. Bouwens et al. (2006) find that $z \sim 6$ galaxies can provide the necessary UV photons to reionise the universe, whereas Bunker et al. (2006) show that the star formation rate at $z \sim 6$ is insufficient for reionisation, so that early star formation at $z \gtrsim 10$ must be responsible.

The first stars were metal-free because they must have been formed out of primordial gas. Due to the primordial composition of the gas, H_2 cooling was essential for the formation of Pop III stars. Only high-mass halos ($M_{\mathrm{halo}} \gtrsim 10^6 M_{\odot}$) were able to cool efficiently, restricting the emergence of the first stars to $z \sim$20–30. Simulations of primordial star formation suggest the lack of fragmentation of the gas, leading to dense massive clumps each harbouring a Pop III protostar (Abel et al. 2002; Bromm et al. 2002). The final stellar mass depends on the gas accretion history governed by the feedback of the Pop III star onto its environment, but the large initial clump mass suggests a top-heavy stellar initial mass function dominated by very massive stars ($M \gtrsim 100 M_{\odot}$). At the end of their life, these high-mass stars collapse directly into Black Holes or explode in Pair Instability Supernovae leading to the complete disruption of the progenitors (e.g. Heger & Woosley 2002). The Black Holes might grow via accretion and mergers, possibly radiating as mini-quasars (e.g. Ricotti & Ostriker 2004a; Kuhlen & Madau 2004).

The feedback of the first stars onto their surroundings is important for constraining their impact to reionisation (for a review see e.g. Ciardi & Ferrara 2005). Radiative feedback occurs due to the ionising radiation from the first stars, which affects locally the star formation in the host halo or neighbouring halos. Dissociation of H_2 suppresses cooling and quenches further star formation. On large scales, the ionising radiation escaping the halo contributes to the reionisation of the IGM and the generation of the UV background. Mechanical feedback from supernovae is able to expel large amounts of gas from the host halo. Finally, chemical feedback is important as the first supernovae pollute the primordial gas with metals that lead to a probably rapid transition in the star formation mode from high-mass Pop III stars to low-mass Pop II stars (Schneider et al. 2002; Bromm & Loeb 2003). However, the transition is likely inhomogeneous, leading to a coeval formation of Pop II and Pop III stars depending on the environment (e.g. Scannapieco et al. 2003).

In summary, the reionisation epoch of H I is likely complex and inhomogeneous, since it depends on the source properties, their feedback onto the surroundings and the source clustering properties. Globally, reionisation can be described in three stages introduced by Gnedin (2000). In the pre-overlap stage isolated H II regions grow around ionising sources. However, due to potential source anisotropy and radiative transfer in the

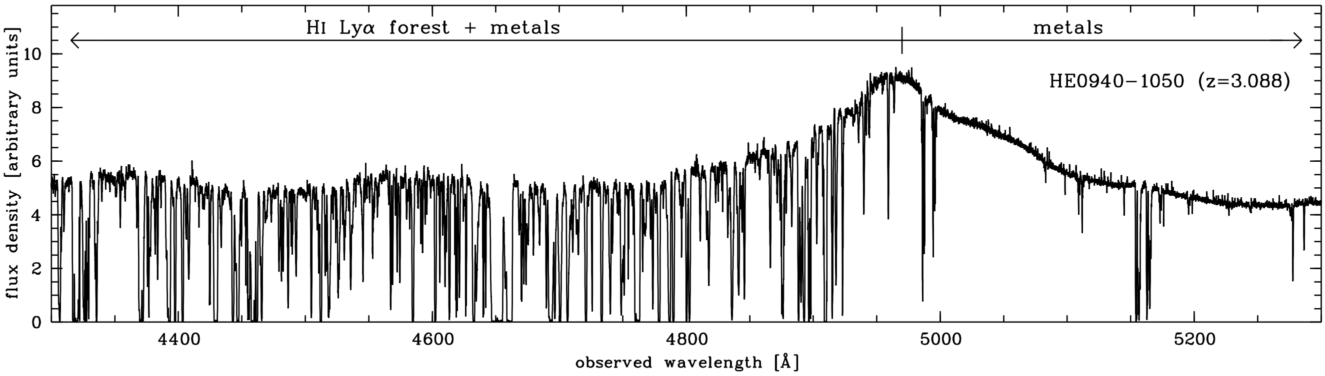

Fig. 1.1. UVES spectrum of the quasar HE 0940−1050 at $z = 3.088$. The spectrum has a resolution $R \sim 45000$ and a $S/N \sim 50$ per 0.05 Å pixel.

inhomogeneous IGM these H II regions have a complex topology. During the overlap stage the individual H II bubbles merge, leading to a rapid reionisation of the low-density IGM and the emergence of a quasi-homogeneous UV background. The post-overlap phase is characterised by the gradual reionisation of the remaining high-density regions. Three-dimensional simulations including cosmological radiative transfer have just begun to capture the complex topology of H I reionisation (Iliev et al. 2006, 2007).

1.1.2. Intergalactic H I *absorption*

Photons emitted by high-redshift sources at shorter wavelengths than Lyα are redshifted as they travel towards us. As they are redshifted to the Lyα wavelength they are resonantly scattered by intergalactic neutral hydrogen. Any reasonable value of the homogeneous H I density results in a large scattering optical depth at any point along the line of sight. From the absence of this large absorption trough blueward of Lyα in a $z \simeq 2$ quasar Gunn & Peterson (1965) concluded that the intergalactic hydrogen is not smoothly distributed and highly ionised. Such troughs have been observed in $z > 6$ quasars found by the Sloan Digital Sky Survey (e.g. Fan et al. 2006), however, they alone do not well constrain the neutral hydrogen fraction.

In contrast, the spectra of $z \lesssim 6$ quasars revealed a plethora of distinct narrow absorption lines of cosmological origin, primarly caused by Lyα absorption of intervening H I clumps along the line of sight (Lynds 1971; Sargent et al. 1980; Rauch 1998). The large number of lines per line of sight that are fully resolved only at high resolution ($R = \lambda/\Delta\lambda \gtrsim 40000$) gives rise to the name Lyα forest.

In Fig. 1.1 we present a high-resolution spectrum of a quasar observed with the UV-Visual Echelle Spectrograph (UVES) at the VLT. The Lyα forest emerges blueward of the Lyα emission line of the quasar. Prominent metal lines fall redward of the Lyα emission line, but they also contaminate the H I Lyα forest. Observationally, the Lyα absorption lines have been categorised into three classes: The Lyα forest contains all the weak lines with column densities $10^{12} \lesssim N \lesssim 10^{17.2}$ cm^{-2}. Higher column density systems at $10^{17.2} \lesssim N \lesssim 10^{20.2}$ cm^{-2} are optically thick to ionising radiation and therefore show breaks at their Lyman limit, so that they are called Lyman limit systems (LLSs). At $N \gtrsim 10^{20.2}$ cm^{-2} damping wings in the absorption profiles characterise damped Lyα systems (DLAs). In this work, only the low-density Lyα forest is of interest as the high column density systems become rapidly opaque to ionising radiation with increasing column density.

Echelle spectrographs at 8 m-class telescopes enabled high-quality spectroscopy of the Lyα forest towards large samples of quasars, so that its statistical properties could be quantified reliably. After decomposing the spectrum into discrete absorption lines, their distributions in redshift z, column density $N_{\mathrm{H\,I}}$ and Doppler parameter b can be obtained.

The redshift evolution of the line number density is well parameterised by a power law

$$\frac{\mathrm{d}\mathcal{N}}{\mathrm{d}z} = A\,(1+z)^{\gamma} \tag{1.1}$$

with the number of counted lines $\mathcal{N}$ and a propotionality constant A. Generally, the power law exponent γ is a function of column density interval and redshift (e.g. Kim et al. 1997). Most notably, at high redshift the line density strongly evolves ($2 \lesssim \gamma \lesssim 3$), whereas at $z \lesssim 1.5$ the line distribution is consistent with no redshift evolution (Kim et al. 1997, 2001, 2002a). Alternatively, the effective optical depth can be used to characterise redshift evolution of the Lyα forest. Assuming that all lines evolve at the same rate Zuo (1993) obtained

$$\tau_{\mathrm{eff}} \equiv -\ln\langle T\rangle = B\,(1+z)^{\gamma+1}\,, \tag{1.2}$$

with the proportionality constant B and the mean Lyα forest transmission $\langle T\rangle$ defined on a redshift bin Δz over all sightlines at the respective redshift. In principle, the effective optical depth is resolution-independent and it has been measured in large samples of forest spectra (e.g. Press et al. 1993; Kim et al. 2002a; Schaye et al. 2003; Bernardi et al. 2003; Songaila 2004; Kirkman et al. 2005; Faucher-Giguère et al. 2007b; Kim et al. 2007). However, the effective optical depths measured in low-resolution data are likely overestimated due to uncertainties in the quasar continuum (Kim et al. 2001; Seljak et al. 2003; Desjacques et al. 2007).

The number of lines per unit column density and unit redshift or pathlength X (Bahcall & Peebles 1969) is well described by a power law

$$\frac{\mathrm{d}^2\mathcal{N}}{\mathrm{d}N_{\mathrm{H\,I}}\mathrm{d}z} = \frac{H_0\,(1+z)^2}{H(z)}\frac{\mathrm{d}^2\mathcal{N}}{\mathrm{d}N_{\mathrm{H\,I}}\mathrm{d}X} \propto N_{\mathrm{H\,I}}^{-\beta} \tag{1.3}$$

with $\beta \simeq 1.5$ for the full column density range $10^{12}\,\mathrm{cm}^{-2} \lesssim N_{\mathrm{H\,I}} \lesssim 10^{22}\,\mathrm{cm}^{-2}$ (e.g. Tytler 1987; Hu et al. 1995). There is evidence that the column density distribution breaks at $N_{\mathrm{H\,I}} \gtrsim 10^{14}\,\mathrm{cm}^{-2}$ (Petitjean et al. 1993; Giallongo et al. 1996) and β may evolve with redshift for a given column density range (Kim et al. 1997, 2001, 2002a).

Finally, the Doppler parameter distribution is accurately fitted by

$$\frac{\mathrm{d}\mathcal{N}}{\mathrm{d}b} \propto \frac{b_\sigma^4}{b^5}\mathrm{e}^{-b_\sigma^4/b^4} \tag{1.4}$$

(Hui & Rutledge 1999) with $b_\sigma \simeq 24$ km s^{-1} (Kim et al. 2001).

Simulations of cosmological structure formation revealed that the Lyα forest arises naturally as a cosmic web of sheets and filaments that are intersected by the line of sight to a background source (e.g Cen et al. 1994; Zhang et al. 1995; Miralda-Escudé et al. 1996; Hernquist et al. 1996; Zhang et al. 1997; Davé et al. 1999; Bryan et al. 1999; Jena et al. 2005), thereby changing the perception of the Lyα forest. Instead of being a collection of discrete absorbers, the Lyα absorption is continuously fluctuating and traces the intergalactic distribution of baryons in their dark matter potentials. Therefore, the forest can be interpreted as a fluctuating Gunn-Peterson effect (e.g. Miralda-Escudé et al. 1996; Croft et al. 1997; Rauch et al. 1997). The intergalactic medium is the main repository for baryons at high redshift, which are kept highly photoionised by the metagalactic UV background (see below). The simulations reproduce the appearance and the statistical properties of the Lyα forest up to moderate overdensities of $\delta \sim 10$. Due to the quasi-linear overdensities simple physical models successfully describe the Lyα forest as well (Bi et al. 1992; Bi & Davidsen 1997; Schaye 2001).

Comparisons of observations and simulations show that the line number density evolution is mainly governed by the Hubble expansion and the evolution of the UV background radiation field (e.g. Davé et al. 1999). Accretion onto more massive structures becomes important at lower redshifts.

1.2. Intergalactic helium

1.2.1. The helium reionisation epoch

The reionisation of helium likely proceeded in two steps due to the different binding energy of the two electrons ($h\nu = 24.6\,\mathrm{eV} = 1.8\,\mathrm{ryd}$ vs. $h\nu = 54.4\,\mathrm{eV} = 4\,\mathrm{ryd}$). Due to the not very different ionisation thresholds of H I and He I both species were likely ionised at similar redshifts by similar sources. Although early He II reionisation could have been accomplished by massive Population III stars at least to some degree (Venkatesan et al. 2003), probably only quasars were able to provide the hard photons required for complete helium reionisation. The declining space density of quasars at $z \gtrsim 3.5$ implies that reionisation of He II is expected to be delayed to $3 \lesssim z \lesssim 4$ according to semianalytic (Madau et al. 1999; Miralda-Escudé et al. 2000; Wyithe & Loeb 2003; Gleser et al. 2005) and hydrodynamical (Sokasian et al. 2002, 2003) models of He II reionisation. Alternatively, redshifted X-ray emission from early Black Holes in small-mass galaxies at $7 \lesssim z \lesssim 20$ could have reionised He II without the need for He II Lyman continuum emission of quasars at $z \lesssim 4$ (Ricotti & Ostriker 2004b). Possibly intergalactic He II was first reionised by massive Pop III stars, followed by recombination due to the rapid transition of the star formation mode towards less massive Pop II stars and permanent reionisation by the emerging quasar population at lower redshifts (Oh et al. 2001; Wyithe & Loeb 2003). In contrast, early complete reionisation of He II at $z \sim 6$ could have been accomplished by thermal emission from shock-heated gas during structure formation (Miniati et al. 2004).

Observational constraints for a late He II reionisation epoch are provided by the reheating of the Lyα forest at $z \sim 3$ inferred from the line widths of thermally broadened H I lines (Schaye et al. 2000; Ricotti et al. 2000; Theuns et al. 2002). At the same redshifts a decrease in the H I effective optical depth has been detected and interpreted as the signature of He II reionisation (Bernardi et al. 2003; Faucher-Giguère et al. 2007b). Moreover, a few lines of sight towards quasars are transparent in the far UV to observe intergalactic He II absorption.

1.2.2. Intergalactic He II absorption

Intergalactic He II absorption at a rest frame wavelength of 303.7822 Å can be observed from space in the far UV towards a small subset of the quasar population due to several constraints. First, the Galactic H I Lyman limit imposes a lower redshift limit $z > 2$. Second, the far UV flux of most high-redshift quasars is attenuated by intervening H I Lyman continuum absorption (the Lyman valley, Møller & Jakobsen 1990) or even completely extinguished by optically thick Lyman limit systems (Picard & Jakobsen 1993; Jakobsen 1998). Third, the quasars must be bright enough for far UV spectroscopy at sufficiently high S/N with current space telescopes.

As a consequence, only six sightlines have been successfully probed so far despite considerable effort. Hubble Space Telescope (HST) observations of the lines of sight towards Q 0302−003 at $z = 3.285$ (Jakobsen et al. 1994; Hogan et al. 1997; Heap et al. 2000), PKS 1935−692 at $z = 3.18$ (Anderson et al. 1999) and SDSS J2346−0016 at $z = 3.50$ (Zheng et al. 2004a) revealed strong intervening He II absorption at $z \gtrsim 3$ that is consistent with a Gunn-Peterson trough ($\tau_{\mathrm{eff,He\,II}} > 3$).

In contrast, three available lines of sight at $z < 3$ towards HS 1700+6416 at $z = 2.72$ (Davidsen et al. 1996; Fechner et al. 2006), HE 2347−2342 at $z = 2.885$ (Reimers et al. 1997; Kriss et al. 2001; Smette et al. 2002; Shull et al. 2004; Zheng et al. 2004b) and QSO 1157+3143 at $z \simeq 3.0$ (Reimers et al. 2005) show patchy intergalactic He II absorption with voids ($\tau_{\mathrm{eff,He\,II}} \lesssim 1$) and troughs ($\tau_{\mathrm{eff,He\,II}} > 3$). At $z < 2.7$ the patchy absorption evolves to a He II Lyα forest that has been resolved in high-resolution spectra obtained with the Far Ultraviolet Spectroscopic Explorer (FUSE, Kriss et al. 2001; Shull et al. 2004; Zheng et al. 2004b; Fechner et al. 2006).

This observed overall evolution of the He II absorption suggests a late reionisation of He II at $z \sim 3$. The patchy structure of the absorption with voids that partly coincide with known quasars along or nearby the line of sight suggests an inhomogeneous fluctuating UV background at the He II ionisation edge and the onset of He II reionisation in Strömgren spheres around quasars (Reimers et al. 1997; Heap et al. 2000; Smette et al. 2002; Jakobsen et al. 2003; Reimers et al. 2005). However, the observed high opacities at $z > 3$ do not necessarily imply that helium is not reionised due to the tiny fraction of He II required, akin to the case of H I. Therefore, the overlap phase of He III zones that ended helium reionisation may have occurred at earlier cosmic times, in accord with the simulations of He II reionisation. Due to the small number of available sightlines cosmic variance likely plays a role, so that a detailed characterisation of the He II reionisation epoch is still impossible.

In several numerical studies the simulated H I and the He II Lyα forests were analysed in parallel, showing that the observations broadly agree with hierarchical cold dark matter structure formation models (Zhang et al. 1995; Miralda-Escudé et al. 1996; Croft et al. 1997; Zhang et al. 1997, 1998; Bolton et al. 2006; Paschos et al. 2007). In particular, He II absorption is a sensitive probe of cosmic voids that do not show pronounced

H I absorption due to noise or continuum fitting errors, but still display strong He II absorption (Croft et al. 1997; Zhang et al. 1998). This is naturally explained by the higher ionisation threshold and the 5.5 times higher recombination rate of He III compared to H II. Besides being a tracer of diffuse underdense matter in the IGM, the He II absorption can be compared to the corresponding H I absorption to estimate the spectral shape of the intergalactic radiation field (see below). Moreover, the resolved He II forest can be used to constrain the dynamics of the absorbing gas or the temperature of the IGM via analysing the line broadening of Lyα absorbers. However, the low quality of the currently available He II forest data ($S/N \sim 4$ at $R \sim 20000$, Zheng et al. 2004b; Fechner et al. 2006) do not permit a robust analysis except for rare unblended lines (Zheng et al. 2004b; Fechner & Reimers 2007a).

1.3. The intergalactic UV radiation field

1.3.1. The H I photoionisation rate

After reionisation of hydrogen, the low-density IGM is kept highly ionised by the metagalactic UV background that is generated by the overall population of quasars and star-forming galaxies. As the radiation propagates through the IGM, it is filtered by the absorbing structures. The amplitude of the UV background at a given frequency is determined by cosmological expansion and the evolution of the population of sources and absorbers of ionising radiation (e.g. Davé et al. 1999). The IGM is largely optically thin to ionising photons that penetrate the remaining neutral structures, leading to a large mean free path of H I ionising photons that is determined by the number density of Lyman limit systems (Madau et al. 1999; Miralda-Escudé et al. 2000; Meiksin & White 2004).

There are several ways to estimate the mean UV background photoionisation rate of a given species in the IGM at a given redshift z

$$\Gamma(z) = \int_{\nu_{\mathrm{LL}}}^{\infty} \frac{4\pi J_\nu(\nu, z)}{h\nu} \sigma(\nu)\,\mathrm{d}\nu \qquad (1.5)$$

with the ionisation cross section $\sigma(\nu)$ and the radiation intensity $J_\nu(\nu, z)$ above the ionisation frequency ν_{LL}.

First, the UV background can be estimated indirectly via integrating the contributions of the observed source population. Given the luminosity function of the sources, their characteristic spectral energy distribution and the observed absorber distribution functions in the IGM, the amplitude and spectral shape of the UV background can be calculated numerically (Bechtold et al. 1987). In particular, these calculations provide estimates on the relative contributions of quasars (Haardt & Madau 1996; Fardal et al. 1998) and star-forming galaxies (Madau et al. 1999; Haardt & Madau 2001) as a function of redshift. However, these estimates depend on the assumed luminosity function and the source spectral energy distribution. The ionising continuum of luminous quasars is well approximated by a power law $f_\nu \propto \nu^{-\alpha}$ with $\alpha \simeq 1.7$ (Telfer et al. 2002). However, there is evidence, that the spectral shape of low-redshift low-luminosity AGN is significantly harder (Scott et al. 2004), which may have an impact on the relative contribution of faint AGN to the UV background. The contribution of galaxies mainly depends on the escape fraction of ionising photons.

Second, the total UV background H I ionisation rate can be inferred from the proximity effect (see below). A quasar contribute significantly to the ionising radiation field in its surroundings and the UV background is determined from its relative impact compared to the quasar (Carswell et al. 1987; Bajtlik et al. 1988). Traditionally, the Lyman limit intensity $J_{\nu_{\mathrm{LL}}}$ is obtained by assuming the same spectral shape of quasars and the UV background above the H I Lyman limit. Many studies yielded estimates of the UV background via the proximity effect at different redshifts, summarised in Fig. 1.2. Despite large statistical and systematic errors, the UV background intensity clearly evolves with redshift. The decline at $z \lesssim 2$ and $z \gtrsim 4$ is likely due to the declining space density of quasars. The UV background inferred from the proximity effect is generally higher than the integrated emission of quasars, so that a contribution by star-forming galaxies is required, at least at $z \gtrsim 3$ in order to keep the IGM ionised (e.g. Madau et al. 1999; Haardt & Madau 2001; Bianchi et al. 2001; Sokasian et al. 2003; Schirber & Bullock 2003). However, the proximity effect estimates are subject to several systematic uncertainties that tend to overestimate the inferred UV background. Unaccounted overdensities near the quasars cause $J_{\nu_{\mathrm{LL}}}$ to be overestimated by a factor ~ 3 (Loeb & Eisenstein 1995; Rollinde et al. 2005; Faucher-Giguère et al. 2007a). Similarly, quasar emission redshifts determined from broad high-ionisation lines are likely underestimated (Gaskell 1982), causing $J_{\nu_{\mathrm{LL}}}$ to be overestimated by a factor ~ 3 (Espey 1993). Quasar variability will also tend to overestimate $J_{\nu_{\mathrm{LL}}}$ due to Malmquist bias in the selected quasar samples. Therefore, a contribution of star-forming galaxies at $z \lesssim 3$ is still debated.

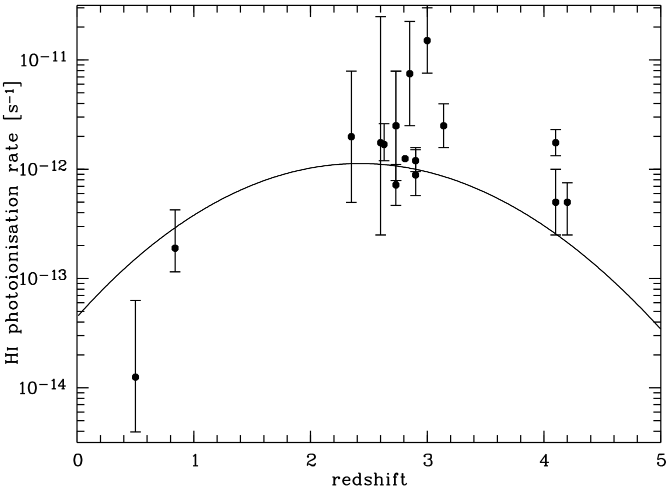

Fig. 1.2. Measurements of the UV background at various redshifts via the proximity effect (Bajtlik et al. 1988; Lu et al. 1991; Espey 1993; Giallongo et al. 1993; Kulkarni & Fall 1993; Bechtold 1994; Williger et al. 1994; Cristiani et al. 1995; Fernández-Soto et al. 1995; Giallongo et al. 1996; Srianand & Khare 1996; Lu et al. 1996; Cooke et al. 1997; Savaglio et al. 1997; Scott et al. 2000; Liske & Williger 2001; Scott et al. 2002). All studies measure $J_{\nu_{\mathrm{LL}}}$ in an Einstein-de Sitter universe. The UV background intensities have been converted to the H I photoionisation rates assuming a power law $J_\nu(\nu) \propto \nu^{-\alpha}$ with $\alpha = 1.8$. The redshift ranges used for determining the UV background are not shown for clarity. The overplotted line denotes the Haardt & Madau (1996) H I photoionisation rate of quasars in an Einstein-de Sitter universe.

The H I photoionisation rate can be also constrained via matching the level of Lyα forest absorption in artificial spectra generated from hydrodynamical simulations to the observed absorption (e.g. Rauch et al. 1997; McDonald et al. 2000; Meiksin & White 2004; Tytler et al. 2004; Bolton et al. 2005; Kirkman et al. 2005; Jena et al. 2005). However, due to the different simulation codes used with different sets of simulation parameters, the best-fit values cannot be readily compared to the estimates via the proximity effect. Bolton et al. (2005) and Jena et al.

(2005) present scaling relations that change the photoionisation rate as a function of simulation parameters.

1.3.2. The spectral shape of the UV background

The integrated estimates of the UV background predict the spectral shape of the UV radiation field for a given source population. The ionising flux of the sources is softened due to radiative transfer in the IGM. The spectral energy distribution of the resulting UV background is typically quantified by the softness parameter

$$S = \frac{\Gamma_{\mathrm{H\,I}}}{\Gamma_{\mathrm{He\,II}}}, \tag{1.6}$$

which is the ratio between the photoionisation rates of H I and He II. If both species are highly ionised, the softness parameter is related to the column density ratio

$$\eta = \frac{N_{\mathrm{He\,II}}}{N_{\mathrm{H\,I}}} \simeq 0.42S \tag{1.7}$$

that can be measured via comparing the forests of H I and He II (Fardal et al. 1998). The column density ratio indicates the spectral shape of the ionising radiation field. Generally, $\eta \gg 1$ due to $\Gamma_{\mathrm{He\,II}} < \Gamma_{\mathrm{H\,I}}$ and the higher recombination rate of He III compared to H II. A UV background generated by quasars alone will result in $50 \lesssim \eta \lesssim 100$ at $2 \lesssim z \lesssim 3$ (Haardt & Madau 1996; Fardal et al. 1998) depending on the parameterisation of the quasar spectral energy distribution, the luminosity function and the radiative transfer effects. An additional contribution by soft star-forming galaxies will result in $\eta \gtrsim 100$ (Haardt & Madau 2001).

The quasar sightlines that show intergalactic He II absorption proved invaluable to infer the spectral energy distribution of the UV background observationally. The strong trough-like He II absorption at $z \gtrsim 3$ requires $\eta \gg 100$ to be compatible with the optically thin H I forest (Reimers et al. 1997; Heap et al. 2000; Smette et al. 2002; Zheng et al. 2004a; Reimers et al. 2005). Exact numbers strongly depend on the incompleteness correction at small H I column densities that could arise in a more diffuse component of the IGM (Reimers et al. 1997; Heap et al. 2000) and the adopted quasar continuum that is not easily defined due to the strong He II absorption. The voids between the spectral ranges of He II Gunn-Peterson absorption generally require local hard ionising sources, such as luminous quasars (Heap et al. 2000; Smette et al. 2002). The FUSE observations of the He II forest at $z \lesssim 2.7$ revealed large η fluctuations ($1 \lesssim \eta \lesssim 1000$) on small scales of $\lesssim 1$ Mpc with a median $\eta \sim$80–100 that slowly decreases with redshift (Kriss et al. 2001; Zheng et al. 2004b; Fechner et al. 2006). Due to the strong blending of the He II lines at $\eta \gg 1$ and the low quality of the available He II spectra ($S/N \lesssim 4$), the much better constrained line parameters from the H I forest (z, $N_{\mathrm{H\,I}}$, $b_{\mathrm{H\,I}}$) have to be used to constrain the He II column density. The large fluctuations are partly explained by the low data quality (Fechner et al. 2006; Liu et al. 2006) and possible systematic errors due to the generally assumed line broadening mechanism (Fechner & Reimers 2007b). However, some of the observed fluctuations are likely real and several physical reasons for these small-scale spectral shape variations have been proposed, such as local density variations (Miralda-Escudé et al. 2000), radiative transfer effects (Maselli & Ferrara 2005; Tittley & Meiksin 2007) and a fluctuating He II ionisation rate caused by the small number of contributing quasars at any given point in the IGM at $z > 2$ (Bolton et al. 2006).

Further constraints on the spectral shape of the UV background come from metal absorption systems, whose ionisation state can be modelled with photoionisation codes (Savaglio et al. 1997; Songaila 1998; Aguirre et al. 2004; Agafonova et al. 2005; Reimers et al. 2006; Agafonova et al. 2007). However, detailed modelling of the spectral shape requires many observed transitions of different ions to avoid strong assumptions. For instance, different ions of the same species are needed in order to be independent on absorber metallicity. Well-suited metal line systems with many observed transitions are often complex, showing a multi-phase structure (e.g. Lopez et al. 1999) that is difficult to model. Moreover, the absorbers have to be optically thin to obtain the shape of the UV background. Finally, the spectral shape derived from strong H I absorbers with strong associated metal absorption might be influenced by (unknown) galaxies or quasars in their vicinity (Miralda-Escudé 2005; Schaye 2006).

There have been attempts to infer the helium reionisation epoch by photoionisation modelling of metal lines, yielding ambiguous results for (Songaila & Cowie 1996; Songaila 1998) and against (Kim et al. 2002b; Aguirre et al. 2004) an abrupt change in the UV spectral shape at $z \sim 3$ due to rapid He II reionisation. Indeed, Agafonova et al. (2007) found a fluctuating spectral shape at $1.8 \lesssim z \lesssim 2.9$ in agreement with the results from the He II forests.

1.4. The proximity effect

1.4.1. A local radiative impact of quasars on the intergalactic medium

Apart from the general redshift evolution of the UV background intensity, spatial variations of the UV radiation field can arise from the discrete source population (Zuo 1992; Fardal & Shull 1993; Croft et al. 1999; Meiksin & White 2004; Croft 2004; McDonald et al. 2005). Due to the large distances between quasars, these spatial variations should occur on large scales ($\gtrsim 100$ comoving Mpc at $z < 4$) and should have a small amplitude, in particular if the more numerous star-forming galaxies homogenise the H I ionisation rate (e.g. Bolton et al. 2006). In the direct vicinity of a UV source, however, the UV radiation field is expected to be enhanced (Fardal & Shull 1993; Croft 2004; McDonald et al. 2005). As a consequence, near the source the IGM will be more highly ionised than far away from it. This results in a statistically decreased Lyα absorption near the quasar compared to an unaffected region in the IGM that is penetrated only by the quasi-homogeneous background radiation field.

The local influence of a UV source onto the surrounding IGM is known as the proximity effect, which was found on sightlines towards luminous quasars after the first large samples of medium-resolution quasar spectra had been gathered in the 1980s. Historically, Weymann et al. (1981) first suggested that the Lyα line number density near the background quasar is systematically lower than in the rest of the spectrum and that the weakness of the Lyα absorption compared to the corresponding strong C IV absorption indicates a high degree of ionisation. Murdoch et al. (1986) showed that inconsistencies among the early estimates of the line number density evolution of the Lyα forest disappeared when accounting for a counterveiling trend of a decreasing line density near the quasar, which they attributed to the locally enhanced UV radiation field. Knowing the luminosity of the quasar, the line deficit yields an estimate of the UV background intensity at the Lyman limit (Carswell et al. 1987). Bajtlik et al. (1988) presented a detailed ionisation model to calculate the strength of the quasar compared to the background as a function of distance in order to combine the proximity effect signatures of several quasars. Besides establishing the existence of the proximity effect for samples of up to ~ 100 quasars (e.g. Scott et al. 2000) or even on single lines of sight (e.g. Williger et al. 1994; Lu et al. 1996), the simple ionisation model by Bajtlik et al. (1988) was used since then to infer the UV background intensity.

In essence, the ionisation model predicts the relative decrease of the line number density (or equivalently the average absorption) in the presence of a nearby quasar. If the absorbers in the IGM are highly ionised and in photoionisation equilibrium with the overall UV background, the higher degree of ionisation near the quasar linearly reduces the column density of an absorber located at redshift z according to

$$N_{\mathrm{H\,I}}(z) = \frac{N_{\mathrm{H\,I},\infty}(z)}{1+\omega(z)}. \tag{1.8}$$

Here, $N_{\mathrm{H\,I}}$ is the observed column density in presence of the quasar, $N_{\mathrm{H\,I},\infty}$ would have been measured if the quasar was located at infinite distance and

$$\omega(z) = \frac{\Gamma_{\mathrm{q}}(z)}{\Gamma_{\mathrm{b}}(z)} \tag{1.9}$$

is the ratio of the H I photoionisation rates of the quasar and the UV background at the respective redshift. The quasar contribution decreases with increasing distance to the absorber, reasonably approximated by geometric dilution of the ionising flux of the quasar without attenuation by intervening absorbers. The parameter ω quantifies the strength of the proximity effect, with large values resulting in a strong reduction of the column density, and hence a strong proximity effect. If we assume that the quasar luminosity is constant, the ionisation rate of the quasar can be inferred. Please refer to Appendix A.3. for a detailed calculation of ω for a flat cosmological model with a cosmological constant. Since one does not know the intergalactic absorption without the impact of the quasar on its own line of sight ($N_{\mathrm{H\,I},\infty}$ is not observable), one either has to extrapolate the absorption from lower redshifts where the impact of the quasar is negligible, or one has to compare the observed absorption near the quasar with the absorption determined on other sightlines towards higher redshift quasars. Thereby it is implicitly assumed that the quasar resides at a random location in the IGM without particularly strong or weak absorption. If the spectral resolution is high enough to measure distinct absorption lines, the line number density near the background quasar should depart from the usual power law evolution in redshift as

$$\frac{\mathrm{d}\mathcal{N}}{\mathrm{d}z} = A\,(1+z)^{\gamma}\,(1+\omega(z))^{1-\beta} \tag{1.10}$$

with the power law index β of the column density distribution (Bajtlik et al. 1988). Alternatively, statistics of the average forest transmission can be used to reveal a relative lack of absorption near the quasar. Similar to (1.10) we can write for the evolution of the effective optical depth in presence of a quasar

$$\tau_{\mathrm{eff}}(z) = \tau_{\mathrm{eff},\infty}\,(1+\omega(z))^{1-\beta} = B\,(1+z)^{\gamma+1}\,(1+\omega(z))^{1-\beta} \tag{1.11}$$

(Liske & Williger 2001). The effective optical depth can be easily measured at high and low resolution without having to define a line sample, which is impossible at low resolution. Even high resolution line samples are not always well defined due to the complex subjective deblending of the forest into distinct lines. However, when revealing the proximity effect by absorption statistics one has to assume a column density distribution, which cannot be determined self-consistently at low resolution.

1.4.2. The transverse proximity effect

The ionising UV flux of a luminous quasar typically affects a region of $\lesssim 10$ proper Mpc on its own line of sight ($\omega \gtrsim 1$). If the UV emission of quasars is rather isotropic, one should expect that they are located in roughly spherical overionised zones, analogous to Strömgren spheres in the case of neutral material. Lyα forest spectra of background sources located in the projected vicinity to foreground quasars should therefore show a lack of absorption near the foreground quasars, corresponding to radiation-induced voids. Figure 1.3 illustrates this so-called transverse proximity effect. The observed Lyα forest line density of the background quasar B generally increases with redshift (distance). Besides the local decrease in the line density near quasar B, the line of sight intersects the proximity effect zone of the foreground quasar F located at $z_{\mathrm{F}} < z_{\mathrm{B}}$ in close projection to the line of sight at a small separation angle ϑ.

Quantitatively, the ionisation model of the line-of-sight proximity effect can be generalised to incorporate additional ionising sources. For an absorber at redshift z the total impact of n local sources is simply

$$\omega\,(z) = \sum_{j=1}^{n} \omega_j\,(z) \tag{1.12}$$

due to the superposition of the photoionisation rates of the quasars. The derivation of the ionisation rates of foreground quasars is rather complex and is carried out in full detail in Appendix A.

Bajtlik et al. (1988) discussed the transverse proximity effect as a further test of the ionisation hypothesis. However, subsequent searches for underdense regions in the H I Lyα forests near foreground quasars were mostly fuitless or ambiguous. Early studies of fortunate constellations of quasar pairs[1], triplets or quadruplets showed no sign of the expected transverse proximity effect (Crotts 1989; Crotts & Fang 1998; Møller & Kjærgaard 1992) or only marginal evidence (Fernández-Soto et al. 1995). Dobrzycki & Bechtold (1991a) found a large ~ 10 Mpc void at $z = 3.17$ towards the quasar Q 0302−003 located near, but not centred on the foreground quasar Q 0301−005 ($z = 3.231$, $\vartheta = 22\farcm9$). They claimed that the bright foreground quasar causes the void, but found also that the quasar had to be implausibly bright to cause the significant void over the large distance between the lines of sight (Dobrzycki & Bechtold 1991b). A similar large significant void was found by Srianand (1997) towards Tol 1038−2712 apparently centred on Tol 1037−2704 ($z = 2.195$, $\vartheta = 17\farcm9$). However, due to the small number of studied quasar pairs chance coincidences cannot be ruled out completely.

More recently, statistical analyses of newly discovered quasar pairs have been conducted. Schirber et al. (2004) selected three promising close projected quasar pairs from the Early Data Release of the Sloan Digital Sky Survey (SDSS)

---

[1] In this work we use the term quasar pair for two quasars seen in close projection on the sky, either at the same redshift or at different redshifts. We do not distinguish between associated quasar pairs (also called binaries) located at the same redshift (e.g. Hennawi et al. 2006b) and projected ones.

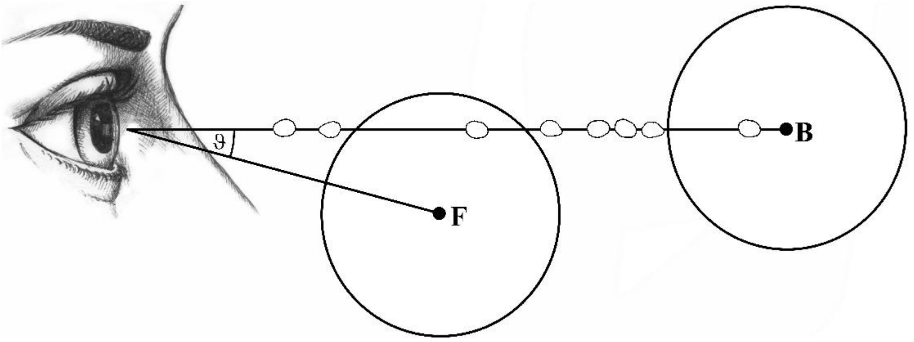

Fig. 1.3. Illustration of the line-of-sight proximity effect of background quasar B and the transverse proximity effect of foreground quasar F.

but did not find the effect. Croft (2004) analysed the absorption near foreground quasars using a larger SDSS sample, but found on average excess absorption instead of the expected excess transmission. However, based on numerical simulations a significant transverse proximity effect was expected only for the $\lesssim 22$ pairs with separations $\lesssim 10h^{-1}$ comoving Mpc. Recently, Kim & Croft (2007) confirmed the average excess absorption using quasar pairs from SDSS Data Release 3. Liske & Williger (2001) studied the transverse proximity effect in a close group of 17 quasars in an area of $\sim 80' \times 80'$ on the sky. Assuming that the effect exists for subsets of their sample grouped by ω they do not find evidence for it in the data, whereas it should have been detectable at the 2–4σ level depending on the number of considered pairs. However, the Lyα forest spectra of four background quasars show common underdense absorption within ±3000 km s^{-1} of a foreground quasar. Liske & Williger (2001) conclude that the transverse proximity effect might be present in this group at the 3.5σ level.

In summary, most existing studies do not find evidence for the general presence of a transverse proximity effect in the H I Lyα forest. Several arguments have been put forward to explain this:

1. *Anisotropic emission:* Unification schemes for active galactic nuclei predict anisotropic emission due to a dusty torus that is opaque to the UV radiation from the accretion disk (e.g. Antonucci 1993; Urry & Padovani 1995). The line-of-sight proximity effect is a common phenomenon in broad-line type I quasars, whose ionisation cone is visible to us. Thus, anisotropic emission might explain either offsets of voids with respect to the quasar (Dobrzycki & Bechtold 1991a) or the absence of the transverse proximity effect (Crotts 1989; Møller & Kjærgaard 1992; Liske & Williger 2001; Schirber et al. 2004). Recently, Hennawi & Prochaska (2007) have inferred an excess of optically thick absorption systems located at $\lesssim 1$ proper Mpc in transverse direction to quasars, which might be explained by anisotropic emission. On the other hand, Schirber et al. (2004) and Croft (2004) argue that unrealistically strong anisotropy is required to fully explain the absence of a transverse proximity effect.
2. *Quasar variability and lifetime:* Quasars are known to be variable on short timescales. Typically, the foreground quasars are located several Mpcs away from the background sightline, corresponding to light travel times of a few to a few tens of Myrs. Variability on timescales of several Myrs will tend to overestimate the predicted transverse proximity effect due to Malmquist bias in the selected quasar pairs (Schirber et al. 2004). Furthermore, the total quasar lifetime (e.g. Martini 2004) sets an upper limit to the extent of the proximity effect zone. Recent numerical simulations of Black Hole growth predict episodic quasar activity (e.g. Hopkins et al. 2005b,a), thereby further complicating the search for a transverse proximity effect (Croft 2004; Adelberger 2004). Thus, quasar variability likely plays a role, but it cannot be the sole explanation for a lacking proximity effect in close pairs (Schirber et al. 2004).
3. *Overdensities:* Quasars likely reside in highly overdense regions compared to the cosmic mean. The expected Lyα absorption without the impact of the quasar is not observable and an unbiased quasar environment is commonly assumed in proximity effect analyses. Consequently, the signature of the proximity effect is likely diminished by unknown intrinsic overdensities (Loeb & Eisenstein 1995; Rollinde et al. 2005; Hennawi & Prochaska 2007; Guimarães et al. 2007; Faucher-Giguère et al. 2007a). In principle, the effect of overdensities can be quantified by numerical simulations (Croft 2004; Rollinde et al. 2005; Faucher-Giguère et al. 2007a). Overdensities near foreground quasars have been revealed by Croft (2004) and Hennawi et al. (2006a), who find optically thick absorption systems at $\Delta v = \pm 1500$ km s^{-1} of 27 foreground quasars in a sample of 149 close pairs.

Wheras a combination of these systematic effects offers enough leverage to explain the absence of a transverse proximity effect, it has been observed near the reionisation epochs of He II (Jakobsen et al. 2003) and H I (Gallerani et al. 2007) as a void in the Gunn-Peterson trough. Already Heap et al. (2000) speculated that a nearby quasar might be responsible for the prominent $z \simeq 3.05$ void in the He II Gunn-Peterson trough towards Q 0302–003. Subsequently, Jakobsen et al. (2003) performed a targeted slitless spectroscopic survey for faint quasars near this sightline and found QSO 03020–0014 coinciding with the void. Due to the vanishingly small probability of chance occurrence, Jakobsen et al. (2003) argued for a transverse proximity effect. Recently, Gallerani et al. (2007) studied a void in the H I Gunn-Peterson trough of SDSS J1148+5251 near the foreground quasar RD J1148+5253 ($z = 5.70$) separated from the background quasar by $1\overset{'}{.}8$. Again the occurrence of the void near the quasar suggests the presence of the transverse proximity effect.

The discovery of the transverse proximity effect provides important constraints on poorly known properties of AGN. The distance between the foreground quasar and the background sightline sets a lower limit to the activity timescale of Black Holes in AGN, a quantity that so far could only be roughly constrained to 1–100 Myr by more indirect means (for a review see e.g. Martini 2004). The detections of the transverse proximity effect yield values of ∼10–30 Myr (Dobrzycki & Bechtold 1991a; Srianand 1997; Jakobsen et al. 2003; Gallerani et al.

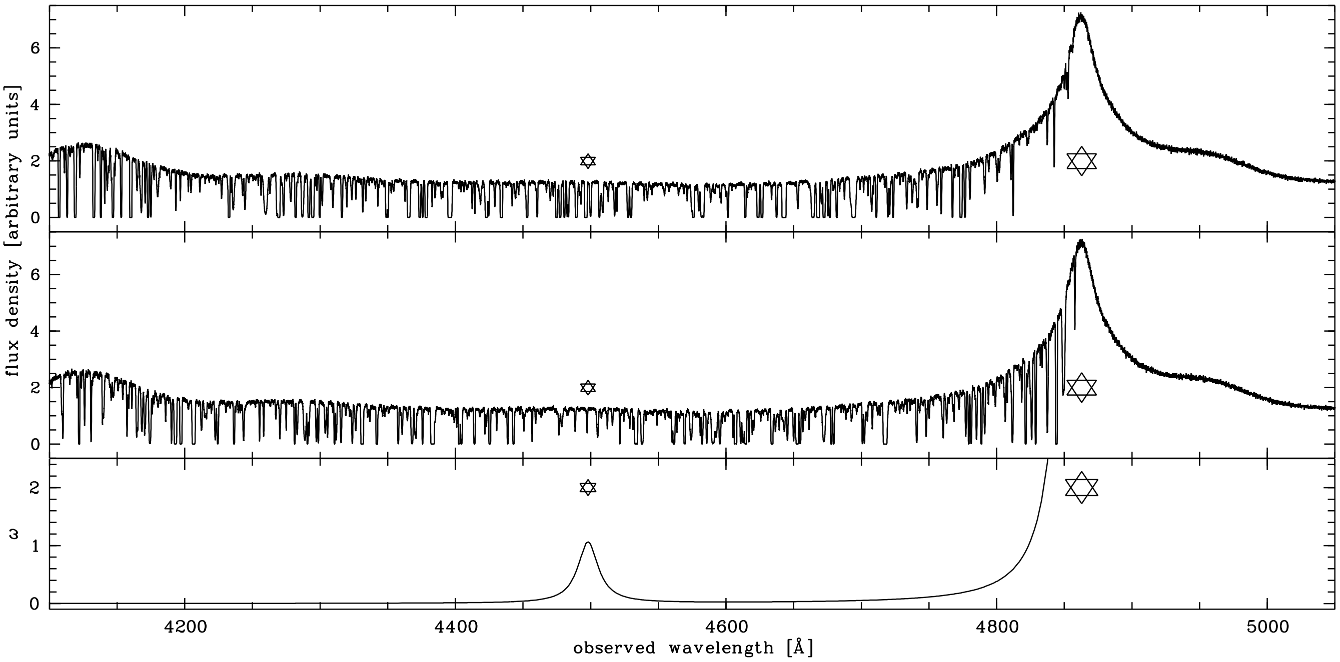

Fig. 1.4. Two simulated quasar spectra with the transverse proximity effect and the line-of-sight proximity effect of two quasars (star symbols). Both spectra have a resolution $R \sim 45000$ and a $S/N \simeq 30$. The proximity effect whose strength is determined by $\omega(z)$ (lowest panel) weakens the simulated H I Lyα forest absorption. The background quasar is at $z = 3.0$ and has a magnitude $V = 17.5$, whereas the foreground quasar is at $z = 2.7$ with a magnitude $V = 20.0$, separated from the background sightline by $\vartheta = 4\farcm6$. In a flat Λ cosmology with $\Omega_\mathrm{m} = 0.3$ and $\Omega_\Lambda = 0.7$ this separation corresponds to 2.19 proper Mpc. The ionising flux of the foreground quasar is lower by a factor 10 compared to the background quasar. Together with the given separation of the sightlines this causes a small $\omega \simeq 1$ of the foreground quasar at its minimum distance.

2007), just within the range of the estimated values. Potential quasar anisotropy can be constrained either by offsets of voids with respect to the quasar or the non-existence of the transverse proximity effect. Finally, even in absence of the transverse proximity effect the surroundings of the quasar can be studied on a background sightline.

Current investigations of the transverse proximity effect are limited by the small number of suitable quasar pairs and groups. Hennawi et al. (2006a) discovered many new quasar pairs by a targeted follow-up of additional quasar candidates near known SDSS quasars. While this study substantially increased the number of quasar pairs, known groups of several quasars around high-redshift quasars are still rare. Conclusive statistical studies of the transverse proximity effect in the H I forest require large numbers of foreground quasars, whose background sightlines are observed at high resolution and high quality in order to reliably quantify the H I absorption near the foreground quasar.

To illustrate this we plot in Fig. 1.4 two simulated high-resolution quasar spectra with a line-of-sight proximity effect and a transverse proximity effect (see Chapter 3 for details on the simulation procedure). Randomly placed Lyα forest lines are superposed on the continuum up to the Lyα emission line of the background quasar at $z = 3.0$. The proximity effect has been simulated by decreasing H I column densities of the lines close to the quasars. We see that the signature of the proximity varies with the H I absorption intrinsically present near the quasars. In the upper panel of Fig. 1.4 the line-of-sight effect is visible by eye, since many lines close to the quasar were intrinsically optically thin and are barely detectable after introducing the line-of-sight proximity effect. The second spectrum was simulated with the same strength of the effect, but strong lines occurring intrinsically near the quasar are just weakened and are therefore still detectable. The faint foreground quasar barely reduces the absorption in its vicinity. In the upper spectrum, strong absorption masks the weak signature of the transverse proximity effect, whereas the in lower spectrum a small decrease in the absorption could be discernable after combining the effect of several such incidences and comparing it to the expected absorption. Given the typically large separations between quasars of several tens of Mpc, any transverse proximity effect is expected to be weak. Thus, statistical studies have to be conducted to infer the transverse proximity effect in the fluctuating absorption of the H I forest.

1.5. Goals and outline of this work

This work has two main objectives

- Discovery of new groups of quasars near known high-redshift quasars in a dedicated survey
- Seach for a transverse proximity effect of foreground quasars in these groups.

Groups of quasars are not only important for studying the transverse proximity effect. They also provide closely spaced sightlines through the intergalactic medium that can be used to characterise its three-dimensional structure. Thus, paired or even grouped quasars offer the potential to gain more widespread insights into the high-redshift IGM. In this work we will discuss only one immediate application of these groups, namely the search for a transverse proximity effect in a statistical manner.

The main part of this work is structured into four chapters, each comprising a stand-alone article. Two manuscripts have been already published in *Astronomy & Astrophysics*, the other two will be submitted in the near future. Each chapter has a separate introduction and a conclusion, which may be redundant in several aspects. With the exception of some figure captions no changes have been made to the manuscripts already published (Chapter 4 and Chapter 5). Thus, they reflect the literature and our knowledge at the time of publication. The analysis presented in Section 5 of Chapter 5 was contributed by Dr. Cora Fechner. The reduction of the UVES data presented in Chapter 3 and Chapter 5 was kindly performed by Aldo Dall' Aglio.

Chapter 2 presents a dedicated slitless spectroscopic survey for faint quasars in the vicinity of 18 well-studied bright high-redshift quasars in order to substantially increase the number of known quasar groups for a study of the transverse proximity effect or the IGM in general. In Chapter 3 we discuss the detectability of the transverse proximity effect in the H I Lyα forest towards these groups of quasars. Two of the quasars in the centres of our survey fields are known to show intergalactic He II absorption. In Chapter 4 we analyse the line of sight towards Q 0302−003 in order to reveal the transverse proximity effect in the H I and/or the He II forest in the projected vicinity of four foreground quasars. In Chapter 5 we perform a similar study of three quasars near the line of sight towards HE 2347−4342. While our attempts to reveal the transverse proximity effect as an underdensity in the forests remain unsuccessful, Chapters 4 and 5 present the first conclusive evidence for a transverse proximity effect detected as a hardness fluctuation in the spectral shape of the intergalactic UV radiation field. We conclude this work with a summary of the main results and a discussion of future perspectives in Chapter 6.

References

Abel, T., Bryan, G. L., & Norman, M. L. 2002, Sci, 295, 93
Adelberger, K. L. 2004, ApJ, 612, 706
Agafonova, I. I., Centurión, M., Levshakov, S. A., & Molaro, P. 2005, A&A, 441, 9
Agafonova, I. I., Levshakov, S. A., Reimers, D., et al. 2007, A&A, 461, 893
Aguirre, A., Schaye, J., Kim, T.-S., et al. 2004, ApJ, 602, 38
Anderson, S. F., Hogan, C. J., Williams, B. F., & Carswell, R. F. 1999, AJ, 117, 56
Antonucci, R. 1993, ARA&A, 31, 473
Bahcall, J. N. & Peebles, P. J. E. 1969, ApJ, 156, L7
Bajtlik, S., Duncan, R. C., & Ostriker, J. P. 1988, ApJ, 327, 570
Bechtold, J. 1994, ApJS, 91, 1
Bechtold, J., Weymann, R. J., Zuo, L., & Malkan, M. A. 1987, ApJ, 315, 180
Bernardi, M., Sheth, R. K., SubbaRao, M., et al. 2003, AJ, 125, 32
Bi, H., Börner, G., & Chu, Y. 1992, A&A, 266, 1
Bi, H. & Davidsen, A. F. 1997, ApJ, 479, 523
Bianchi, S., Cristiani, S., & Kim, T.-S. 2001, A&A, 376, 1
Bolton, J. S., Haehnelt, M. G., Viel, M., & Carswell, R. F. 2006, MNRAS, 366, 1378
Bolton, J. S., Haehnelt, M. G., Viel, M., & Springel, V. 2005, MNRAS, 357, 1178
Bouwens, R. J., Illingworth, G. D., Blakeslee, J. P., & Franx, M. 2006, ApJ, 653, 53
Bromm, V., Coppi, P. S., & Larson, R. B. 2002, ApJ, 564, 23
Bromm, V. & Loeb, A. 2003, Nat, 425, 812
Bryan, G. L., Machacek, M., Anninos, P., & Norman, M. L. 1999, ApJ, 517, 13
Bunker, A., Stanway, E., Ellis, R., et al. 2006, New Astronomy Reviews, 50, 94
Carswell, R. F., Webb, J. K., Baldwin, J. A., & Atwood, B. 1987, ApJ, 319, 709
Cen, R., Miralda-Escudé, J., Ostriker, J. P., & Rauch, M. 1994, ApJ, 437, L9
Ciardi, B. & Ferrara, A. 2005, Space Science Reviews, 116, 652
Cooke, A. J., Espey, B., & Carswell, R. F. 1997, MNRAS, 284, 552
Cristiani, S., D'Odorico, S., Fontana, A., Giallongo, E., & Savaglio, S. 1995, MNRAS, 273, 1016
Croft, R. A. C. 2004, ApJ, 610, 642
Croft, R. A. C., Weinberg, D. H., Katz, N., & Hernquist, L. 1997, ApJ, 488, 532
Croft, R. A. C., Weinberg, D. H., Pettini, M., Hernquist, L., & Katz, N. 1999, ApJ, 520, 1
Crotts, A. P. S. 1989, ApJ, 336, 550
Crotts, A. P. S. & Fang, Y. 1998, ApJ, 502, 16
Davé, R., Hernquist, L., Katz, N., & Weinberg, D. H. 1999, ApJ, 511, 521
Davidsen, A. F., Kriss, G. A., & Zheng, W. 1996, Nat, 380, 47
Desjacques, V., Nusser, A., & Sheth, R. K. 2007, MNRAS, 374, 206
Dobrzycki, A. & Bechtold, J. 1991a, ApJ, 377, L69
Dobrzycki, A. & Bechtold, J. 1991b, in ASP Conf. Ser. 21: The Space Distribution of Quasars, 272
Espey, B. R. 1993, ApJ, 411, L59
Fan, X., Narayanan, V. K., Lupton, R. H., et al. 2001, AJ, 122, 2833
Fan, X., Strauss, M. A., Becker, R. H., et al. 2006, AJ, 132, 117
Fardal, M. A., Giroux, M. L., & Shull, J. M. 1998, AJ, 115, 2206
Fardal, M. A. & Shull, J. M. 1993, ApJ, 415, 524
Faucher-Giguère, C.-A., Lidz, A., Zaldarriaga, M., & Hernquist, L. 2007a, ApJ,submitted, astro-ph/0701042
Faucher-Giguère, C.-A., Prochaska, J. X., Lidz, A., Hernquist, L., & Zaldarriaga, M. 2007b, ApJ,submitted, arXiv:0709.2382
Fechner, C. & Reimers, D. 2007a, A&A, 463, 69
Fechner, C. & Reimers, D. 2007b, A&A, 461, 847
Fechner, C., Reimers, D., Kriss, G. A., et al. 2006, A&A, 455, 91
Fernández-Soto, A., Barcons, X., Carballo, R., & Webb, J. K. 1995, MNRAS, 277, 235
Gallerani, S., Ferrara, A., Fan, X., & Roy Choudhury, T. 2007, MNRAS, submitted, arXiv:0706.1053
Gaskell, C. M. 1982, ApJ, 263, 79
Giallongo, E., Cristiani, S., D'Odorico, S., Fontana, A., & Savaglio, S. 1996, ApJ, 466, 46
Giallongo, E., Cristiani, S., Fontana, A., & Trèvese, D. 1993, ApJ, 416, 137
Gleser, L., Nusser, A., Benson, A. J., Ohno, H., & Sugiyama, N. 2005, MNRAS, 361, 1399
Gnedin, N. Y. 2000, ApJ, 535, 530
Guimarães, R., Petitjean, P., Rollinde, E., et al. 2007, MNRAS, 377, 657
Gunn, J. E. & Peterson, B. A. 1965, ApJ, 142, 1633
Haardt, F. & Madau, P. 1996, ApJ, 461, 20
Haardt, F. & Madau, P. 2001, in Clusters of Galaxies and the High Redshift Universe Observed in X-rays, ed. D. M. Neumann & J. T. T. Van, 64
Heap, S. R., Williger, G. M., Smette, A., et al. 2000, ApJ, 534, 69
Heger, A. & Woosley, S. E. 2002, ApJ, 567, 532
Hennawi, J. F. & Prochaska, J. X. 2007, ApJ, 655, 735
Hennawi, J. F., Prochaska, J. X., Burles, S., et al. 2006a, ApJ, 651, 61
Hennawi, J. F., Strauss, M. A., Oguri, M., et al. 2006b, AJ, 131, 1
Hernquist, L., Katz, N., Weinberg, D. H., & Miralda-Escudé, J. 1996, ApJ, 457, L51
Hogan, C. J., Anderson, S. F., & Rugers, M. H. 1997, AJ, 113, 1495
Hopkins, P., Hernquist, L., Cox, T. J., et al. 2005a, ApJ, 630, 705
Hopkins, P., Hernquist, L., Martini, P., et al. 2005b, ApJ, 625, L71
Hu, E. M., Kim, T.-S., Cowie, L. L., & Songaila, A. 1995, AJ, 110, 1526
Hui, L. & Rutledge, R. E. 1999, ApJ, 517, 541
Hunt, M. P., Steidel, C. C., Adelberger, K. L., & Shapley, A. E. 2004, ApJ, 605, 625
Iliev, I. T., Mellema, G., Pen, U.-L., et al. 2006, MNRAS, 369, 1625
Iliev, I. T., Mellema, G., Shapiro, P. R., & Pen, U.-L. 2007, MNRAS, 376, 534
Jakobsen, P. 1998, A&A, 335, 876
Jakobsen, P., Boksenberg, A., Deharveng, J. M., et al. 1994, Nat, 370, 35
Jakobsen, P., Jansen, R. A., Wagner, S., & Reimers, D. 2003, A&A, 397, 891
Jena, T., Norman, M. L., Tytler, D., et al. 2005, MNRAS, 361, 70
Kim, T.-S., Bolton, J. S., Viel, M., Haehnelt, M. G., & Carswell, R. F. 2007, MNRAS,accepted, arXiv:0711.1862
Kim, T.-S., Carswell, R. F., Cristiani, S., D'Odorico, S., & Giallongo, E. 2002a, MNRAS, 335, 555
Kim, T.-S., Cristiani, S., & D'Odorico, S. 2001, A&A, 373, 757
Kim, T.-S., Cristiani, S., & D'Odorico, S. 2002b, A&A, 383, 747
Kim, T.-S., Hu, E. M., Cowie, L. L., & Songaila, A. 1997, AJ, 114, 1
Kim, Y.-R. & Croft, R. 2007, MNRAS,submitted, astro-ph/0701012
Kirkman, D., Tytler, D., Suzuki, N., et al. 2005, MNRAS, 360, 1373
Kriss, G. A., Shull, J. M., Oegerle, W., et al. 2001, Sci, 293, 1112
Kuhlen, M. & Madau, P. 2004, MNRAS, 363, 1069
Kulkarni, V. P. & Fall, S. M. 1993, ApJ, 413, L63
Liske, J. & Williger, G. M. 2001, MNRAS, 328, 653
Liu, J., Jamkhedkar, P., Zheng, W., Feng, L.-L., & Fang, L.-Z. 2006, ApJ, 645, 861
Loeb, A. & Eisenstein, D. J. 1995, ApJ, 448, 17
Lopez, S., Reimers, D., Rauch, M., Sargent, W. L. W., & Smette, A. 1999, ApJ, 513, 598
Lu, L., Sargent, W. L. W., Womble, D. S., & Takada-Hidai, M. 1996, ApJ, 472, 509
Lu, L., Wolfe, A. M., & Turnshek, D. A. 1991, ApJ, 367, 19
Lynds, R. 1971, ApJ, 164, L73
Madau, P., Haardt, F., & Rees, M. J. 1999, ApJ, 514, 648
Martini, P. 2004, in Carnegie Observatories Astrophysics Series Vol. 1: Coevolution of Black Holes and Galaxies, ed. L. C. Ho (Cambridge University Press), 170

Maselli, A. & Ferrara, A. 2005, MNRAS, 364, 1429
McDonald, P., Miralda-Escudé, J., Rauch, M., et al. 2000, ApJ, 543, 1
McDonald, P., Seljak, U., Cen, R., Bode, P., & Ostriker, J. P. 2005, MNRAS, 360, 1471
Meiksin, A. 2005, MNRAS, 356, 596
Meiksin, A. & White, M. 2004, MNRAS, 350, 1107
Miniati, F., Ferrara, A., White, S. D. M., & Bianchi, S. 2004, MNRAS, 348, 964
Miralda-Escudé, J. 2005, ApJ, 620, L91
Miralda-Escudé, J., Cen, R., Ostriker, J. P., & Rauch, M. 1996, ApJ, 471, 582
Miralda-Escudé, J., Haehnelt, M., & Rees, M. J. 2000, ApJ, 530, 1
Møller, P. & Jakobsen, P. 1990, A&A, 228, 299
Møller, P. & Kjærgaard, P. 1992, A&A, 258, 234
Murdoch, H. S., Hunstead, R. W., Pettini, M., & Blades, J. C. 1986, ApJ, 309, 19
Oh, S. P., Nollett, K. M., Madau, P., & Wasserburg, G. J. 2001, ApJ, 562, L1
Page, L., Hinshaw, G., Komatsu, E., et al. 2007, ApJS, 170, 335
Paschos, P., Norman, M. L., Bordner, J. O., & Harkness, R. 2007, arXiv:0711.1904
Petitjean, P., Webb, J. K., Carswell, R. F., & Lanzetta, K. 1993, MNRAS, 262, 499
Picard, A. & Jakobsen, P. 1993, A&A, 276, 331
Press, W. H., Rybicki, G. B., & Schneider, D. P. 1993, ApJ, 414, 64
Rauch, M. 1998, ARA&A, 36, 267
Rauch, M., Miralda-Escudé, J., Sargent, W. L. W., et al. 1997, ApJ, 489, 7
Reimers, D., Agafonova, I. I., Levshakov, S. A., et al. 2006, A&A, 449, 9
Reimers, D., Fechner, C., Hagen, H.-J., et al. 2005, A&A, 442, 63
Reimers, D., Köhler, S., Wisotzki, L., et al. 1997, A&A, 327, 890
Ricotti, M., Gnedin, N. Y., & Shull, J. M. 2000, ApJ, 534, 41
Ricotti, M. & Ostriker, J. P. 2004a, MNRAS, 350, 539
Ricotti, M. & Ostriker, J. P. 2004b, MNRAS, 352, 547
Rollinde, E., Srianand, R., Theuns, T., Petitjean, P., & Chand, H. 2005, MNRAS, 361, 1015
Sargent, W. L. W., Young, P. J., Boksenberg, A., & Tytler, D. 1980, ApJS, 42, 41
Savaglio, S., Christiani, S., D'Odorico, S., et al. 1997, A&A, 318, 347
Scannapieco, E., Schneider, R., & Ferrara, A. 2003, ApJ, 589, 35
Schaye, J. 2001, ApJ, 559, 507
Schaye, J. 2006, ApJ, 643, 59
Schaye, J., Aguirre, A., Kim, T.-S., et al. 2003, ApJ, 596, 768
Schaye, J., Theuns, T., Rauch, M., Efstathiou, G., & Sargent, W. L. W. 2000, MNRAS, 318, 817
Schirber, M. & Bullock, J. S. 2003, ApJ, 584, 110
Schirber, M., Miralda-Escudé, J., & McDonald, P. 2004, ApJ, 610, 105
Schmidt, M., Schneider, D. P., & Gunn, J. E. 1995, AJ, 110, 68
Schneider, D. P., Richards, G. T., Fan, X., et al. 2002, AJ, 123, 567
Scott, J., Bechtold, J., Dobrzycki, A., & Kulkarni, V. P. 2000, ApJS, 130, 67
Scott, J., Bechtold, J., Morita, M., Dobrzycki, A., & Kulkarni, V. P. 2002, ApJ, 571, 665
Scott, J., Kriss, G. A., Brotherton, M., et al. 2004, ApJ, 615, 135
Seljak, U., McDonald, P., & Makarov, A. 2003, MNRAS, 342, L79
Shull, J. M., Tumlinson, J., Giroux, M. L., Kriss, G. A., & Reimers, D. 2004, ApJ, 600, 570
Smette, A., Heap, S. R., Williger, G. M., et al. 2002, ApJ, 564, 542
Sokasian, A., Abel, T., & Hernquist, L. 2002, MNRAS, 332, 601
Sokasian, A., Abel, T., & Hernquist, L. 2003, MNRAS, 340, 473
Songaila, A. 1998, AJ, 115, 2184
Songaila, A. 2004, AJ, 127, 2598
Songaila, A. & Cowie, L. L. 1996, AJ, 112, 335
Spergel, D. N., Bean, R., Doré, O., et al. 2007, ApJS, 170, 377
Srianand, R. 1997, ApJ, 478, 511
Srianand, R. & Khare, P. 1996, MNRAS, 280, 767
Telfer, R. C., Zheng, W., Kriss, G. A., & Davidsen, A. F. 2002, ApJ, 565, 773
Theuns, T., Zharoubi, S., Kim, T.-S., Tzanavaris, P., & Carswell, R. F. 2002, MNRAS, 332, 367
Tittley, E. R. & Meiksin, A. 2007, MNRAS, 380, 1369
Tytler, D. 1987, ApJ, 321, 49
Tytler, D., Kirkman, D., O'Meara, J. M., et al. 2004, ApJ, 617, 1
Urry, C. M. & Padovani, P. 1995, PASP, 107, 803
Venkatesan, A., Tumlinson, J., & Shull, J. M. 2003, ApJ, 584, 621
Warren, S. J., Hewett, P. C., & Osmer, P. S. 1994, ApJ, 421, 412
Weymann, R. J., Carswell, R. F., & Smith, M. G. 1981, ARA&A, 19, 41
Williger, G. M., Baldwin, J. A., Carswell, R. F., et al. 1994, ApJ, 428, 574
Wyithe, J. S. B. & Cen, R. 2007, ApJ, 659, 890
Wyithe, J. S. B. & Loeb, A. 2003, ApJ, 586, 693
Zhang, Y., Anninos, P., & Norman, M. L. 1995, ApJ, 453, L57
Zhang, Y., Anninos, P., Norman, M. L., & Meiksin, A. 1997, ApJ, 485, 496
Zhang, Y., Meiksin, A., Anninos, P., & Norman, M. L. 1998, ApJ, 495, 63
Zheng, W., Chiu, K., Anderson, S. F., et al. 2004a, AJ, 127, 656
Zheng, W., Kriss, G. A., Deharveng, J.-M., et al. 2004b, ApJ, 605, 631
Zuo, L. 1992, MNRAS, 258, 36
Zuo, L. 1993, A&A, 278, 343

Chapter 2

A slitless spectroscopic survey for quasars near quasars[⋆]

G. Worseck

ABSTRACT

We present the results of a CCD-based slitless spectroscopic survey for faint $V \lesssim 22$ quasars at $1.7 \lesssim z \lesssim 3.6$ on 18 $26\farcm2 \times 33\farcm5$ fields centred on bright quasars at $2.76 < z < 4.69$. In total 169 quasar candidates with emission lines were selected from the extracted flux-calibrated spectra on the basis of well-defined automatic selection criteria followed by visual inspection and verification. With follow-up spectroscopy of 81 candidates that were likely to reside at $z > 1.7$ we were able to confirm 80 new quasars at $0.580 \leq z \leq 3.586$ on 16 of our fields. 64 of the newly discovered quasars are located at $z > 1.7$. The overall high success rate implies that most of the remaining 88 candidates are quasars as well, although the majority of them likely resides at $z < 1.7$ on the basis of the observed line shapes and strengths. Due to the insufficient depth of the input source catalogues needed for extraction of the slitless spectra our survey is not well defined in terms of limiting magnitude for faint $2.5 \lesssim z \lesssim 3.6$ quasars whose Lyα emission is detectable well beyond $V = 22$, albeit at a continuum $S/N \lesssim 1$. While not useful for characterising the evolving space density of quasars, our sample provides many new closely spaced quasar sightlines around intensely studied quasars for further investigations on the three-dimensional distribution of the intergalactic medium.

2.1. Introduction

Recent large surveys such as the Sloan Digital Sky Survey (SDSS) and the 2dF QSO Redshift Survey (2QZ) have revealed thousands of previously unknown quasars selected on the basis of their broadband optical colours (Schneider et al. 2007; Croom et al. 2004). Colour selection is efficient if quasar candidates are well separated from main-sequence stars in multidimensional colour space, most notably at $z \lesssim 2.2$ (UV excess) and at $z \gtrsim 3.5$. However, even multicolour surveys are systematically incomplete at $2.5 \lesssim z \lesssim 3.5$, where the colours of quasars and stars are similar (e.g. Warren et al. 1991; Richards et al. 2002a). Incompleteness due to similar broadband colours can be significantly reduced by a finer tracing of the quasar spectral energy distributions via mediumband filters, e.g. in the COMBO-17 survey (Wolf et al. 2003).

Alternatively, slitless spectroscopy can be used to select high-redshift quasars on the basis of their broad emission lines. Large slitless spectroscopic surveys based on digitised photographic plates, such as the Large Bright Quasar Survey (LBQS, Hewett et al. 1995) or the Hamburg/ESO Survey (HES, Wisotzki et al. 2000), focused on finding bright $z \lesssim 3$ quasars. In conjunction with the multi-colour surveys, the systematic CCD-based slitless survey for $2.7 \lesssim z \lesssim 4.8$ quasars by Schneider et al. (1994) quantified the declining space density of high-redshift quasars (Warren et al. 1994; Schmidt et al. 1995). Automatic quasar detection routines enabled the quantification of selection effects in slitless surveys (Clowes et al. 1984; Hewett et al. 1985; Schmidt et al. 1986).

The combination of a bright magnitude limit and a reduced selection efficiency limits the prospects to find projected quasar pairs and groups at $2.2 \lesssim z \lesssim 3.5$ in colour surveys (however see Hennawi et al. 2006). Indeed, many well-studied close groups of quasars at $z > 2$ have been found by slitless spectroscopy. Already early deep slitless quasar surveys established groups of high-redshift quasars that became invaluable for probing the three-dimensional distribution of the intergalactic matter. Follow-up spectroscopy of candidates by Bohuski & Weedman (1979) on 2.1 deg^2 revealed 13 $z > 1.5$ quasars (Jakobsen & Perryman 1992) with two quasars showing correlated complex intergalactic C IV absorption at $1.48 < z < 2.15$, indicative of an elongated supercluster extending over $17\farcm9$ on the sky (e.g. Jakobsen et al. 1986; Dinshaw & Impey 1996). Another remarkable group discovered by Sramek & Weedman (1978) contains up to now 6 QSOs at $2.49 \leq z \leq 3.45$ within a radius of $20'$ around Q 1623+2653 that are bright enough for correlation studies of the intergalactic medium (e.g. Crotts & Fang 1998) and its relation to galaxies (Adelberger et al. 2005). Furthermore, Williger et al. (1996) reported 25 $1.5 \lesssim z \lesssim 3.4$ quasars within a ~ 1 deg^2 region from an objective prism survey in the south Galactic cap and used these to reveal large-scale structure in the intergalactic Lyα and C IV absorption (Williger et al. 2000; Liske et al. 2000). At lower redshifts, slitless surveys revealed large associations of quasars at similar redshift among other projected quasars (Crampton et al. 1990; Clowes et al. 1999).

Recent deep multi-wavelength surveys on selected fields have also been successful to discover groups of quasars. Among the fields recently investigated are the Chandra Deep Field North (Barger et al. 2003; Cowie et al. 2004) and South (Szokoly et al. 2004; Wolf et al. 2004), the Marano field (Zitelli et al. 1992; Krumpe et al. 2007) or the COSMOS field (Prescott et al. 2006; Trump et al. 2007). However, the majority of the revealed quasars and AGN are typically too faint for follow-up studies at high resolution with current instruments, leaving only sparse distributions of sufficiently bright quasars that can be observed at medium spectral resolution.

Targeted deep surveys of sky regions around well-studied high-redshift quasars are rare. Many of the fields selected for

---

[⋆] A version of this chapter will be submitted to *Astronomy & Astrophysics*. The complete list of authors will appear on the submitted manuscript.

the Lyman-break galaxy survey by Steidel et al. (2003) had been centred on bright quasars to correlate the galaxies with the intergalactic absorption along the sightline (Adelberger et al. 2005). The tomography of the $z > 1.7$ intergalactic medium at high resolution has so far been limited by the small number of suitable groups of bright quasars (e.g. D'Odorico et al. 2002, 2006). However, groups of $V \gtrsim 20$ quasars only allow for medium-resolution spectroscopy at best. Therefore, fainter quasars near bright ones provide a reasonable compromise. In fact, low-resolution spectra of faint quasars in the surroundings of bright quasars improve the velocity reconstruction of high-resolution spectra of the bright quasars in attempts to recover the large-scale topology of the intergalactic medium in three dimensions (Pichon et al. 2001).

In order to increase the number of $1.7 \lesssim z \lesssim 3.6$ quasar groups on the southern hemisphere we embarked on a slitless spectroscopic survey for faint $V \lesssim 22$ quasars in the vicinity of known bright $z > 2.7$ quasars that had been observed with the UV-Visual Echelle Spectrograph (UVES) at the VLT. Results on two fields were reported in Worseck & Wisotzki (2006) (Chapter 4) and Worseck et al. (2007) (Chapter 5 of this thesis). This paper is devoted to the entire survey. In Sect. 2.2 we describe the slitless survey observations. Section 2.3 presents the automatic reduction pipeline developed for this dataset. Section 2.4 elucidates the semi-automatic selection of quasar candidates. Slit spectroscopy of a subset of the candidates is presented in Sect. 2.5, followed by a comparison of the confirmed quasars and the remaining candidates (Sect. 2.6). In Sect. 2.7 we analyse the completeness of our survey and compare it to the results of other surveys. We conclude in Sect. 2.8.

2.2. Survey observations

The survey was carried out using the ESO Wide Field Imager (WFI, Baade et al. 1999) at the ESO/MPI 2.2 m Telescope (La Silla) in its slitless spectroscopic mode (Wisotzki et al. 2001). Since this mode was not frequently used we will shortly describe its main characteristics.

The WFI is a focal-reducer type camera offering a field of view of $34' \times 33'$ sampled by a mosaic of 8 2k×4k CCDs with $0\farcs238$/pixel. In the slitless spectroscopic mode a low-resolution grism is placed in the converging beam of the telescope in front of the WFI in order to disperse the light of every object in the field of view. A blue-blazed grism and a red-blazed grism are available, however, the red-blazed grism (R50, dispersion ~ 7Å/pixel, blaze wavelength 6000Å, $\Delta\lambda \sim 50$Å FWHM) has a much higher throuhput for 1st-order spectroscopy even in the blue (Wisotzki et al. 2001), rendering the blue-blazed B50 grism almost obsolete. The grisms do not yield usable spectra on a $7\farcs2$ strip on the left side of the chip mosaic, effectively reducing the original field of view to $25' \times 33'$ given by 6 of the 8 WFI CCDs.

During two visitor mode runs in October 2002 and February 2003 we observed in total 18 $26\farcm2 \times 33\farcm5$ fields centred on bright high-redshift quasars in order to find faint quasars in their surroundings. The sky transparency during the October 2002 run was variable with some thick cirrus clouds passing occasionally, but mostly the sky was clear. Conditions were clear to photometric in the February 2003 run. The seeing varied during the nights and ranged from $0\farcs8$ to $> 2''$. With the inserted R50 grism ($\lambda/\Delta\lambda = 30$–$50$ depending on the seeing) slitless spectra were recorded. We employed the broadband B and V filters of the WFI to reduce the effectively undispersed sky background and the degree of crowding by limiting the length of the spectra. Crowding was further accounted for by taking the spectra in two instrument rotations (0° and 10°). For all fields except the one centred on BR 1202−0725 three dithered 600 s exposures were taken per band and rotation, resulting in a total exposure time of 1 h per band and yielding a limiting magnitude of $V_{\mathrm{lim}} \simeq 22$. Figure 2.1 illustrates the observing pattern. The dithered exposures produced a contiguous $\sim 26\farcm2 \times 33\farcm5$ field of view per rotation angle. The combination of the R50 grism with the broadband B and V filters resulted in a spectral coverage from the blue grism sensitivity cutoff at 4200 Å to 5800 Å. An unfiltered spectrum of the low-redshift emission-line galaxy HE 1250−0256 provided a rough wavelength calibration of the slitless data. The spectrophotometric standard stars HD 49798, LTT 7987 and GD 108 were observed in astronomical twilight for relative flux calibration. Blank sky fields observed during twilight provided accurate flatfields. The V band exposures of the field centred on PKS 0528−250 were retrieved from the ESO Science Archive (PI L. Vanzi). Table 2.1 summarises the slitless survey observations.

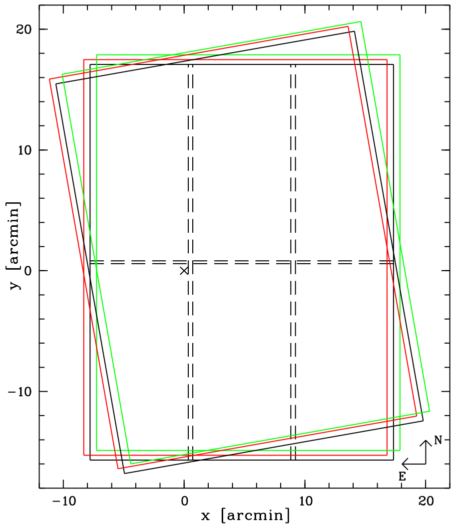

Fig. 2.1. Schematic view of the WFI dither pattern. The full lines denote the edges of the $25\farcm1 \times 32\farcm7$ field of view in the dithered 600 s exposures. Dashed lines mark the 6 2k×4k chips with the inter-chip gaps. After rotating the instrument by 10° about its origin in the focal plane (cross) three further 600 s exposures were taken.

Due to the rotation of the instrument the field edges got only $\sim 1/2$ of the exposure time. Moreover, spectra located near chip gaps are affected by dithering. The net exposure time per field is further decreased for some objects due to contamination by nearby other sources or spectral orders of bright stars (see Fig. 2.3 below). However, the two instrument rotations ensured that a clean spectrum of almost every object was obtained. Due to these effects that are difficult to calculate in detail, we assume a quasi-homogeneously exposed nominal field of view of $26\farcm2 \times 33\farcm5$ per field, yielding a total surveyed area of $\simeq 4.39$ deg^2.

Direct images are necessary for object identification in the slitless data. We primarily relied on images from the First Generation Digitised Sky Survey (DSS) available for all our fields. Three fields were also analysed with direct WFI BVR images taken in service mode.

Table 2.1. Observing log of the slitless survey observations. The columns list the quasar at the field centre with redshift and celestial coordinates, the night of observation, the employed filters, instrument rotations, total exposure time per band and the seeing.

Field	$z_{\rm QSO}$	α (J2000)	δ (J2000)	Night	Filters	Rotations [°]	Exposure [s]	Seeing [$''$]
Q 0000−26	4.125	$00^{\rm h}03^{\rm m}22.^{\rm s}91$	$-26^\circ03'16.''8$	03 Oct 2002	*B*, *V*	0	1800	0.7–1.0
				04 Oct 2002	*B*, *V*	10	1800	0.9–1.4
Q 0002−422	2.767	$00^{\rm h}04^{\rm m}48.^{\rm s}11$	$-41^\circ57'28.''8$	01 Oct 2002	*B*, *V*	0, 10	3600	1.3–1.6
H 0055−269	3.665	$00^{\rm h}57^{\rm m}57.^{\rm s}92$	$-26^\circ43'14.''2$	02 Oct 2002	*B*, *V*	0, 10	3600	0.9–1.5
Q 0302−003	3.285	$03^{\rm h}04^{\rm m}49.^{\rm s}86$	$-00^\circ08'13.''4$	03 Oct 2002	*B*, *V*	0	1800	0.9
				03 Oct 2002	*B*	10	1800	0.9
				04 Oct 2002	*V*	10	1800	0.9–1.1
Q 0347−383	3.220	$03^{\rm h}49^{\rm m}43.^{\rm s}68$	$-38^\circ10'31.''3$	27 Feb 2003	*B*, *V*	10	1800	1.0
				27 Feb 2003	*V*	0	1800	1.0
				28 Feb 2003	*B*	0	1800	1.9
CTQ 0247	3.025	$04^{\rm h}07^{\rm m}17.^{\rm s}99$	$-44^\circ10'13.''4$	30 Sep 2002	*B*, *V*	0	1800	1.3–1.8
				01 Oct 2002	*B*, *V*	10	1800	1.4–1.8
Q 0420−388	3.120	$04^{\rm h}22^{\rm m}14.^{\rm s}81$	$-38^\circ44'52.''9$	26 Feb 2003	*B*, *V*	0, 10	3600	0.8
PKS 0528−250	2.813	$05^{\rm h}30^{\rm m}07.^{\rm s}96$	$-25^\circ03'29.''9$	03 Nov 2002	*V*	10	1800	1.1
				04 Nov 2002	*V*	0	1800	1.2
				28 Feb 2003	*B*	0, 10	3600	1.2
HE 0940−1050	3.088	$09^{\rm h}42^{\rm m}53.^{\rm s}40$	$-11^\circ04'25.''0$	26 Feb 2003	*B*, *V*	0, 10	3600	0.8
CTQ 0460	3.139	$10^{\rm h}39^{\rm m}09.^{\rm s}51$	$-23^\circ13'25.''7$	27 Feb 2003	*B*, *V*	0, 10	3600	1.0–1.5
BR 1117−1329	3.958	$11^{\rm h}20^{\rm m}10.^{\rm s}30$	$-13^\circ46'25.''0$	28 Feb 2003	*B*, *V*	0, 10	3600	> 2
BR 1202−0725	4.690	$12^{\rm h}05^{\rm m}23.^{\rm s}12$	$-07^\circ42'32.''5$	26 Feb 2003	*B*, *V*	0	1800	0.8
				27 Feb 2003	*V*	10	1800	1.6
Q 1209+0919	3.291	$12^{\rm h}11^{\rm m}34.^{\rm s}95$	$+09^\circ02'20.''9$	27 Feb 2003	*B*, *V*	0, 10	3600	1.6
Q 1451+123	3.246	$14^{\rm h}54^{\rm m}18.^{\rm s}61$	$+12^\circ10'54.''8$	28 Feb 2003	*B*, *V*	0, 10	3600	0.8–2.0
PKS 2126−15	3.285	$21^{\rm h}29^{\rm m}12.^{\rm s}18$	$-15^\circ38'41.''0$	30 Sep 2002	*B*, *V*	0, 10	3600	0.8–1.0
Q 2139−4434	3.214	$21^{\rm h}42^{\rm m}25.^{\rm s}81$	$-44^\circ20'17.''2$	03 Oct 2002	*B*, *V*	0, 10	3600	1.0–1.5
HE 2243−6031	3.010	$22^{\rm h}47^{\rm m}09.^{\rm s}10$	$-60^\circ15'45.''0$	02 Oct 2002	*B*, *V*	0, 10	3600	1.0–1.7
HE 2347−4342	2.885	$23^{\rm h}50^{\rm m}34.^{\rm s}21$	$-43^\circ25'59.''6$	04 Oct 2002	*B*, *V*	0, 10	3600	0.8–1.2

2.3. Survey data reduction

2.3.1. Pipeline processing

The slitless data were reduced with a semi-automatic pipeline under ESO MIDAS using existing software developed for HES and writing new programmes where necessary. Each exposure was reduced separately before combining the extracted spectra. Data reduction comprised the following steps:

1. *Bias subtraction:* Bias subtraction was performed by taking the median of the overscan regions of each WFI chip and subtracting it from the science exposure. This procedure assured that the actual bias got subtracted, since restarts of the electronics were necessary a few times, altering the bias level.
2. *Flatfielding:* The flatfielding of slitless spectroscopic data is complicated by the fact that in a science exposure a pixel of a slitless spectrum receives the effectively undispersed broadband sky background and nearly monochromatic light from the object, whereas it is exposed only to the undispersed broadband skylight when obtaining the twilight flatfield. After some experimentation, we obtained good master flatfields by normalising the individual flatfield frames by a smoothed 3rd-order polynomial fit along the dispersion direction followed by averaging the normalised images. Flatfielding of the science data was performed by dividing by the appropriate master flatfield.
3. *Sky subtraction:* The sky background was subtracted using a background image created after masking the spectra using a programme developed for HES. First, the mode of the image was estimated in coarse cells before masking the regions containing spectra by a σ-clipping algorithm. After that the average of the unmasked pixels was computed on a finer grid and the variable background is determined by bilinear interpolation. The parameters for creating the masks were varied until the sky-subtracted image was free from artifacts due to over- or undersubtraction near the spectra of bright objects and the sky level was consistent with zero.
4. *Astrometric transformation:* Bright stars on the Digitised Sky Survey images were used for an astrometric transformation that yielded the coordinates for the extraction of the spectra. An automated object search routine developed for HES was used to generate source lists of the DSS images that were then matched to their 1st order spectra on the slitless images. In fact, the initial visual matching of several objects on each field taking into account the rotated field of view was the only major reduction step requiring human intervention. The computed linear plate model was then refined by automatically locating spectra of fainter objects and excluding outliers (overlapping spectra) interactively. The cutoff of the object flux at the red end of the used filter yielded a well-defined fixpoint for all considered sources. Finally, each chip contained a grid of $\sim$ 15–50 sources that provided an accurate mapping between the DSS coordinates and the 1st-order spectral positions on the WFI field.
5. *Input source catalogue:* The object search routine was used to generate deep source lists of the DSS images. We required an object to have at least 3 pixels 4σ above the background level. The lists also contained objects located at the field edges that were not recorded in every exposure due to dithering or instrument rotation. The corresponding coordinates of the sources on the slitless images were given by the astrometric transformation.
6. *Masking of spectral orders and defects:* In contrast to objective prism spectra, grism spectra show different spectral orders. Figure 2.2 shows a combined $26.'2 \times 33.'5$ slitless spectroscopic WFI image centred on HE 0940−1050 taken in the *B* filter. The grism disperses the light of every object in the field of view. More than 60% of the flux is concentrated in the 1st order spectra (Wisotzki et al. 2001). Inevitably, bright stars are recorded in different spectral orders that contaminate the spectra of other objects. In par-

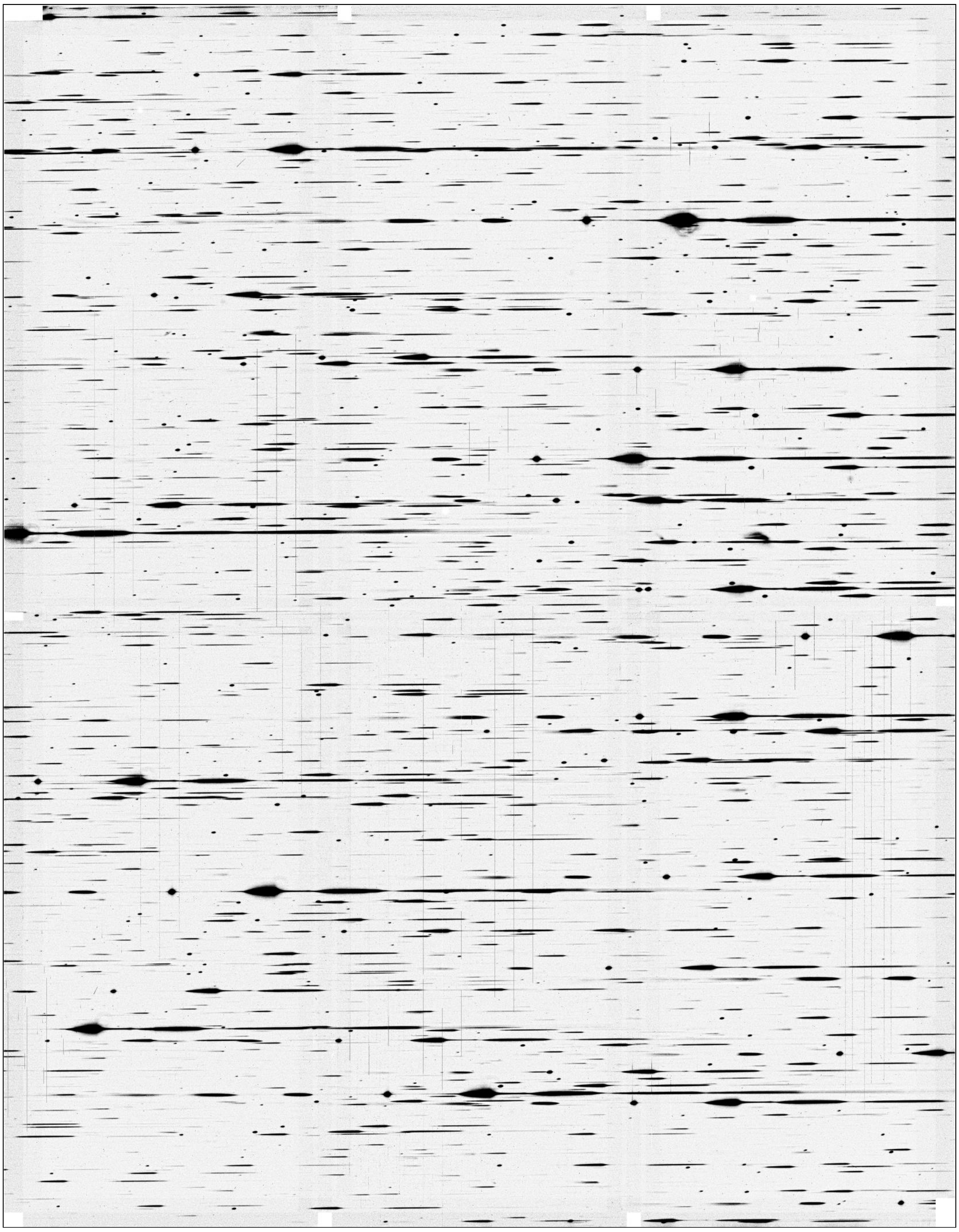

Fig. 2.2. Flatfielded sky-subtracted and combined slitless spectroscopic WFI field in the vicinity of HE 0940−1050. The spectra were taken with the *B* filter and without rotation (i.e. north is up and east is left on the image). The dispersion runs horizontally from left to right. The three dithered 600 s exposures were combined to fill the inter-chip gaps. The (linear) intensity of each pixel is weighted by its effective exposure time. The total dimension of the combined image is $26\overset{\prime}{.}16 \times 33\overset{\prime}{.}53$.

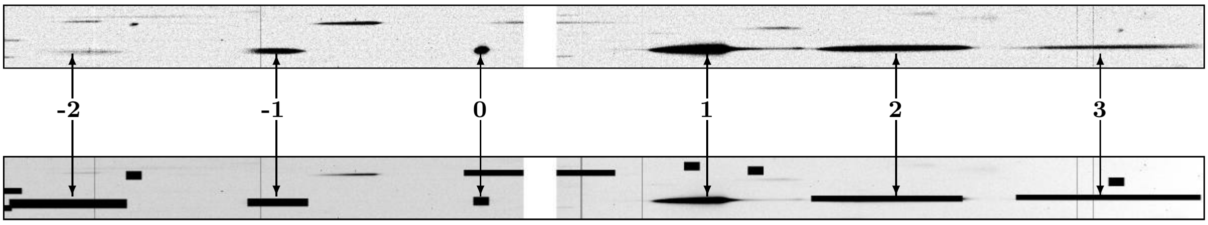

Fig. 2.3. Masking of unwanted spectral orders. The upper panel shows a $850'' \times 45''$ region of a sky-subtracted 600 s *B* band exposure of the field around HE 0940−1050. A bright star in this region generates the indicated different spectral orders in the slitless exposure that may contaminate 1st-order spectra of nearby sources. The white stripe marks a vertical inter-chip gap. The lower panel displays the corresponding region of the variance image. Black rectangles show masked spectral orders of the bright star and other objects, where the variance has been practically increased to infinity. Dark vertical stripes correspond to masked bad columns on the chips.

ticular, zero-order images superposed on other spectra will result in spurious emission lines. Therefore, we masked the regions contaminated by the unwanted spectral orders depending on the magnitude of the recorded object. All fixpoints for masking were given by the measured inter-order distance. The lengths of the contaminating orders were measured for bright stars. Figure 2.3 shows a comparison between a slitless spectroscopic exposure and its corresponding variance frame with masked contaminating spectral orders. Moreover, we masked the bad pixels of the chip mosaic.

7. *Optimal extraction:* The slitless spectra of the sources in the input catalogues of each exposure were optimally extracted with a modified version of the algorithm by Horne (1986), assuming a Gaussian spatial profile with determined centroid and full width at half maximum (FWHM). We found the bright sources used for the coordinate transformation to be reliable tracers of the centroid of a spectrum and its FWHM. The centroid slightly drifts along the columns due to an imperfect alignment of the dispersion axis with the CCD rows. The FWHM is primarily set by the seeing, but also increases from east to west over the field of view. All objects in the input catalogue were then extracted with the pre-determined centroid and FWHM of each exposure, thereby maximising the signal-to-noise ratio (S/N) of faint objects. This also reduced the effect of seeing variations on data quality. Possible overlaps of extracted spectra with other 1st order spectra or unwanted orders were flagged for visual inspection. The extracted spectra of the 600 s exposures were scaled to correct for sky transparency variations before averaging them by weighting with their inverse variances.
8. *Wavelength calibration:* Gaussian fits to emission lines of the high-S/N spectrum of the low-redshift emission-line galaxy HE 1250−0256 yielded an approximate wavelength scale with a linear dispersion of ≃ 6.7Å/pixel. The red filter edge of the combined extracted spectra was used as wavelength zero point. Both the dispersion and the zero point might change slightly over the field of view due to optical distortions induced by the R50 grism (Wisotzki et al. 2001).
9. *Flux calibration:* Observations of the spectrophotometic standard HD 49798 yielded the instrument sensitivity curves of the spectra taken in the two filters (Fig. 2.4). Flux calibration of the spectra was achieved by dividing the extracted spectra by the respective sensitivity curve scaled to the nominal exposure time of 600 s. Due to the changes in sky transparency during the first observing run and the long intervals between standard star observations, the flux scale should be considered as relative, although we found good agreement between the published magnitudes and the integrated slitless magnitudes of the known quasars in the fields.
10. *Final catalogue of slitless spectra:* The calibrated filtered spectra were spliced together in their overlapping spectral range. The spectra taken in both instrument rotations were reduced separately and then combined by weighting with their inverse variances. The final catalogue of slitless spectra from a field contained every source from the DSS input catalogue that had been recorded even in a single exposure due to dithering and field rotation.

Compared to standard imaging with the WFI, the inserted red-blazed R50 grism reduces the instrument throughput by ∼ 15% and ∼ 36% in the V and the B band, respectively. However, to some extent the low sensitivity in the blue is balanced by a lower sky background compared to the V band. After inspecting the extracted spectra of one field we constrained the useful wavelength range to 4200 Å≤ λ ≤5800 Å. Depending on the stellar density varying with Galactic latitude, the DSS catalogue yielded 800–1600 meaningful spectra per field. In total, slitless spectra of ∼ 29000 objects were extracted from the 18 fields.

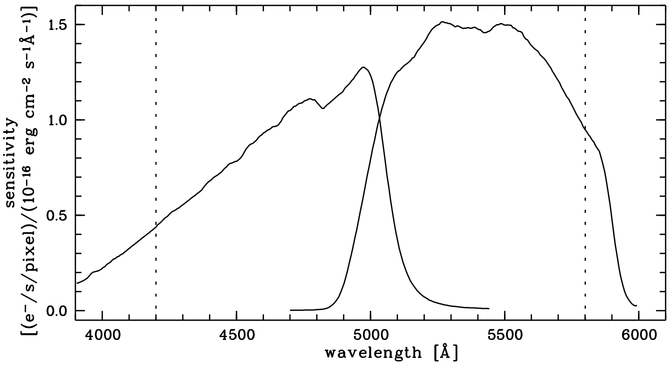

Fig. 2.4. Sensitivity curves of the WFI B and V filters derived from the spectrophotometric standard HD 49798. At ∼ 4700 Å one triggered photoelectron per second per ≃ 6.7 Å pixel corresponds to a flux density of 10^{-16} erg cm^{-2} s^{-1} Å^{-1}. Dotted lines mark the considered wavelength range.

2.3.2. Survey depth

The depth of our survey depends on the depth of the slitless data and the depth of the input source catalogues. The limiting magnitude of the slitless survey material was determined by analysing the continuum S/N of the extracted spectra. The V magnitude of each object was calculated by integrating the flux over the V band that is completely covered in the spectra. We estimate that the V magnitudes of $V \lesssim 20$ objects are accurate to $\lesssim 0.1$ mag, mainly limited by the rough flux calibration. Fainter sources have larger uncertainties due to their lower S/N. The S/N is a function of system sensitivity (Fig. 2.4) and source spectral energy distribution. We chose the median S/N in the V band as a characteristic value. In Fig. 2.5 we plot the V magnitude of all extracted ∼ 1800 spectra in the field of HE 0940−1050 as a function of their median S/N. Some objects appear to be too bright for their S/N due to shorter net exposure times induced by dithering and field rotation. After excluding the outliers we fitted $V_{\mathrm{WFI}}(S/N)$ by a log-linear function over the range $1 \leq S/N \leq 100$. The S/N of bright objects is lower than expected because of large non-Gaussian tails of the PSF which were not taken into account and detector saturation occurring at $V_{\mathrm{WFI}} \lesssim 13.4$ (corresponding to 130000 e$^-$ per pixel in 600 s). We found that the $V_{\mathrm{WFI}}(S/N)$ fits to the individual fields agree well and can be reasonably described by

$$V_{\mathrm{WFI}} = -2.5 \log (S/N) + 22.05. \qquad (2.1)$$

The root-mean-square deviation between individual fields is ∼ 0.1 mag due to the rough flux calibration and small sky transparency variations. Nevertheless, the spectra of each field reach a continuum $S/N \simeq 1$ at $V_{\mathrm{WFI}} \simeq 22.0$, which we adopt as a characteristic limiting magnitude of the slitless data for emission line search.

We estimated the completeness of the source catalogues from the differential source surface density as a function of

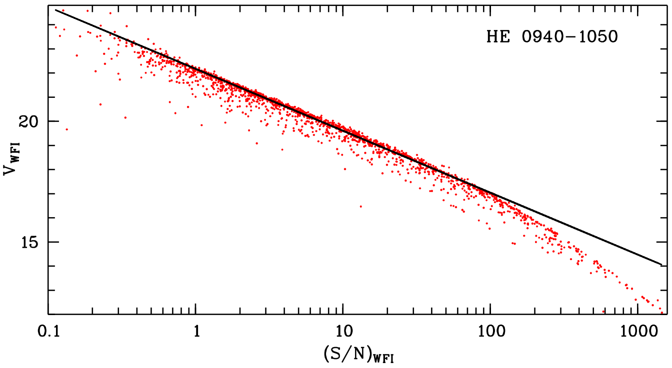

Fig. 2.5. Integrated WFI V magnitude vs. median S/N in the WFI spectra in the field of HE 0940−1050 (dots). The line shows the fitted log-linear relation of the magnitude and the S/N for this field.

Table 2.2. Approximate photometric completeness of the DSS catalogues as a function of V magnitude.

$V_{\rm lim}$	V	completeness	Fields
20.5	20.5	∼ 90%	BR 1202−0725, CTQ 0460,
	21.0	∼ 65%	Q 0302−003, Q 0420−388,
	21.5	∼ 33%	Q 1209+0919, Q 1451+123,
	22.0	∼ 11%	PKS 2126−15
21.0	20.5	∼ 100%	BR 1117−1329, HE 0940−1050,
	21.0	∼ 90%	HE 2243−6031, PKS 0528−250,
	21.5	∼ 53%	Q 2139−4434
	22.0	∼ 23%	
21.5	20.5	∼ 100%	CTQ 0247, H 0055−269,
	21.0	∼ 90%	HE 2347−4342, Q 0000−26,
	21.5	∼ 75%	Q 0002−422, Q 0347−383
	22.0	∼ 38%	

magnitude that breaks at the magnitude limit of the image used. The three upper panels in Fig. 2.6 show the differential surface densities per $\Delta V = 0.5$ mag obtained from the DSS source catalogues in the 18 fields. From the breaks in the differential number counts we conclude that the DSS images vary in depth from $V_{\rm lim} \simeq 20.5$ to $V_{\rm lim} \simeq 21.5$. We also compared the differential source counts per field to the expected surface densities of stars at high Galactic latitude (Bahcall & Soneira 1981) and galaxies (Colless et al. 2001) in order to get an estimate of the catalogue completeness. Table 2.2 gives the resulting average completeness levels for the different catalogue depths. Field-to-field completeness variations per class reach ∼ 10% at each considered V magnitude due to the less accurate V estimates at low S/N and spectral overlaps that underestimate the magnitude. The $V_{\rm lim} \simeq 20.5$ and $V_{\rm lim} \simeq 21.0$ fields reach ∼ 90% completeness at the limiting magnitudes estimated from Fig. 2.6. The deepest DSS fields seem to be somewhat shallower than indicated by Fig. 2.6, but their completeness at $V \simeq 21.5$ is still ∼ 75%.

In the lowest panel in Fig. 2.6 we compare the source densities of the three fields analysed with the DSS and the WFI source catalogues. Due to the non-photometric conditions during the imaging observations we matched the zero points to the V magnitudes derived from the slitless spectra. The difference at $V \lesssim 21$ is largest for the field of PKS 2126−15, where the co-added WFI images are deeper than the DSS image by ≃ 1 mag. However, the WFI images of the HE 0940−1050 field were taken at airmass ∼ 1.6 and a seeing of 1.″6, creating only minor differences in the source counts. The estimated completeness at $V \simeq 21.0$ is close to 100% on the fields of PKS 2126−15 and Q 2139−4434, but only ≃ 80% for HE 0940−1050. At $V \simeq 21.5$ the completeness levels are ≃ 65% and ≃ 43%, respectively.

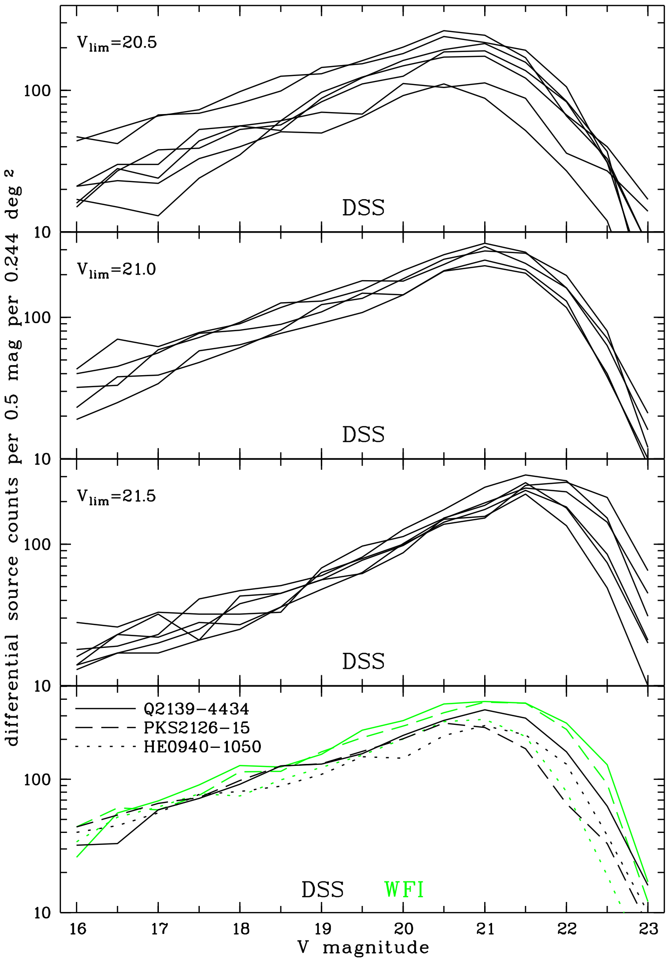

Fig. 2.6. Differential source density of the survey fields in $\Delta V = 0.5$ mag bins. The three upper panels show the source counts obtained from the DSS source catalogues grouped by estimated limiting magnitude ($V_{\rm lim} \simeq 20.5$: BR 1202−0725, CTQ 0460, Q 0302−003, Q 0420−388, Q 1209+0919, Q 1451+123, PKS 2126−15, $V_{\rm lim} \simeq 21.0$: BR 1117−1329, HE 0940−1050, HE 2243−6031, PKS 0528−250, Q 2139−4434, $V_{\rm lim} \simeq 21.5$: CTQ 0247, H 0055−269, HE 2347−4342, Q 0000−26, Q 0002−422, Q 0347−383). The lowest panel shows the differential source densities on the fields of Q 2139−4434, PKS 2126−15 and HE 0940−1050 obtained with the DSS catalogues (black) and the WFI catalogues (green/grey).

We conclude that both source catalogues will miss faint $V \sim 22$ objects recorded in the slitless data with a $S/N \sim 1$ due to the lacking depth of the direct images. Moreover, the direct WFI catalogues did not contain all processable sources near the field edges due to small differences in pointing and the single rotation of the direct WFI images. However, incompleteness in the source catalogues will affect only the detection of very faint high-redshift quasars that show Lyα in the observed wavelength range (see Sect. 2.7.1 below).

2.4. Selection of quasar candidates

2.4.1. Selection criteria

Quasar candidates were semi-automatically selected from the calibrated slitless spectra on the basis of prominent emission lines. Figure 2.7 shows the redshift ranges in which major

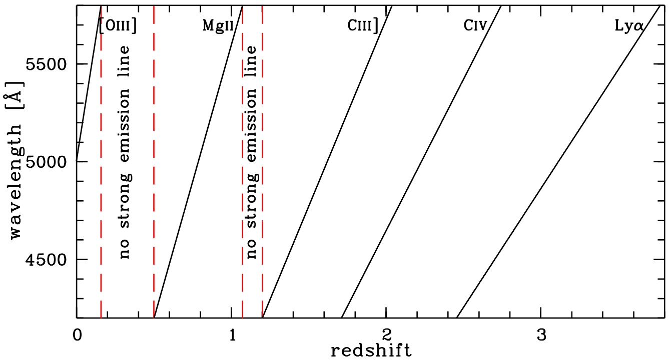

Fig. 2.7. Visibility of strong emission lines over the covered wavelength range. Dashed lines mark gaps without major emission lines where quasar candidates are missed.

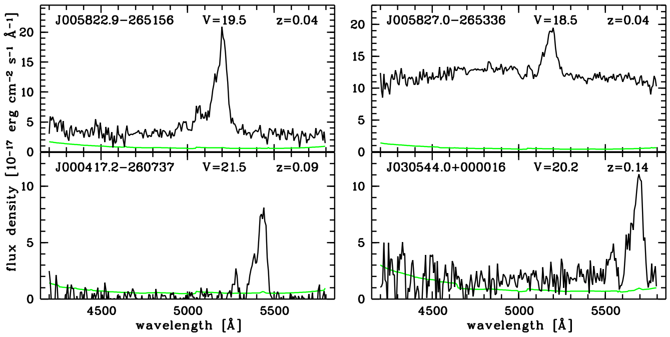

Fig. 2.9. Slitless spectra (black) and corresponding 1σ noise arrays (green/grey) of four emission line galaxies showing blended [O III] emission. Hβ can be recognised as well.

quasar emission lines can be observed in the slitless spectra. The detectability of the various emission lines depends on their equivalent widths and the S/N in the data (Sect. 2.7.1). Moreover, quasar candidates could not be selected in two narrow low-redshift ranges due to the lack of major emission lines.

After removing the continua by filtering the spectra with a median filter, the continuum-subtracted spectra were searched automatically for emission-line objects by cross-correlating them with Gaussian emission line templates. The fields around Q 0000−26, Q 0302−003 and Q 2139−4434 were chosen for testing the continuum subtraction and the line detection algorithm, ensuring that all emission line objects selected by eye were also found automatically. Finally, we chose two Gaussians with $\sigma_\lambda = 40$ Å and $\sigma_\lambda = 70$ Å in order to select emission lines with small and large widths, respectively. Only features detected with a total in the line $(S/N)_{\mathrm{line}} \geq 3$ and an observed equivalent width of $W_{\mathrm{obs}} \geq 20$ Å were kept.

Due to the fact that the broad emission lines of quasars cover a large part of their slitless spectra, the continua of the spectra could only roughly be removed without losing quasars displaying prominent emission lines, in particular Lyα. Therefore, many remaining features of stars were selected by the sensitive line detection algorithm, so that the initial samples of emission line objects contained $\gtrsim 1/4$ of the extracted spectra. However, many of the selected stars had red colours and had no detected features in the V band. With the average fluxes at 4200 Å$\leq \lambda \leq$5000 Å (B) and 5000 Å$\leq \lambda \leq$5800 Å (V) we defined a hardness ratio

$$H = \frac{f_{\lambda,V} - f_{\lambda,B}}{f_{\lambda,V} + f_{\lambda,B}} \qquad (2.2)$$

that served as a colour index, with $H > 0$ corresponding to a red colour. Based on the S/N of the spectra we also derived errors of H. Quasar candidates were finally selected with following two criteria

1. strong line with $(S/N)_{\mathrm{line}} \geq 3$ and $W_{\mathrm{obs}} \geq 100$ Å:
   - detection in B band: $H - \sigma_H \leq 0.046$
   - detection in V band: no further restriction
2. weak line with $(S/N)_{\mathrm{line}} \geq 3$ and 100 Å$< W_{\mathrm{obs}} \leq$20 Å and $H - \sigma_H > -1$ and $H + \sigma_H < 0.15$.

The first criterion selected prominent lines with large estimated equivalent widths (Lyα and sometimes C IV or [O III]). The colour restriction in the B band prevented the selection of too many red stars with a strong feature in the blue part of the spectrum caused by imperfect removal of the continuum. The second criterion was used to select quasar candidates with smaller emission line equivalent widths (C IV, C III], Mg II and [O III]) and a somewhat blue colour. The colour restriction against red objects prevented the selection of too many M stars whose TiO absorption bands arise near the red end of the spectral range. Quasar candidates were *not* selected solely on the basis of their colours.

After this automatic selection, the set of emission line sources still consisted of $\lesssim 20\%$ of the total sample per field. Instead of tightening the selection criteria that would have resulted in a loss of obvious candidates, we visually inspected the selected objects to cull the prime quasar candidates from the remaining sample of slitless spectra dominated by M stars, low-redshift emission line galaxies ([O III] visible at $z \lesssim 0.15$) and defective spectra. At the low resolution of the WFI spectra the [O III] doublet is blended, resulting in an asymmetric single line that could be unambiguously identified in almost all cases (Fig. 2.9). Since emission line galaxies are interesting in their own right, we kept them in the sample of emission line objects. Defective spectra were overlapping 1st order spectra of two close objects, spectra with unrecognised zero order contamination or spectra with unphysical breaks at $\sim$ 5000 Å resulting from an imperfect splicing of the two bandpasses. Any remaining spectral overlaps were easily identified by comparing the spectra obtained at the two instrument rotation angles. All emission-line object candidates that passed the visual check of the one-dimensional spectra were finally verified on the slitless WFI images to check for any remaining flaws that could result in a spurious emission line. For objects at the field edges detected in only one instrument rotation (Fig. 2.1) this visual examination was essential. In total, 387 emission line objects were selected from the $\sim$ 29000 objects detected on the DSS images.

2.4.2. Three additional candidates from the WFI catalogues

While confirming the DSS-selected emission line objects we thoroughly inspected the sky-subtracted slitless images of all fields for additional candidates that were missed due to the lacking depth of the DSS plates or unresolved neighbours. Three additional quasar candidates were visually selected on the slitless images, one on the field of HE 0940−1050 and two near PKS 2126−15. In fact, these two fields were selected for reanalysis with the direct WFI source catalogues because of these additional candidates. One near PKS 2126−15 was not de-

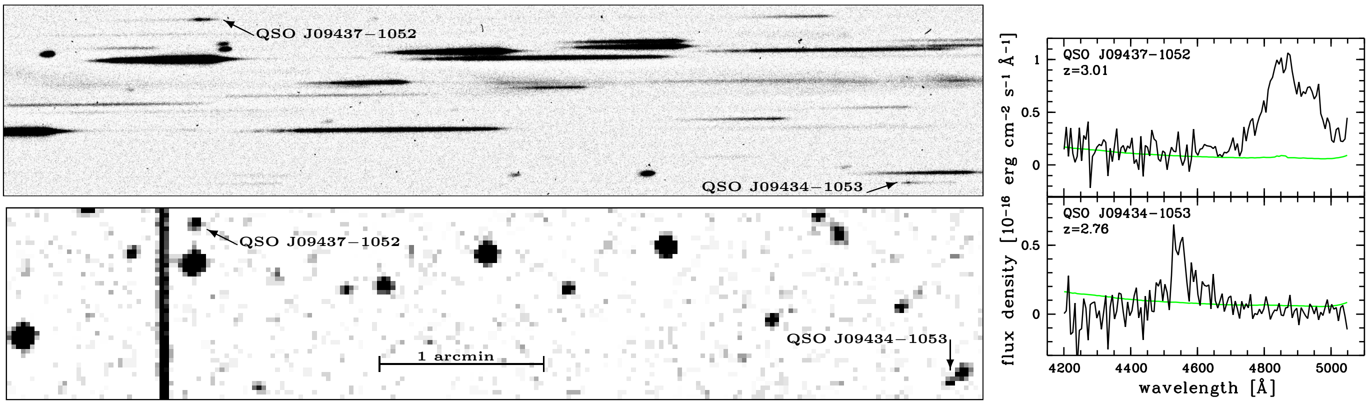

Fig. 2.8. Slitless WFI spectra of two newly discovered quasars near HE 0940−1050. The upper left panel shows a close-up of the combined slitless *B*-filtered exposures in the field of HE 0940−1050 taken without rotation (Fig. 2.2). The dispersion runs horizontally from left to right. The lower left panel shows a direct image of the corresponding sky region north-east of HE 0940−1050 from the DSS1 ($5\overset{'}{.}98 \times 1\overset{'}{.}19$). The indicated objects display prominent emission lines in the slitless data. The DSS1 resolution is insufficient to separate QSO J09434−1053 from a foreground object. However, it was in the source catalogue generated from the direct WFI data of this field, resulting in a successful location and extraction of the slitless spectrum of QSO J09434−1053. The right panels show the automatically reduced and calibrated one-dimensional *B* band spectra of the two quasars (black) and their 1σ noise arrays (green/grey). Both of them display Lyα emission at the indicated redshifts.

tected on the DSS plate (probably due to its high redshift of $z = 3.52$), the other one was missed due to a close-by foreground object on the DSS image. Also the additional candidate near HE 0940−1050 appeared merged with a another object on the DSS image. Figure 2.8 presents the slitless *B* band data and the corresponding direct DSS image of a region north-east of HE 0940−1050 where two prime quasar candidates were discovered. Their strong emission lines are clearly detectable by eye and were unambiguously identified in the extracted spectra as Lyα at $z = 3.01$ and $z = 2.76$. Whereas QSO J09437−1052 was readily detected on the DSS image, QSO J09434−1053 was the object first undetected due to the insufficient DSS resolution. Since the WFI object catalogues contained these candidates, their spectra could be reduced by our pipeline and they were automatically ranked as quasar candidates by the line detection algorithm. These were the only additional candidates that remained after the necessary visual removal of remaining stars, defective spectra and overlaps. The reanalysis of the field of Q 2139−4434 did not reveal new quasar candidates.

Since Lyα emission is detectable down to $V \simeq 22$ (Sect. 2.7.1) where the input catalogues are incomplete, we concentrated our visual examination of the slitless data on faint emission features without any discernable continuum. Zero order images were easily identified by their corresponding 1st order spectra. The visual search on the remaining fields did not yield previously undetected emission line candidates. However, this approach is clearly limited to quasars with strong Lyα emission and lacks the sensitivity to discover lines weakened by quasar outflows or strong intergalactic absorption. Very faint quasars showing an appreciable emission line signal only after extraction of the spectra will be lost as well.

The second purpose of visual examination was to look for lost candidates due to overlapping direct images. Except the two cases from above no other candidate was seen in a closely projected object pair, confirming our expectation that the fraction of candidates lost in overlapping direct images is small (a few percent).

2.4.3. The sample of quasar candidates

In total, our semi-automatic search for emission line objects yielded 390 sources on the surveyed 4.39 deg^2. Of those, 38 were rejected as dubious due to very low S/N resulting in an uncertain classification. The remaining sample of 352 objects consists of 38 known quasars, 169 unknown quasar candidates and 145 low-redshift star-forming galaxy candidates. The classification was purely based on the slitless spectra. No morphological selection was made.

Most of the emission line galaxies were identified by their blended [O III] doublet. However, due to low S/N at this low resolution $R \sim 50$, we could not determine whether the Hβ lines seen in the spectra are broad or narrow, so that this sample of low-redshift objects might still contain low-redshift AGN. The calibrated slitless spectra of the 145 likely emission line galaxies are presented in Appendix B.4..

We rediscovered all 37 previously published quasars in the survey fields at $V \lesssim 22$ with detectable emission lines in the observed wavelength range, whose spectra are shown in Appendix B.1.. Three of the central quasars (Q 0000−26, BR 1117−1329 and BR 1202−0725) reside at too high redshift to be detected in emission. However, due to the prominent DLAs along its line of sight Q 0000−26 was automatically classified as quasar candidate by the line detection programme. Known AGN fainter than the redshift-dependent limiting magnitude were not recovered from the slitless data. We measured the redshifts of the rediscovered quasars in the slitless data and found them to be consistent ($\sigma_z \simeq 0.03$) with the published values (see Fig. 2.12 below). The scatter between the redshift measurements is primarily due to uncertainties in the wavelength calibration over the field of view.

Redshifts of the 169 quasar candidates were estimated from the slitless data and the candidates were grouped by redshift confidence. The redshifts were considered to be almost secure if either two emission lines with a consistent redshift were present in the spectral range or the redshift could be estimated due to the shape of the emission line and/or the continuum. In particular, Lyα emission blended with N V was unambiguously identified (Fig. 2.8). Bright low-redshift candidates displayed lines with small equivalent widths (likely C III] or Mg II) superimposed on a blue continuum. Redshift assignments of the remaining quasar candidates were more uncertain due to the similar equivalent widths of the C IV, C III] and Mg II emission lines. At low S/N the equivalent widths were overestimated due to the uncertain continuum flux. We decided to assign the highest plausible redshifts to the candidates.

For ten of our fields WFI+grism R band data were available (PI L. Vanzi), eight of which we retrieved from the ESO Science Archive. The data were reduced with our pipeline, yielding calibrated R band spectra of our candidates in the range 5800 Å$\leq \lambda \leq$7400 Å. Due to the higher sky background, however, the R band spectra are much noisier than the B and V band spectra. Therefore, only emission lines of brighter objects of our sample were unambiguously detected. Nevertheless, the R band spectra confirmed the low redshift designations of 8 candidates. No systematic search for further emission line objects was performed on the R band spectra.

2.5. Spectroscopic follow-up

2.5.1. Observations

Follow-up spectroscopy of 81 quasar candidates was obtained with the Focal Reducer/Low Dispersion Spectrograph 2 (FORS2, Appenzeller et al. 1998) on ESO VLT UT1/Antu in Visitor Mode on November 17–19, 2004 and in Service Mode between April and July 2005. We restricted the follow-up campaign to candidates that either had an almost secure slitless WFI redshift $z \geq 1.7$ or were likely to reside at high redshift. Quasar candidates that are likely to reside at lower redshifts (C III] or Mg II seen in the slitless spectra) were not followed up. The field of PKS 0528−250 was not selected for follow-up and also the field of Q 1451+123 was not included due to the lack of high-quality candidates with a likely redshift $z > 1.7$. Longslit spectra with a 1″ slit kept at the parallactic angle were taken either with the 300V grism or the 600B grism, resulting in a spectral resolution of $\sim$ 10 Å FWHM and $\sim$ 4.5 Å FWHM, respectively. Each resolution element is oversampled by a factor of $\sim$ 3 (300V: 3.36 Å/pixel, 600B: 1.5 Å/pixel). No order separation filter was employed, leading to possible order overlap at $\lambda >$ 6600 Å in the spectra taken with the 300V grism. Exposure times were adjusted to yield $S/N \sim 20$ in the quasar continuum and ranged between one and 40 minutes. The sky was clear to photometric during the Visitor Mode run, but the seeing varied strongly during the nights, resulting in some slit losses for some of the 53 targeted objects. The remaining 28 prime quasar candidates were observed in Service Mode under variable conditions. The spectra were calibrated in wavelength against the FORS2 He/Ne/Ar/HgCd arc lamps and flux-calibrated via spectrophotometric standard stars taken each night. However, absolute spectrophotometry was not achieved due to the narrow slit and the sometimes variable or poor sky transparency in the Service Mode observations. Table 2.3 lists the quasars targeted in the spectroscopic follow-up observations.

2.5.2. Data reduction

Data reduction was performed with standard IRAF [1] tasks. The bias value was taken from the overscan regions. Dome flatfields were used to correct pixel sensitivity variations. After sky subtraction by fitting both spatial regions close to the target by 2nd-order Chebychev polynomials, the spectrum was extracted with the optimal extraction algorithm by Horne (1986). The root-mean-square residuals of the wavelength calibration with low-order Chebychev polynomials were $\lesssim$ 0.05 Å and $\sim$ 0.2 Å for the 600B and the 300V grism, respectively. The relative flux calibration at $\lambda \lesssim$ 3800 Å is somewhat uncertain due to the strongly decreasing sensitivity of the FORS2 CCDs. The spectra were corrected for atmospheric extinction.

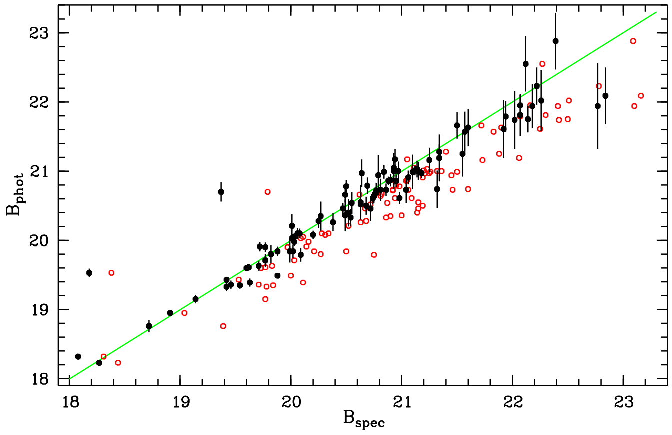

Fig. 2.10. Correlation of the B magnitudes integrated from the FORS2 spectra $B_{\rm spec}$ and the photometric B magnitudes $B_{\rm phot}$ obtained from the FORS2 aquisition images. Full (open) circles correspond to $B_{\rm spec}$ with (without) correction for slit losses. Error bars denote the 1σ errors of $B_{\rm phot}$. The line marks a perfect correlation.

In order to correct the spectra for slit losses we carried out aperture photometry on the FORS2 aquisition images taken in the B filter, which were calibrated against photometric standard stars (Landolt 1992) taken each night. Since the images were mainly used to locate the targets for slit spectroscopy, the exposure times were too short to determine accurate magnitudes of the fainter objects. Table 2.3 provides the airmass-corrected Johnson B magnitudes and their calculated standard deviations. Apparent magnitudes were also derived by integrating the flux-calibrated slit spectra. Slit losses were estimated by calculating the expected loss over the used 1″ slit for a Gaussian PSF with a FWHM equal to the seeing during the observations that we measured on the aquisition images. Figure 2.10 presents the correlation of the integrated and photometric magnitudes. The integrated magnitudes are consistent with the photometric ones after correcting for slit losses. The photometry of fainter targets is less accurate and slit loss corrections are uncertain due to the longer spectroscopic exposure times at variable seeing. The two outliers are the two quasars QSO J09425−1048 and QSO J21294−1521 that were observed in strongly variable clearly non-photometric conditions. Some additional objects at $B_{\rm phot} > B_{\rm spec}$ are probably affected by thin cirrus.

2.6. Results

2.6.1. Redshift determination

Redshifts of all candidates observed with FORS2 were determined by taking into account all detectable emission lines. Peak positions of the lines were measured by eye and errors were estimated by considering the S/N of the lines, blending with other emission lines and the presence of absorption lines,

---

[1] IRAF is distributed by the National Optical Astronomy Observatories, which are operated by the Association of Universities for Research in Astronomy, Inc., under cooperative agreement with the National Science Foundation.

Table 2.3. Observing log of the spectroscopic follow-up. The quasars reported in Chapter 4 and Chapter 5 have been included for completeness. The columns list the quasar field, the name of the confirmed quasar, its right ascension and declination, its redshift with estimated error, its B magnitude with 1σ error, night of observation, the grism used, the exposure time, the seeing and the sky conditions during observation.

Field	Object	α (J2000)	δ (J2000)	z_QSO	B	Night	Grism	t_exp [s]	Seeing	Transparency
Q 0000−26	QSO J00025−2558	$00^\mathrm{h}02^\mathrm{m}34^\mathrm{s}.83$	$-25^\circ58'44''.0$	0.887 ± 0.002	20.26 ± 0.13	18 Nov 2004	300V	300	$0''.9$	clear
	QSO J00040−2603	$00^\mathrm{h}04^\mathrm{m}05^\mathrm{s}.33$	$-26^\circ03'41''.9$	2.002 ± 0.003	20.54 ± 0.16	18 Nov 2004	600B	1000	$1''.0$	clear
	QSO J00035−2610	$00^\mathrm{h}03^\mathrm{m}31^\mathrm{s}.88$	$-26^\circ10'54''.8$	2.771 ± 0.003	21.61 ± 0.42	18 Nov 2004	600B	1800	$1''.0$	clear
	QSO J00028−2547	$00^\mathrm{h}02^\mathrm{m}53^\mathrm{s}.86$	$-25^\circ47'43''.1$	2.812 ± 0.004	19.84 ± 0.10	18 Nov 2004	600B	400	$0''.8$	clear
	QSO J00035−2551	$00^\mathrm{h}03^\mathrm{m}33^\mathrm{s}.84$	$-25^\circ51'49''.8$	2.875 ± 0.004	20.99 ± 0.25	18 Nov 2004	600B	1600	$1''.1$	clear
	QSO J00038−2617	$00^\mathrm{h}03^\mathrm{m}51^\mathrm{s}.44$	$-26^\circ17'37''.8$	3.073 ± 0.003	22.09 ± 0.41	18 Nov 2004	300V	1200	$1''.0$	clear
Q 0002−422	QSO J00043−4151	$00^\mathrm{h}04^\mathrm{m}19^\mathrm{s}.05$	$-41^\circ51'10''.6$	0.743 ± 0.001	19.84 ± 0.16	19 Nov 2004	300V	300	$1''.3$	photometric
	QSO J00041−4158	$00^\mathrm{h}04^\mathrm{m}09^\mathrm{s}.01$	$-41^\circ58'32''.4$	1.720 ± 0.004	20.36 ± 0.23	19 Nov 2004	300V	400	$1''.3$	photometric
	QSO J00045−4201	$00^\mathrm{h}04^\mathrm{m}32^\mathrm{s}.75$	$-42^\circ01'33''.9$	2.157 ± 0.002	20.35 ± 0.21	19 Nov 2004	300V	400	$1''.5$	photometric
H 0055−269	QSO J00576−2626	$00^\mathrm{h}57^\mathrm{m}36^\mathrm{s}.26$	$-26^\circ26'57''.1$	1.942 ± 0.004	20.73 ± 0.19	18 Nov 2004	300V	300	$1''.2$	clear
	QSO J00582−2649	$00^\mathrm{h}58^\mathrm{m}13^\mathrm{s}.94$	$-26^\circ49'19''.2$	2.572 ± 0.003	22.02 ± 0.44	18 Nov 2004	300V	1800	$0''.9$	clear
	QSO J00583−2626	$00^\mathrm{h}58^\mathrm{m}19^\mathrm{s}.50$	$-26^\circ26'12''.8$	2.720 ± 0.006	21.00 ± 0.26	18 Nov 2004	300V	300	$1''.2$	clear
Q 0302−003	QSO J03052−0016	$03^\mathrm{h}05^\mathrm{m}15^\mathrm{s}.62$	$-00^\circ16'14''.4$	2.290 ± 0.002	20.05 ± 0.06	17 Nov 2004	300V	300	$0''.7$	clear
	QSO J03052+0000	$03^\mathrm{h}05^\mathrm{m}16^\mathrm{s}.80$	$+00^\circ00'45''.1$	2.808 ± 0.004	21.79 ± 0.22	17 Nov 2004	300V	600	$0''.9$	clear
Q 0347−383	QSO J03494−3814	$03^\mathrm{h}49^\mathrm{m}24^\mathrm{s}.35$	$-38^\circ14'34''.2$	1.471 ± 0.002	19.60 ± 0.04	17 Nov 2004	300V	60	$0''.8$	clear
	QSO J03500−3820	$03^\mathrm{h}50^\mathrm{m}04^\mathrm{s}.26$	$-38^\circ20'51''.2$	1.819 ± 0.002	20.03 ± 0.05	17 Nov 2004	300V	120	$0''.6$	clear
	QSO J03490−3812	$03^\mathrm{h}49^\mathrm{m}03^\mathrm{s}.60$	$-38^\circ12'35''.8$	1.945 ± 0.003	21.66 ± 0.19	17 Nov 2004	300V	600	$0''.9$	clear
	QSO J03496−3821	$03^\mathrm{h}49^\mathrm{m}39^\mathrm{s}.31$	$-38^\circ21'34''.1$	2.351 ± 0.003	19.43 ± 0.03	17 Nov 2004	600B	300	$0''.7$	clear
	QSO J03496−3810	$03^\mathrm{h}49^\mathrm{m}36^\mathrm{s}.28$	$-38^\circ10'02''.1$	2.433 ± 0.003	20.87 ± 0.09	17 Nov 2004	600B	1800	$0''.8$	clear
	QSO J03495−3806	$03^\mathrm{h}49^\mathrm{m}32^\mathrm{s}.61$	$-38^\circ06'45''.1$	2.475 ± 0.003	20.86 ± 0.09	17 Nov 2004	600B	1800	$0''.7$	clear
	QSO J03508−3812	$03^\mathrm{h}50^\mathrm{m}50^\mathrm{s}.70$	$-38^\circ12'39''.0$	2.705 ± 0.003	20.86 ± 0.06	17 Nov 2004	300V	360	$0''.6$	clear
	QSO J03503−3800	$03^\mathrm{h}50^\mathrm{m}20^\mathrm{s}.01$	$-38^\circ00'03''.6$	2.734 ± 0.003	20.67 ± 0.07	17 Nov 2004	600B	900	$0''.6$	clear
	QSO J03490−3825	$03^\mathrm{h}49^\mathrm{m}02^\mathrm{s}.58$	$-38^\circ25'21''.5$	2.777 ± 0.003	20.52 ± 0.06	17 Nov 2004	600B	1000	$0''.7$	clear
	QSO J03494−3826	$03^\mathrm{h}49^\mathrm{m}28^\mathrm{s}.40$	$-38^\circ26'11''.6$	2.782 ± 0.002	20.97 ± 0.07	17 Nov 2004	600B	1800	$0''.6$	clear
CTQ 0247	QSO J04061−4401	$04^\mathrm{h}06^\mathrm{m}10^\mathrm{s}.38$	$-44^\circ01'00''.0$	2.410 ± 0.020	19.35 ± 0.05	19 Nov 2004	600B	900	$1''.0$	photometric
	QSO J04075−4416	$04^\mathrm{h}07^\mathrm{m}35^\mathrm{s}.34$	$-44^\circ16'04''.1$	3.034 ± 0.003	21.75 ± 0.19	19 Nov 2004	600B	2000	$1''.1$	photometric
	QSO J04084−4420	$04^\mathrm{h}08^\mathrm{m}29^\mathrm{s}.02$	$-44^\circ20'14''.4$	3.080 ± 0.004	22.88 ± 0.41	19 Nov 2004	300V	1800	$1''.7$	photometric
Q 0420−388	QSO J04217−3847	$04^\mathrm{h}21^\mathrm{m}45^\mathrm{s}.70$	$-38^\circ47'44''.9$	0.771 ± 0.002	20.73 ± 0.09	18 Nov 2004	600B	800	$0''.9$	clear
	QSO J04229−3831	$04^\mathrm{h}22^\mathrm{m}59^\mathrm{s}.97$	$-38^\circ31'37''.1$	1.990 ± 0.002	19.98 ± 0.06	18 Nov 2004	600B	400	$0''.8$	clear
	QSO J04222−3829	$04^\mathrm{h}22^\mathrm{m}17^\mathrm{s}.31$	$-38^\circ29'33''.4$	2.168 ± 0.003	20.91 ± 0.10	18 Nov 2004	300V	300	$0''.8$	clear
	QSO J04215−3857	$04^\mathrm{h}21^\mathrm{m}34^\mathrm{s}.81$	$-38^\circ57'03''.4$	2.235 ± 0.003	22.23 ± 0.27	18 Nov 2004	300V	1400	$1''.4$	clear
	QSO J04215−3854	$04^\mathrm{h}21^\mathrm{m}32^\mathrm{s}.16$	$-38^\circ54'50''.6$	2.270 ± 0.010	19.49 ± 0.04	18 Nov 2004	600B	200	$0''.7$	clear
	QSO J04212−3853	$04^\mathrm{h}21^\mathrm{m}12^\mathrm{s}.49$	$-38^\circ53'28''.5$	2.723 ± 0.003	20.08 ± 0.06	18 Nov 2004	600B	1000	$0''.7$	clear
	QSO J04230−3853	$04^\mathrm{h}23^\mathrm{m}01^\mathrm{s}.12$	$-38^\circ53'14''.5$	3.042 ± 0.005	21.95 ± 0.15	18 Nov 2004	300V	1800	$0''.7$	clear
HE 0940−1050	QSO J09422−1117	$09^\mathrm{h}42^\mathrm{m}13^\mathrm{s}.67$	$-11^\circ17'37''.5$	0.741 ± 0.003	20.10 ± 0.07	06 Apr 2005	600B	420	$0''.9$	thin cirrus
	QSO J09437−1109	$09^\mathrm{h}43^\mathrm{m}42^\mathrm{s}.67$	$-11^\circ09'47''.6$	1.456 ± 0.002	21.00 ± 0.13	06 Apr 2005	300V	600	$0''.8$	thin cirrus
	QSO J09427−1108	$09^\mathrm{h}42^\mathrm{m}44^\mathrm{s}.14$	$-11^\circ08'00''.3$	1.517 ± 0.004	19.91 ± 0.07	12 May 2005	600B	300	$1''.2$	photometric
	QSO J09430−1108	$09^\mathrm{h}43^\mathrm{m}00^\mathrm{s}.27$	$-11^\circ08'06''.3$	1.730 ± 0.003	21.03 ± 0.12	10 May 2005	300V	1800	$0''.7$	clear
	QSO J09424−1047	$09^\mathrm{h}42^\mathrm{m}24^\mathrm{s}.17$	$-10^\circ47'58''.5$	1.971 ± 0.003	20.61 ± 0.09	12 May 2005	300V	240	$0''.7$	photometric
	QSO J09437−1057	$09^\mathrm{h}43^\mathrm{m}45^\mathrm{s}.15$	$-10^\circ57'58''.8$	2.023 ± 0.004	20.64 ± 0.10	09 Jun 2005	300V	240	$0''.6$	clear
	QSO J09435−1049	$09^\mathrm{h}43^\mathrm{m}30^\mathrm{s}.04$	$-10^\circ49'58''.9$	2.216 ± 0.003	20.79 ± 0.12	06 Apr 2005	600B	720	$0''.9$	thin cirrus
	QSO J09425−1048	$09^\mathrm{h}42^\mathrm{m}30^\mathrm{s}.58$	$-10^\circ48'50''.8$	2.325 ± 0.005	19.80	02 May 2005	600B	720	$1''.2$	thick cirrus
	QSO J09434−1053	$09^\mathrm{h}43^\mathrm{m}24^\mathrm{s}.21$	$-10^\circ53'32''.9$	2.760 ± 0.003	21.16 ± 0.18	12 May 2005	300V	1400	$1''.3$	photometric
	QSO J09427−1121	$09^\mathrm{h}42^\mathrm{m}44^\mathrm{s}.42$	$-11^\circ21'38''.9$	2.963 ± 0.003	20.99 ± 0.10	19 Nov 2004	600B	1200	$1''.2$	photometric
						05 Apr 2005	600B	600	$0''.9$	thick cirrus
	QSO J09437−1052	$09^\mathrm{h}43^\mathrm{m}42^\mathrm{s}.99$	$-10^\circ52'31''.7$	3.018 ± 0.003	20.78 ± 0.09	19 Nov 2004	600B	1200	$1''.3$	photometric
						06 Apr 2005	600B	1200	$0''.5$	thick cirrus
CTQ 0460	QSO J10399−2321	$10^\mathrm{h}39^\mathrm{m}58^\mathrm{s}.77$	$-23^\circ21'40''.3$	2.216 ± 0.004	20.73 ± 0.16	07 May 2005	600B	900	$0''.6$	thin cirrus
	QSO J10388−2258	$10^\mathrm{h}38^\mathrm{m}50^\mathrm{s}.12$	$-22^\circ58'08''.9$	2.326 ± 0.003	19.63 ± 0.07	28 Jun 2005	600B	420	$0''.7$	thin cirrus
	QSO J10385−2317	$10^\mathrm{h}38^\mathrm{m}31^\mathrm{s}.54$	$-23^\circ17'55''.3$	3.099 ± 0.004	21.28 ± 0.11	09 Jun 2005	600B	1800	$0''.6$	clear
BR 1117−1329	QSO J11208−1345	$11^\mathrm{h}20^\mathrm{m}48^\mathrm{s}.50$	$-13^\circ45'35''.6$	1.893 ± 0.002	20.10 ± 0.08	27 Jun 2005	300V	180	$0''.9$	thin cirrus
	QSO J11205−1343	$11^\mathrm{h}20^\mathrm{m}34^\mathrm{s}.09$	$-13^\circ43'28''.9$	1.910 ± 0.002	19.84 ± 0.07	27 Jun 2005	300V	180	$0''.8$	thin cirrus
	QSO J11197−1340	$11^\mathrm{h}19^\mathrm{m}46^\mathrm{s}.71$	$-13^\circ40'47''.1$	2.220 ± 0.004	18.32 ± 0.04	27 Jun 2005	600B	420	$0''.9$	thin cirrus
	QSO J11192−1334	$11^\mathrm{h}19^\mathrm{m}12^\mathrm{s}.37$	$-13^\circ34'05''.5$	3.252 ± 0.005	22.55 ± 0.40	27 Jun 2005	300V	1600	$0''.8$	thin cirrus
BR 1202−0725	QSO J12059−0754	$12^\mathrm{h}05^\mathrm{m}55^\mathrm{s}.33$	$-07^\circ54'33''.7$	0.773 ± 0.001	20.40 ± 0.20	06 May 2005	600B	900	$1''.5$	clear
	QSO J12062−0727	$12^\mathrm{h}06^\mathrm{m}14^\mathrm{s}.24$	$-07^\circ27'41''.1$	1.478 ± 0.003	20.46 ± 0.08	29 Jun 2005	300V	180	$0''.9$	thin cirrus
	QSO J12061−0745	$12^\mathrm{h}06^\mathrm{m}08^\mathrm{s}.91$	$-07^\circ45'49''.8$	1.730 ± 0.002	19.15 ± 0.06	06 May 2005	600B	600	$1''.5$	clear
Q 1209+0919	QSO J12124+0851	$12^\mathrm{h}12^\mathrm{m}29^\mathrm{s}.08$	$+08^\circ51'58''.9$	0.729 ± 0.003	19.61 ± 0.05	28 Jun 2005	600B	300	$0''.8$	thin cirrus
	QSO J12111+0906	$12^\mathrm{h}11^\mathrm{m}06^\mathrm{s}.59$	$+09^\circ06'43''.6$	2.534 ± 0.002	21.17 ± 0.15	29 Jun 2005	600B	2400	$0''.7$	thin cirrus
PKS 2126−15	QSO J21294−1521	$21^\mathrm{h}29^\mathrm{m}29^\mathrm{s}.91$	$-15^\circ21'57''.9$	0.580 ± 0.001	18.38	04 May 2005	600B	180	$0''.8$	thin cirrus
	QSO J21291−1524A	$21^\mathrm{h}29^\mathrm{m}10^\mathrm{s}.09$	$-15^\circ24'45''.1$	0.782 ± 0.001	21.81 ± 0.30	04 May 2005	300V	2400	$0''.9$	thin cirrus
	QSO J21297−1536	$21^\mathrm{h}29^\mathrm{m}46^\mathrm{s}.75$	$-15^\circ36'51''.9$	1.509 ± 0.003	20.50 ± 0.13	06 May 2005	300V	180	$1''.3$	clear
	QSO J21286−1528	$21^\mathrm{h}28^\mathrm{m}40^\mathrm{s}.43$	$-15^\circ28'15''.7$	1.925 ± 0.005	19.79 ± 0.10	06 May 2005	300V	120	$1''.6$	clear
	QSO J21291−1524B	$21^\mathrm{h}29^\mathrm{m}10^\mathrm{s}.85$	$-15^\circ24'23''.7$	2.480 ± 0.030	20.33 ± 0.12	04 May 2005	600B	720	$1''.0$	thin cirrus
	QSO J21301−1533	$21^\mathrm{h}30^\mathrm{m}07^\mathrm{s}.46$	$-15^\circ33'20''.9$	3.487 ± 0.003	21.94 ± 0.32	05 May 2005	600B	2200	$0''.9$	clear
Q 2139−4434	QSO J21434−4432	$21^\mathrm{h}43^\mathrm{m}25^\mathrm{s}.26$	$-44^\circ32'11''.0$	2.709 ± 0.004	19.33 ± 0.06	05 May 2005	600B	540	$1''.1$	clear
HE 2243−6031	QSO J22454−6020	$22^\mathrm{h}45^\mathrm{m}27^\mathrm{s}.22$	$-60^\circ20'25''.2$	1.984 ± 0.015	20.94 ± 0.29	19 Nov 2004	300V	300	$1''.6$	photometric
	QSO J22455−6015	$22^\mathrm{h}45^\mathrm{m}34^\mathrm{s}.64$	$-60^\circ15'45''.9$	2.036 ± 0.002	21.74 ± 0.42	19 Nov 2004	300V	800	$1''.2$	photometric
	QSO J22460−6024	$22^\mathrm{h}46^\mathrm{m}01^\mathrm{s}.23$	$-60^\circ24'57''.5$	2.041 ± 0.003	21.25 ± 0.33	19 Nov 2004	300V	1800	$1''.1$	photometric
	QSO J22454−6011	$22^\mathrm{h}45^\mathrm{m}29^\mathrm{s}.42$	$-60^\circ11'17''.1$	2.324 ± 0.003	19.36 ± 0.06	17 Nov 2004	600B	300	$0''.9$	clear
	QSO J22463−6009	$22^\mathrm{h}46^\mathrm{m}18^\mathrm{s}.47$	$-60^\circ09'02''.5$	2.329 ± 0.003	19.71 ± 0.09	17 Nov 2004	600B	500	$1''.0$	clear
	QSO J22484−6002	$22^\mathrm{h}48^\mathrm{m}29^\mathrm{s}.20$	$-60^\circ02'19''.4$	3.586 ± 0.002	20.97 ± 0.20	17 Nov 2004	600B	600	$1''.0$	clear
						19 Nov 2004	600B	600	$1''.4$	photometric

Table 2.3. continued.

Field	Object	α (J2000)	δ (J2000)	$z_{\rm QSO}$	B	Night	Grism	$t_{\rm exp}$ [s]	Seeing	Transparency
HE 2347−4342	QSO J23510−4336	$23^{\rm h}51^{\rm m}05\overset{\rm s}{.}50$	$-43^{\circ}36'57\overset{\prime\prime}{.}2$	0.720 ± 0.002	20.74 ± 0.27	19 Nov 2004	300V	1200	$1\overset{\prime\prime}{.}3$	photometric
	QSO J23507−4319	$23^{\rm h}50^{\rm m}44\overset{\rm s}{.}97$	$-43^{\circ}19'26\overset{\prime\prime}{.}0$	0.850 ± 0.003	19.90 ± 0.07	17 Nov 2004	600B	360	$0\overset{\prime\prime}{.}7$	clear
	QSO J23507−4326	$23^{\rm h}50^{\rm m}45\overset{\rm s}{.}39$	$-43^{\circ}26'37\overset{\prime\prime}{.}0$	1.635 ± 0.003	21.05 ± 0.14	17 Nov 2004	300V	200	$1\overset{\prime\prime}{.}0$	clear
	QSO J23509−4330	$23^{\rm h}50^{\rm m}54\overset{\rm s}{.}80$	$-43^{\circ}30'42\overset{\prime\prime}{.}2$	1.762 ± 0.004	18.23 ± 0.03	17 Nov 2004	600B	300	$0\overset{\prime\prime}{.}7$	clear
	QSO J23502−4334	$23^{\rm h}50^{\rm m}16\overset{\rm s}{.}18$	$-43^{\circ}34'14\overset{\prime\prime}{.}7$	1.763 ± 0.003	18.95 ± 0.04	17 Nov 2004	300V	60	$0\overset{\prime\prime}{.}7$	clear
	QSO J23503−4328	$23^{\rm h}50^{\rm m}21\overset{\rm s}{.}55$	$-43^{\circ}28'43\overset{\prime\prime}{.}7$	2.282 ± 0.003	20.66 ± 0.11	17 Nov 2004	300V	400	$0\overset{\prime\prime}{.}7$	clear
	QSO J23495−4338	$23^{\rm h}49^{\rm m}34\overset{\rm s}{.}53$	$-43^{\circ}38'08\overset{\prime\prime}{.}7$	2.690 ± 0.006	20.21 ± 0.17	19 Nov 2004	300V	360	$1\overset{\prime\prime}{.}2$	photometric
	QSO J23511−4319	$23^{\rm h}51^{\rm m}09\overset{\rm s}{.}44$	$-43^{\circ}19'41\overset{\prime\prime}{.}6$	3.020 ± 0.004	21.00 ± 0.14	17 Nov 2004	600B	1000	$1\overset{\prime\prime}{.}1$	clear
	QSO J23514−4339	$23^{\rm h}51^{\rm m}25\overset{\rm s}{.}54$	$-43^{\circ}39'02\overset{\prime\prime}{.}9$	3.240 ± 0.004	21.57 ± 0.29	17 Nov 2004	300V	1400	$1\overset{\prime\prime}{.}2$	clear
	QSO J23503−4317	$23^{\rm h}50^{\rm m}21\overset{\rm s}{.}94$	$-43^{\circ}17'30\overset{\prime\prime}{.}0$	3.542 ± 0.005	21.94 ± 0.62	19 Nov 2004	300V	1800	$1\overset{\prime\prime}{.}2$	photometric
						19 Nov 2004	600B	1800	$1\overset{\prime\prime}{.}2$	photometric

sky residuals or line asymmetries. We confirmed that in many objects high-ionisation lines (Lyα, N v, Si iv+O iv], C iv) are blueshifted with respect to low-ionisation lines (Gaskell 1982; Tytler & Fan 1992; McIntosh et al. 1999; Richards et al. 2002b). However, the low-ionisation lines O i+Si ii and C ii were often weak and noisy, resulting in larger individual redshift errors. Mg ii could be measured only for quasars at $z \lesssim 2.30$ ($z \lesssim 1.25$) taken with the 300V (600B) grism. Therefore, we estimated the systemic redshift of each quasar by weighting the measurements of individual lines, giving a lower weight to high-ionisation lines or discarding them completely in case of large blueshifts. The redshift uncertainty of each quasar was estimated from the redshift scatter between the remaining lines and their positioning errors. Appendix C contains all redshift measurements of the newly discovered objects. The adopted quasar redshifts and their errors are also listed in Table 2.3.

2.6.2. The sample of 80 confirmed quasars

With the follow-up spectra we confirmed that 80 of our 81 candidates are broad-line AGN in the redshift range $0.580 \leq z \leq 3.586$. Only one of the candidates turned out to be a low-redshift galaxy with narrow emission lines (object J03490−3820, α(J2000)=$03^{\rm h}49^{\rm m}00\overset{\rm s}{.}56$, δ(J2000)= $-38^{\circ}20'31\overset{\prime\prime}{.}9$, $z = 0.2848$). Appendix D shows the spectra of the confirmed quasars grouped by field together with the quasar distributions on the sky and the angular distribution with respect to the central quasar. As an example, we plot in Figure 2.11 the spectra of the 11 discovered quasars in the vicinity of HE 0940−1050.

In Fig. 2.12 we compare the apparent magnitudes and the redshifts derived from the FORS2 spectra and the slitless WFI spectra, respectively. The FORS2 V magnitudes were integrated from the spectra after correcting for slit losses. The magnitudes are correlated, but show a large scatter (root-mean-square deviation 0.46). This is mainly due to the random photometric errors in the short FORS2 aquisition exposures and the uncertain WFI magnitudes that were obtained by integration of the noisy slitless spectra subject to transparency variations and possible variations of the photometric zero point across the WFI field of view. Indeed, the scatter increases with magnitude and the slitless magnitudes of faint $V \gtrsim 21$ objects may have been slightly overestimated. Quasar variability on the ~ 2 yr time scale between the observations might also contribute to the scatter.

The redshifts determined from the slitless WFI spectra were confirmed for the majority of candidates (54/81). The WFI redshifts of the other 27 objects in the follow-up had been overestimated because we assigned the highest plausible redshifts. We confirmed the slitless redshifts of 39 (15) candidates with almost secure (estimated) WFI redshifts with a scatter of $\sigma_z \simeq 0.03$. The scatter is caused by variations of the wavelength scale over the WFI field of view and the redshift estimation from broad high-ionisation emission lines in the low-dispersion low-S/N WFI spectra, whereas the FORS2 redshifts are mostly based on low-ionisation lines. Of the 27 candidates whose redshifts were not confirmed only 5 were thought to be estimated correctly with high confidence. This indicates that the majority of remaining candidates with high redshift confidence likely reside at those redshifts. After completion of the follow-up observations we compared the WFI spectra with underestimated redshifts to the WFI spectra of the remaining candidates and adjusted the estimates if necessary. Appendix B.2. presents the slitless spectra of the 81 quasar candidates in the follow-up observations.

2.6.3. Quasar candidates not included in the follow-up

Appendix B.3. lists the slitless spectra of the remaining 88 quasar candidates with celestial coordinates, WFI redshift and level of redshift confidence. We gauge the WFI redshifts of 23 candidates to be correct, either due to the consistent measurement of two emission lines or the shape and equivalent width of single detected lines. The redshifts of the other candidates remain either plausible (28) or uncertain estimates (37). As an example we show in Fig. 2.13 the slitless spectra of 10 quasar candidates in the field of PKS 0528−250 that was not considered in the spectroscopic follow-up. Three of these candidates have a secure redshift $z > 2.5$. The remaining candidates on the other fields are either faint with noisy WFI spectra or they likely reside at redshifts $z < 1.7$.

We summarise the redshift distribution of the quasar sample in Fig. 2.14. The open histogram shows the redshift distribution of all detected known quasars, newly discovered quasars and remaining candidates assuming that the inferred WFI redshifts of the candidates are correct. In total, 205 quasars and candidates are shown. The gaps in the distribution arise from the visibility of quasar emission lines in the observed spectral range. The sample of 37 rediscovered quasars is dominated by the bright central $z \sim 3$ quasars in the fields. 64 of the 80 confirmed quasars are above our low-redshift cutoff $z = 1.7$ set for inclusion in the follow-up.

2.6.4. Absolute magnitudes

In order to avoid uncertain K corrections we computed the absolute magnitudes of the confirmed quasars and candidates at a rest frame wavelength of 1450 Å in the AB system. For confirmed $z \geq 1.7$ quasars the continuum flux density $f_\nu(1450\text{Å}[1+z])$ is directly estimated from a power law fit to the quasar con-

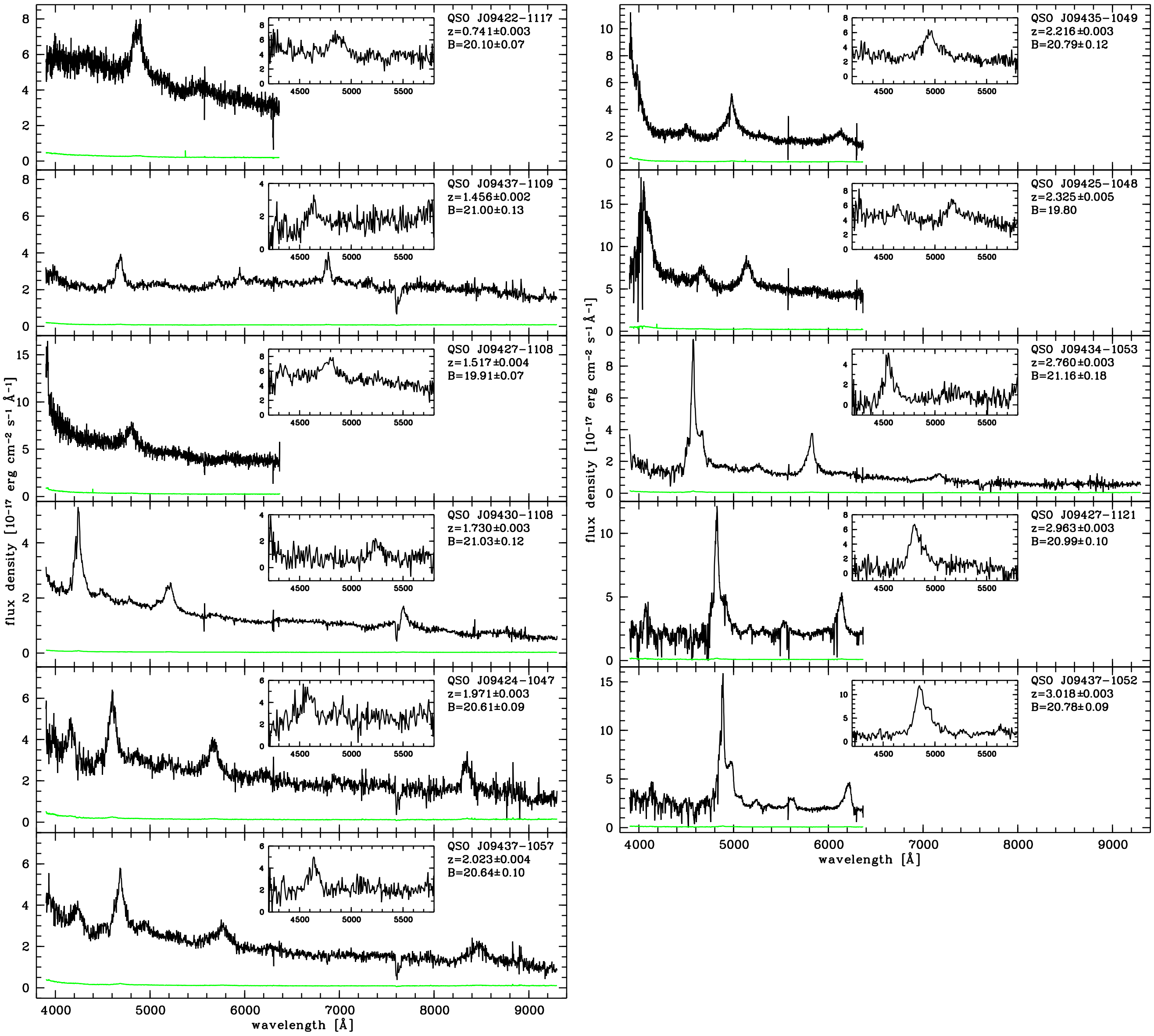

Fig. 2.11. VLT/FORS2 spectra of the 11 discovered quasars in the vicinity of HE 0940−1050. The spectra are shown in black together with their 1σ noise arrays (green/grey). The spectra have been scaled to yield the measured photometric B magnitudes. The small inserts show the corresponding slitless WFI spectra in the same units.

tinuum scaled to the photometric B magnitude and corrected for Galactic extinction (see Chapter 3 for details). The observed rest frame AB magnitude is then

$$m_{\mathrm{AB},1450} = -2.5\log\left(f_\nu(1450\text{Å}[1+z])\right) - 48.60 \qquad (2.3)$$

and the absolute magnitude is

$$M_{\mathrm{AB},1450} = m_{\mathrm{AB},1450} - 5\log\left(\frac{d_L}{\mathrm{Mpc}}\right) + 2.5\log(1+z) - 25 \quad (2.4)$$

with the luminosity distance d_L of the quasar. We assume a flat cosmological model with density parameters $\Omega_\mathrm{m} = 0.3$, $\Omega_\Lambda = 0.7$ and a Hubble constant $H_0 = 70$ km s^{-1} Mpc^{-1}. For $z < 1.7$ quasars and all remaining candidates we estimated $m_{\mathrm{AB},1450}$ from the SDSS quasar composite spectrum (Vanden Berk et al. 2001) shifted to the (estimated) redshift and scaled to the Vega V magnitude. Uncertain redshifts of candidates cause large systematic errors in $M_{\mathrm{AB},1450}$. Figure 2.15 presents the resulting $M_{\mathrm{AB},1450}(z)$ for all discovered quasars and quasar candidates. We also show the redshift track of the SDSS composite at Vega magnitude $V = 22.0$ which provides a good match to the spectroscopic limiting magnitude. However, the lack of the expected increase of the density of objects towards the limiting magnitude suggests magnitude-dependent selection effects that will be quantified in the following.

2.7. Discussion

2.7.1. Survey selection function

We performed extensive Monte Carlo simulations to characterise the spectroscopic survey completeness that depends on the equivalent width distribution of the detectable emission lines (Schmidt et al. 1986; Gratton & Osmer 1987). We first generated several template quasar spectra via a Monte Carlo routine. The quasar emission lines of Lyα, Si IV+O IV], C IV, C III] and

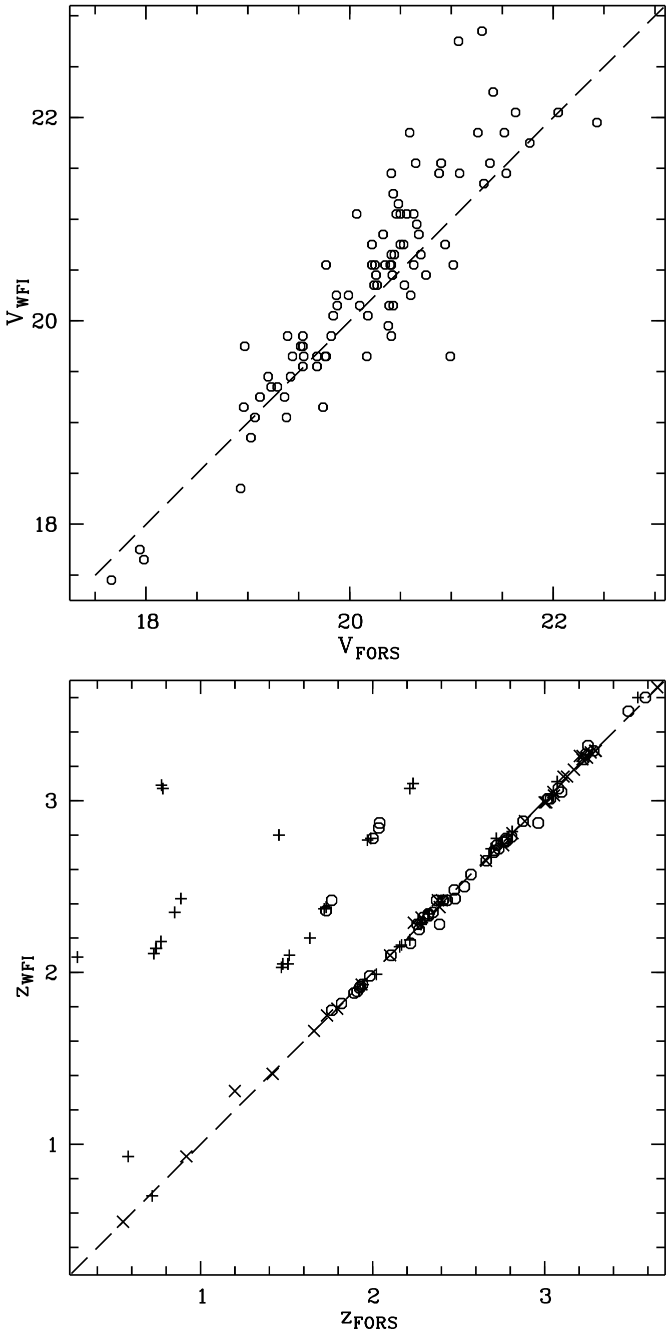

Fig. 2.12. Comparison of the magnitudes and redshifts obtained with FORS2 and WFI. The upper panel shows the correlation between the integrated *V* magnitude of the FORS2 spectra (corrected for slit losses) and the integrated *V* magnitude of the slitless WFI spectra. The lower panel shows the correlation of the redshifts obtained with FORS2 and WFI for quasar candidates with almost secure WFI redshifts (circles) and estimated redshifts (+ signs). The previously known quasars in the fields have been added with their published redshift in comparison to the redshift estimated from the slitless data (× signs). Dashed lines in both panels mark a perfect correlation.

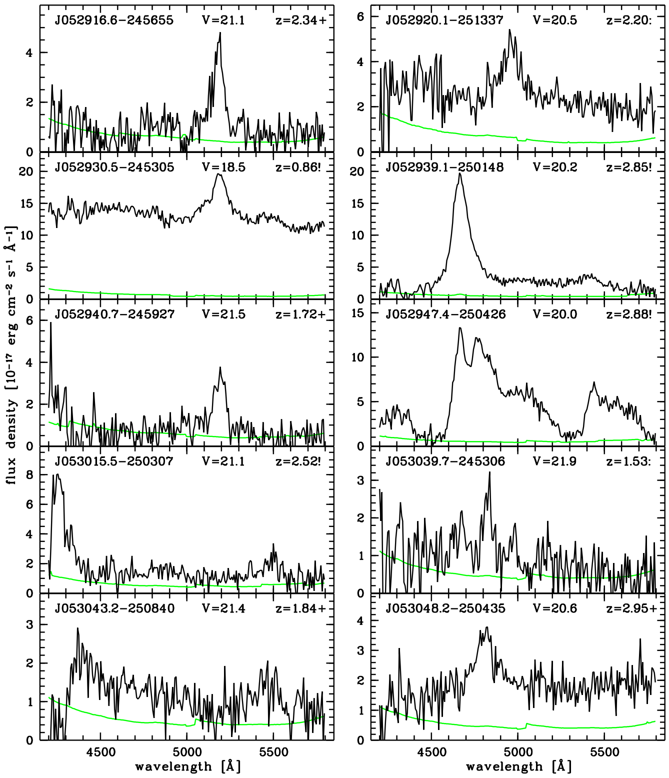

Fig. 2.13. Slitless spectra (black) and corresponding 1σ noise arrays (green/grey) of 10 quasar candidates in the field of PKS 0528−250 with celestial coordinates (format: `HHMMSS.S±DDMMSS`, J2000), approximate *V* magnitude and estimated redshift with confidence level (!=secure, +=plausible, :=estimated).

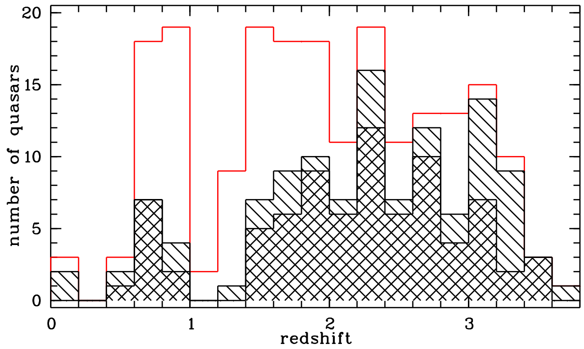

Fig. 2.14. Redshift histograms of confirmed previously unknown quasars (cross-hashed), rediscovered quasars (hashed) and remaining quasar candidates (open).

Mg II were modelled as Gaussian profiles with mean equivalent widths and line dispersions from the quasar template spectrum by Vanden Berk et al. (2001) superposed on a power law continuum $f_\nu \propto \nu^{-\alpha}$ with a mean spectral index $\alpha = 0.5$. We incorporated variations in the model parameters by assuming Gaussian distributions with a standard deviation of 20% around the mean. We then generated 200 random spectral templates in the quasar rest frame. The template spectra might not be very realistic, but the neglect of non-Gaussian line shapes, line blends and intrinsic or intervening absorption probably does not have an influence on our completeness estimates, especially at low S/N.

Mock slitless WFI quasar spectra were created by shifting the templates to the desired redshift, degrading them to the WFI resolution and dispersion followed by adding Gaussian noise that varied with wavelength according to the overall throughput of the spectrograph (Fig. 2.4). In reality, the resolution of the slitless spectra is set by the seeing which varied from field to field or even between the exposures. However, the impact of the seeing is reduced by the optimal extraction of the spectra. Moreover, a seeing FWHM of 2″ corresponds to a resolution of $\Delta\lambda \simeq 60$ Å, which is smaller than the FWHM of the

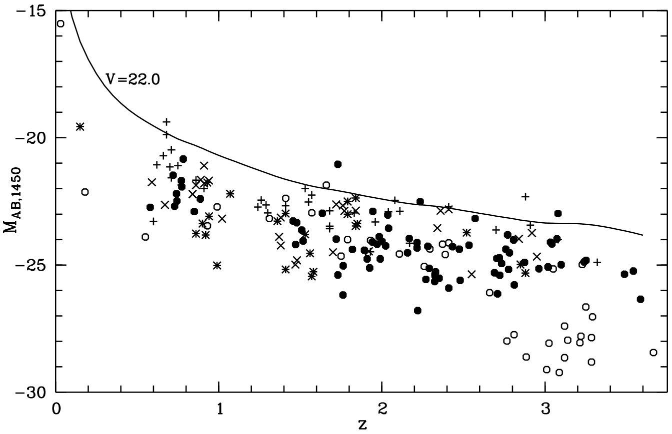

Fig. 2.15. Absolute AB magnitude at 1450 Å rest frame $M_{\mathrm{AB},1450}$ as function of redshift z. Full and open circles mark newly discovered confirmed quasars and known quasars, respectively. Remaining candidates are coded by redshift confidence (+: estimated, ×: plausible, ∗: secure). The line denotes $M_{\mathrm{AB},1450}(z)$ of a quasar having a Vega magnitude $V = 22$.

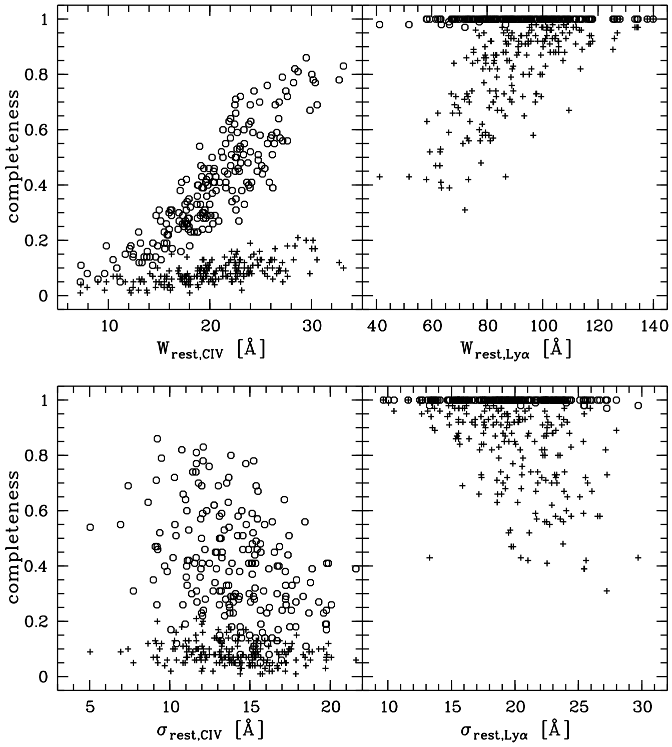

Fig. 2.16. Dependence of the completeness on rest frame equivalent width (upper panels) and line dispersion (lower panels) of C IV (left) and Lyα (right). Crosses (circles) show the mean detection fraction per simulated template at $S/N = 1$ ($S/N = 2$) in the WFI spectrum near 5400 Å. The simulated lines are observed at ∼ 5000 Å, corresponding to $z = 2.2$ (C IV) and $z = 3.1$ (Lyα).

broad quasar emission lines. The S/N in the simulated spectra was normalised in the quasar continuum near the maximum throughput at 5400 Å. The S/N is related to the V magnitude by eq. (2.1). For simplicity we did not account for small S/N correlations with the seeing or different net exposure times per band.

We then performed Monte Carlo simulations of the detection rates of quasars as a function of redshift ($0.6 \le z \le 3.7$) and S/N ($0.5 \le S/N \le 50$). At each considered redshift and S/N WFI spectra of the 200 quasar templates were generated and subjected to our automated selection routines (Sect. 2.4.1). Each quasar template was simulated 100 times in order to decrease the impact of noise on the detection rate per object. We also performed the subsequent visual screening done for the real candidates on several hundred simulated spectra to investigate visual selection effects, finding that $\gtrsim 90\%$ of the automatically selected candidates would have been finally selected by eye. Of course, this a posteriori probability is only an estimate. The rate of non-detections for both the automatic routine and the visual examination depends on the particular noise pattern at very low $S/N \lesssim 2$.

Figure 2.16 shows the dependence of the detection rate on the rest frame equivalent width, line dispersion and S/N for the 200 template spectra. At low S/N the completeness depends on the range of typical equivalent widths for each detected line. Due to its strength Lyα emission remains detectable even at a $S/N \sim 1$, whereas lines with lower equivalent widths are not selected anymore. At low S/N the detection rate also rises with equivalent width for a given line. All considered lines reach a detection rate of unity at $S/N \gtrsim 5$. Moreover, the completeness and the line dispersion are weakly anticorrelated at low S/N. Again the dependence disappears at high S/N.

In spite of these correlations we decided to consider the median completeness of the simulated templates in order to obtain a simplified mapping of the completeness to redshift and apparent magnitude. This is justified since the intrinsic line equivalent widths for every detected quasar cannot be measured reliably in the slitless spectra because of uncertainties in the automatic continuum placement and the rough feature detection with two Gaussian emission line templates. Figure 2.17 presents the contour map of the median completeness together with the quasars and quasar candidates from our survey as a function of redshift and apparent V magnitude. The completeness varies with the visibility of different emission lines in the spectrum. Due to its high equivalent width Lyα emission is detectable for ∼ 80% of the simulated spectra at $V \simeq 22$ corresponding to a continuum $S/N \sim 1$. At both ends of the spectral range the completeness drops because Lyα falls close to the end the spectrum, causing difficulties in the automatic continuum definition. The cutoff is sharper at the red end ($z \simeq 3.60$) than at the blue end due to the decreasing sensitivity in the blue part of the spectrum, resulting in a decreasing completeness before Lyα leaves the spectral range at $z \simeq 2.5$. At lower redshifts the completeness is smaller due to the lower equivalent widths of C IV and C III]. Again the completeness is redshift-dependent due to the varying sensitivity. At $z \lesssim 1.3$ C III] emission remains undetected due to the selection effects at the end of the spectral range. The gap at $1.05 \lesssim z \lesssim 1.30$ naturally arises because of the lack of strong emission lines in the spectral range before Mg II gets selected at lower redshifts.

The selected quasars and quasar candidates fill the full range of completeness values spanned by the simulated redshifts and magnitudes (S/N). The known quasars at the field centres are separated from the other quasars and candidates in magnitude and redshift. Since we concentrated our follow-up campaign on bona fide candidates at probable high redshift, many faint objects at likely low redshift were not verified. Candidates with uncertain redshifts have uncertain completeness levels. Moreover, the assignment of selection probabilities to faint objects is limited by the larger photometric errors.

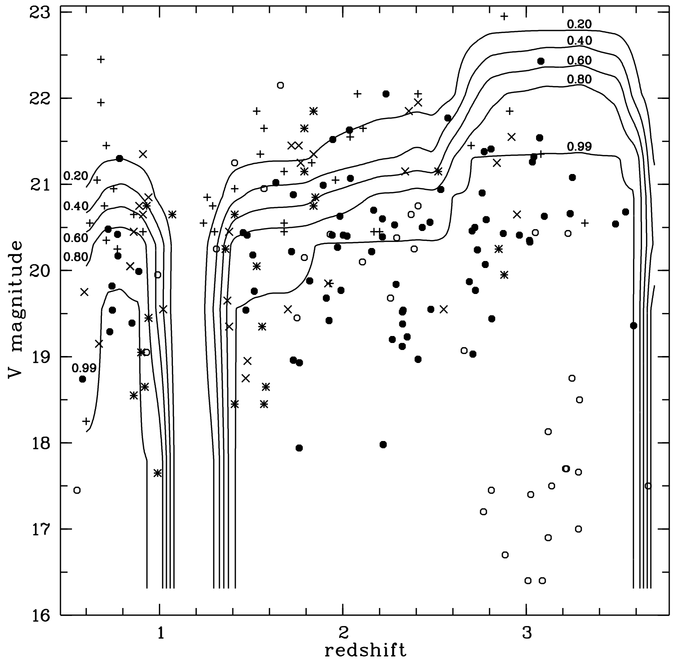

Fig. 2.17. Completeness of our survey as a function of redshift and apparent V magnitude. Contours correspond to median simulated detection probabilities $p \in \{0.2, 0.4, 0.6, 0.8, 0.99\}$. Quasars and quasar candidates are overplotted and marked as in Fig. 2.15.

The overall completeness of our survey crucially depends on the completeness of the input source catalogues (Sect. 2.3.2). As most of the DSS input catalogues are fairly complete up to $V \simeq 21$ (Table 2.2), the selection of $z \lesssim 2.5$ quasars via emission lines with low equivalent widths should not be much affected by photometric incompleteness. However, lacking depth of the source catalogues is important for $z \gtrsim 2.5$ quasars that remain detectable by their Lyα emission well beyond $V \simeq 22$. Lyα of faint quasars is easily visually recognised in the slitless data. Indeed, two of the quasars undetected in the DSS display prominent Lyα emission (Sect. 2.4.2). However, in spite of our trained eyes we cannot be sure to have found all further Lyα emitting quasars in our visual search.

2.7.2. Comparison to other surveys

With the survey selection function from above we are able to compare our number counts of quasars with those of other surveys. The only comparably deep slitless survey is the Palomar Scan Grism Survey (PSGS, Schneider et al. 1999) which yielded 39 quasars on 1.10 deg^2 at $R \lesssim 22$. The PSGS covered the wavelength range 4400–7500 Å, with a line equivalent width limit $W_{\mathrm{obs}} > 50$ Å and a total S/N limit in the line $(S/N)_{\mathrm{line}} > 5.95$. Disregarding the known bright quasars at the field centres our survey detected 190 quasars and highly promising candidates on 4.39 deg^2, resulting in a $\simeq 1.2$ times higher total surface density. The wavelength coverage of the PSGS is larger, providing contiguous redshift coverage in comparison to our survey that has a small redshift gap. High-redshift quasars are rare, so that the extension towards the red does not have a big effect. The difference in the surface densities is likely due to the higher selection limits of the PSGS. Thus, both surveys are consistent with each other.

A more quantitative comparison is possible by comparing our survey to the photometric COMBO-17 survey (Wolf et al. 2003). Since COMBO-17 is defined in the R band whereas our survey is best defined in V, we assumed a quasar colour of $V - R = 0.2$ to convert the surface densities. In Fig. 2.18 we plot the cumulative and differential surface densities of quasars of both surveys corrected for the survey selection function. The bright central quasars of our fields have been excluded, whereas other known quasars in the fields remained in the sample. Candidates are assumed to be quasars at the estimated redshifts. The total cumulative surface densities are in very good agreement at $20.5 \lesssim V \lesssim 22$. At $V < 20.5$ the surface density implied by our survey is lower by a factor ~ 2. However, this is not significant due to the small number of quasars at the bright end. Furthermore, a comparison in terms of total number counts is somehow misleading due to the low-redshift cut of COMBO-17 at $z = 1.2$ and the excluded redshift range $1.05 \lesssim z \lesssim 1.30$ of our survey. We cannot detect the $z \gtrsim 3.65$ quasars of COMBO-17, but they do not affect the number counts in the common magnitude range because the majority of them has $R > 22$ (Wolf et al. 2003). Restricting both samples to $z > 1.8$ we see that the COMBO-17 surface density is higher by a factor ~ 2 compared to our survey over most of the common magnitude range, pointing towards a systematic incompleteness of our survey.

We therefore also considered the differential surface densities. The total differential surface densities are consistent as well as the differential number counts restricted to $z > 1.8$ at $V \lesssim 20$. In contrast, at $V \gtrsim 21$ the $z > 1.8$ differential surface densities of our survey are lower than those of COMBO-17 by a factor ~ 2.4, being inconsistent at the $> 2\sigma$ level. At the first glance this might be explained by the photometric incompleteness of our source catalogues at $V \gtrsim 21$ (Sect. 2.3.2). However, even adopting a conservatively low photometric completeness of 65% at $V \simeq 21$ (Table 2.2) does not solve the discrepancy, so that other effects might play a role.

1. *Visual selection effects:* The visual selection of quasar candidates from the automatically selected sample might have been too restrictive, so that faint quasars with low-quality slitless spectra were lost. In this study we neglected 38 objects of the selected sample because their emission line features are extremely weak, so that their reality is questionable. Since all of them are very faint on the direct images some might not be real. We therefore decided to exclude all of them. However, due to their low completeness levels, the real objects among them could boost the number counts significantly.
2. *Wrong redshifts:* Wrong redshift estimates of quasar candidates might also have an influence. In Fig. 2.17 we note six faint $z < 1.6$ candidates with purely estimated redshifts (emission feature treated as C III] or Mg II). Their redshift assignment is based on similarity of the candidate spectra and the slitless spectra of verified low-redshift quasars. Nevertheless, if the emission line is C IV these candidates could reside at $z > 1.8$ as well.
3. *Simplifications in completeness estimates:* The assumed similar data quality for all fields is certainly an approximation because of slight differences in sky transparency and considerable seeing variations among the slitless data. Most prominent in this respect is the field centred on Q 1451+123 that was observed at moderate to poor seeing and high airmasses between 1.3 and 1.9, yielding only two low-priority quasar candidates. Seeing variations mostly affect faint quasars showing weak lines in the covered wavelength range. For quantifying the survey selection function we also assumed that all quasars were recorded without contamina-

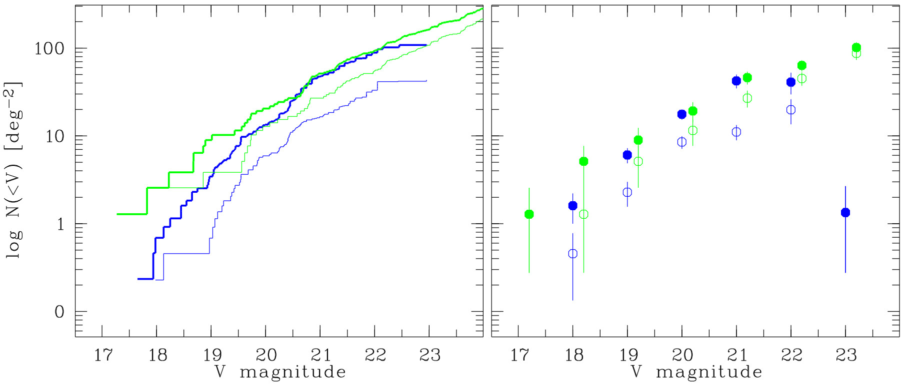

Fig. 2.18. *Left:* Cumulative quasar surface density $N(< V)$ per deg^2 as a function of V derived from our survey (blue/black) and COMBO-17 (green/grey). The thin (thick) lines denote the $z > 1.8$ (total) surface densities. *Right:* Differential quasar surface density per magnitude and deg^2 of our survey (black) and COMBO-17 (grey). Full symbols show the total differential surface densities, whereas the open symbols are for $z > 1.8$. Error bars assume Poisson statistics.

tion in every exposure leading to a tight relation between the spectral S/N and the magnitude. In reality, net exposure times differ due to dithering, field rotation and overlapping spectra. Moreover, we assumed for our completeness map that the quasars do not vary much in emission line equivalent width and line dispersion. Refining the survey selection function of each quasar separately will induce some shifts in the distribution of Fig. 2.17, but the net effect is probably negligible.

In summary, a combination of incompleteness of the input source catalogues, biases in the sample definition at faint magnitudes and redshift uncertainties of faint quasar candidates likely explains the discrepancy of the differential surface density at the faint end of our survey compared to COMBO-17. However, one has to keep in mind that the selection of quasar candidates from spectra at a continuum $S/N \lesssim 2$ (corresponding to $V \gtrsim 21.2$) is not trivial. Probably, the visual screening of the automatically selected candidates lead to a preference of survey efficiency over completeness at the faint end of the survey. This is also supported by the high success rate in the spectroscopic follow-up. All emission line objects selected for follow-up were confirmed, suggesting the reality of the vast majority of the selected emission features of the complete sample. Definitely, our survey would have have been better defined at the faint end with sufficiently deep object catalogues, but apart from Lyα the reality of very noisy features is difficult to judge. We have shown that it is possible to reach $V \sim 22$ in slitless spectra with a 2 m-class telescope which we did not expect a priori. This demonstrates that wide-field slitless spectrographs on (nowadays) small telescopes can compete with those on larger telescopes. For example, the effective exposure time per object in the PSGS was 585 s on the Hale 5 m telescope (Schneider et al. 1999). Accounting for the difference in aperture yields a required ∼ 1 h total exposure time on a 2.2 m telescope to reach $R \sim 22$, which agrees extremely well with our survey parameters.

2.7.3. New quasar groups

The main goal of this survey was to reveal new groups of quasars for further studies of the three-dimensional distribution of the intergalactic medium. In the follow-up observations we concentrated on likely high-redshift $z > 1.7$ quasars, of which ∼ 50% could be confirmed at their estimated redshifts. In total, 80% of the newly established quasars are at $z > 1.7$.

The densest groups of quasars now contain several high-redshift quasars in addition to the few previously known quasars rediscovered in our survey. For instance, we have revealed 4 quasars at $2.77 < z < 3.07$ around Q 0000−26 and a dense group of 4 quasars at $2.70 < z < 2.78$ around Q 0347−383. Other new discoveries include 5 $z > 2$ quasars near Q 0420−388 and HE 2243−6031. The remarkable group of 5 $z > 2.28$ quasars around HE 2347−4342 is discussed in Chapter 5. The number of $z > 2$ quasars around HE 0940−1050 is even higher (6). As an example we plot in Fig. 2.19 the angular distribution of quasars and quasar candidates with respect to Q 0420−388 together with the distribution of the quasars on the sky. The known $z = 2.42$ quasar near Q 0420−388 was readily rediscovered in our survey. In total, there are now seven $z > 2$ quasars in this field and two other candidates with estimated high redshifts. Similar figures for the other survey fields are presented in Appendix D.

The group around HE 2243−6031 is of particular interest for further studies of quasar-absorber clustering (D'Odorico et al. 2002; Hennawi et al. 2006). In this field our survey revealed two bright quasars (QSO J22463−6009 and QSO J22454−6011 from Table 2.3) that coincide in redshift with the $z = 2.33$ damped Lyα absorber towards HE 2243−6031 discussed by Lopez et al. (2002). The foreground quasars are separated from the central line of sight by 9$'\!.$2 and 13$'\!.$2, corresponding to transverse comoving distances of 15.1 and 21.6 Mpc in the Λ concordance model, respectively. This underlines the potential of our present quasar sample and the need for further investigations.

2.8. Conclusions

We performed a CCD-based slitless spectroscopic survey for faint $V \lesssim 22$ quasars at $1.7 \lesssim z \lesssim 3.6$ around 18 well-studied bright quasars at $2.76 < z < 4.69$, covering a total area of $\simeq 4.39$ deg^2. In order to analyse the slitless data we developed a data reduction pipeline that performs an optimal extraction of the spectra and that is able to cope with contaminating spectral orders of slitless grism data. From the ∼ 29000 extracted flux-calibrated spectra we selected 169 previously unknown quasar candidates and > 100 likely low-redshift emission line galaxy candidates on the basis of emission features that fall in the covered wavelength range 4200 Å$\leq \lambda \leq$5800 Å. A semi-automatic selection routine limited potential biases of purely visual selection and allowed to quantify selection effects.

Follow-up spectroscopy confirmed 80 out of 81 selected quasar candidates on 16 fields. 64 of these newly established quasars reside at $z > 1.7$. The highest redshift quasar is QSO J22484−6002 at $z = 3.586$. The brightest newly discovered high-redshift quasar in our sample is QSO J11197−1340 ($z = 2.220$, $B = 18.3$). Given the high success rate of the follow-up, the vast majority of the remaining 88 candidates will be quasars as well, although most of them likely reside at lower redshifts. Our redshift estimates of 23 candidates are robust, ei-

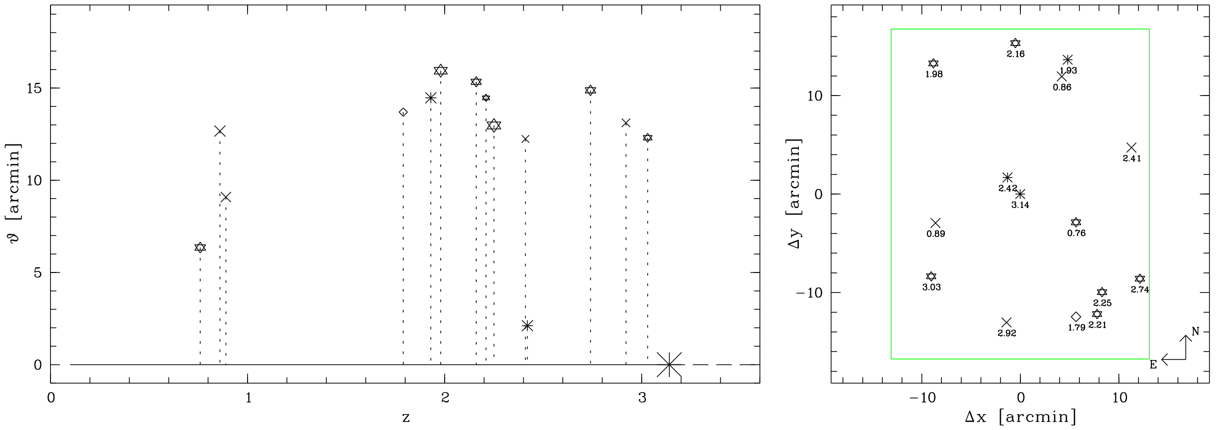

Fig. 2.19. *Left:* Angular distribution of quasars and quasar candidates with respect to the central quasar Q 0420−388 as a function of redshift. Asterisks and star symbols mark known quasars and newly discovered confirmed quasars, respectively. Apart from the central quasar only rediscovered known quasars are shown (inside surveyed field, brighter than $V \simeq 22$, emission line in the observed wavelength range). Lozenges (crosses) show remaining WFI quasar candidates with secure (estimated) redshifts. Symbol size indicates apparent optical magnitude. All redshifts have been measured in the slitless WFI spectra ($\sigma_z \lesssim 0.03$). *Right:* Quasar distribution on the sky centred on Q 0420−388 with indicated redshifts. The green/grey rectangle marks the nominal contiguous slitless WFI field of view ($26\farcm2 \times 33\farcm5$) without rotating the instrument, for simplicity centred on Q 0420−388.

ther due to the detection of two emission features yielding a consistent redshift, or due to the strength or shape of an isolated emission line.

Our survey is not well defined in terms of limiting magnitude because of photometric incompleteness in the source catalogues needed for automatic extraction of the slitless spectra. Together with the fact that not all selected quasar candidates could be included in the spectroscopic follow-up, our survey probably is of limited use for constraining quasar evolution. However, the primary aim of this survey was to provide new groups of quasars for medium-resolution spectroscopy. Therefore, focusing on survey efficiency rather than on completeness at the faint end was justified. In fact, we did not expect to reach as faint as $V \sim 22$ in the survey observations and the faintest quasars discovered will remain beyond the limits for medium-resolution spectroscopy. On the other hand, the $V \lesssim 21$ quasars are well suited for follow-up studies with current (e.g. ESI at Keck) or upcoming (e.g. X-shooter at VLT) high-throughput spectrographs at 8–10 m-class telescopes. Thus, the main goal of this survey could be accomplished.

Together with the central quasars in the fields already observed at high resolution, these quasar groups can be used to perform a tomography of the intergalactic medium (e.g Pichon et al. 2001). Large-scale clustering of the Lyα forest or correlations of metal line systems can be investigated as well (Williger et al. 2000; D'Odorico et al. 2002, 2006). Some of the discovered quasars reside at similar redshifts or approximately at the same redshift of the central quasar in the field, giving potentially insights to quasar clustering along overdense filaments in the plane of the sky. We have identified two quasars coinciding with a damped Lyα absorber on one central line of sight, as well as a large-scale group of quasars at $z = 2.70$–2.78, but there might be more of these associations. Moreover, our study provides new foreground quasars to search for the transverse proximity effect of quasars (e.g. Liske & Williger 2001, and the following chapters of this thesis). In combination with the already available high-resolution spectra of the central quasars, medium-resolution spectra of these quasar groups will offer great opportunities to study the large-scale cosmic web in three dimensions.

Acknowledgements. We thank the staff of the ESO observatories La Silla and Paranal for their professional assistance in obtaining the data presented in this paper. Based on observations collected at the European Southern Observatory, Chile (Proposals 70.A-0425, 074.A-0273 and 075.A-0141). Data taken under proposals 68.A-0330 and 70.A-0384 were obtained from the ESO Science Archive.

The Digitized Sky Surveys were produced at the Space Telescope Science Institute under U.S. Government grant NAG W-2166. The images of these surveys are based on photographic data obtained using the Oschin Schmidt Telescope on Palomar Mountain and the UK Schmidt Telescope. The plates were processed into the present compressed digital form with the permission of these institutions.

References

Adelberger, K. L., Shapley, A. E., Steidel, C. C., et al. 2005, ApJ, 629, 636
Appenzeller, I., Fricke, K., Furtig, W., et al. 1998, The Messenger, 94, 1
Baade, D., Meisenheimer, K., Iwert, O., et al. 1999, The Messenger, 95, 15
Bahcall, J. N. & Soneira, R. M. 1981, ApJS, 47, 357
Barger, A. J., Cowie, L. L., Capak, P., et al. 2003, AJ, 126, 632
Bohuski, T. J. & Weedman, D. W. 1979, ApJ, 231, 653
Clowes, R. G., Campusano, L. E., & Graham, M. J. 1999, MNRAS, 309, 48
Clowes, R. G., Cooke, J. A., & Beard, S. M. 1984, MNRAS, 207, 99
Colless, M., Dalton, G., Maddox, S., et al. 2001, MNRAS, 328, 1039
Cowie, L. L., Barger, A. J., Hu, E. M., Capak, P., & Songaila, A. 2004, AJ, 127, 3137
Crampton, D., Cowley, A. P., & Hartwick, F. D. A. 1990, AJ, 100, 47
Croom, S. M., Smith, R. J., Boyle, B. J., et al. 2004, MNRAS, 349, 1397
Crotts, A. P. S. & Fang, Y. 1998, ApJ, 502, 16
Dinshaw, N. & Impey, C. D. 1996, ApJ, 458, 73
D'Odorico, V., Petitjean, P., Cristiani, S., & D'Odorico, S. 2002, A&A, 390, 13
D'Odorico, V., Viel, M., Saitta, F., et al. 2006, MNRAS, 372, 1333
Gaskell, C. M. 1982, ApJ, 263, 79
Gratton, R. G. & Osmer, P. S. 1987, PASP, 99, 899
Hennawi, J. F., Prochaska, J. X., Burles, S., et al. 2006, ApJ, 651, 61
Hewett, P. C., Foltz, C. B., & Chaffee, F. H. 1995, AJ, 109, 1498
Hewett, P. C., Irwin, M. J., Bunclark, P., et al. 1985, MNRAS, 213, 971
Horne, K. 1986, PASP, 98, 609
Jakobsen, P. & Perryman, M. A. C. 1992, ApJ, 392, 432
Jakobsen, P., Perryman, M. A. C., Ulrich, M. H., Macchetto, F., & di Serego Alighieri, S. 1986, ApJ, 303, L27
Krumpe, M., Lamer, G., Schwope, A. D., et al. 2007, A&A, 466, 41
Landolt, A. U. 1992, AJ, 104, 340
Liske, J., Webb, J. K., Williger, G. M., Fernández-Soto, A., & Carswell, R. F. 2000, MNRAS, 311, 657
Liske, J. & Williger, G. M. 2001, MNRAS, 328, 653
Lopez, S., Reimers, D., D'Odorico, S., & Prochaska, J. X. 2002, A&A, 385, 778
McIntosh, D. H., Rix, H.-W., Rieke, M. J., & Foltz, C. B. 1999, ApJ, 517, L73

Pichon, C., Vergely, J. L., Rollinde, E., Colombi, S., & Petitjean, P. 2001, MNRAS, 326, 597
Prescott, M. K. M., Impey, C. D., Cool, R. J., & Scoville, N. Z. 2006, ApJ, 644, 100
Richards, G. T., Fan, X., Newberg, H. J., et al. 2002a, AJ, 123, 2945
Richards, G. T., Vanden Berk, D. E., Reichard, T. A., et al. 2002b, AJ, 124, 1
Schmidt, M., Schneider, D. P., & Gunn, J. E. 1986, ApJ, 306, 411
Schmidt, M., Schneider, D. P., & Gunn, J. E. 1995, AJ, 110, 68
Schneider, D. P., Hall, P. B., Richards, G. T., et al. 2007, AJ, 134, 102
Schneider, D. P., Schmidt, M., & Gunn, J. E. 1994, AJ, 107, 1245
Schneider, D. P., Schmidt, M., & Gunn, J. E. 1999, AJ, 117, 40
Sramek, R. A. & Weedman, D. W. 1978, ApJ, 221, 468
Steidel, C. C., Adelberger, K. L., Shapley, A. E., et al. 2003, ApJ, 592, 728
Szokoly, G. P., Bergeron, J., Hasinger, G., et al. 2004, ApJS, 155, 271
Trump, J. R., Impey, C. D., McCarthy, P. J., et al. 2007, ApJS, 172, 383
Tytler, D. & Fan, X. 1992, ApJS, 79, 1
Vanden Berk, D. E., Richards, G. T., Bauer, A., et al. 2001, AJ, 122, 549
Warren, S. J., Hewett, P. C., Irwin, M. J., & Osmer, P. S. 1991, ApJS, 76, 1
Warren, S. J., Hewett, P. C., & Osmer, P. S. 1994, ApJ, 421, 412
Williger, G. M., Hazard, C., Baldwin, J. A., & McMahon, R. G. 1996, ApJS, 104, 145
Williger, G. M., Smette, A., Hazard, C., Baldwin, J. A., & McMahon, R. G. 2000, ApJ, 532, 77
Wisotzki, L., Christlieb, N., Bade, N., et al. 2000, A&A, 358, 77
Wisotzki, L., Selman, F., & Gilliotte, A. 2001, The Messenger, 104, 8
Wolf, C., Meisenheimer, K., Kleinheinrich, M., et al. 2004, A&A, 421, 913
Wolf, C., Wisotzki, L., Borch, A., et al. 2003, A&A, 408, 499
Worseck, G., Fechner, C., Wisotzki, L., & Dall' Aglio, A. 2007, A&A, 473, 805
Worseck, G. & Wisotzki, L. 2006, A&A, 450, 495
Zitelli, V., Mignoli, M., Zamorani, G., Marano, B., & Boyle, B. J. 1992, MNRAS, 256, 349

Chapter 3

On the detectability of the transverse proximity effect in the H I Lyman alpha forest[⋆]

G. Worseck

ABSTRACT

We study the Lyα forest of quasars in 16 closely spaced groups on the sky in order to search for the transverse proximity effect as a decreased effective optical depth. We perform extensive Monte Carlo simulations to quantify the intrinsic small-scale fluctuations of the forest absorption and quasar continuum errors, which both mask any weak predicted transverse proximity effect. From our initial sample of 39 quasar pairs only three foreground quasars are expected to show the effect at the 1–2σ level. In contrast, the data does not show any sign of the transverse proximity effect. In fact, for the most prominent pair (Q 2138−4427 at $z = 3.120$ near Q 2139−4434 at $z = 3.214$) we find evidence for excess absorption instead of the predicted excess transmission. As in most existing studies, the transverse proximity effect might be hidden due to the systematic effects of potential quasar anisotropy, long-term variability and intrinsically overdense environments. We show that an unambiguous measurement of a transverse proximity effect in the Lyα forest requires $\gtrsim 5$ medium-resolution spectra of background quasars near foreground quasars that exceed the UV background intensity by a factor of $\gtrsim 3$. Thus even disregarding probable systematic effects, cosmic variance clearly limits the detectability of the weak transverse proximity effect in small samples like ours.

3.1. Introduction

High-resolution spectra of quasars reveal a plethora of absorption lines that are primarily caused by Lyα absorption of intervening neutral hydrogen along the line of sight through the intergalactic medium (IGM, Lynds 1971; Sargent et al. 1980; Rauch 1998). This Lyα forest is in photoionisation equilibrium with the intergalactic UV radiation field generated by the overall population of quasars and star-forming galaxies (e.g. Haardt & Madau 1996; Fardal et al. 1998; Madau et al. 1999).

The UV radiation field is expected to be inhomogeneous due to the discreteness of the ionising sources (Zuo 1992; Fardal & Shull 1993; Croft et al. 1999; Meiksin & White 2004; Croft 2004; McDonald et al. 2005). In particular, the IGM will be more highly ionised in the vicinity of a luminous quasar that should result in a statistically lower Lyα absorption. This so-called proximity effect has been found in lines of sight towards luminous quasars as a reduced line density (e.g. Bajtlik et al. 1988; Giallongo et al. 1996; Cooke et al. 1997; Scott et al. 2000) and as a reduced optical depth (Liske & Williger 2001; Rollinde et al. 2005; Guimarães et al. 2007). Knowing the UV luminosity of the quasar, a comparison of its relative impact onto the IGM compared to the UV background yields a measurement of the latter (e.g. Bajtlik et al. 1988). The proximity effect on the quasar's own line of sight has been established statistically using samples of up to ∼ 100 quasars (Bajtlik et al. 1988; Lu et al. 1991; Bechtold 1994; Giallongo et al. 1996; Cooke et al. 1997; Scott et al. 2000; Liske & Williger 2001; Rollinde et al. 2005; Guimarães et al. 2007) and also towards single lines of sight (Williger et al. 1994; Cristiani et al. 1995; Lu et al. 1996; Savaglio et al. 1997; Dall'Aglio et al. 2007).

Given the large characteristic size of the proximity effect region around a luminous quasar (∼ 10 proper Mpc), a background sightline intersecting the proximity effect zone of a foreground quasar should show an underdense region due to the radiative impact of the foreground quasar in the plane of the sky. Generally, this transverse proximity effect (TPE) has not been clearly detected in the H I forest. Two large H I voids have been claimed to be due to the TPE. Dobrzycki & Bechtold (1991a) found a large void in the H I forest towards Q 0302−003, very close but not centred on the luminous foreground quasar Q 0301−005 at $z = 3.231$, separated from the line of sight by $\vartheta = 22\farcm9$. However, because of the large distance between the quasar and the void, Q 0301−005 must have been implausibly bright to cause the large clearing in the forest (Dobrzycki & Bechtold 1991b). The soft radiation field also argues against a connection of the quasar and the void (see Chapter 4). Srianand (1997) found a similar large significant void towards Tol 1038−2712 from the high-resolution line list obtained by Dinshaw & Impey (1996). The void is apparently centred on Tol 1037−2704 ($z = 2.195$, $\vartheta = 17\farcm9$). Based on the low probability of chance occurrence, Dobrzycki & Bechtold (1991a) and Srianand (1997) argued for a transverse proximity effect.

On the other hand, several studies found at best marginal evidence for a transverse proximity effect. (Fernández-Soto et al. 1995) searched for the effect in three pairs, but found evidence for it only at the ∼ 1σ level. Liske & Williger (2001) performed a systematic study for a TPE in a group of 17 quasars. They did not find evidence for a general presence of the TPE, but presented a fortunate constellation of 4 background sightlines showing underdensities at $\Delta v = \pm 3000\ \mathrm{km\,s^{-1}}$ with respect to a foreground quasar. According to Liske & Williger (2001) these 4 sightlines yield the TPE at a significance level of 3.5σ. However, most attempts to discover the TPE resulted in non-detections (Crotts 1989; Møller & Kjærgaard 1992; Crotts

---

[⋆] A version of this chapter will be submitted to *Astronomy & Astrophysics*. The complete list of authors will appear on the submitted manuscript.

& Fang 1998; Schirber et al. 2004; Croft 2004; Kim & Croft 2007). In particular, the large number of quasars discovered in the Sloan Digital Sky Survey (SDSS) has been frequently used to search for underdense absorption near foreground quasars. Schirber et al. (2004) selected three fortunate pairs from the SDSS Early Data Release, but did not find the effect predicted at high significance. Using larger samples of quasar pairs at larger projected separations from subsequent SDSS data releases Croft (2004) and Kim & Croft (2007) reveal excess absorption instead of excess transmission close to foreground quasars.

A combination of several systematic effects may be responsible for the frequent non-detections of the TPE. The UV emission of quasars may be intrinsically anisotropic, explaining either redshift offsets of voids (Dobrzycki & Bechtold 1991a) or the lack of the TPE (e.g. Crotts 1989; Møller & Kjærgaard 1992; Schirber et al. 2004). Due to the long light travel times between the lines of sight ($\gtrsim 1$ Myr), quasar variability likely plays a role (Liske & Williger 2001; Croft 2004), but it it cannot be the sole explanation in case of close quasar pairs (Schirber et al. 2004). The lifetimes of quasars may be shorter than the required light travel times or may be episodic (Croft 2004; Adelberger 2004; Hopkins et al. 2005b,a), so that the quasar UV flux and the flux inferred on the background sightline are uncorrelated. Finally, quasars are likely to reside in the most massive haloes, so that intrinsic overdensities can diminish the expected proximity effect (Loeb & Eisenstein 1995; Rollinde et al. 2005; Guimarães et al. 2007; Faucher-Giguère et al. 2007a). Closely projected quasar pairs (proper separations $\lesssim 1$ Mpc) even show excess clustering of optically thick absorption systems in transverse direction, which in turn could be explained by anisotropy or variability (Hennawi et al. 2006; Hennawi & Prochaska 2007).

In contrast to the non-detections in the Lyα *forest*, the TPE has been discovered in few individual objects as a void in the Gunn-Peterson troughs of He II (Jakobsen et al. 2003) and H I (Gallerani et al. 2007). This might be explained by the smaller opacity variations of the IGM and a lower UV background close to the reionisation epoch, leading to a stronger signature of the TPE compared to the fully ionised universe. Moreover, in Worseck & Wisotzki (2006) and Worseck et al. (2007) (Chapters 4 and 5 of this thesis) we revealed the TPE as a systematic hardening of the spectral shape of the UV radiation field in the vicinity of seven foreground quasars by comparing the H I absorption to the corresponding He II absorption towards Q 0302−003 and HE 2347−4342. The regions near most of the foreground quasars were consistent with excess H I absorption and the predicted TPE in H I was small, so the spectral hardness is able to reveal even a weak TPE in overdense regions. Thus, it might be premature to claim an apparent absence of the TPE due to the above systematic effects.

However, the TPE in the Lyα forest is unlikely to be revealed at high significance in the projected vicinity of a single quasar (Dobrzycki & Bechtold 1991b). Therefore, many close quasar pairs are needed in order to find the effect statistically. Due to the lack of suitable quasar pairs on the southern hemisphere, we conducted a survey for faint quasars in the vicinity of 16 bright quasars with available high-quality high-resolution spectra (Chapter 2). Here we analyse the 16 quasar groups for signatures of the transverse proximity effect as an underdense region in the H I forest. The paper is organised as follows. In Sect. 3.2 we describe the available data and the sample selection process. In Sect. 3.3 we use Monte Carlo simulations to quantify statistical fluctuations in the Lyα forest and systematic errors due to continuum fitting which likely affect the detectability of the TPE. Sect. 3.4 is devoted to our non-detection of the TPE. In Sect. 3.5 we discuss the general detectability of the TPE and the considerable systematic uncertainties. Sect. 3.6 presents our conclusions. Throughout the paper we adopt a flat cosmological model with $\Omega_{\mathrm{m}} = 0.3$, $\Omega_\Lambda = 0.7$ and $H_0 = 70\ \mathrm{km\,s^{-1}\,Mpc^{-1}}$. All distances are proper unless stated otherwise.

3.2. Available data and sample selection

3.2.1. The initial quasar sample

The majority of quasars that we use to search for the transverse proximity effect were discovered in our slitless spectroscopic survey for faint quasars in the vicinity of 16 well-studied bright quasars (Chapter 2). Using the ESO Wide Field Imager in its slitless spectroscopic mode (Wisotzki et al. 2001), quasar candidates on the $\sim 26' \times 33'$ fields were identified as emission line sources among the slitless spectra of $V \lesssim 22$ objects. Follow-up spectroscopy with FORS2 confirmed 80 bona fide quasar candidates. A detailed description of the survey is presented in Chapter 2. Here we use the reduced FORS2 spectra of our 64 newly discovered quasars at $z > 1.7$ that were taken with the 600B and the 300V grisms at respective resolutions of $\Delta\lambda \simeq 4.5$Å and $\Delta\lambda \simeq 10$Å (FWHM).

The survey fields were centred on 16 bright high-redshift quasars, of which we obtained FORS2 600B spectra in the course of the survey campaign. These data are partly discussed in Dall'Aglio et al. (2007). We also took spectra of 9 other previously known quasars in the survey fields in order to gain additional sightlines for our study and to estimate their systematic redshifts and their spectrophotometric properties.

We searched the ESO Science Archive for low-resolution spectra of previously known quasars in the fields, yielding FORS1 spectra of five quasars. We retrieved and reduced the spectra of QSO 03022−0023 and QSO 03020−0014 (Jakobsen et al. 2003), QSO J23508−4335 and QSO J23500−4319 (Chapter 5) and Q 2138−4427 (PI J. Fynbo). The spectrum of Q 0301−005 was obtained from the archive of the Sloan Digital Sky Survey (SDSS).

Properties of 30 remaining known quasars without accessible spectroscopic data were obtained from the NED and the quasar catalogue by Véron-Cetty & Véron (2006). Table 3.1 lists all 125 $z > 1.7$ quasars within a radius of $30'$ around the central quasars in the fields. The redshift constraint $z > 1.7$ is required in order to observe Lyα from the ground.

3.2.2. Quasars with UVES spectra

The 16 survey fields were centred on quasars with available UVES spectra, which we retrieved from the ESO Science Archive (Table 3.2). A. Dall'Aglio kindly reduced the data with the UVES data reduction pipeline (Ballester et al. 2000). Most of the vacuum-barycentric corrected co-added spectra reach $S/N \gtrsim 30$ in the Lyα forest at $R \sim 45000$. The data of BR 1117−1329 and BR 1202−0725 had to be excluded due to reduction problems. The data of Q 0000−26 and Q 0302−003 were taken during the commissioning of UVES and could not be processed with the UVES pipeline. Instead, we generated Lyα forest spectra of these two quasars based on published line lists (Q 0302−003: Hu et al. (1995); Kim et al. (2002), Q 0000−26: Lu et al. (1996)) and added noise to resemble the original spectra. In addition to the bright quasars in the centres of the fields we retrieved the UVES spectra of Q 2138−4427.

All UVES quasar spectra were normalised with our automatic cubic spline fitting programme based on the algorithms

Table 3.1. Spectrophotometry of the quasar sample. The columns list the field (name of the central bright quasar), the QSO name, redshift, magnitude, filter, colour excess from Schlegel et al. (1998), logarithmic flux density at the Lyman limit in the QSO rest frame (in erg cm^{-2} s^{-1} Hz^{-1}), spectral index ($f_\nu \propto \nu^{-\alpha}$), the FORS grism used and the reference for the quasar photometry.

Field	QSO	z	Mag.	Filter	$E(B-V)$	$\log f_{\nu_{\rm LL}}$	α	FORS grism	reference
Q 0000−26	QSO J00040−2603	2.002	20.54	*B*	0.016	−27.83	0.57 ± 0.03	600B	1
	QSO J00035−2610	2.771	21.61	*B*	0.014	−28.16	0.47 ± 0.10	600B	1
	QSO J00028−2547	2.812	19.84	*B*	0.017	−27.32	0.16 ± 0.13	600B	1
	QSO J00035−2551	2.875	20.99	*B*	0.017	−27.78	0.60 ± 0.08	600B	1
	Q 0000-C14	3.057	25.33	*g*		−29.88	1.88		2
	QSO J00038−2617	3.073	22.09	*B*	0.014	−28.19	0.56 ± 0.04	300V	1
	Q 0000-C7	3.426	24.28	*g*		−29.41	1.88		2
	Q 0000-C5	3.791	24.70	*g*		−29.42	1.88		2
	Q 0000−26	4.125				−26.60		600B	
Q 0002−422	QSO J00041−4158	1.720	20.36	*B*	0.011	−27.74	0.52 ± 0.02	300V	1
	QSO J00045−4201	2.157	20.35	*B*	0.010	−27.62	0.12 ± 0.02	300V	1
	Q 0000−4239	2.190	21.10	*V*		−28.30	1.88		3
	Q 0001−4227	2.260	19.80	*B*	0.012	−27.47	0.27 ± 0.02	300V	1
	Q 0002−422	2.767	17.20	*V*	0.011	−26.46	0.32 ± 0.02	600B	3
H 0055−269	Q 0053−2656	1.882	19.67	*V*		−27.73	1.88		3
	QSO J00576−2626	1.942	20.73	*B*	0.018	−27.74	0.28 ± 0.02	300V	1
	Q 0056−2700	2.294	20.55	*B*	0.020	−27.85	0.73 ± 0.04	600B	1
	Q 0055−2654	2.389	20.46	*B*	0.019	−27.75	0.52 ± 0.03	300V	1
	QSO J00582−2649	2.572	22.02	*B*	0.019	−28.34	0.36 ± 0.02	300V	1
	QSO J00583−2626	2.720	21.00	*B*	0.018	−27.76	0.35 ± 0.02	300V	1
	H 0055−269	3.665	17.50	*V*	0.020	−26.61	0.97 ± 0.07	600B	3
Q 0302−003	QSO 03022−0023	2.142	22.46	*V*	0.088	−28.70	1.05 ± 0.06	300V	4
	QSO J03052−0016	2.290	20.05	*B*	0.077	−27.47	0.36 ± 0.02	300V	5, 1
	SDSS J0303−0020B	2.718	19.67	*r*		−27.71	1.88		6
	QSO J03052+0000	2.808	21.79	*B*	0.093	−28.13	0.68 ± 0.03	300V	5, 1
	Q 0302-D113	2.920	24.68	*g*		−29.63	1.88		2
	QSO 03020−0014	3.050	20.44	*V*	0.094	−27.74	0.70 ± 0.02	300V	4
	Q 0301−005	3.231	17.64	*r*	0.113	−26.53	0.51 ± 0.02		7, 4
	Q 0302−003	3.285	18.76	*B*	0.092	−26.59	0.09 ± 0.02	600B	1
Q 0347−383	QSO J03500−3820	1.819	20.03	*B*	0.011	−27.62	0.51 ± 0.02	300V	1
	QSO J03490−3812	1.945	21.66	*B*	0.012	−28.29	0.61 ± 0.02	300V	1
	QSO J03496−3821	2.351	19.43	*B*	0.010	−27.41	0.74 ± 0.02	600B	1
	QSO J03496−3810	2.433	20.87	*B*	0.009	−27.99	1.03 ± 0.03	600B	1
	QSO J03495−3806	2.475	20.86	*B*	0.009	−27.85	0.47 ± 0.02	600B	1
	QSO J03508−3812	2.705	20.86	*B*	0.013	−27.81	0.66 ± 0.02	300V	1
	QSO J03503−3800	2.734	20.67	*B*	0.011	−27.79	0.92 ± 0.03	600B	1
	QSO J03490−3825	2.777	20.52	*B*	0.011	−27.74	1.08 ± 0.06	600B	1
	QSO J03494−3826	2.782	20.97	*B*	0.011	−27.87	0.42 ± 0.06	600B	1
	Q 0347−383	3.220	18.66	*B*	0.010	−26.67	0.45 ± 0.02	600B	4
CTQ 0247	QSO J04061−4401	2.410	19.35	*B*	0.013	−27.22	0.47 ± 0.01	600B	1
	CTQ 0247	3.025	17.40	*V*	0.014	−26.62	0.97 ± 0.02	600B	8
	QSO J04075−4416	3.034	21.75	*B*	0.015	−28.15	0.67 ± 0.11	600B	1
	QSO J04084−4420	3.080	22.88	*B*	0.014	−28.55	0.36 ± 0.04	300V	1
Q 0420−388	MS 0420−3838B	1.931	20.61	*B*	0.021	−27.77	0.32 ± 0.04	300V	1
	QSO J04229−3831	1.990	19.38	*B*	0.028	−27.58	0.71 ± 0.02	600B	1
	QSO J04222−3829	2.168	20.91	*B*	0.025	−27.94	0.58 ± 0.02	300V	1
	QSO J04215−3857	2.235	22.23	*B*	0.019	−28.54	0.56 ± 0.02	300V	1
	QSO J04215−3854	2.270	19.49	*B*	0.018	−27.42	1.01 ± 0.05	600B	1
	PKS 0422−389	2.346	18.00	*V*		−27.07	1.88		3
	Q 0420−3850	2.410	21.01	*B*	0.024	−27.90	0.32 ± 0.03	600B	1
	QSO J04212−3853	2.723	20.08	*B*	0.017	−27.51	0.46 ± 0.03	600B	1
	QSO J04230−3853	3.042	21.95	*B*	0.025	−28.04	0.25 ± 0.02	300V	1
	Q 0420−388	3.120	16.90	*V*	0.024	−26.37	0.75 ± 0.02	600B	3, 4
HE 0940−1050	QSO J09430−1108	1.730	21.03	*B*	0.044	−28.83	0.07 ± 0.02	300V	1
	QSO J09424−1047	1.971	20.61	*B*	0.047	−27.81	0.74 ± 0.03	300V	1
	QSO J09437−1057	2.023	20.64	*B*	0.047	−27.74	0.42 ± 0.02	300V	1
	QSO J09435−1049	2.216	20.79	*B*	0.046	−27.92	0.71 ± 0.04	600B	1
	QSO J09425−1048	2.325	19.80	*B*	0.047	−27.37	0.30 ± 0.08	600B	1
	QSO J09434−1053	2.760	21.16	*B*	0.047	−27.84	0.02 ± 0.02	300V	1
	QSO J09427−1121	2.963	20.99	*B*	0.050	−27.88	1.48 ± 0.05	600B	1
	QSO J09437−1052	3.018	20.78	*B*	0.047	−27.70	0.39 ± 0.06	600B	1
	HE 0940−1050	3.088	16.96	$B_{\rm J}$	0.044	−26.16	0.90 ± 0.01	600B	9
CTQ 0460	QSO J10399−2321	2.216	20.73	*B*	0.050	−27.88	0.93 ± 0.03	600B	1
	QSO J10388−2258	2.326	19.63	*B*	0.053	−27.45	0.80 ± 0.05	600B	1
	QSO J10385−2317	3.099	21.28	*B*	0.055	−27.91	1.16 ± 0.06	600B	1
	CTQ 0460	3.139	17.50	*V*	0.055	−26.55	0.25 ± 0.03	600B	8
BR 1117−1329	QSO J11208−1345	1.893	20.10	*B*	0.041	−27.70	0.82 ± 0.04	300V	1
	QSO J11205−1343	1.910	19.84	*B*	0.041	−27.53	0.62 ± 0.03	300V	1
	QSO J11197−1340	2.220	18.32	*B*	0.048	−26.90	0.95 ± 0.02	600B	1
	QSO J11192−1334	3.252	20.55	*B*	0.049	−28.04	1.29 ± 0.01	300V	1
	BR 1117−1329	3.958						600B	
BR 1202−0725	QSO J12061−0745	1.730	19.15	*B*	0.033	−27.14	0.32 ± 0.02	600B	1
	CIRSI 05	2.661	19.39	*B*	0.035	−27.32	0.97 ± 0.03	600B	1
	BR 1202−0725	4.690						600B	
Q 1209+0919	QSO J12111+0906	2.534	21.17	*B*	0.017	−27.90	0.32 ± 0.03	600B	1
	Q 1209+0919	3.291	19.04	*g*	0.019	−26.92	0.11 ± 0.02	600B	10
PKS 2126−15	QSO J21286−1528	1.925	19.79	*B*	0.070	−27.36	0.45 ± 0.05	300V	1
	QSO J21291−1524B	2.480	20.33	*B*	0.077	−27.64	1.85 ± 0.02	600B	1
	PKS 2126−15	3.285	17.00	*V*	0.080	−26.42	1.15 ± 0.01	600B	3, 8
	QSO J21301−1533	3.487	21.94	*B*	0.061	−27.75	0.69 ± 0.15	600B	1

Table 3.1. continued.

Field	QSO	z	Mag.	Filter	$E(B-V)$	$\log f_{\nu_{\rm LL}}$	α	FORS grism	reference
Q 2139−4434	QSO J214207.67−440310.1	1.732	19.38	*B*		−27.55	1.88		11, 12
	QSO J214238.71−440639.0	1.736	21.10	*B*		−28.24	1.88		12
	QSO J214329.62−441011.9	1.768	21.71	*B*		−28.48	1.88		12
	QSO J214251.50−443043.2	1.795	20.26	*B*		−27.89	1.88		12
	QSO J214243.93−443250.8	1.849	21.44	*B*		−28.36	1.88		12
	QSO J214229.03−435838.6	1.853	21.96	*B*		−28.56	1.88		12
	QSO J214020.82−443253.1	1.863	20.69	*B*		−28.05	1.88		12
	QSO J214239.38−443115.2	2.036	22.79	*B*		−28.87	1.88		12
	QSO J214013.40−440918.7	2.045	20.78	*B*		−28.06	1.88		11, 12
	Q 2138−4420	2.107	20.28	*B*	0.020	−27.66	0.50 ± 0.03	300V	1
	QSO J214039.08−440307.6	2.097	20.31	*B*		−27.88	1.88		12
	QSO J214122.88−440648.8	2.106	19.95	*B*		−27.73	1.88		12
	QSO J214429.09−441203.4	2.140	22.86	*B*		−28.90	1.88		12
	QSO J214420.92−442349.8	2.162	20.49	*B*		−27.96	1.88		12
	QSO J214337.66−440801.5	2.166	22.02	*B*		−28.58	1.88		12
	QSO J214115.43−435600.7	2.202	21.51	*B*		−28.38	1.88		12
	QSO J214323.56−435638.6	2.223	21.82	*B*		−28.52	1.88		12
	QSO J214154.94−444200.8	2.224	21.89	*B*		−28.54	1.88		12
	Q 2139−4444	2.372	21.19	*B*	0.020	−28.04	1.18 ± 0.01	300V	1
	QSO J214231.33−443016.8	2.388	21.24	*B*		−28.28	1.88		12
	QSO J214220.67−435920.0	2.458	21.59	*B*		−28.41	1.88		12
	QSO J21434−4432	2.709	19.33	*B*	0.018	−27.22	0.49 ± 0.03	600B	1
	QSO J214417.56−440702.0	2.725	21.04	*B*		−28.14	1.88		12
	QSO J214323.39−443524.0	2.725	22.02	*B*		−28.53	1.88		12
	Q 2138−4427	3.120	18.13	*V*	0.020	−26.80	0.42 ± 0.01	600B	4, 8
	Q 2140−4406	3.180	20.18	*V*		−27.92	1.88		3
	Q 2139−4434	3.214	17.70	*V*	0.020	−26.93	2.26 ± 0.02	600B	3
	Q 2138−4433	3.228	21.63	*B*	0.020	−27.85	0.71 ± 0.06	600B	1
HE 2243−6031	QSO J22454−6020	1.984	20.94	*B*	0.020	−27.91	0.63 ± 0.02	300V	1
	QSO J22455−6015	2.036	21.74	*B*	0.021	−28.23	0.41 ± 0.04	300V	1
	QSO J22460−6024	2.041	21.25	*B*	0.019	−28.04	0.50 ± 0.02	300V	1
	QSO J22454−6011	2.324	19.36	*B*	0.022	−27.28	0.39 ± 0.03	600B	1
	QSO J22463−6009	2.329	19.71	*B*	0.023	−27.45	0.48 ± 0.02	600B	1
	HE 2243−6031	3.010	16.40	*V*	0.020	−26.11	0.52 ± 0.01	600B	8
	QSO J22484−6002	3.586	20.97	*B*	0.021	−27.25	0.07 ± 0.10	600B	1
HE 2347−4342	QSO J23509−4330	1.762	18.23	*B*	0.013	−26.89	0.57 ± 0.01	600B	13, 1
	QSO J23502−4334	1.763	18.95	*B*	0.014	−27.47	1.17 ± 0.02	300V	13, 1
	QSO J23508−4335	1.778	22.01	*V*	0.013	−28.92	2.01 ± 0.11	300V	13, 4
	QSO J23503−4328	2.282	20.66	*B*	0.013	−27.78	0.20 ± 0.01	300V	13, 1
	QSO J23500−4319	2.302	22.61	*V*	0.015	−29.00	0.84 ± 0.10	300V	13, 4
	QSO J23495−4338	2.690	20.21	*B*	0.015	−27.51	0.31 ± 0.02	300V	13, 1
	HE 2347−4342	2.885	17.18	*B*	0.014	−26.20	0.13 ± 0.02	600B	4
	QSO J23511−4319	3.020	21.00	*B*	0.015	−27.63	0.05 ± 0.06	600B	13, 1
	QSO J23514−4339	3.240	21.57	*B*	0.011	−27.85	0.49 ± 0.02	300V	13, 1
	QSO J23503−4317	3.542	21.94	*B*	0.015	−27.72	0.25 ± 0.03	300V	13, 1

photometry references: (1) Chapter 2 of this thesis, (2) Steidel et al. (2003), (3) Véron-Cetty & Véron (2006), (4) own measurement from archival data, (5) Worseck & Wisotzki (2006), (6) Hennawi et al. (2006), (7) Abazajian et al. (2004), (8) estimated from slit spectrum, (9) Wisotzki et al. (2000), (10) Abazajian et al. (2005), (11) Hawkins (2000), (12) Francis et al. (2004), (13) Worseck et al. (2007)

of Young et al. (1979) and Carswell et al. (1982). Its accuracy is assessed in Sect. 3.3.5. In spectral regions containing damped Lyα absorption the algorithm fails, so that manual interpolation with linear functions was necessary.

3.2.3. Quasar spectrophotometry

An accurate prediction of the proximity effect relies on spectrophotometric observations in order to obtain reasonable estimates of the quasar rest frame Lyman limit fluxes. Although most quasars are intrinsically variable and absolute spectrophotometry is difficult from the ground, we tried to obtain the best-possible estimates of their ionising fluxes.

Most of the spectra from our survey were taken under clear conditions with variable seeing. Relative spectrophotometry was achieved by rotating the slit to the parallactic angle in addition to the automatic correction by the FORS2 Atmospheric Dispersion Corrector. After scaling the spectra to correct for slit losses we found good agreement between the B magnitudes integrated from the spectra and the B band photometry carried out on the aquisition images (Chapter 2). The spectra were corrected for galactic extinction adopting the $E(B-V)$ values by Schlegel et al. (1998) and the extinction curve by Cardelli et al. (1989) with a ratio of selective extinction to total extinction in the V band $R_V = 3.1$, the average value for the diffuse interstellar medium. However, since all our quasars are at high galactic latitude, the extinction corrections were usually very small.

Since the quasar's rest frame Lyman limit flux is not directly observable due to blanketing by the Lyman forest, we extrapolated power laws $f_\nu \propto \nu^{-\alpha}$ from regions without obvious emission or absorption redward of Lyα. We avoided to fit the continuum at the Small Blue Bump and at $\lambda_{\rm obs} > 6600$ Å due to 2nd order contamination in the spectra taken with the 300V grism. The resulting rest-frame Lyman limit fluxes $f_{\nu_{\rm LL}}$ and the spectral indices α are listed in Table 3.1 for all quasars with available spectra. Figure 3.1 shows two examples of fitted spectra. Some quasar continua are poorly described by power laws, so this parameterisation is only an approximation. Moreover, the extrapolated Lyman limit fluxes could be overestimated, since the intrinsic spectral energy distribution (SED) of quasars may have a break near Lyα (Telfer et al. 2002; Shang et al. 2005) that may depend on luminosity (Scott et al. 2004). Due to the blanketing of the Lyα forest, such a break cannot be inferred for high-redshift quasars at low resolution (Steidel & Sargent 1987). Moreover, the rest frame wavelength range to estimate the power law continuum varies with redshift and spectrograph

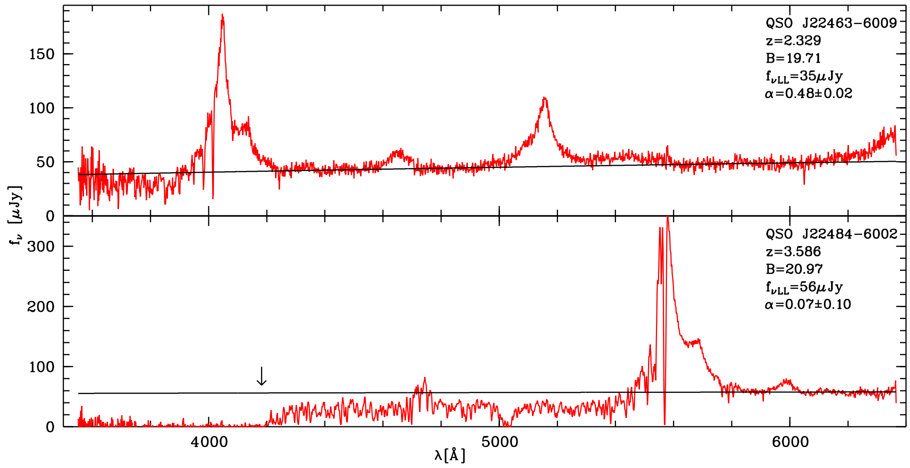

Fig. 3.1. Two "Quasars near Quasars" spectra with fitted power law continua. The scaled and extinction-corrected flux density f_ν is shown vs. observed wavelength λ (red/grey). The black curves represent the fitted continua $f_\nu \propto \nu^{-\alpha}$. The quasar in the upper panel is well described by a power law. QSO J22484−6002 (lower panel) is the highest-redshift quasar discovered in the survey with only limited coverage of the continuum redward of Lyα. Therefore the extrapolated Lyman limit flux (arrow) is likely more uncertain. Moreover, QSO J22484−6002 has a proximate Lyman limit system that truncates the flux at the Lyman limit.

Table 3.2. Quasars with UVES data. The columns list the quasar name, the total exposure time, the programmes and principal investigators.

QSO	exposure	programme	PI
Q 0002−422	54.1 h	166.A-0106	J. Bergeron
H 0055−269	26.1 h	065.O-0296	S. D'Odorico
Q 0347−383	46.4 h	068.A-0106	P. Petitjean
		068.B-0115	P. Molaro
CTQ 0247	52.2 h	068.A-0361	S. Lopez
		068.A-0600	C. Ledoux
		070.A-0017	P. Petitjean
Q 0420−388	32.0 h	166.A-0106	J. Bergeron
HE 0940−1050	18.0 h	065.O-0474	P. Molaro
		166.A-0106	J. Bergeron
CTQ 0460	12.0 h	068.B-0115	P. Molaro
Q 1209+0919	13.2 h	067.A-0146	G. Vladilo
		073.B-0787	M. Dessauges-Zavadsky
PKS 2126−15	56.1 h	166.A-0106	J. Bergeron
Q 2139−4434	8.5 h	065.O-0299	V. D'Odorico
		069.A-0204	V. D'Odorico
Q 2138−4427	14.9 h	067.A-0078	C. Ledoux
		067.A-0146	G. Vladilo
HE 2243−6031	25.6 h	065.O-0411	S. Lopez
		074.A-0201	R. Srianand
HE 2347−4342	40.2 h	166.A-0106	J. Bergeron
		071.A-0066	D. Reimers

configuration (Fig. 3.1). Considering these systematic effects, the error of the Lyman limit flux might well be larger than the typical flux error of 20% estimated from the photometry of the fainter quasars. At the high redshifts of BR 1117−1329, BR 1202−0725 and Q 0000−26 the continuum redward of Lyα was not covered and no extrapolated Lyman limit flux could be obtained. For Q 0000−26 we adopted the Lyman limit flux $f_{\nu_{\mathrm{LL}}} = 250\,\mu$Jy from Savaglio et al. (1997).

The aquisition images of the central quasars were taken without a filter, so we had to rely on published magnitudes from catalogues or on estimates from the FORS slit spectra (Dall'Aglio et al. 2007). We obtained own estimates for the quasars located by chance on the calibrated aquisition images of our survey. We adopted the accurate SDSS magnitudes if available.

The Lyman limit fluxes of the 30 quasars without spectroscopic data were estimated by matching a quasar template spectrum to the observed filter and extrapolating the UV slope of the template to the rest frame Lyman limit. The template SED contains the break shortward of Lyα, corresponding to $\alpha \simeq 1.88$. At high redshifts the observed filter bands covered part of the Lyα forest, whose absorption we did not take into account. Thus, the Lyman limit fluxes reported in Table 3.1 are only rough estimates.

3.2.4. Systemic quasar redshifts

It is well-known that quasar redshifts determined from broad high-ionisation emission lines generally underestimate the systemic redshifts due to blueshifts with respect to low-ionisation lines or narrow forbidden lines (Gaskell 1982; Tytler & Fan 1992; McIntosh et al. 1999; Richards et al. 2002). Due to the still considerable disagreement on the actual values of the blueshifts, empirical corrections cannot be applied to single objects. Moreover, different emission lines are present in the spectra depending on redshift and instrument setup. We therefore estimated the systemic redshift of every quasar with available spectroscopic data from the redshifts determined from the available emission lines. We discarded obviously blueshifted lines and gave lower weights to high-ionisation lines. The redshift uncertainties of $\sigma_z \lesssim 0.005$ do not much affect our results, because they are much smaller than the expected proximity effect zones of the quasars in our sample ($0.02 \lesssim \Delta z \lesssim 0.08$, see below). We refined the redshift estimate of Q 2138−4427 ($z = 3.170$), made on a low S/N spectrum by Morris et al. (1991) to $z = 3.120 \pm 0.005$ based on the $S/N \gtrsim 200$ FORS1 spectrum. The measured redshifts of the remaining known quasars were in good agreement with the previously reported values.

3.2.5. The predicted strength of the transverse proximity effect

Bajtlik et al. (1988) derived a simple ionisation model of the proximity effect that has been adopted in all proximity effect studies to date (e.g. Giallongo et al. 1996; Cooke et al. 1997; Scott et al. 2000; Liske & Williger 2001). Assuming that the IGM consists of highly ionised isothermal pure hydrogen clouds, the observed column density of an absorber near a quasar is

$$N = \frac{N_\infty}{1 + \omega}, \tag{3.1}$$

with the column density N_∞ that would have been observed in absence of the local quasar and the parameter ω, which is the ratio between the ionisation rates of local individual quasars and the UV background. Considering n quasars that contribute to the quasar ionisation rate at a given point at redshift z, we have for the ratio of ionisation rates

$$\omega(z) = \sum_{j=1}^{n} \frac{f_{\nu_{\rm LL},j}}{4\pi J_{\nu_{\rm LL}}(z)} \frac{\left(1+z'_j\right)^{-\alpha_j+1}}{\left(1+z_j\right)} \left(\frac{\alpha_{J_\nu}+3}{\alpha_j+3}\right) \left(\frac{d_L\left(z_j,0\right)}{d_L\left(z_j,z\right)}\right)^2 \qquad (3.2)$$

(see Appendix A.3. for a detailed derivation). The n quasars are located at redshifts z_j with rest frame Lyman limit fluxes $f_{\nu_{\rm LL},j}$. The luminosity distances of QSO j, as inferred today $d_L(z_j, 0)$ and as seen at the absorber $d_L(z_j, z)$, were calculated numerically for our assumed flat Λ-concordance model. The redshift of the quasar as seen at the absorber is z'_j (Liske 2000). We assumed a constant UV background Lyman limit intensity of $J_{\nu_{\rm LL}} = 7 \times 10^{-22}$ erg cm^{-2} s^{-1} Hz^{-1} sr^{-1} with a power-law shape $J_\nu \propto \nu^{-\alpha_{J_\nu}}$ and $\alpha_{J_\nu} = 1.8$ over the redshift range of interest. Our adopted value numerically corresponds to the UV background intensity of Scott et al. (2000), who adopted the Einstein-de Sitter model instead of the Λ model used here. In the redshift range of interest, we have $J_{\nu,\Lambda} \simeq 0.7 J_{\nu,\rm EdS}$, so our UV background value corresponds to $J_{\nu_{\rm LL}} = 10^{-21}$ erg cm^{-2} s^{-1} Hz^{-1} sr^{-1} in the Einstein-de Sitter model, consistent with the results by Bajtlik et al. (1988) and Cooke et al. (1997). Compared to recent studies (e.g. Scott et al. 2000; Liske & Williger 2001) this value could be too high. However, as the UV background is still uncertain to a factor of ~ 3 due to several systematic uncertainties, its value adopted here can only serve as an order of magnitude estimate. In particular, the ionisation model assumes that the quasars lie at random locations in the IGM, radiate at constant luminosity, have an infinite lifetime and emit isotropically (in case of the TPE). These assumptions will lead to an overestimated ω and hence overestimated values of J_ν (see discussion in Sect. 3.5.1).

Other implicit assumptions of the ionisation model are unlikely to have a strong impact. The IGM is highly ionised and optically thin to ionising photons at 1 ryd over large distances (Haardt & Madau 1996; Madau et al. 1999; Meiksin & White 2004), so that the flux density of the quasar at the absorber will be approximately determined by geometric dilution assumed in eq. (3.2). Extra heating of the IGM due to the quasar is probably small (Adelberger 2004, however see Misawa et al. 2007) and metals do not significantly alter the photoionisation balance (Scott et al. 2000, 2002). Due to the decline of the ionisation cross section at high frequencies, substantial amounts of singly ionised helium in the absorbers neither change the hydrogen photoionisation rate.

A parameter $\omega \gg 1$ predicts a strong proximity effect, lowering the line number density and the effective optical depth in the Lyα forest. For a single power-law column density distribution $\mathrm{d}\mathcal{N}/\mathrm{d}N \propto N^{-\beta}$ the line number density departs from the general power-law redshift evolution as

$$\frac{\mathrm{d}\mathcal{N}}{\mathrm{d}z} \propto (1+z)^{\gamma} (1+\omega)^{1-\beta} \qquad (3.3)$$

(Bajtlik et al. 1988). The effective optical depth of the Lyα forest changes accordingly to

$$\tau_{\rm eff}(z,\omega) = \tau_{\rm eff,\infty}(z)(1+\omega)^{1-\beta} = B(1+z)^{\gamma+1}(1+\omega)^{1-\beta} \qquad (3.4)$$

(Liske & Williger 2001). Here,

$$\tau_{\rm eff,\infty} = B(1+z)^{\gamma+1} \qquad (3.5)$$

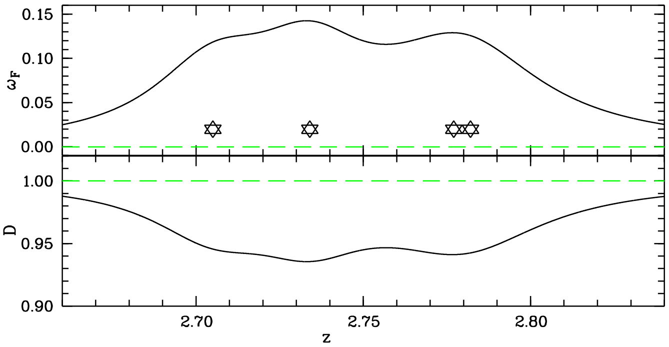

Fig. 3.2. Predicted combined $\omega_{\rm F}$ and predicted normalised effective optical depth D (for $\beta = 1.5$) of four FQSOs (stars) near Q 0347−383. Dashed lines mark the case of no transverse proximity effect.

(Zuo 1993) is the effective optical depth that is observed on lines of sight without the impact of local ionising sources. Removing the general redshift evolution of $\tau_{\rm eff}$, we define the normalised effective optical depth as

$$D(\omega(z)) = \frac{\tau_{\rm eff}}{\tau_{\rm eff,\infty}} = (1+\omega(z))^{1-\beta}, \qquad (3.6)$$

where $D \ll 1$ denotes a strong proximity effect. The change will be most significant for the background quasar (BQSO) that has $\omega(z) = \omega_{\rm B}(z) \to \infty$ for $z \to z_{\rm B}$. The transverse proximity effect of foreground quasars (FQSOs) will be smaller due to large separations to the BQSO sightline, requiring a distinction between the line-of-sight proximity effect zone towards the BQSO (large $\omega_{\rm B}$ from single BQSO) and the predicted TPE zones of the FQSOs (large $\omega_{\rm F}$ either due to single or several FQSOs). In the analysis we excluded all spectral regions with a non-negligible line-of-sight proximity effect. Figure 3.2 presents the predicted $\omega_{\rm F}(z)$ and $D(z)$ of the four foreground quasars in the vicinity of Q 0347−383 that are closely spaced in redshift (Table 3.1). The individual projected proximity effect zones overlap according to eq. (3.2), but their $\omega_{\rm F}(z)$ is low, yielding only a minor decrease of the average absorption. Moreover, the predicted $D(z)$ cannot be measured in real data because of small-scale fluctuations of the effective optical depth due to cosmic variance (see Sect. 3.3.3 below).

Finally, in order to quantify the predicted impact of a single FQSO we can write its maximum ratio of ionisation rates $\omega_{\rm max} = \omega(z_{\rm F})$ as

$$\omega_{\rm max} = \frac{f_{\nu_{\rm LL},\rm F}}{4\pi J_{\nu_{\rm LL}}} \left(\frac{\alpha_{J_\nu}+3}{\alpha_{\rm F}+3}\right) \frac{(1+z_{\rm F})^3 \left(1+z'_{\rm F}\right)^{-\alpha_{\rm F}-1}}{(2-2\cos\vartheta)}, \qquad (3.7)$$

(Appendix A.6.) valid for any flat cosmological model. ϑ is the observed separation angle between the lines of sight.

3.2.6. Suitable quasar pairs

FORS quasar pairs

In total, Table 3.1 yields 694 possible pair combinations including also those BQSOs for which we do not have a FORS spectrum. FORS spectra were available for 94 quasars. Due to large systematic errors in local continuum fitting of the low-resolution FORS data (see Sect. 3.3.5 below) we adopted the extrapolated power-law continua to normalise the spectra. Therefore, only 91 FORS spectra could serve as BQSO spectra, reducing the number of possible pairs to 383. Furthermore, we estimated from simulated data (see below) that the extrapolated power laws are usable in the rest frame wavelength range

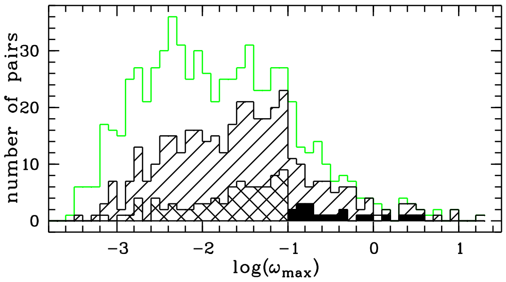

Fig. 3.3. Histograms of quasar pairs vs. log ($\omega_{\rm max}$). The open histogram shows the $\omega_{\rm max}$ distribution of all possible pairs from Table 3.1. The hatched histograms denote pairs with available FORS data of the BQSO and pairs fulfilling constraint (3.8). The full histogram denotes $\omega_{\rm max}$ for the selected 19 pairs with $\omega_{\rm max} \geq 0.1$.

1050 Å< $\lambda_{\rm rest}$ <1150 Å due to the emission line wings and the emerging Lyβ forest blueward of Lyβ. This yielded the constraint

$$\frac{1050}{1215.67}\,(1+z_{\rm B}) < z_{\rm F}+1 < \frac{1150}{1215.67}\,(1+z_{\rm B})\,, \qquad (3.8)$$

thereby reducing the number of usable FORS pairs to 100 and excluding any line-of-sight proximity effect of the BQSOs. Knowing that continuum errors in the FORS data will mask the weakest proximity effects of the remaining 100 FQSOs, we selected only those reaching individual maximum values $\omega_{\rm max} \geq 0.1$, yielding the 19 FORS pairs that will be considered in the following (Table 3.3). Figure 3.3 shows the $\omega_{\rm max}$ of the sample with and without the imposed constraints.

UVES quasar pairs

In total, echelle spectra for 11 quasars in the fields were available (nine UVES spectra, two generated from published linelists). Due to the accurate local definition of the continuum it could be possible to measure even very weak signatures of the transverse proximity effect at $\omega_{\rm max} \lesssim 0.1$. However, decontamination of the low-redshift Lyα forest from higher-redshift Lyβ lines is beyond the scope of this paper, so we restricted the FQSO redshifts to $z_{\rm F} > 1025.72/1215.67\,(1+z_{\rm B})-1$, yielding the 31 pairs listed in Table 3.4. Six FQSOs are located in the proximity effect regions of the luminous BQSOs and had do be excluded in the analysis (Sect. 3.4.4).

3.3. Generation of simulated data

3.3.1. Monte Carlo Lyα forest spectra

A statistical analysis of the transverse proximity effect requires large-scale simulations of the Lyα forest. Accurate three-dimensional hydrodynamical simulations of the Lyα forest are beyond the scope of this paper. Moreover, the spectra generated from hydrodynamical simulations are generally shorter than the length scale of the proximity effect. The approach to describe the forest as a lognormal density field successfully reproduces many of its observed properties (Bi et al. 1992; Bi & Davidsen 1997) and spectra of arbitrary length can be generated. However, since the ionisation model of the proximity effect is itself very simplistic (neglect of quasar variablity, quasar anisotropy or overdensity near the quasar), we do not require a completely realistic representation of the Lyα forest. Instead, we considered the simplest representation of the forest as a random collection of uncorrelated Lyα lines obeying the line distribution functions derived from observations. Given that the ionisation model assumes random locations of quasars in the forest, the lack of large-scale structure in the simulated spectra helps to assess the statistical significance of the TPE without the systematic effects. In reality, these estimates have to be regarded as upper limits due to the adverse unmodelled systematics.

Every line is characterised by the three parameters redshift z, column density N and Doppler parameter b, randomly drawn from their probability distribution functions (PDFs). We parameterised the redshift evolution of the effective optical depth, which is closely related to the evolution in line number density, as a power law (eq. (3.5)). We adopted the normalisation $B = 0.0032$ and the power law index $\gamma = 2.37$ from the fit to high-resolution spectra by Kim et al. (2002). The line distribution in column density can be approximated as a single power law $\mathrm{d}\mathcal{N}/\mathrm{d}N \propto N^{-\beta}$ with $\beta = 1.5$, consistent with the results from high-resolution spectra (e.g. Hu et al. 1995). There is evidence that the observed column density distribution shows a break at $N \sim 10^{1}4$–$10^{1}5$ cm^{-2} (Petitjean et al. 1993; Giallongo et al. 1996) that may evolve with redshift (Kim et al. 1997, 2001, 2002). However, the break is not very pronounced and is rather unimportant for the overall appearance of our Monte Carlo spectra. We therefore consider a single power law index to be sufficient. In addition, a single power law index is generally assumed in studies of the proximity effect. A proper accounting for the break would require line counting statistics neglecting the strong lines (Giallongo et al. 1996), which is difficult as their column densities are not well constrained due to saturation of Lyα. Finally, the Doppler parameter distribution can be accurately described by

$$\frac{\mathrm{d}\mathcal{N}}{\mathrm{d}b} \propto \frac{b_\sigma^4}{b^5}\,\mathrm{e}^{-b_\sigma^4/b^4} \qquad (3.9)$$

(Hui & Rutledge 1999) with $b_\sigma \simeq 24\,\mathrm{km\,s^{-1}}$ (Kim et al. 2001), which we assumed to be redshift-independent.

A set of 1000 Lyα forest spectra was generated by populating an observed wavelength range 3300 Å≤ λ ≤6300 Å with random Lyα absorption lines modelled as Voigt profiles using the approximation by Tepper-García (2006) at a wavelength sampling of $\Delta\lambda = 0.05$ Å. After adding a line to the spectrum under construction, the programme computed the root-mean-square deviation between the specified $\tau_{\rm eff,\infty}$ power law and the $\tau_{\rm eff,\infty}$ measured in several redshift bins along the spectrum. A spectrum was considered complete if the root-mean-square deviation stopped decreasing, thereby ensuring that the spectra generally follow the specified redshift evolution of the forest absorption. We limited the column density range to $12 \leq \log\left(N/\mathrm{cm}^2\right) \leq 17$ and the Doppler parameter range to $10\,\mathrm{km\,s^{-1}} \leq b \leq 100\,\mathrm{km\,s^{-1}}$.

3.3.2. The probability density function of the Lyα forest transmission

By definition the simulated spectra agree with the observed line distribution functions. In order to test the validity of our simple Monte Carlo approach we computed the probability distribution functions of the transmission $P(T)$ at $z = 2.0$, 2.5, 3.0 and 3.5 in the high-resolution mock data without noise or continuum fitting errors. We avoided distortions of the PDFs due to redshift evolution in the forest by selecting narrow redshift ranges of $\Delta z = 0.01$ at the considered redshifts before merging the 1000

Table 3.3. Selected quasar pairs with $\omega_{\max} \geq 0.1$ in the FORS data. The columns list the BQSO name, BQSO redshift, FQSO name, FQSO redshift, FQSO rest frame Lyman limit flux (in erg cm^{-2} s^{-1} Hz^{-1}), FQSO spectral index ($f_\nu \propto \nu^{-\alpha}$), angular separation ϑ, transverse proper distance $d_\perp$ at z_F and maximum ratio of ionisation rates $\omega_{\max}$.

BQSO	z_B	FQSO	z_F	$\log f_{\nu_\mathrm{LL}}$	α	ϑ [′]	$d_\perp$ [Mpc]	$\omega_{\max}$
Q 0420−388	3.120	QSO J04212−3853	2.723	−27.51	0.46	14.88	7.06	0.13
Q 2139−4434	3.214	QSO J21434−4432	2.709	−27.22	0.49	15.92	7.57	0.22
QSO J00038−2617	3.073	QSO J00035−2610	2.771	−28.16	0.47	8.02	3.79	0.11
Q 0302−003	3.285	QSO 03020−0014	3.050	−27.74	0.70	6.48	2.98	0.50
QSO J03494−3826	2.782	QSO J03496−3821	2.351	−27.41	0.74	5.10	2.50	0.97
QSO J03490−3825	2.777	QSO J03496−3821	2.351	−27.41	0.74	8.13	3.99	0.38
QSO J04212−3853	2.723	QSO J04215−3854	2.270	−27.42	1.01	4.07	2.01	1.29
QSO J04222−3829	2.168	MS 0420−3838B	1.931	−27.77	0.32	5.58	2.81	0.27
QSO J04222−3829	2.168	QSO J04229−3831	1.990	−27.58	0.71	8.60	4.32	0.16
QSO J09437−1052	3.018	QSO J09434−1053	2.760	−27.84	0.02	4.71	2.23	0.74
QSO J09435−1049	2.216	QSO J09437−1057	2.023	−27.74	0.42	8.81	4.42	0.12
QSO J09425−1048	2.325	QSO J09424−1047	1.971	−27.81	0.74	1.76	0.89	2.25
QSO J09434−1053	2.760	QSO J09425−1048	2.325	−27.37	0.30	14.01	6.89	0.15
Q 2139−4433	3.228	QSO J21434−4432	2.709	−27.22	0.49	16.97	8.07	0.20
Q 2139−4444	2.372	QSO J214239.38−443115.2	2.036	−27.87	1.88	1.75	0.88	0.16
QSO J22454−6011	2.324	QSO J22455−6015	2.036	−28.23	0.41	4.53	2.27	0.15
QSO J22484−6002	3.586	HE 2243−6031	3.010	−26.11	0.52	16.73	7.72	3.24
QSO J23514−4339	3.240	HE 2347−4342	2.885	−26.20	0.13	16.01	7.48	2.95
QSO J23503−4317	3.542	QSO J23511−4319	3.020	−27.63	0.05	8.92	4.11	0.40

Table 3.4. Selected quasar pairs with available high-resolution data of the BQSOs. The columns list the BQSO name, BQSO redshift, FQSO name, FQSO redshift, FQSO rest frame Lyman limit flux (in erg cm^{-2} s^{-1} Hz^{-1}), FQSO spectral index ($f_\nu \propto \nu^{-\alpha}$), angular separation ϑ, transverse proper distance $d_\perp$ at z_F and maximum ratio of ionisation rates $\omega_{\max}$.

BQSO	z_B	FQSO	z_F	$\log f_{\nu_\mathrm{LL}}$	α	ϑ [′]	$d_\perp$ [Mpc]	$\omega_{\max}$
Q 0002−422	2.767	QSO J00038−4211	2.260	−27.47	0.27	17.29	8.54	0.077
		Q 0000−4239	2.190	−28.30	1.88	29.01	14.40	0.002
Q 0302−003	3.285	QSO J03052+0000	2.808	−28.13	0.68	11.22	5.29	0.056
		Q 0302-D113	2.920	−29.63	1.88	4.88	2.27	0.008
		Q 0301−005	3.231	−26.53	0.51	22.92	10.35	0.768
		QSO 03020−0014	3.050	−27.74	0.70	6.48	2.98	0.499
		SDSS J0303−0020B	2.718	−27.71	1.88	22.03	10.46	0.027
Q 0347−383	3.220	QSO J03494−3826	2.782	−27.87	0.42	15.96	7.53	0.053
		QSO J03490−3825	2.777	−27.74	1.08	16.89	7.98	0.053
		QSO J03508−3812	2.705	−27.81	0.66	13.34	6.34	0.077
		QSO J03503−3800	2.734	−27.79	0.92	12.67	6.01	0.086
CTQ 0247	3.025	QSO J04061−4401	2.410	−27.22	0.47	15.24	7.44	0.189
Q 0420−388	3.120	QSO J04230−3853	3.042	−28.04	0.25	12.30	5.66	0.078
		QSO J04212−3853	2.723	−27.51	0.46	14.88	7.06	0.133
HE 0940−1050	3.088	QSO J09434−1053	2.760	−27.84	0.02	13.23	6.26	0.093
		QSO J09437−1052	3.018	−27.70	0.39	16.99	7.84	0.084
		QSO J09427−1121	2.963	−27.88	1.48	17.38	8.06	0.038
CTQ 0460	3.139	QSO J10385−2317	3.099	−27.91	1.16	9.85	4.51	0.134
Q 2139−4434	3.214	Q 2140−4406	3.180	−27.92	1.88	28.52	12.95	0.014
		QSO J21434−4432	2.709	−27.22	0.49	15.92	7.57	0.222
		Q 2138−4427	3.120	−26.80	0.42	8.30	3.79	3.017
		QSO J214417.56−440702.0	2.725	−28.14	1.88	23.99	11.38	0.008
		QSO J214323.39−443324.0	2.725	−28.53	1.88	18.25	8.66	0.006
HE 2347−4342	2.885	QSO J23503−4328	2.282	−27.78	0.20	3.58	1.76	0.921
		QSO J23495−4338	2.690	−27.51	0.31	16.28	7.75	0.113
		QSO J23500−4319	2.302	−29.00	0.84	8.78	4.32	0.008
Q 0000−26	4.125	Q 0000-C5	3.791	−29.42	1.88	2.54	1.08	0.085
		Q 0000-C7	3.426	−29.41	1.88	1.47	0.65	0.207
Q 2138−4427	3.120	QSO J214323.39−443324.0	2.725	−28.53	1.88	26.55	12.60	0.003
		QSO J214417.56−440702.0	2.725	−28.14	1.88	25.52	12.11	0.007
		QSO J21434−4432	2.709	−27.22	0.49	24.18	11.49	0.096

simulated spectra. Figure 3.4 compares the resulting PDFs of the noise-free transmission to a theoretical PDF and a PDF constrained from observations. For random collections of lines Zuo & Phinney (1993) showed that the PDF of the optical depth $P(\tau)$ is

$$P_\mathrm{theory}\left(\tau\right) = \frac{\tau_{\mathrm{eff},\infty}}{2\sqrt{\pi}\tau^{3/2}}\mathrm{e}^{-\frac{\tau^2_{\mathrm{eff},\infty}}{4\tau}} \tag{3.10}$$

for a continuous column density distribution with $\beta = 1.5$. Recently, Becker et al. (2007) used 55 Keck HIRES spectra to parameterise $P(\tau)$ as a lognormal distribution

$$P_\mathrm{lognormal}\left(\tau\right) = \frac{1}{\sqrt{2\pi}\sigma\tau}\mathrm{e}^{-\frac{(\ln\tau-\mu)^2}{2\sigma^2}} \tag{3.11}$$

with $\mu(z) = -9.35 + 1.79(1 + z)$ and $\sigma(z) = 4.19 - 0.46(1 + z)$. The PDF of the transmission is simply $P(T) = P(\tau)/T$.

The transmission PDFs generated from the Monte Carlo spectra generally agree very well with the observed and the theoretical PDF. As expected the data accurately traces its theoretical PDF by Zuo & Phinney (1993) except at $T \rightarrow 1$. This is due to the fact that we restricted the column density to $N \geq 10^{12}\,\mathrm{cm}^2$, whereas eq. (3.10) is derived for $N > 0$. At high redshifts and high transmission values the PDFs by Becker et al. (2007) are larger than the simulated PDFs, which is probably due to continuum uncertainties in the observed data due to the strongly increasing blending of the forest even at high resolution. The slight differences at smaller T might be caused

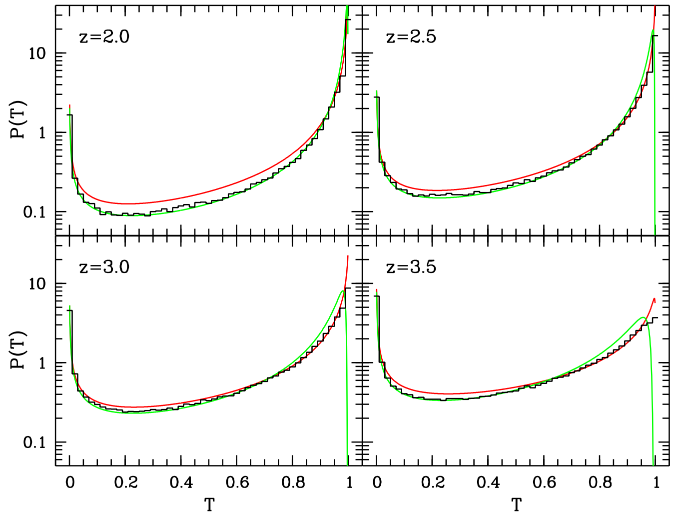

Fig. 3.4. Probability density functions $P(T)$ of the Lyα forest transmission T at different redshifts on a scale $\Delta z = 0.01$. The black histograms show the PDFs without noise and continuum errors as obtained from the Monte Carlo simulations. The fitted PDF from Becker et al. (2007) (red/dark grey) and the theoretical PDF from Zuo & Phinney (1993) (green/light grey) are shown for comparison. Note that the logarithmic scale amplifies (suppresses) the deviations between the PDFs at small (large) $P(T)$.

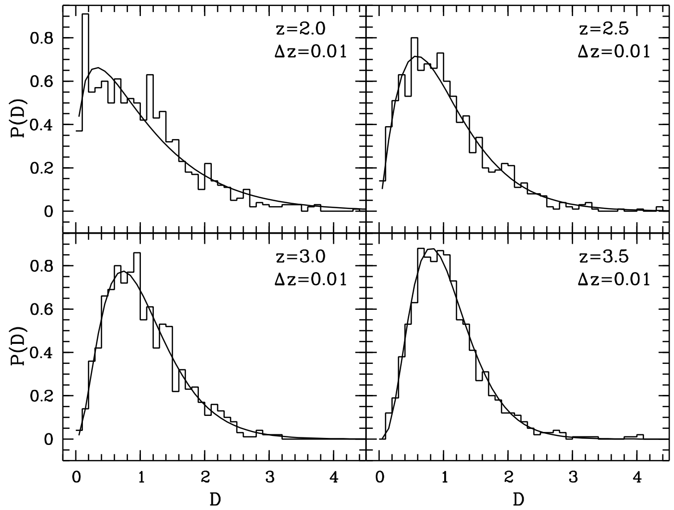

Fig. 3.5. Probability density functions $P(D)$ of the normalised effective optical depth $D = \tau_{\mathrm{eff},\infty,\ \mathrm{recovered}}/\tau_{\mathrm{eff},\infty,\ \mathrm{simulated}}$ on a scale $\Delta z = 0.01$ at different redshifts z. The histograms show the PDFs without noise and continuum errors as obtained from the Monte Carlo simulations. The curves are the best-fitting Gamma distributions.

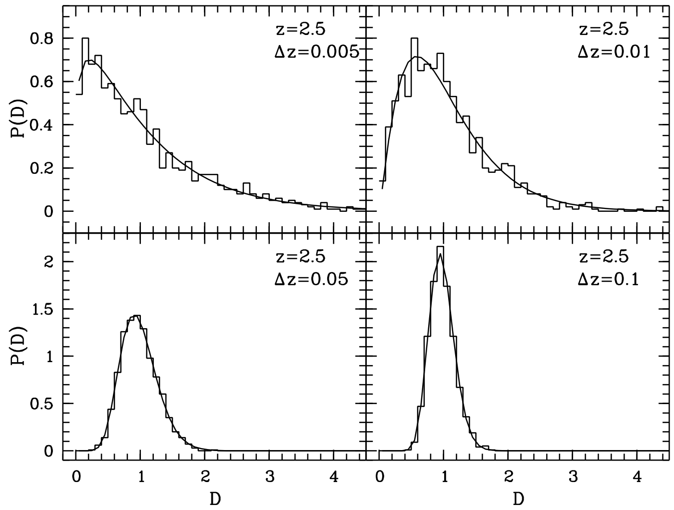

Fig. 3.6. Probability density functions $P(D)$ of the normalised effective optical depth $D = \tau_{\mathrm{eff},\infty,\ \mathrm{recovered}}/\tau_{\mathrm{eff},\infty,\ \mathrm{simulated}}$ at $z = 2.5$ for various scales Δz. The histograms show the PDFs without noise and continuum errors as obtained from the Monte Carlo simulations. The curves are the best-fitting Gamma distributions.

by the different functional forms of $\tau_{\mathrm{eff},\infty}(z)$ and our assumption of a constant $\beta = 1.5$ for all column densities and redshifts. Nevertheless, the simulated PDFs demonstrate that our Monte Carlo spectra capture the main observed properties of the forest. Our simplified picture of the forest as a random collection of lines is adequate and well matched to the simple ionisation model of the proximity effect.

3.3.3. The probability density function of the effective optical depth

Given the transmission probability density function on the smallest possible scale in the fully resolved Lyα forest, we explored the PDF of the mean transmission $\langle T\rangle$, or equivalently the effective optical depth $\tau_{\mathrm{eff},\infty} = -\ln\langle T\rangle$, on different scales Δz as a function of redshift in our simulated spectra. We removed the general redshift evolution of the effective optical depth by normalising the effective optical depth in a spectrum to the one specified in the simulations, so

$$D\,(z,\Delta z) \equiv \frac{\tau_{\mathrm{eff},\infty,\ \mathrm{recovered}}\,(z,\Delta z)}{\tau_{\mathrm{eff},\infty,\ \mathrm{simulated}}} \tag{3.12}$$

is a measure of overdensity ($D > 1$) or underdensity ($D < 1$) as a function of a redshift window with size Δz centred at redshift z.

Figure 3.5 shows the PDFs of D obtained from the 1000 noise-free high-resolution Monte Carlo spectra on a scale $\Delta z = 0.01$ at $z = 2.0$–3.5. Empirically, we found that the binned PDFs created from the 1000 independent D measurements are well fitted by a Gamma distribution

$$P\,(D) = \frac{p^q D^{q-1}}{\Gamma(q)}\mathrm{e}^{-pD} \tag{3.13}$$

with the Gamma function $\Gamma(q)$ and its two parameters $p > 0$ and $q > 0$ that are related to the mean $\langle D\rangle = q/p$ and the standard deviation $\sigma_D = \sqrt{q}/p$ (e.g. Rinne 1997). Figure 3.6 shows the evolution of the PDFs of D at $z = 2.5$ for different scales $\Delta z = 0.01$–0.1. Clearly, the Gamma distribution also fits the measured PDFs on the considered scales. It converges to a Gaussian distribution on large scales $\Delta z \gtrsim 0.1$ due to the Central Limit Theorem. Given the success of the fitting procedure on the considered scales over the whole redshift range covered by the Monte Carlo spectra, we proceeded without fitting other obvious distribution functions and parameterised the PDF of D by a Gamma distribution. Due to the simple scaling relation between D and $\tau_{\mathrm{eff},\infty}$ the effective optical depth of our simulated spectra is Gamma-distributed as well.

By definition, we have $\langle D\rangle \simeq 1$ on all scales significantly larger than the forest autocorrelation length. The standard deviation σ_D is a simple measure of cosmic variance in the simulations. In order to further describe these parameters, we obtained $\langle D\rangle$ and σ_D on various scales Δz at $1.8 \leq z \leq 4.1$ from the

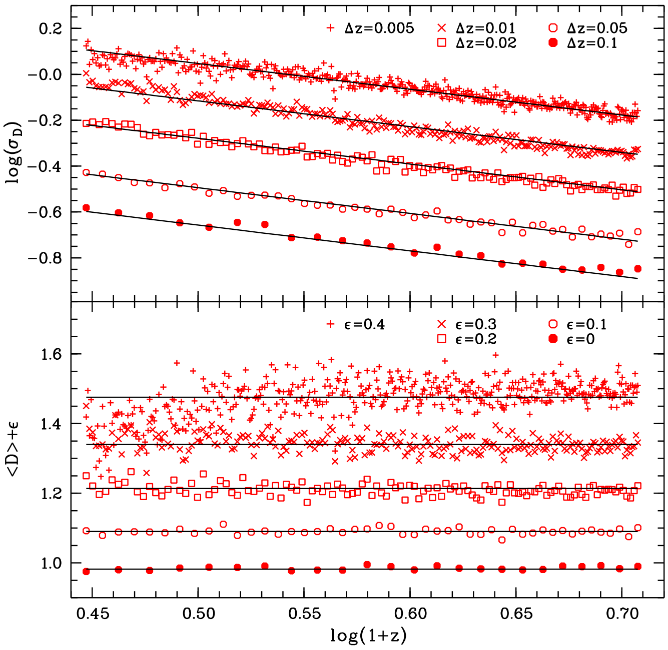

Fig. 3.7. Standard deviation σ_D and mean $\langle D \rangle$ of the normalised effective optical depth D as a function of redshift z. The symbols in both panels denote measurements from the Monte Carlo simulations on different scales Δz that are fitted by straight lines. For clarity $\langle D \rangle$ has been shifted by a value $\epsilon(\Delta z)$. The fits on different scales Δz are *not* independent, but represent (3.14) and (3.15).

simulated data by fitting the measured PDFs. The results are displayed in Fig. 3.7. The standard deviation is well fitted by a double power law in $1 + z$ and Δz yielding

$$\sigma_D\,(z, \Delta z) \simeq 0.231\,(1 + z)^{-1.12}\,(\Delta z)^{-0.54}\,. \tag{3.14}$$

For the mean normalised effective optical depth we get

$$\langle D \rangle\,(\Delta z) \simeq 1.006\,(\Delta z)^{0.02 \log \Delta z + 0.03}\,. \tag{3.15}$$

Note that $\langle D \rangle$ slightly fluctuates around 1 for different Δz, but is rather constant in redshift. On small scales at $z \lesssim 2.1$ there is a trend that $\langle D \rangle$ is not constant. This could be due to small-scale patchiness of the forest at low redshifts due to the decreasing line density. At small scales similar to the forest autocorrelation length ($\Delta z \lesssim 0.002$) the PDFs still follow the Gamma distribution, but the mean and the standard deviation cannot be fitted easily. This is actually expected, since these small scales trace individual absorbers, where the effective optical depth is ill defined. We also studied the effect of spectral resolution, confirming the relations (3.14) and (3.15) up to scales similar to the spectral resolution. Moreover, since the redshift scales of interest for the proximity effect are large ($\Delta z \gg 0.01$), the D distributions should be rather independent on the S/N in the spectra.

The scaling relations obtained from the ideal spectra might change in the presence of continuum fitting errors. Large-scale systematic errors in the quasar continuum change the normalisation of D rather than the shape of its distribution. However, small-scale systematic errors of the quasar continuum will enhance the scatter of $\langle D \rangle$ and σ_D around their scaling relations (see below). On the other hand, small statistical errors in the continuum fit have no influence on the mean normalised effective optical depth and its standard deviation. We conclude that we have found a simple parameterisation for the mean absorption and the cosmic variance in the simulated spectra that is largely unaffected by noise, spectral resolution and small continuum fitting errors.

Table 3.5. Simulated instrument specifications. The columns list the instrument, the FWHM $\Delta\lambda$ of the Gaussian line spread function, the pixel size p and the resolution R.

Instrument	$\Delta\lambda$ [Å]	p [Å]	$R = \lambda/\Delta\lambda$
UVES	0.1	0.05	~ 45000
X-shooter	1.0	0.5	~ 4500
FORS	4.5	1.5	~ 1000

Recently Tepper-García & Fritze (2007) presented similar Monte Carlo simulations of the Lyα forest to describe the distribution of $D_{\mathrm{A}} = 1 - \mathrm{e}^{-\tau_{\mathrm{eff},\infty}}$. They claim that D_{A} is lognormally distributed which leads to a Gaussian distribution of $\tau_{\mathrm{eff},\infty}$. However, due to their definition of D_{A} in the rest frame of the observed quasar it yields the average absorption on small (large) scales at low (high) redshift. This naturally explains the evolution in the D_{A} distributions and the poor lognormal fit to D_{A} at low redshifts (Tepper-García & Fritze 2007, their Fig. 5). As shown above, the effective optical depth is Gaussian distributed only on large scales Δz, but is generally highly skewed in accord with the results by Meiksin & White (2004).

3.3.4. Generation of realistic mock quasar spectra

In order to estimate the error budget in the Lyα forest due to continuum fitting we generated mock quasar spectra. Since the continuum fitting accuracy depends on the spectral resolution, we simulated three characteristic resolutions (high, medium, low) matched to three existing or upcoming VLT instruments (UVES, X-shooter, FORS). The simulated Lyα forest spectra were convolved with the line spread function and resampled to match the instrument specifications listed in Table 3.5. Since at UVES resolution the forest is fully resolved, i.e. the line spread function only marginally changes the absorption lines, the initial simulated spectra (Sect. 3.3.1) resemble UVES spectra.

The Lyα forest spectra were then multiplied onto artificial quasar spectral energy distributions. These were generated via the principal component method as described by Suzuki (2006). The principal component method assumes that each rest frame quasar spectrum $f_\lambda(\lambda_{\mathrm{rest}})$ can be decomposed as $f_\lambda(\lambda_{\mathrm{rest}}) = \mu(\lambda_{\mathrm{rest}}) + \sum_j c_j p_j(\lambda_{\mathrm{rest}})$ with a mean spectrum μ, the principal component spectra p_j and the coefficients c_j. Suzuki et al. (2005) determined μ and p_j at 1020 Å$< \lambda_{\mathrm{rest}} <$1600 Å from 50 HST FOS spectra of low-redshift quasars. Suzuki (2006) showed that the coefficients c_j are approximately Gaussian distributed. After generating 1000 SEDs by drawing the c_j from their Gaussian distributions we selected the first 200 SEDs showing no associated absorption or BAL features. For illustration, four Monte Carlo SEDs are shown in Fig. 3.8. Some of the SEDs might be unrealistic, nevertheless they are well suited to test continuum fitting algorithms (see below). A specific quasar was statistically simulated by shifting the SEDs to its redshift, followed by resampling them at the desired spectral resolution and multiplying them with the simulated Lyα forest spectra in the range 1020 Å$< \lambda_{\mathrm{rest}} <$1215.67 Å. Each modelled SED was used five times to yield the 1000 independent forest realisations per quasar spectrum.

The noise that we added to the quasar spectra was modelled by a Gaussian distribution with zero mean and variance $\sigma^2_{\mathrm{noise}} = \sigma^2_{\mathrm{photon}} + \sigma^2_{\mathrm{read}}$. The photon noise was assumed to vary

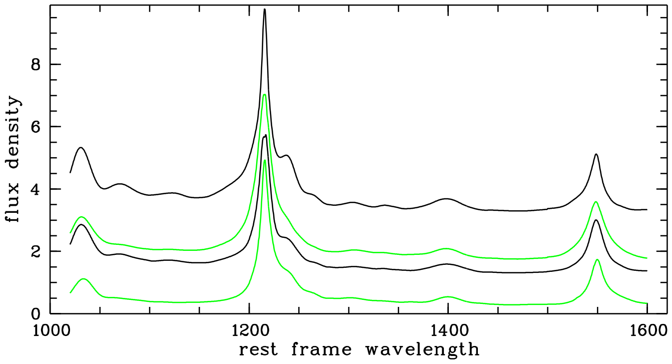

Fig. 3.8. Four Monte Carlo SEDs of quasars with different line strengths and shapes. For clarity, each SED has been offset by an appropriate amount.

with the quasar flux as $\sigma_{\mathrm{photon}} \propto \sqrt{f_\lambda}$ normalised at a reference wavelength $\lambda_{\mathrm{rest}} = 1450$ Å. Consequently, the readout noise component in σ_{noise} was important only at low fluxes (saturated absorption lines). We did not consider the telescope throughput so that the quasar SED determines the S/N as a function of wavelength.

3.3.5. Estimation of continuum fitting errors

Reliable continuum fitting of quasar spectra is crucial to determine the amount of absorption in the forest. Since the transverse proximity effect is generally weak, its detectability depends on the reliability of the assumed quasar continua. We developed an automatic continuum fitting programme based on the algorithms by Young et al. (1979) and Carswell et al. (1982). Essentially, a continuum is fitted by interpolating a cubic spline through a number of wavelength bins in each of which the continuum flux is found by removing the pixels with the largest deviation from the mean until the standard deviation of the remaining pixels is less than the average noise in the bin. The fitting routine was extensively tested on the simulated data with known quasar continua to obtain reasonable input parameter values. We found that local continuum fits to low-resolution FORS data are generally not very reliable at the low S/N of the confirmation spectra from our survey. In particular, they recover a much too shallow redshift evolution of the effective optical depth, because nearly every forest pixel deemed to represent the continuum in fact contains some stochastic absorption in addition to the random fluctuations induced by noise. Instead of the local FORS continua we adopted power law fits to continuum regions redward of Lyα of the quasar SEDs which are able to reveal the redshift evolution of the forest absorption. Figure 3.9 shows one simulated quasar spectrum at the three considered resolutions and a $S/N \sim 30$ with the fitted continua. We obtained the error budget of our continuum fitting routine by analysing the statistics of the ratio between the fitted continua and the real continua of the 200 quasar SEDs. At high and medium resolution the local continuum fitting was performed on each SED shifted to $z_{\mathrm{QSO}} \in \{2.5, 3.0, 3.5, 4.0\}$ multiplied by a separate Lyα forest spectrum at $S/N \sim 30$. Figure 3.10 presents the mean and the standard deviation of the continuum ratio for the 200 SEDs, corresponding to the systematic and the statistical continuum error, respectively. Both errors evolve with redshift since continuum fitting becomes difficult at high redshift due to the increasing blanketing of the forest. At high resolution the systematic underestimation of the Lyα forest absorption gradually increases from $\lesssim 1\%$ at $z \sim 2$ to $\sim 3\%$ at $z \sim 4$. The statistical error is $\lesssim 1\%$ at $z \sim 2$ and increases to $\sim 2.5\%$ at $z \sim 4$. The errors are larger in the emission line wings of Lyα and Lyβ due to the steep gradients in the flux in presence of the forest absorption that result in imperfect spline interpolations. However, since we did not introduce any line-of-sight proximity effect the absorption in the Lyα line wing is overestimated, leading to likely overestimated errors in the continuum. Due to the stronger line blending at medium resolution, the recovered X-shooter continua show higher systematic errors ($\lesssim 1\%$ at $z \sim 2$, $\sim 7\%$ at $z \sim 4$) as well as increased statistical fluctuations. Nevertheless, visual inspection revealed that the spectra are well traced by the spline continua. Tests with spectra at $S/N \sim 10$ showed that the accuracy of the fits only weakly depends on the S/N of the data. We conclude that the routine generates reliable fits to Lyα forests without strong Lyman limit systems or DLAs at high and medium resolution. The error budget is objectively assessible and comparable to estimates obtained by manual fitting (Tytler et al. 2004; Kirkman et al. 2005; Faucher-Giguère et al. 2007b; Kim et al. 2007).

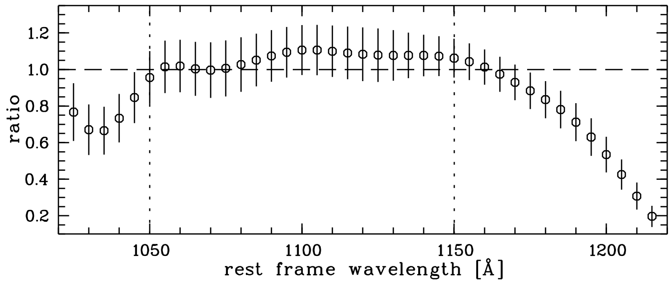

Fig. 3.11. Average ratio of the extrapolated power law and the input continuum for the 200 QSO SEDs in the Lyman forest region (circles). Error bars mark the standard deviation of the distribution around the mean. The horizontal line denotes unity, whereas the vertical lines mark the rest frame wavelength range used to measure $\tau_{\mathrm{eff},\infty}$.

The error budget of the power law extrapolation at low resolution was estimated from the 200 modelled SEDs by fitting power laws to the continua redward of Lyα. The accuracy of the power law continuum does not depend on redshift. The resulting mean ratio between the extrapolated power law blueward of Lyα and the model continuum is presented in Fig. 3.11. Apart from the line wings of Lyα and Lyβ where the power law obviously does not fit the SED, the extrapolated power law systematically overestimates the absorption at 1050 Å$\lesssim \lambda_{\mathrm{rest}} \lesssim$1150 Å by $\sim 7\%$. Evidently, the systematic error of the power law fit is much larger than the corresponding error of the local fits at higher resolution. This systematic error is a direct consequence of the general spectral break in the modelled SEDs around Lyα, in agreement with observations (Telfer et al. 2002; Shang et al. 2005). We consider the almost flat wavelength range 1050 Å$\leq \lambda_{\mathrm{rest}} \leq$1150 Å to measure the effective optical depth in the Lyα forest. The overestimation of $\tau_{\mathrm{eff},\infty}$ due to power law extrapolation is known (see e.g. Kim et al. 2001; Seljak et al. 2003; Desjacques et al. 2007) and we predict it to be an additional constant $\simeq 0.07$. The statistical error exceeds 10% due to the varying amplitude of small-scale deviations from the power-law continuum in different spectra caused by weak emission lines in the forest (Vanden Berk et al. 2001; Telfer et al. 2002; Bernardi et al. 2003; Suzuki 2006).

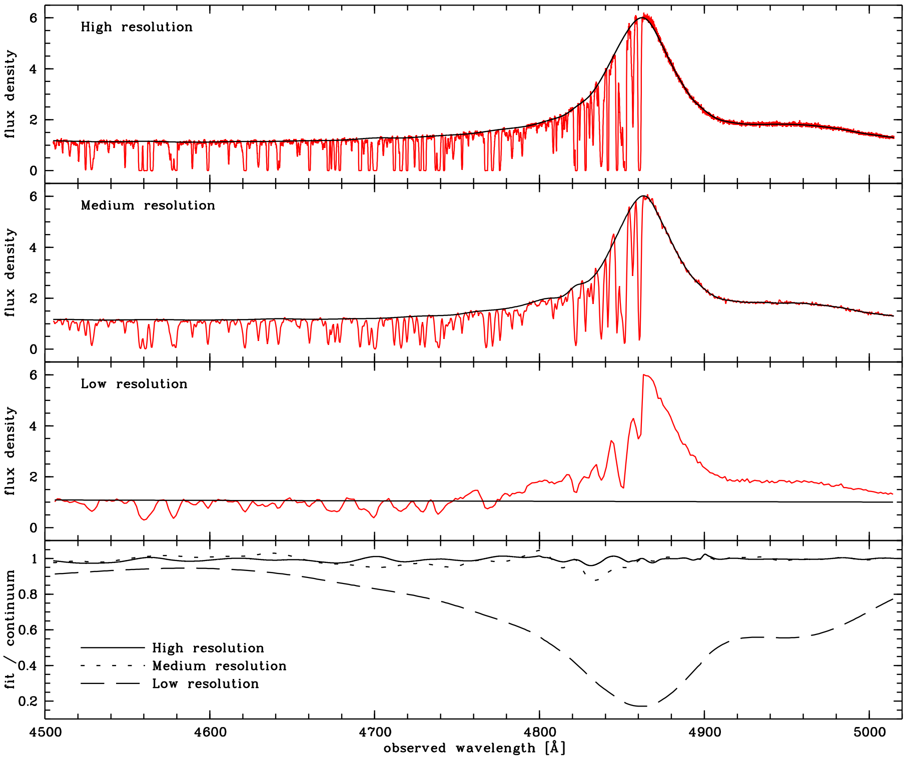

Fig. 3.9. A simulated quasar spectrum at high, medium and low resolution. The three upper panels show the same simulated quasar at $z = 3.0$ taken with $S/N \sim 30$ (red/grey) and the continuum fits (black). No line-of-sight proximity effect was simulated. At high and medium resolution automatic spline continuum fits were performed. At low resolution a power law was extrapolated from the continuum redward of Lyα (not shown). The lowest panel displays the ratio between the fitted continuum and the simulated input continuum obtained at the three considered resolutions, respectively.

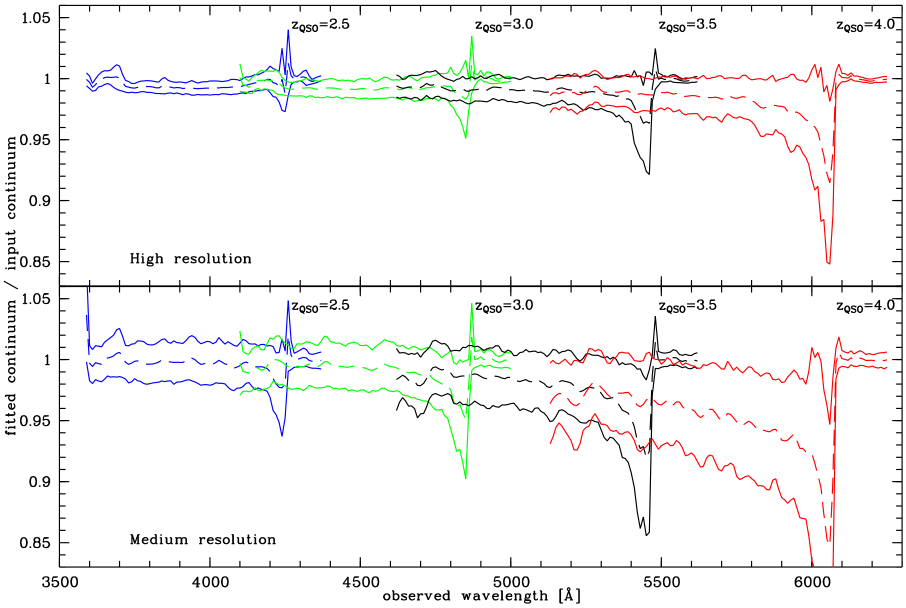

Fig. 3.10. Statistics of the ratio between the fitted continuum and the input continuum at high resolution (upper panel) and medium resolution (lower panel). The dashed lines show the mean ratio of the 200 simulated input continua as a function of observed wavelength for four representative quasar redshifts ($z_{\rm QSO} = 2.5$, 3.0, 3.5 and 4.0). The full lines delineate the standard deviation of the 200 independent measurements around the mean.

3.4. The absence of the transverse proximity effect

3.4.1. Detection method

In principle, the TPE can be revealed either as a local decrease in the Lyα forest line density or as a decreased effective optical depth in the projected vicinity of the FQSO. At the low resolution of FORS the Lyα forest is unresolved, so that we are restricted to effective optical depth statistics. Due to its simplicity we will use this technique also on the high-resolution data. Liske et al. (1998) showed that absorption statistics are significantly more sensitive to reveal structure in the Lyα forest than correlation studies based on the traditional line counting approach.

We have shown in Sect. 3.3.3 that the PDF of the effective optical depth in our Monte Carlo spectra is well described by a Gamma distribution. The modelled TPE of a quasar will decrease $\tau_{\rm eff,\infty}$ in each simulated spectrum, thereby changing the PDF. We found that the PDF of D in the proximity effect zone is still described by a Gamma distribution with $\langle D\rangle < 1$ depending on ω (see also Fig. 3.18 below). The modelled fluctuations in the proximity effect zone σ_D are smaller than the general fluctuations from cosmic variance predicted by eq. (3.14). Thus, the relative absorption D measured in the real data can be easily compared to the expected distribution functions with or without a transverse proximity effect, yielding estimates of its significance.

We searched for the TPE in two ways separately in low- and high-resolution data. In the first method we combined all available BQSO forests as a function of $\omega_{\rm F}$ to detect the effect as an average underdensity near the FQSOs. Since $\tau_{\rm eff}$ and D are ill-defined on scales smaller than the Lyα forest autocorrelation length and/or the spectral resolution (FORS: $\Delta z \gtrsim 0.008$, UVES: $\Delta z \gtrsim 0.002$), we binned the data in $\Delta z = 0.02$ bins and obtained $D(z)$ by dividing by the expected effective optical depth (see below). Then we computed the expected $\omega_{\rm F}(z)$ on the binned forests and merged the $D(\omega_{\rm F})$ measurements. In the second method we considered the spectral regions centred on the FQSOs and estimated the individual sizes of the proximity effect zones from the expected $\omega_{\rm F}(z)$. We then measured D on the estimated scale. The TPE of all FQSOs was implemented in the 1000 Monte Carlo spectra in order to quantify statistical and systematic errors.

3.4.2. The redshift evolution of the effective optical depth

The detection of the proximity effect as an underdense region near a quasar requires a self-consistent estimate of the general absorption without the influence of local sources on the same dataset. Since local continuum fitting is not satisfactory on our low-resolution FORS spectra, we had to rely on the extrapolated power law continua to normalise the spectra. Based on the simulations with the artificial SEDs we restricted the rest frame wavelength range to 1050 Å$\lesssim \lambda_{\rm rest} \lesssim$1150 Å thereby excluding the region of the line-of-sight proximity effect in the Lyα line wing. Due to flux calibration uncertainties and very low S/N we restricted the forests to $z > 1.95$, i.e. $z_{\rm QSO} > 2.188$. We further excluded four quasars with prominent DLAs in the considered wavelength range (CTQ 0247, CTQ 0460, Q 0347−383, Q 2138−4427), two quasars taken with the blue blocking filter GG435 (QSO 03020−0014, QSO J23500−4319), the BAL QSO J21291−1524B, and Q 2139−4434 whose SED in the forest is not well described by the extrapolated power law. The remaining sample consists of 59 quasars.

We then merged the transmission spectra and computed $\tau_{\rm eff,\infty}$ on $\Delta z = 0.1$ bins in the range $1.95 < z < 3.35$. Due to the combination of several forest spectra, any TPE should be insignificant. The result is shown in Fig. 3.12. The best-fit power law to the FORS spectra is $\tau_{\rm eff,\infty} = 0.0046\,(1+z)^{3.37}$. We do not state errors on the estimated parameters because they are highly correlated and not easy to interpret (e.g. Seljak et al. 2003; Meiksin & White 2004). Evidently, our measured effective optical depths are somewhat higher than the ones obtained on similar low-resolution data (e.g. Press et al. 1993) and much higher than suggested by high resolution data (e.g. Kim et al. 2002; Schaye et al. 2003). In order to obtain error estimates on the observed data we performed Monte Carlo simulations employing the techniques and the mock data described in Sect. 3.3. We simulated the 59 quasar spectra 1000 times at $S/N \sim 15$ in the forest, followed by fitting power laws to the Monte Carlo SEDs. We then randomly drew 1000 mock forest samples from the 59000 spectra and computed the mean and the standard deviation of $\tau_{\rm eff,\infty}$ that is Gaussian distributed on scales $\Delta z \gtrsim 0.1$ (Sect. 3.3.3). The simulated data are fitted by $\tau_{\rm eff,\infty} = 0.0060\,(1+z)^{3.00}$ and overpredict the simulated $\tau_{\rm eff,\infty}$ evolution by ~ 0.07. This is due to the extrapolated power law continuum, in agreement with the estimate of Sect. 3.3.5. The 1σ error bars include the continuum error and cosmic variance. Higher error bars at high redshift result from the small number of contributing sightlines. For the actual FORS data we adopted the relative error from the simulations. The additional difference between observed and simulated data is probably caused by metal contamination (not modelled), unrecognised high column density systems (excluded in the fit of Kim et al. (2002)) and additional uncertainties in the power law extrapolation due to varying wavelength ranges available to fit the FORS continua (fixed range in the simulations). However, our self-consistent estimate of the intergalactic absorption in the FORS data still allows a search for the transverse proximity effect.

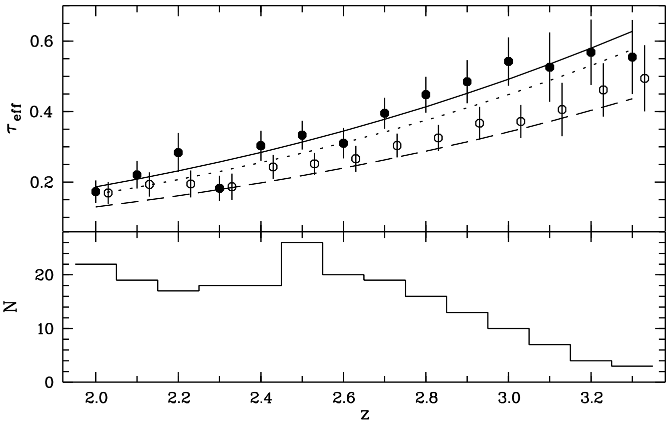

Fig. 3.12. Redshift evolution of the effective optical depth $\tau_{\rm eff,\infty}$ for the FORS low-resolution spectra. The upper panel shows $\tau_{\rm eff,\infty}$ in $\Delta z = 0.1$ bins measured from the FORS spectra (filled circles) and the mean $\tau_{\rm eff,\infty}$ recovered from the Monte Carlo simulations of the sample (empty circles). For clarity the recovered $\tau_{\rm eff,\infty}$ is offset by $\epsilon = 0.03$ in redshift. Error bars denote the standard deviation of the recovered $\tau_{\rm eff,\infty}$ that have been rescaled to the actual measurements. The full, dashed and dotted lines represent the best-fit power law to the FORS data, the fit by Kim et al. (2002) used for the simulations and the fit by Press et al. (1993), respectively. The lower panel shows the number of spectra that contribute to each redshift bin.

For the high-resolution UVES spectra we adopted the fit of $\tau_{\rm eff,\infty}(z)$ to 9 quasars by Kim et al. (2002), who decontaminated the forest from metal lines and excluded high-column density systems. Although the absorption appears somewhat too shallow at high redshift compared to more recent larger studies (Schaye et al. 2003; Kim et al. 2007), the difference is small in the redshift range of interest ($\sim 6\%$). Using our 11 high-resolution spectra excluding regions with DLAs, we found higher effective optical depths, in particular at low redshifts. To some extent this is probably due to the evolving metal line contamination of the Lyα forest. In the following we will compare the total effective optical depth in the Lyα forest near our foreground quasars to the generally expected effective optical depth of H I. Metal line contamination near the quasars will overestimate $\tau_{\rm eff}$ and weakens a TPE. However, metal line subtraction via line fitting of the forest is beyond the scope of the present paper.

3.4.3. Search for a transverse proximity effect in 16 FORS spectra

First, we searched for a combined signal of the TPE in the FORS data. We measured $\tau_{\rm eff}$ in the 18 BQSO FORS spectra on regular $\Delta z = 0.02$ bins. The bins were not forced to be centred on the FQSOs. We then obtained D by dividing by our $\tau_{\rm eff,\infty}$ fit to the FORS spectra and computed the predicted $\omega_{\rm F}$ on the binned spectra. Any background proximity effect is negligible due to the restricted rest frame wavelength range of the BQSO forests, whereas $\omega_{\rm F}(z)$ slowly increases from zero to $\omega_{\max}$ at the

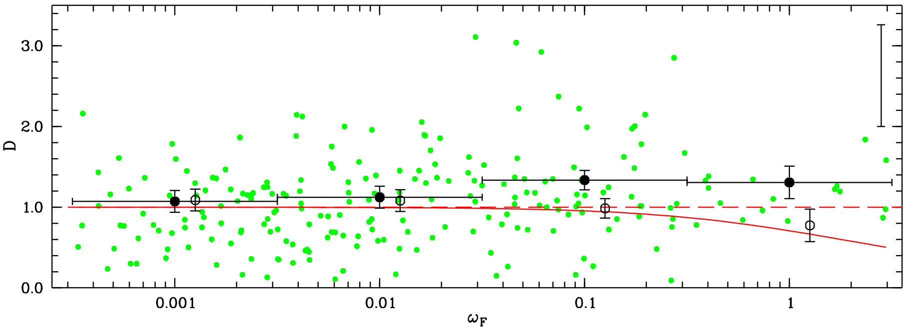

Fig. 3.13. Combined $D(\omega_{\mathrm{F}})$ of the FORS data on a scale $\Delta z = 0.02$. Small symbols show the measured D for $z > 2$. The error bar in the upper right corner marks the average error of a single D value estimated from simulations. The big filled circles with vertical error bars represent the mean D (assuming a lognormal D distribution) and its standard error on $\Delta \log \omega_{\mathrm{F}} = 1$ bins. Open big circles with vertical error bars show the average $\langle D \rangle$ and its standard deviation obtained from the simulations including the TPE and fitting errors. The symbols are offset by 0.1 dex for clarity. The full (dashed) line marks the modelled $D(\omega_{\mathrm{F}})$ with (without) TPE.

redshift of the FQSO. We restricted the data to $z > 2$ due to low S/N at lower redshifts that resulted in very large or unphysically negative D values. This reduced the sample of 19 FQSOs from Table 3.3 to 16. Figure 3.13 shows the merged $D(\omega_{\mathrm{F}})$. The scatter in the normalised effective optical depth is large due to the large small-scale cosmic variance and the continuum errors. The distribution of $D(\omega_{\mathrm{F}})$ does not show the predicted TPE.

In order to decrease the scatter we binned the D measurements in $\Delta \log \omega_{\mathrm{F}} = 1$ bins. Due to the small number of contributing sightlines it is not possible to fit a Gamma distribution to D in each ω_{F} bin. A maximum-likelihood fit to the point distribution was difficult to implement numerically. Therefore we approximated the Gamma distribution by a lognormal distribution that provides simple analytic maximum-likelihood estimators of its parameters. The choice of the lognormal distribution is justified due to the distortions of the D distribution induced by the continuum errors (see Fig. 3.18 below) and the uncertainty in the estimated parameters induced by the scarcity of data.

We verified our procedure with simulated mock FORS data including the expected TPE. For each BQSO we used the set of 1000 Monte Carlo forest spectra, modified the column densities near the FQSO according to eq. (3.1), and obtained fitted mock FORS forest data via the procedures outlined in Sect. 3.3. We then binned the forests in the same $\Delta z = 0.02$ bins, obtained D and computed $\omega_{\mathrm{F}}(z)$. We drew 1000 random realisations of the FORS $D(\omega_{\mathrm{F}})$ sample from the sets of simulated D distributions and fitted a lognormal distribution to each realisation. From the 1000 realisations we find that $\langle D \rangle$ is Gaussian distributed. Its standard deviation yields an estimate of the standard error of $\langle D \rangle$ in the real data. We overplot in Fig. 3.13 the average $\langle D \rangle$ from the simulations. It follows the imposed TPE model well, confiming the relative accuracy of the lognormal approximation. Thus, *on average* the TPE could have been revealed in FORS sample despite the continuum errors. However, a significant deviation from the general $\tau_{\mathrm{eff},\infty}$ evolution is expected only in the highest ω_{F} bin.

In contrast, the real data does not show the expected decrease. The binned $\langle D \rangle$ estimates of the two highest ω_{F} bins deviate from the TPE model at the $\gtrsim 2\sigma$ level and are consistent with overdensities at the $\gtrsim 1\sigma$ level. However, the evidence for overdensities is not very strong because of the correlated large continuum errors in individual FORS spectra that may have been underestimated due to shorter accessible continuum wavelength ranges compared to the model SEDs. Moreover, 15 out of 18 measurements in the highest ω_{F} bin stem from the projected vicinity of just two FQSOs (HE 2243−6031 and HE 2347−4342), so small number statistics likely affects the $\langle D \rangle$ estimate there. This is also reflected in the larger statistical error in the simulations.

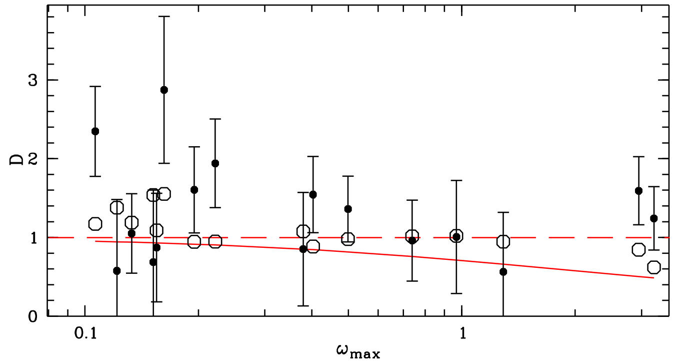

Fig. 3.14. Measured D values centred on 16 $z > 2$ FORS FQSOs vs. their maximum ω (full circles). Error bars denote the standard deviation of D obtained from simulations. Empty circles show $\langle D \rangle$ recovered from 1000 simulations with proximity effect. The full (dashed) line marks the model with (without) the effect.

Concerning our 2nd method to reveal the TPE, we measured τ_{eff} in regions centred on the FQSOs. For each FQSO, a redshift scale $0.02 \lesssim \Delta z \lesssim 0.08$ was estimated from the expected projected extent of the proximity effect zone in the BQSO spectrum. Errors were estimated by fitting Gamma distributions to the mock data on the same redshift windows. The resulting D values for the 16 $z > 2$ FQSOs are presented in Fig. 3.14. Again, the data are consistent with the absence of a TPE. The majority of D values suggests local overdensities. However, fitting the D distributions recovered from the simulations including a TPE reveals only marginal evidence for its existence even at the highest predicted $\omega_{\max}$. The fitted $\langle D \rangle$ values do not follow the imposed model even after 1000 realisations. This is due to the large distortions of the initial Gamma distribution of D induced by the continuum errors. Thus, it is necessary to combine several incidences of the TPE to reduce the impact of cosmic variance and continuum errors on single FORS spectra.

3.4.4. Search for a transverse proximity effect in 11 high-resolution spectra

The analysis of the previous section was repeated on the 11 echelle spectra of the bright BQSOs. Figure 3.15 presents the normalised Lyα forest spectra of the BQSOs in the projected vicinity of the FQSOs. Regions with a predicted $\omega \geq 0.1$ either due to the FQSOs or the BQSOs are marked.

After computing τ_{eff} on $\Delta z = 0.02$ bins that were not intentionally centred in the FQSOs, we obtained D by dividing by the fit to $\tau_{\mathrm{eff},\infty}$ by Kim et al. (2002). For every BQSO we considered

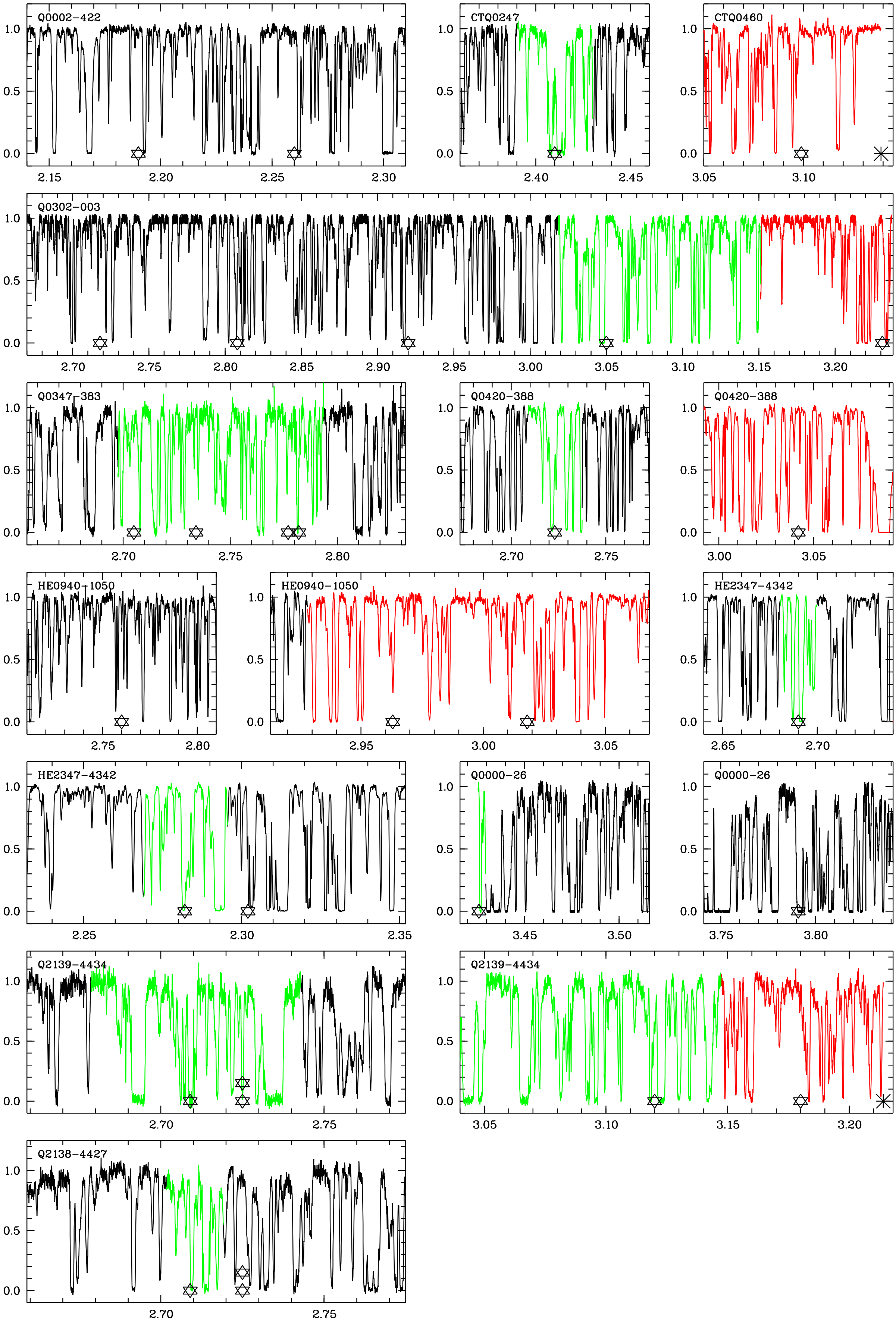

Fig. 3.15. The high-resolution Lyα forests of the BQSOs (asterisks) in the projected vicinity of the FQSOs (stars). Every panel shows the transmission vs. redshift. Regions with $\omega < 0.1$ are shown in black, whereas the FQSO proximity effect regions with $\omega_F \geq 0.1$ and the BQSO proximity effect regions with $\omega_B \geq 0.1$ are shown in green/light grey and red/dark grey, respectively. The spectra of Q 0302−003 and Q 0000−26 have been generated from line lists.

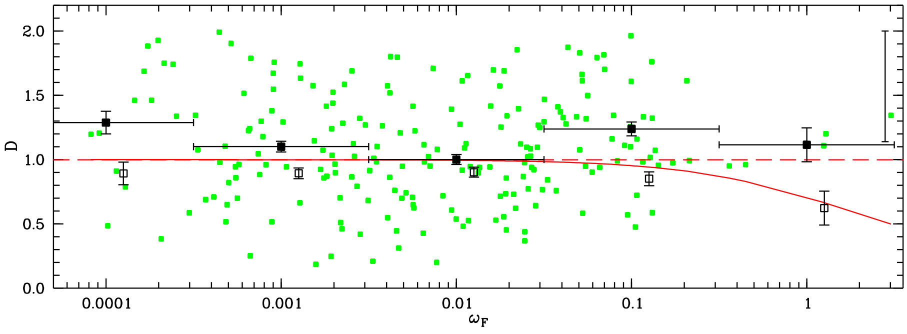

Fig. 3.16. Combined $D(\omega_{\rm F})$ of the high-resolution spectra on a scale $\Delta z = 0.02$. Small symbols show the measured D for $D < 2$ and $\omega_{\rm B} < 0.1$. The error bar in the upper right corner marks the average error of a single D value estimated from simulations. The big filled squares with vertical error bars represent the mean D (assuming a lognormal D distribution) and its standard error on $\Delta \log \omega_{\rm F} = 1$ bins. Open big circles with vertical error bars show the average $\langle D\rangle$ and its standard deviation obtained from the simulations including the TPE, offset by 0.1 dex for clarity. The full (dashed) line marks the modelled $D(\omega_{\rm F})$ with (without) TPE.

the maximum covered wavelength range between the Lyα and the Lyβ emission line. We estimate from the Gamma distributions of Sect. 3.3.3 a probability $p \gtrsim 95\%$ that $D > 2$ values are affected by DLAs or strong metal absorption. Prominent DLAs are present in some spectra and towards HE 2347−4342 the O VI absorption from its associated system (Fechner et al. 2004) resulted in artificially high D values in the lowest redshift bins. We therefore excluded the $D > 2$ values from our analysis. On each binned forest we computed the predicted ω as a combination of the BQSO and all FQSOs via eq. (3.2). We also computed the separate contributions of the FQSOs ($\omega_{\rm F}$) and the BQSOs ($\omega_{\rm B}$). A restriction to D values with $\omega_{\rm B} < 0.1$ was made to separate the proximity effects of the FQSOs from the BQSOs. The line-of-sight proximity effect is clearly detected towards almost every BQSO (Dall'Aglio et al., in preparation).

Figure 3.16 presents the resulting D distribution as a function of $\omega_{\rm F}$. Again we see a large scatter of D around unity arising from the expected small-scale cosmic variance. The very small continuum errors do not contribute significantly to the scatter. The D distribution does not show a sign of the predicted TPE.

Again we compared the real data to mock data including the expected TPE. We modified the absorption in the sets of simulated spectra according to the TPE model, simulated UVES spectra at $S/N \sim 30$ and applied the automatic continuum fitting. From the $D(\omega_{\rm F})$ distributions we drew 1000 random mock samples and estimated $\langle D\rangle$ on $\Delta \log \omega_{\rm F} = 1$ bins via the lognormal maximum-likelihood estimators. We overplot the average $\langle D\rangle$ in Fig. 3.16 together with its standard deviation obtained from the 1000 realisations. $\langle D\rangle$ is Gaussian distributed and underpredicts the absorption in the simulations. This shows that the D distribution is not lognormal, but the estimation of the distribution parameters on such small samples is difficult in any case.

With the lognormal approximation we obtained a maximum-likelihood estimate of $\langle D\rangle$ in the real data. Like the initial D distribution, also the binned $\langle D\rangle$ stays roughly constant and does not follow the TPE model. The standard deviation of $\langle D\rangle$ from the simulations gives the standard error of $\langle D\rangle$ in the real data. The measured absorption is slightly higher than the one predicted by the $\tau_{\rm eff,\infty}(z)$ fit by Kim et al. (2002). Schaye et al. (2003) found a $\sim 6\%$ higher absorption at $z \sim 3$ in their larger sample of high-resolution spectra. Adopting their higher normalisation, we do not find evidence for strong overdensities near the FQSOs. However, the data is still inconsistent with the predicted TPE at the $\gtrsim 2\sigma$ level. The mock data show the TPE in the highest $\omega_{\rm F}$ bin in most cases, so we should have detected it. Again, small number statistics may affect the highest $\omega_{\rm F}$, since only two FQSOs (QSO 03020−0014 and Q 2138−4427) reach such $\omega_{\rm F}$ values. In spite of the resulting larger statistical error, the simulations indicate that a small number of FQSOs should be sufficient to detect the TPE in high-resolution data.

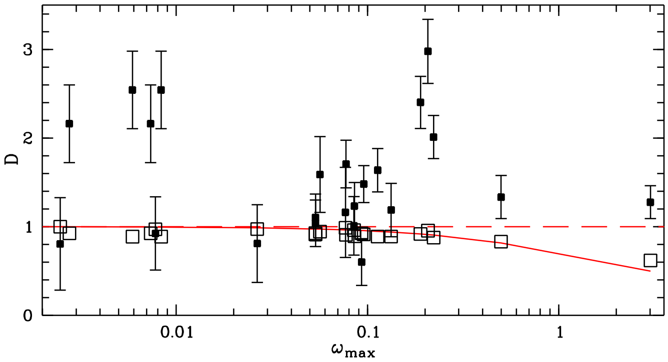

Fig. 3.17. Measured D values centred on 23 UVES foreground quasars vs. their maximum ω (full squares). Error bars denote the expected standard deviation due to cosmic variance. Open squares show $\langle D\rangle$ recovered from 1000 simulations with proximity effect. The full (dashed) line marks the model with (without) a transverse proximity effect.

We then analysed the regions near individual FQSOs. An unbiased analysis of D in redshift bins centred on the FQSOs requires a negligible influence of the BQSO. Therefore, all six FQSOs with $z_{\rm F} > z(\omega_{\rm B} = 0.1)$ had to be discarded. Furthermore, we excluded QSO J23503−4328 and QSO J23500−4319 due to the O VI absorption towards HE 2347−4342 (Chapter 5). We then estimated the redshift windows from the expected TPE zone sizes for the remaining 23 individual FQSOs without regarding possible combined proximity effects of closely projected FQSOs (e.g. towards Q 0347−383, Fig. 3.2). We analysed the D distributions in the mock data with the expected TPE by fitting Gamma distributions to obtain $\langle D\rangle$ and σ_D. From Fig. 3.17 we find that the average region around an FQSO is overdense with respect to the fitted effective optical depth by Kim et al. (2002). An inspection of Fig. 3.15 reveals strong absorbers near most of the FQSOs and Fig. 3.17 confirms this quantitatively. At small $\omega_{\rm F}$ significant underdensities are not expected even if the TPE exists, but for Q 2138−4427 with an inferred $\omega_{\rm max} \simeq 3$ a significant departure from unity to $\langle D\rangle \simeq 0.5$ is predicted. Instead, Fig. 3.17 reveals a $\gtrsim 1\sigma$ overdensity with respect to the cosmic mean that is inconsistent with the proximity effect model at the $\gtrsim 3\sigma$ level. On the estimated redshift window of $\Delta z = 0.08$ around Q 2138−4427 the probability for D values larger than the measured $\simeq 1.3$ is only $\simeq 7\%$ even without considering the expected TPE. The expected $\langle D\rangle \simeq 0.8$ for QSO 03020−0014 can be easily washed out by cosmic variance, but the data are again consistent with an overdensity at the

$\gtrsim 1\sigma$ level. Adopting the higher normalisation by Schaye et al. (2003) still reveals a slight overdensity near both FQSOs. On the other hand, we cannot confirm any systematic trend for overdensities near the FQSOs, neither as a function of ω_{F}, nor as a function of distance to the background line of sight. Interloping metal lines may lead to artificial overdensities in some cases, but their impact is too weak to completely mask a proximity effect of Q 2138−4427. The only significant underdensity is detected around QSO J09434−1053, which is, however, predicted to be too faint to create the effect individually ($\omega_{\max} \simeq 0.1$). In contrast, the TPE is revealed in the mock data. The D distributions are well described by Gamma distributions with a predicted $\langle D\rangle$ that follows the model with a small scatter.

In summary, the TPE is present neither as a systematic trend towards underdensities in the combined samples, nor near individual FQSOs. For most of the pairs a significant TPE is not expected because of cosmic variance that can mask the TPE up to $\omega \sim 1$. According to the simulations, the TPE is marginally detectable even at FORS resolution, but the continuum errors still contribute considerably to the uncertainties of the effective optical depth. Thus, much larger FQSO samples at high ω might reveal the TPE at low resolution. At the high resolution of UVES continuum errors are negligible and the TPE should be detectable even near individual FQSOs. In particular, we expect the TPE for Q 2138−4427 ($\omega_{\max} \simeq 3$). Instead, the data reveal slight overdensities that are inconsistent with the TPE model. Thus, we may conclude that the TPE does not exist due to strongly anisotropic emission or a short quasar lifetime. Whereas anisotropy might exist, the strong line-of-sight proximity effect detected in individual quasars is evidence for rather long-lived quasars that sustained their high luminosity for at least several Myrs (Dall'Aglio et al. 2007). Alternatively, the TPE might be present, but is diluted by moderate anisotropic radiation, variability or intrinsic overdensities, which are difficult to model.

In the following, we will discuss the uncertainties in modelling the proximity effect zone before assessing the detectability of the TPE regarding spectral resolution, sample properties and cosmic variance in Sect. 3.5.2.

3.5. Discussion

3.5.1. Uncertainties and systematic effects

The predicted impact of a quasar onto the IGM depends on several assumptions regarding the quasar and its surroundings. While some parameters can be constrained from observations, others remain systematic uncertainties.

Non-systemic redshifts

Quasar redshifts determined from broad high-ionisation emission lines generally underestimate the true systemic redshifts due to blueshifts with respect to low-ionisation lines or narrow forbidden lines (Gaskell 1982; Tytler & Fan 1992; McIntosh et al. 1999; Richards et al. 2002). However, the projected proximity effect regions of FQSOs with high $\omega_{\max}$ are typically much larger ($\Delta z \sim 0.08$) than the redshift uncertainties or any systemic correction. Therefore, non-systemic redshifts have a negligible impact on the bare detectability of the TPE.

Quasar Lyman limit flux

Absolute spectrophotometry is necessary to infer the quasar's Lyman limit flux. While this as such is difficult from the ground, the Lyman limit flux is not directly observable due to the blanketing by the Lyman series absorption in low- to moderate-resolution spectra. Usually, the Lyman limit flux is inferred by extrapolating a power law fit from the quasar continuum redward of Lyα. This will overestimate the Lyman forest absorption (Sect. 3.3.5) and the Lyman limit flux, if the continuum shows a break towards higher spectral indices α ($f_\nu \propto \nu^{-\alpha}$). Telfer et al. (2002) found $\alpha = 0.69$ ($\alpha = 1.71$) in their composite UV SED at $\lambda_{\mathrm{rest}} \gtrsim 1250$ Å ($\lambda_{\mathrm{rest}} \lesssim 1250$ Å). Shang et al. (2005) observed similar breaks in individual quasars at $\lambda_{\mathrm{rest}} \sim 1100$ Å. The appearance of a break in the SED may depend on luminosity, since low-luminosity AGN are consistent with single power law indices (Scott et al. 2004). Adopting the values from Telfer et al. (2002) we conclude that the Lyman limit fluxes of luminous quasars may be overestimated by ∼ 30%. On the other hand, our adopted value for the UV background intensity is likely overestimated as well (see below), so that ω stays roughly constant.

Considering that the intrinsic SEDs are traced by absorption-free regions, flux-calibrated high-resolution spectra may yield a direct estimate of the Lyman limit fluxes. However, accurate relative flux calibration of echelle spectra is difficult to achieve. Low-resolution spectrophotometric quasar spectra might help to calibrate high-resolution spectra to get a direct estimate of the unabsorbed Lyman limit flux.

Quasar variability and quasar lifetime

The simplistic ionisation model assumes that a quasar shone forever at a constant luminosity L prior to our observation. In practice, the ability to distinguish the quasar flux from the UV background determines the timescale for assuming $L \simeq$ const.. Luminous quasars have large predicted proximity effect zones that extend up to ∼ 10 proper Mpc to reach $\omega \sim 1$ (Fig. 3.20), corresponding to light travel times $t_{\mathrm{trav}} \sim 32$ Myr. The light travel time is always much larger than the photoionisation timescale $t_{\mathrm{ion}} = [\Gamma_{\mathrm{b}}(1+\omega)]^{-1} \lesssim 18$ kyr, which is the minimum timescale of observable changes in the ionisation state near the quasar (Martini 2004). The observed ionisation state will correspond to the quasar luminosity averaged over t_{ion}. Any variability will affect the estimated ω. However, since $t_{\mathrm{trav}} \gg t_{\mathrm{ion}}$, long-term variability on timescales of several Myrs will dominate the uncertainty in ω of FQSOs as well as BQSOs.

These long timescales are comparable to the quasar lifetime t_{Q} inferred from several indirect arguments. Demographic estimates constrain the total time a Black Hole accretes matter as a luminous quasar by comparing the local and the high-redshift Black Hole mass density (Haehnelt et al. 1998; Yu & Tremaine 2002). Alternatively, the coevolution of quasars, Black Holes and galaxies can be modelled both semianalytically (Kauffmann & Haehnelt 2000), or using hydrodynamical simulations (Di Matteo et al. 2005; Hopkins et al. 2005b,a). Moreover, quasar clustering yields estimates on the quasar lifetime, since the clustering strength increases with the typical halo mass of a quasar, and thus its lifetime in order to reproduce the observed quasar space density (Martini & Weinberg 2001; Hui & Haiman 2001; Porciani et al. 2004; Croom et al. 2005; Shen et al. 2007). All the above approaches are consistent with a broad range of quasar lifetimes, $1 \lesssim t_{\mathrm{Q}} \lesssim 100$ Myr (Martini 2004). Traditionally, the line-of-sight proximity effect in the Lyα *forest* was considered to yield only a lower limit to the lifetime $t_Q > t_{\mathrm{ion}}$ (Bajtlik et al. 1988), whereas stronger constraints might be set by determining the line-of-sight effect more accurately even on individual sightlines (Dall'Aglio et al. 2007). Strong constraints of $t_Q \gtrsim 10$ Myr can be obtained by modelling the sharply defined Strömgren spheres of quasars at the reionisation epoch of H I (Pentericci et al. 2002; Haiman & Cen 2002) and He II (Hogan et al. 1997; Anderson et al. 1999). Likewise, the TPE detected via opacity gaps in the Gunn-Peterson troughs of both species corresponds to $t_Q \gtrsim 10$ Myr (Jakobsen et al. 2003) and $t_Q \gtrsim 18$ Myr (Gallerani et al. 2007). Finally, the TPE detected in spectral hardness yields lower limits in the range $t_Q \gtrsim$10–30 Myr (Chapters 4 & 5).

The quasar lifetime can have a strong impact on the detectability of the TPE. For luminous quasars we have $\omega \gtrsim 1$ for $t_{\mathrm{trav}} \lesssim t_Q$, so the quasar radiation might not yet have reached the background line of sight. The TPE of faint quasars cannot be detected at large separations with $t_{\mathrm{trav}} \sim t_Q$. Quasar variability cannot explain the lack of the TPE in close pairs, but it is likely that we overestimate the quasar flux at a given point in the proximity effect zone due to Malmquist bias (Schirber et al. 2004). Moreover, real quasar light curves may be more complicated with several episodes of quasar activity (e.g. Croft 2004; Adelberger 2004; Hopkins et al. 2005b,a). As a consequence, $\omega(t_{\mathrm{trav}})$ that is projected on the background line of sight may significantly differ from $\omega \propto 1/d_\perp^2$ expected for a constant luminosity. On the other hand, existing estimates of the quasar lifetime from the transverse proximity effect and the more indirect methods point to sufficiently long quasar lifetimes for the foreground quasars of interest that have to be located near the line of sight to render the effect visible.

Intrinsically anisotropic emission

Intrinsically anisotropic emission has been frequently invoked to explain the lack of the TPE or offsets of the FQSOs to underdense regions (Crotts 1989; Dobrzycki & Bechtold 1991a; Møller & Kjærgaard 1992; Liske & Williger 2001; Schirber et al. 2004). The TPE model maximises the projected $\omega_F(z)$ for a constant luminosity assuming isotropic radiation. In contrast, unified models of active galactic nuclei predict anisotropic emission due to the dusty torus that is opaque to ionising radiation (e.g. Antonucci 1993; Urry & Padovani 1995). However, the high-redshift space density of type II quasars is still highly uncertain (Ueda et al. 2003; Szokoly et al. 2004; Akylas et al. 2006; Treister & Urry 2006), so that the obscured fraction and correspondingly the opening angles of high-redshift quasars are not well constrained. Furthermore, our findings of the TPE in spectral hardness are consistent with a rather isotropic UV emission of high-redshift quasars (Chapters 4 & 5). On the other hand, Hennawi & Prochaska (2007) find anisotropic clustering of optically thick absorbers around quasars at $d_\perp \lesssim 1$ Mpc, which is difficult to reconcile with isotropic UV emission.

Multiple sightlines probing a given foreground quasar may yield stronger constraints on intrinsically anisotropic emission. These could be background LBGs (Adelberger 2004) or fortunate constellations of quasar sightlines. For instance, Liske & Williger (2001) found an underdensity near a FQSO towards four BQSOs that is hardly explained assuming anisotropic emission. The detection of the underdensity in all four BQSO spectra (total significance 3.5σ) points towards a TPE and not a chance occurrence.

Overdensities near quasars

Quasars are likely to reside in highly biased regions in the universe corresponding to large overdensities compared to the cosmic mean. Since the simple ionisation model assumes that the quasar environment is not biased, traditional studies of the proximity effect are likely affected by unknown intrinsic overdensities (Loeb & Eisenstein 1995; Rollinde et al. 2005; Hennawi & Prochaska 2007; Guimarães et al. 2007; Faucher-Giguère et al. 2007a). Assuming that the UV background is reliably inferred by rescaling the effective optical depth determined from cosmological simulations to observations, the local overdensities near quasars can be quantified (Rollinde et al. 2005; Guimarães et al. 2007; Faucher-Giguère et al. 2007a). Apart from clear cases of quasars with associated absorption, the line-of-sight proximity effect of most quasars can be detected, albeit at variable strength (Dall'Aglio et al. 2007). However, the predicted signature of the TPE is much smaller, so that even small overdensities will render the effect invisible. The Lyα forest absorption is significantly correlated in transverse direction on scales of $\sim$ 1–7 proper Mpc (e.g. Liske et al. 2000; D'Odorico et al. 2002, 2006; Rollinde et al. 2003; Coppolani et al. 2006) or even up to $\sim$ 14 Mpc (Williger et al. 2000; Liske et al. 2000), so that the projected vicinity of foreground quasars may reveal overdense filaments of the cosmic web across the plane of the sky. For close quasar pairs strong or even damped Lyα absorption has been revealed near foreground quasars (Adelberger et al. 2006; Hennawi et al. 2006; Rix et al. 2007) which probably persists on larger scales (D'Odorico et al. 2002, 2006).

UV background

The predicted TPE relies on an accurate estimate of the UV background, which is estimated by the line-of-sight proximity effect (e.g. Bajtlik et al. 1988; Scott et al. 2000; Liske & Williger 2001) under the assumption of the simple ionisation model that is prone to be affected by the above systematic effects. Local overdensities cause the UV background intensity to be overestimated by a factor of $\sim$ 3 (Loeb & Eisenstein 1995; Rollinde et al. 2005; Faucher-Giguère et al. 2007a). Underestimated non-systemic quasar redshifts may cause the background to be overestimated by a factor of $\sim$ 3 (Espey 1993). Furthermore, due to Malmquist bias quasar variability likely overestimates the effective UV flux of the quasars, and thus the UV background. The assumed quasar spectral energy distribution adds uncertainty to the derived UV flux. Moreover, the UV background depends on the assumed cosmological model (Phillipps et al. 2002).

In summary, the systematic effects all tend to overestimate the UV background. Our adopted value for the UV background intensity $J_{\nu_{\mathrm{LL}}} = 7 \times 10^{-22}$ erg cm^{-2} s^{-1} Hz^{-1} sr^{-1} for the adopted concordance cosmology corresponds to $J_{\nu_{\mathrm{LL}}} \simeq 10^{-21}$ erg cm^{-2} s^{-1} Hz^{-1} sr^{-1} in the Einstein-de Sitter universe, which is rather high (see the compilation in Liske & Williger 2001). Thus, the predicted signature of the TPE might be somewhat underestimated, although it may be balanced by the intrinsic overestimation of the quasar Lyman limit flux.

3.5.2. Detectability of the transverse proximity effect

We found in Sect. 3.3.5 that an accurate continuum placement is crucial to reliably determine the effective optical depth in single spectra on small scales. Systematic continuum errors affect the general redshift evolution of $\tau_{\mathrm{eff},\infty}$. These can be taken out by a self-consistent fit of $\tau_{\mathrm{eff},\infty}(z)$ due to the fact that the proximity

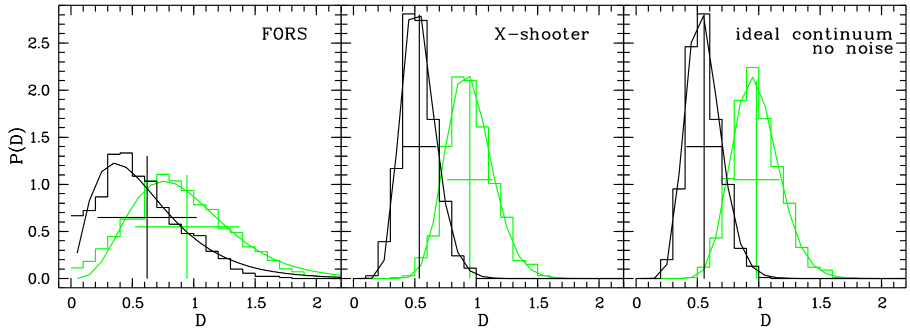

Fig. 3.18. Simulated TPE of HE 2243−6031 ($z = 3.010$, $\omega_{\rm max} = 3.24$) on the line of sight towards QSO J22484−6002 ($z = 3.586$) in a redshift window $\Delta z = 0.08$ at FORS resolution (left), X-shooter resolution (middle) and without noise or continuum errors (right). The simulated FORS and X-shooter spectra contain noise and continuum fitting errors. The black (green/grey) histograms show the simulated D distributions with (without) TPE together with the best-fit Gamma distributions. Large crosses mark $\langle D\rangle$ and σ_D.

effect is a *relative* decrease of the total absorption. However, random continuum errors will affect the spectra on the scales of a predicted transverse proximity effect.

To illustrate the effect of continuum errors, we present in Fig. 3.18 results of simulations with and without the TPE of HE 2243−6031 ($z = 3.010$, $\omega_{\rm max} = 3.24$) on the line of sight towards QSO J22484−6002 ($z = 3.586$). We modified the Monte Carlo forest spectra according to the $\omega_{\rm F}(z)$ of HE 2243−6031 and created mock data at $S/N \sim 30$ with continuum errors (Sect. 3.3.4 and 3.3.5) at low and medium resolution (corresponding to FORS and X-shooter, see Table 3.5). For each of the 1000 spectra in the sets we then computed D on a scale $\Delta z = 0.08$ centred on the quasar. The analysis was repeated on sets of spectra without the TPE. Figure 3.18 shows a significant overlap of the distributions with and without proximity effect at FORS resolution, which is due to cosmic variance and the large statistical continuum fitting errors. The noise in individual pixels is unimportant to determine $\tau_{\rm eff}$. Without any noise or continuum fitting errors, the distributions are well separated with D peaking at $D_{\rm max} \simeq 1/\sqrt{1+\omega_{\rm max}} = 0.49$. Thus, the TPE of HE 2243−6031 or any other FQSO reaching $\omega_{\rm F} \sim 3$ should be detectable on average in a single spectrum. However, the unavoidable errors due to power law continua at low resolution are able to mask the proximity effect. Therefore, very large quasar samples would be required in order to find the effect statistically.

In contrast, the simulations at medium spectral resolution of $R \sim 4500$ show only tiny differences to the ideal spectra. This clearly illustrates the advantage of local continuum fits that trace the SED of the BQSO spectrum much better than an extrapolated power law. The accurate continuum enables a search also in smaller samples of pairs with a predicted strong TPE. In the regime of low ω, however, the statistical fluctuations of the IGM absorption render the proximity effect invisible. At $\omega_{\rm F} \sim 0.5$ we have $\langle D\rangle \sim 0.8$, which is still different from unity, but a clear separation from cosmic variance is progressively difficult as $\langle D\rangle \to 1$.

On the basis of statistical tests we estimated the sample size required for a significant detection of the TPE. We ran Kolmogorov-Smirnov tests on the simulated D distributions for FQSOs at different $\omega_{\rm max}$ comparing a given number of realisations with proximity effect to the same number of realisations without it. We also performed tests comparing the distribution with proximity effect to the fully specified PDF (eq. (3.14) and (3.15)). Low Kolmogorov-Smirnov probabilities $p_{\rm KS}$ indicate a significant difference in the estimated cumulative distribution functions, and hence a significant TPE. Since we are interested in the mean number of required FQSOs, we considered the median $p_{\rm KS}$ computed from 200 realisations per sample size n. Figure 3.19 presents the results obtained for the ideal noise-free inferred TPE zones of HE 2243−6031 ($\omega_{\rm max} = 3.24$), Q 2138−4427 ($\omega_{\rm max} = 3.02$), QSO 03020−0014 ($\omega_{\rm max} = 0.50$) and QSO J09434−1053 ($\omega_{\rm max} = 0.09$). As expected, the required sample size for a significant detection of the TPE strongly increases with decreasing ω. At $\omega \sim 3$, only ~ 5 pairs are needed to distinguish the effect from cosmic variance at the $\sim 3\sigma$ level, whereas at $\omega \sim 0.5$ large samples of $\gtrsim 50$ pairs are necessary. At even lower ω the D distributions with and without a proximity effect completely overlap, rendering the effect undetectable. The probabilities obtained by comparing n spectra with and without proximity effect are always larger than the ones from the comparison to the PDF. This is due to the fact that there are substantial variations in the estimated $P(D)$ in small samples of spectra. Conversely, a significant detection of the TPE in small samples requires a well-constrained PDF that is based on many sightlines. However, $n \sim 10$ FQSOs reaching $\omega \sim 3$ at $z \sim 3$ are still sufficient.

On the basis of these estimates it is possible to detect the TPE even in single instances in the present sample of quasar groups, although not at very high significance due to the lack of pairs with high ω values. At the high resolution of UVES the continuum errors are negligible, but only two FQSOs (Q 03020−0014 and Q 2138−4427) are promising candidates for a detectable TPE. Stacking their simulated TPE reveals the effect on average (Fig. 3.16), but single FQSOs require $\omega_{\rm max} \gtrsim 1$. In Fig. 3.20 we summarise the prospects to detect the TPE in the present sample by plotting $\omega_{\rm max}$ as a function of transverse proper distance $d_\perp$. Most FORS pair combinations are not shown due to the selection threshold of $\omega_{\rm F} \geq 0.1$ (Sect. 3.2.6). We also show $\omega_{\rm max}(d_\perp)$ for four characteristic Lyman limit luminosities $L_{\nu_{\rm LL}} \in \left\{10^{29}, 10^{30}, 10^{31}, 10^{32}\right\}$ erg s^{-1} Hz^{-1} corresponding to observed Vega magnitudes at 1450 Å rest frame of $m_{1450} \in \{24.3, 21.8, 19.3, 16.8\}$ at $z \sim 3$. The majority of FQSOs in our sample has moderate luminosities, reaching $\omega_{\rm max} \sim 1$ at $d_\perp \sim 2$ Mpc. Because our quasar survey covered distances $\lesssim 8$ Mpc, most of these quasars have small ω parameters. Hence, their TPE signal will not exceed cosmic variance. At large distances, only very luminous quasars (like HE 2243−6031 or HE 2347−4342) are able to influence a background sightline.

In summary, we can identify the following observational requirements to statistically detect the transverse proximity effect:

1. moderate spectral resolution ($R \sim 4500$) in order to accurately measure the IGM absorption near the FQSO
2. moderate spectral quality ($S/N \gtrsim 20$) in order to place a reliable continuum
3. enough comparison spectra to quantify the expected absorption without TPE ($\gtrsim 10$ per $\Delta z = 0.1$ bin)
4. sufficiently large ω of the FQSOs to statistically overcome cosmic variance ($\omega_{\rm max} \gtrsim 0.5$)
5. moderate to large sample size depending on the characteristic ω ($\gtrsim 10$ FQSOs at $\omega \sim 3$, $\gtrsim 100$ FQSOs at $\omega \sim 0.5$).

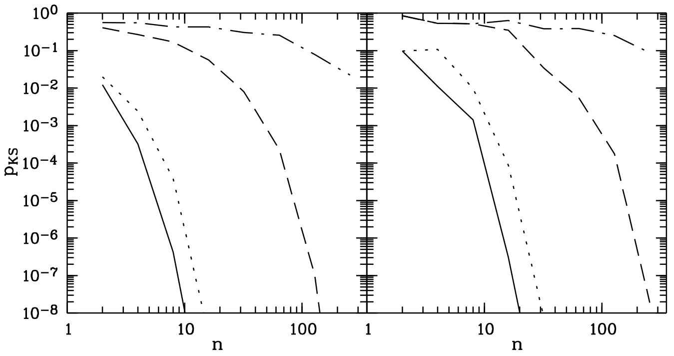

Fig. 3.19. Median Kolmogorov-Smirnov probability $p_{\rm KS}$ for the predicted TPE of HE 2243−6031 (full, $\omega_{\rm max} = 3.24$), Q 2138−4427 (dotted, $\omega_{\rm max} = 3.02$), QSO 03020−0014 (dashed, $\omega_{\rm max} = 0.50$) and QSO J09434−1053 (dash-dotted, $\omega_{\rm max} = 0.09$) vs. sample size n. The left panel shows the results for the test against the PDF without a TPE, whereas the right panel shows the results for a test against a set of n spectra without TPE.

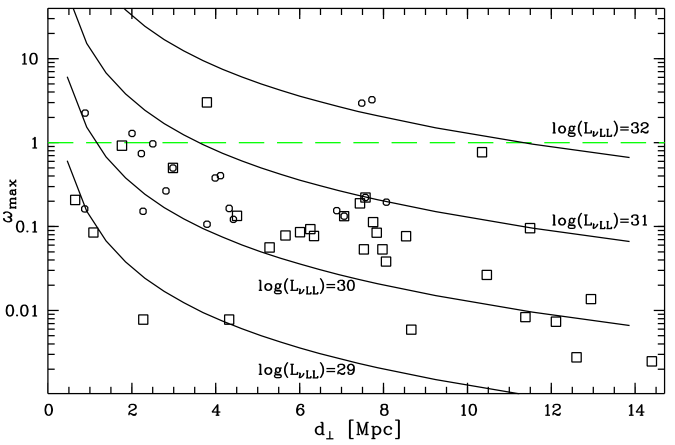

Fig. 3.20. Maximum ω parameters of the 19 considered FORS quasar pairs (circles) and all 31 UVES quasar pairs (squares) as a function of transverse proper distance $d_\perp$. The dashed line denotes $\omega = 1$. The curves show $\omega_{\rm max}(d_\perp)$ for quasars with monochromatic Lyman limit luminosity $L_{\nu_{\rm LL}} \in \left\{10^{29}, 10^{30}, 10^{31}, 10^{32}\right\}$ erg s^{-1} Hz^{-1}.

Thus, our present sample is clearly too small and some of the promising BQSO spectra lack the required resolution. Moreover, the above estimates on the sample size are likely lower limits due to the systematic effects. In particular, intrinsic overdensities near the quasars will mask the TPE. If quasars are preferentially located in $D \gg 1$ regions the TPE changes the absorption only to values around the average, leading to an apparent absence of the TPE (Fig. 3.18).

3.6. Conclusions

We have searched for underdensities in the Lyα forest towards background quasars in the projected vicinity of foreground quasars in 16 fields on the sky in order to reveal the transverse proximity effect. From the initial sample of 125 quasars we selected 16 (23) projected pairs with available low-resolution FORS spectra (high-resolution UVES spectra) of the background quasar. We performed a statistical analysis of the predicted transverse proximity effect and its significance based on realistic artificial Lyα forest spectra derived from Monte Carlo simulations. We estimated the cosmic variance in the Lyα forest by quantifying the fluctuations of the effective optical depth in the Monte Carlo simulations as a function of scale length and redshift. While it is known that the flux statistic approach is more sensitive to reveal underdensities in the Lyα forest than traditional line counting (Liske et al. 1998), our binning analysis on a fixed scale is much simpler than the smoothing method by Liske et al. (1998) whose transmission triangles are difficult to analyse (Liske & Williger 2001). We also investigated the effect of continuum fitting errors at low and high resolution.

Based on the simulated data, the transverse proximity effect should have been detectable, although only at the 1–2σ level. However, the real data does not systematic underdensities near quasars. This might be due to several statistical effects:

1. The studied foreground quasars are generally faint and/or reside at large separations (several proper Mpc) from the background line of sight, so that the predicted signature of the transverse proximity effect is small (Fig. 3.20).
2. Cosmic variance effectively masks any weak transverse proximity effect at $\omega \lesssim 1$.
3. The applicability of low-resolution spectra is limited by large continuum uncertainties.

Taken together, these effects limit the number of interesting cases to just two FORS pairs and one UVES pair in the present sample. Due to small number statistics no robust conclusions can be drawn concerning the presence or absence of the transverse proximity effect. Cosmic variance in small quasar samples might be the main reason for the frequent non-detection of the transverse proximity effect, at least at low ω. We estimate that an unambiguous detection of the transverse proximity effect of quasars reaching $\omega_{\rm max} \sim 3$ requires $\gtrsim 5$ moderate-resolution spectra ($R \sim 4500$) of background sources. More pairs are needed at lower resolution or smaller ω.

Furthermore, the apparent absence of the transverse proximity effect can be explained by the adverse effects of anisotropic emission, long-term quasar variability and intrinsic overdensities. These systematic effects cannot be disentangled in sparsely sampled H I Lyα forest data. At present, they cannot be quantified and our Monte Carlo simulations likely yield only lower limits on the required number of quasars due to the lacking large-scale structure in the forest. Future studies will have to consider multiple sightlines near foreground quasars from fortunate constellations of background quasars (Liske & Williger 2001) or from more numerous, but fainter LBGs (Adelberger 2004). In addition, there might be further coincidences of quasars and voids in Gunn-Peterson troughs where optical depth fluctuations are smaller and background ionisation rates are lower compared to the forests (Jakobsen et al. 2003; Gallerani et al. 2007). Finally, more sensitive diagnostics applicable in intrinsically overdense regions, like fluorescent Lyα emission (Adelberger et al. 2006; Cantalupo et al. 2007) or the spectral shape of the ambient UV radiation field (Chapters 4 & 5), are able to reveal the elusive transverse proximity effect in the weak-field regime.

Acknowledgements. Based on observations collected at the European Southern Observatory, Chile (Proposals 70.A-0425, 074.A-0273 and 075.A-0141). Data collected under Proposals 68.A-0194, 70.A-0376, 072.A-0073 and the various UVES observation programmes listed in Table 3.2 were obtained from the ESO Science Archive.

This research has made use of the NASA/IPAC Extragalactic Database (NED) which is operated by the Jet Propulsion Laboratory, California Institute of Technology, under contract with the National Aeronautics and Space Administration.

References

Abazajian, K., Adelman-McCarthy, J. K., Agüeros, M. A., et al. 2004, AJ, 128, 502

Abazajian, K., Adelman-McCarthy, J. K., Agüeros, M. A., et al. 2005, AJ, 129, 1755

Adelberger, K. L. 2004, ApJ, 612, 706

Adelberger, K. L., Steidel, C. C., Kollmeier, J. A., & Reddy, N. A. 2006, ApJ, 637, 74

Akylas, A., Georgantopoulos, I., Georgakakis, A., Kitsionas, S., & Hatziminaoglou, E. 2006, A&A, 459, 693

Anderson, S. F., Hogan, C. J., Williams, B. F., & Carswell, R. F. 1999, AJ, 117, 56

Antonucci, R. 1993, ARA&A, 31, 473

Bajtlik, S., Duncan, R. C., & Ostriker, J. P. 1988, ApJ, 327, 570

Ballester, P., Mondigliani, A., Boitquin, O., et al. 2000, The Messenger, 101, 31

Bechtold, J. 1994, ApJS, 91, 1

Becker, G. D., Rauch, M., & Sargent, W. L. W. 2007, ApJ, 662, 72

Bernardi, M., Sheth, R. K., SubbaRao, M., et al. 2003, AJ, 125, 32

Bi, H., Börner, G., & Chu, Y. 1992, A&A, 266, 1

Bi, H. & Davidsen, A. F. 1997, ApJ, 479, 523

Cantalupo, S., Lilly, S. J., & Porciani, C. 2007, ApJ, 657, 135

Cardelli, J. A., Clayton, G. C., & Mathis, J. S. 1989, ApJ, 345, 245

Carswell, R. F., Whelan, J. A. J., Smith, M. G., Boksenberg, A., & Tytler, D. 1982, MNRAS, 198, 91

Cooke, A. J., Espey, B., & Carswell, R. F. 1997, MNRAS, 284, 552

Coppolani, F., Petitjean, P., Stoehr, F., et al. 2006, MNRAS, 370, 1804

Cristiani, S., D'Odorico, S., Fontana, A., Giallongo, E., & Savaglio, S. 1995, MNRAS, 273, 1016

Croft, R. A. C. 2004, ApJ, 610, 642

Croft, R. A. C., Weinberg, D. H., Pettini, M., Hernquist, L., & Katz, N. 1999, ApJ, 520, 1

Croom, S. M., Boyle, B. J., Shanks, T., et al. 2005, MNRAS, 356, 415

Crotts, A. P. S. 1989, ApJ, 336, 550

Crotts, A. P. S. & Fang, Y. 1998, ApJ, 502, 16

Dall'Aglio, A., Wisotzki, L., & Worseck, G. 2007, submitted to A&A

Desjacques, V., Nusser, A., & Sheth, R. K. 2007, MNRAS, 374, 206

Di Matteo, T., Springel, V., & Hernquist, L. 2005, Nat, 433, 604

Dinshaw, N. & Impey, C. D. 1996, ApJ, 458, 73

Dobrzycki, A. & Bechtold, J. 1991a, ApJ, 377, L69

Dobrzycki, A. & Bechtold, J. 1991b, in ASP Conf. Ser. 21: The Space Distribution of Quasars, 272

D'Odorico, V., Petitjean, P., Cristiani, S., & D'Odorico, S. 2002, A&A, 390, 13

D'Odorico, V., Viel, M., Saitta, F., et al. 2006, MNRAS, 372, 1333

Espey, B. R. 1993, ApJ, 411, L59

Fardal, M. A., Giroux, M. L., & Shull, J. M. 1998, AJ, 115, 2206

Fardal, M. A. & Shull, J. M. 1993, ApJ, 415, 524

Faucher-Giguère, C.-A., Lidz, A., Zaldarriaga, M., & Hernquist, L. 2007a, ApJ,submitted, astro-ph/0701042

Faucher-Giguère, C.-A., Prochaska, J. X., Lidz, A., Hernquist, L., & Zaldarriaga, M. 2007b, ApJ,submitted, arXiv:0709.2382

Fechner, C., Baade, R., & Reimers, D. 2004, A&A, 418, 857

Fernández-Soto, A., Barcons, X., Carballo, R., & Webb, J. K. 1995, MNRAS, 277, 235

Francis, P. J., Palunas, P., Teplitz, H. I., Williger, G. M., & Woodgate, B. E. 2004, ApJ, 614, 75

Gallerani, S., Ferrara, A., Fan, X., & Roy Choudhury, T. 2007, MNRAS, submitted, arXiv:0706.1053

Gaskell, C. M. 1982, ApJ, 263, 79

Giallongo, E., Cristiani, S., D'Odorico, S., Fontana, A., & Savaglio, S. 1996, ApJ, 466, 46

Guimarães, R., Petitjean, P., Rollinde, E., et al. 2007, MNRAS, 377, 657

Haardt, F. & Madau, P. 1996, ApJ, 461, 20

Haehnelt, M. G., Natarajan, P., & Rees, M. J. 1998, MNRAS, 300, 817

Haiman, Z. & Cen, R. 2002, ApJ, 578, 702

Hawkins, M. R. S. 2000, A&AS, 143, 465

Hennawi, J. F. & Prochaska, J. X. 2007, ApJ, 655, 735

Hennawi, J. F., Prochaska, J. X., Burles, S., et al. 2006, ApJ, 651, 61

Hogan, C. J., Anderson, S. F., & Rugers, M. H. 1997, AJ, 113, 1495

Hopkins, P., Hernquist, L., Cox, T. J., et al. 2005a, ApJ, 630, 705

Hopkins, P., Hernquist, L., Martini, P., et al. 2005b, ApJ, 625, L71

Hu, E. M., Kim, T.-S., Cowie, L. L., & Songaila, A. 1995, AJ, 110, 1526

Hui, L. & Haiman, Z. 2001, ApJ, 547, 27

Hui, L. & Rutledge, R. E. 1999, ApJ, 517, 541

Jakobsen, P., Jansen, R. A., Wagner, S., & Reimers, D. 2003, A&A, 397, 891

Kauffmann, G. & Haehnelt, M. G. 2000, MNRAS, 311, 576

Kim, T.-S., Bolton, J. S., Viel, M., Haehnelt, M. G., & Carswell, R. F. 2007, MNRAS,accepted, arXiv:0711.1862

Kim, T.-S., Carswell, R. F., Cristiani, S., D'Odorico, S., & Giallongo, E. 2002, MNRAS, 335, 555

Kim, T.-S., Cristiani, S., & D'Odorico, S. 2001, A&A, 373, 757

Kim, T.-S., Hu, E. M., Cowie, L. L., & Songaila, A. 1997, AJ, 114, 1

Kim, Y.-R. & Croft, R. 2007, MNRAS,submitted, astro-ph/0701012

Kirkman, D., Tytler, D., Suzuki, N., et al. 2005, MNRAS, 360, 1373

Liske, J. 2000, MNRAS, 319, 557

Liske, J., Webb, J. K., & Carswell, R. F. 1998, MNRAS, 301, 787

Liske, J., Webb, J. K., Williger, G. M., Fernández-Soto, A., & Carswell, R. F. 2000, MNRAS, 311, 657

Liske, J. & Williger, G. M. 2001, MNRAS, 328, 653

Loeb, A. & Eisenstein, D. J. 1995, ApJ, 448, 17

Lu, L., Sargent, W. L. W., Womble, D. S., & Takada-Hidai, M. 1996, ApJ, 472, 509

Lu, L., Wolfe, A. M., & Turnshek, D. A. 1991, ApJ, 367, 19

Lynds, R. 1971, ApJ, 164, L73

Madau, P., Haardt, F., & Rees, M. J. 1999, ApJ, 514, 648

Martini, P. 2004, in Carnegie Observatories Astrophysics Series Vol. 1: Coevolution of Black Holes and Galaxies, ed. L. C. Ho (Cambridge University Press), 170

Martini, P. & Weinberg, D. H. 2001, ApJ, 547, 12

McDonald, P., Seljak, U., Cen, R., Bode, P., & Ostriker, J. P. 2005, MNRAS, 360, 1471

McIntosh, D. H., Rix, H.-W., Rieke, M. J., & Foltz, C. B. 1999, ApJ, 517, L73

Meiksin, A. & White, M. 2004, MNRAS, 350, 1107

Misawa, T., Tytler, D., Iye, M., et al. 2007, AJ, 134, 1634

Møller, P. & Kjærgaard, P. 1992, A&A, 258, 234

Morris, S. L., Weymann, R. J., Anderson, S. F., et al. 1991, AJ, 102, 1627

Pentericci, L., Fan, X., Rix, H.-W., et al. 2002, AJ, 123, 2151

Petitjean, P., Webb, J. K., Carswell, R. F., & Lanzetta, K. 1993, MNRAS, 262, 499

Phillipps, S., Horleston, N. J., & White, A. C. 2002, MNRAS, 336, 587

Porciani, C., Magliocchetti, M., & Norberg, P. 2004, MNRAS, 355, 1010

Press, W. H., Rybicki, G. B., & Schneider, D. P. 1993, ApJ, 414, 64

Rauch, M. 1998, ARA&A, 36, 267

Richards, G. T., Vanden Berk, D. E., Reichard, T. A., et al. 2002, AJ, 124, 1

Rinne, H. 1997, Taschenbuch der Statistik (Verlag Harri Deutsch)

Rix, S. A., Pettini, M., Steidel, C. C., et al. 2007, ApJ, accepted, arXiv:0708.0007

Rollinde, E., Petitjean, P., Pichon, C., et al. 2003, MNRAS, 341, 1279

Rollinde, E., Srianand, R., Theuns, T., Petitjean, P., & Chand, H. 2005, MNRAS, 361, 1015

Sargent, W. L. W., Young, P. J., Boksenberg, A., & Tytler, D. 1980, ApJS, 42, 41

Savaglio, S., Christiani, S., D'Odorico, S., et al. 1997, A&A, 318, 347

Schaye, J., Aguirre, A., Kim, T.-S., et al. 2003, ApJ, 596, 768

Schirber, M., Miralda-Escudé, J., & McDonald, P. 2004, ApJ, 610, 105

Schlegel, D. J., Finkbeiner, D. P., & Davis, M. 1998, ApJ, 500, 525

Scott, J., Bechtold, J., Dobrzycki, A., & Kulkarni, V. P. 2000, ApJS, 130, 67

Scott, J., Bechtold, J., Morita, M., Dobrzycki, A., & Kulkarni, V. P. 2002, ApJ, 571, 665

Scott, J., Kriss, G. A., Brotherton, M., et al. 2004, ApJ, 615, 135

Seljak, U., McDonald, P., & Makarov, A. 2003, MNRAS, 342, L79

Shang, Z., Brotherton, M. S., Green, R. F., et al. 2005, ApJ, 619, 41

Shen, Y., Strauss, M. A., Oguri, M., et al. 2007, AJ, 133, 2222

Srianand, R. 1997, ApJ, 478, 511

Steidel, C. C., Adelberger, K. L., Shapley, A. E., et al. 2003, ApJ, 592, 728

Steidel, C. C. & Sargent, W. L. W. 1987, ApJ, 313, 171

Suzuki, N. 2006, ApJS, 163, 110

Suzuki, N., Tytler, D., Kirkman, D., O'Meara, J. M., & Lubin, D. 2005, ApJ, 618, 592

Szokoly, G. P., Bergeron, J., Hasinger, G., et al. 2004, ApJS, 155, 271

Telfer, R. C., Zheng, W., Kriss, G. A., & Davidsen, A. F. 2002, ApJ, 565, 773

Tepper-García, T. 2006, MNRAS, 369, 2025

Tepper-García, T. & Fritze, U. 2007, submitted to MNRAS, arXiv:0705.1242

Treister, E. & Urry, C. M. 2006, ApJ, 652, L79

Tytler, D. & Fan, X. 1992, ApJS, 79, 1

Tytler, D., Kirkman, D., O'Meara, J. M., et al. 2004, ApJ, 617, 1

Ueda, Y., Akiyama, M., Ohta, K., & Miyaji, T. 2003, ApJ, 598, 886

Urry, C. M. & Padovani, P. 1995, PASP, 107, 803

Vanden Berk, D. E., Richards, G. T., Bauer, A., et al. 2001, AJ, 122, 549

Véron-Cetty, M.-P. & Véron, P. 2006, A&A, 455, 773

Williger, G. M., Baldwin, J. A., Carswell, R. F., et al. 1994, ApJ, 428, 574

Williger, G. M., Smette, A., Hazard, C., Baldwin, J. A., & McMahon, R. G. 2000, ApJ, 532, 77

Wisotzki, L., Christlieb, N., Bade, N., et al. 2000, A&A, 358, 77

Wisotzki, L., Selman, F., & Gilliotte, A. 2001, The Messenger, 104, 8

Worseck, G., Fechner, C., Wisotzki, L., & Dall' Aglio, A. 2007, A&A, 473, 805

Worseck, G. & Wisotzki, L. 2006, A&A, 450, 495
Young, P. J., Sargent, W. L. W., Boksenberg, A., Carswell, R. F., & Whelan, J. A. J. 1979, ApJ, 229, 891
Yu, Q. & Tremaine, S. 2002, MNRAS, 335, 965
Zuo, L. 1992, MNRAS, 258, 36
Zuo, L. 1993, A&A, 278, 343
Zuo, L. & Phinney, E. S. 1993, ApJ, 418, 28

Chapter 4

Quasars near the line of sight towards Q 0302−003 and the transverse proximity effect[⋆]

G. Worseck and L. Wisotzki

Astrophysikalisches Institut Potsdam, An der Sternwarte 16, 14482 Potsdam, Germany

ABSTRACT

We report the discovery of the faint ($V \simeq 21.7$) quasar QSO 03027−0010 at $z = 2.808$ in the vicinity of Q 0302−003, one of the few quasars observed with STIS to study intergalactic He II absorption. Together with another newly discovered QSO at $z = 2.29$, there are now 6 QSOs known near the line of sight towards Q 0302−003, of which 4 are located within the redshift region $2.76 \lesssim z \lesssim 3.28$ covered by the STIS spectrum. We correlated the opacity variations in the H I and He II Lyman forest spectra with the locations of known quasars. There is no significant proximity effect in the H I Lyα forest for any of the QSOs, except for the well-known line of sight effect for Q 0302−003 itself. By comparing the absorption properties in H I and He II, we estimated the fluctuating hardness of the extragalactic UV radiation field along this line of sight. We find that close to each foreground quasar, the ionizing background is considerably harder than on average. In particular, our newly discovered QSO 03027−0010 shows such a hardness increase despite being associated with an overdensity in the H I Lyman forest. We argue that the spectral hardness is a sensitive physical measure to reveal the influence of QSOs onto the UV background even over scales of several Mpc, and that it breaks the density degeneracy hampering the traditional transverse proximity effect analysis. We infer from our sample that there is no need for significantly anisotropic UV radiation from the QSOs. From the transverse proximity effect detected in the sample we obtain minimum quasar lifetimes in the range ~10–30 Myr.

4.1. Introduction

Observations of high-redshift quasars enable us to study the intergalactic medium (IGM) along their lines of sight via the absorption of quasar radiation by various chemical elements in different ionization stages. Hydrogen and helium are by far the most abundant elements in the universe and the Lyα transitions of H I and He II in an incompletely ionized medium cause a Gunn-Peterson trough at redshifts smaller than the emission redshift of the observed quasar (Gunn & Peterson 1965). If the IGM is highly ionized, a plethora of discrete absorption lines stemming from the remaining neutral fraction is visible both in H I Lyα and He II Lyα, giving rise to the name Lyα forest.

The intensity of the metagalactic UV radiation field at a characteristic frequency (typically the ionization energy of a given element) varies in time due to the temporal evolution of the source population. Spatial fluctuations induced by the discreteness of the source population have been examined for randomly distributed sources and absorbers by Zuo (1992) and Fardal & Shull (1993). They are also treated in recent numerical simulations trying to quantify their impact on the Lyα flux power spectrum (Croft et al. 1999; Meiksin & White 2004; Croft 2004; McDonald et al. 2005). The spatial fluctuations of the UV radiation field computed from these simulations along random lines of sight are generally gentle (few per cent around the mean) and occur on large scales ($\gtrsim$ 100 Mpc comoving) at $z < 4$. This simple picture with only mild large-scale fluctuations is expected to change considerably for lines of sight that pass close to sources of the UV background, such as luminous quasars (Fardal & Shull 1993; Croft 2004; McDonald et al. 2005). The source flux acts as a local enhancement of the UV radiation field. As a consequence, the absorbers in the region affected by this excess flux will be statistically more ionized than the rest of the Lyα forest along the line of sight, resulting in a statistically increased transmission, a radiation-induced 'void' in the H I Lyα forest in the vicinity of the UV source. This so-called proximity effect has been detected with high statistical significance in lines of sight towards luminous quasars (e.g. Bajtlik et al. 1988; Scott et al. 2000). However, a transverse proximity effect created by foreground ionizing sources nearby the line of sight has not been clearly detected in the H I Lyα forest. The full range of possible results extends from large voids claimed to be due to the transverse proximity effect by Dobrzycki & Bechtold (1991a, however see Dobrzycki & Bechtold 1991b) and Srianand (1997), over marginal detections (Fernández-Soto et al. 1995; Liske & Williger 2001) to non-detections (Crotts 1989; Møller & Kjærgaard 1992; Crotts & Fang 1998; Schirber et al. 2004). Croft (2004) measured the average transverse Lyα transmission from all projected quasar pairs in the SDSS DR1 and even found excess absorption near foreground quasars instead of the expected excess transmission caused by the transverse proximity effect.

The detectability of the transverse proximity effect is hampered by several systematic effects. Anisotropic radiation of quasars has been invoked to explain redshift offsets between the void and the foreground quasar (Dobrzycki & Bechtold 1991a) or to explain the lack of the transverse proximity effect (Crotts 1989; Møller & Kjærgaard 1992; Schirber et al. 2004). Also quasar variability affects the detection of the proximity effect (Schirber et al. 2004). Finally, the possible gravitational clustering around quasars that are assumed to reside in the densest environments may dilute the proximity effect (Loeb & Eisenstein

---

[⋆] This chapter is published in *Astronomy & Astrophysics*, 2006, 450, 495.

1995; Schirber et al. 2004; Rollinde et al. 2005). According to Schirber et al. (2004) only a combination of these systematic effects may explain the apparent absence of the transverse proximity effect.

He II Lyα 303.78 Å absorption can be studied only towards a few lines of sight to date because most of the quasars at $z > 2$ have intervening optically thick Lyman limit systems that truncate the flux in the observable He II Lyα wavelength range in the far UV. The observations of the lines of sight towards Q 0302−003 at $z = 3.285$ (Jakobsen et al. 1994; Hogan et al. 1997; Heap et al. 2000), PKS 1935−692 at $z = 3.18$ (Anderson et al. 1999) and recently SDSS J2346−0016 at $z = 3.50$ (Zheng et al. 2004a) show in most parts of their He II absorption spectra very strong absorption at $z > 3$ that is consistent with a Gunn-Peterson trough ($\tau_{\mathrm{He\,II}} > 3$). In contrast, the three lines of sight at $z < 3$ probed so far towards HS 1700+6416 at $z = 2.72$ (Davidsen et al. 1996; Reimers et al. 2004), HE 2347−4342 at $z = 2.885$ (Reimers et al. 1997; Kriss et al. 2001; Smette et al. 2002; Shull et al. 2004; Zheng et al. 2004b) and recently QSO 1157+3143 at $z \simeq 3$ (Reimers et al. 2005) display patchy intergalactic He II absorption with voids ($\tau_{\mathrm{He\,II}} \lesssim 1$) and troughs ($\tau_{\mathrm{He\,II}} > 3$) that evolves to a He II Lyα forest at $z < 2.7$ resolved with FUSE (Kriss et al. 2001; Shull et al. 2004; Zheng et al. 2004b; Reimers et al. 2004). In combination with the observed evolution of H I line widths (Schaye et al. 2000; Ricotti et al. 2000; Theuns et al. 2002) these observations point to a late He II reionization between $z \sim 2.7$ and $z \sim 3$.

By comparing the H I absorption with the corresponding He II absorption one can estimate the hardness of the ionizing radiation field that penetrates the IGM, since H I is ionized at $h\nu > 13.6$ eV, whereas He II is ionized at $h\nu > 54.4$ eV. The amount of He II compared to H I gives a measure of the spectral hardness. Already low-resolution He II observations obtained with HST indicated a fluctuating radiation field in the voids (hard) and the troughs (soft) (Reimers et al. 1997; Heap et al. 2000; Smette et al. 2002). The recent high-resolution FUSE observations of the He II Lyα forest reveal large fluctuations on very small scales of $\Delta z \sim 10^{-3}$ (Kriss et al. 2001; Shull et al. 2004; Reimers et al. 2004). Due to the hard ionizing field required in the He II voids that is consistent with the integrated radiation of a surrounding quasar population, these He II voids have been interpreted as the onset of He II reionization in Strömgren spheres around hard He II photoionizing sources along or near the line of sight (Reimers et al. 1997; Heap et al. 2000; Smette et al. 2002). A subsequent survey for putative quasars that may cause the prominent He II void at $z = 3.05$ towards Q 0302−003 yielded the quasar QSO 03020−0014 located 6.′5 away on the sky that coincides with this He II void (Jakobsen et al. 2003). Thus, the He II void in Q 0302−003 is the first clear case of a transverse proximity effect due to a luminous quasar.

In this paper we report on results from a slitless spectroscopic quasar survey that resulted in the discovery of another foreground quasar in the vicinity of Q 0302−003. The structure of the paper is as follows. Sect. 4.2 describes the observation and the supplementary data employed for the paper. In Sect. 4.3 and 4.4 we examine the evidence for opacity variations in the H I and He II Lyα forest regions caused by intensity fluctuations in the UV radiation field towards Q 0302−003 at 1 ryd and 4 ryd, respectively. In Sect. 4.5 we consider the possibility to detect the transverse proximity effect via spectral hardness diagnostics of the ionizing radiation. We argue that this is actually the most sensitive method, and we demonstrate that essentially each quasar near the line of sight is associated with a local hardening of the radiation field. Finally, we use these observations to estimate a lower limit to the quasar lifetime (Sect. 4.7). We present our conclusions in Sect 4.8. Throughout the paper we adopt a flat cosmological model with $\Omega_{\mathrm{m}} = 0.3$, $\Omega_\Lambda = 0.7$ and $H_0 = 70\ \mathrm{km\,s^{-1}\,Mpc^{-1}}$.

4.2. Observations & data reduction

4.2.1. Search for quasar candidates near Q 0302−003

In October 2002 and February 2003 we conducted a quasar survey with the ESO Wide Field Imager (WFI) at the ESO/MPI 2.2 m Telescope at La Silla in its slitless spectroscopic mode (Wisotzki et al. 2001). The survey fields of $25' \times 33'$ were centered on bright high-redshift QSOs, and our aim was to find faint quasars in their vicinity. Details about this survey will be given in a separate paper. Here we report the results of the field centered on Q 0302−003 at $z = 3.285$ observed on October 3 and 4, 2002, and we only briefly summarize the survey technique. We recorded our slitless spectra with the R50 grism ($\lambda/\Delta\lambda = 30$–$50$ depending on the seeing) in the B and the V band by 3 dithered 600 s exposures in 2 instrument rotations each, resulting in a total exposure time of 1 h per band and yielding a limiting magnitude of $V_{\mathrm{lim}} \simeq 22$. The filters were employed to reduce the sky background and the degree of crowding by limiting the length of the recorded spectra. Crowding was further accounted for by taking the spectra in two instrument rotations (0° and 10°). The combination of the R50 grism with the broadband B and V filters resulted in a spectral coverage from the blue grism sensitivity cutoff at 4200 Å to 5800 Å, permitting us to search for Lyα emission in the redshift range $2.46 \lesssim z \lesssim 3.77$ and for C IV emission in the range $1.71 \lesssim z \lesssim 2.74$.

All sources detected in the Digitized Sky Survey (which has approximately the same depth as our slitless spectroscopic data) were automatically extracted, yielding flux-calibrated low-resolution spectra of ~ 800 objects in the field. The spectra were searched automatically for emission-line objects. The lower panel of Fig. 4.1 shows the slitless spectra of four $z > 2$ quasars that were found by our survey. One of them was (unsurprisingly) Q 0302−003 itself, and we also unambiguously rediscovered QSO 03020−0014 discovered recently by Jakobsen et al. (2003). Our search revealed two further quasar candidates in the vicinity of Q 0302−003 that fall into our redshift range of interest. The first showed clearly Lyα emission at $z \simeq 2.79$ whereas the second displayed an emission line which we tentatively identified as C IV at $z \simeq 2.29$.

4.2.2. Spectroscopic follow-up

Follow-up spectroscopy of these two quasar candidates was obtained with the Focal Reducer/Low Dispersion Spectrograph 2 (FORS2) on ESO VLT UT1/Antu in Visitor Mode on November 17, 2004. The sky was clear throughout the night. The spectra were taken with the 300V grism and a $1''$ slit kept at the parallactic angle, resulting in a spectral resolution of ~ 10 Å FWHM. In order to maximize throughput, the order separation filter was omitted, leading to possible order overlap at $\lambda > 6600$ Å. Exposure times were adjusted to yield a S/N of ~ 20 in the quasar continuum. We also recorded a FORS2 spectrum of Q 0302−003 with the 600B grism on November 19, 2004, at a resolution of ~ 4.5 Å FWHM. Seeing conditions were poor and highly variable during the observations of Q 0302−003, resulting in some slit losses but still a S/N of ~ 70 in the Lyα forest could be achieved. The spectra were calibrated in wavelength

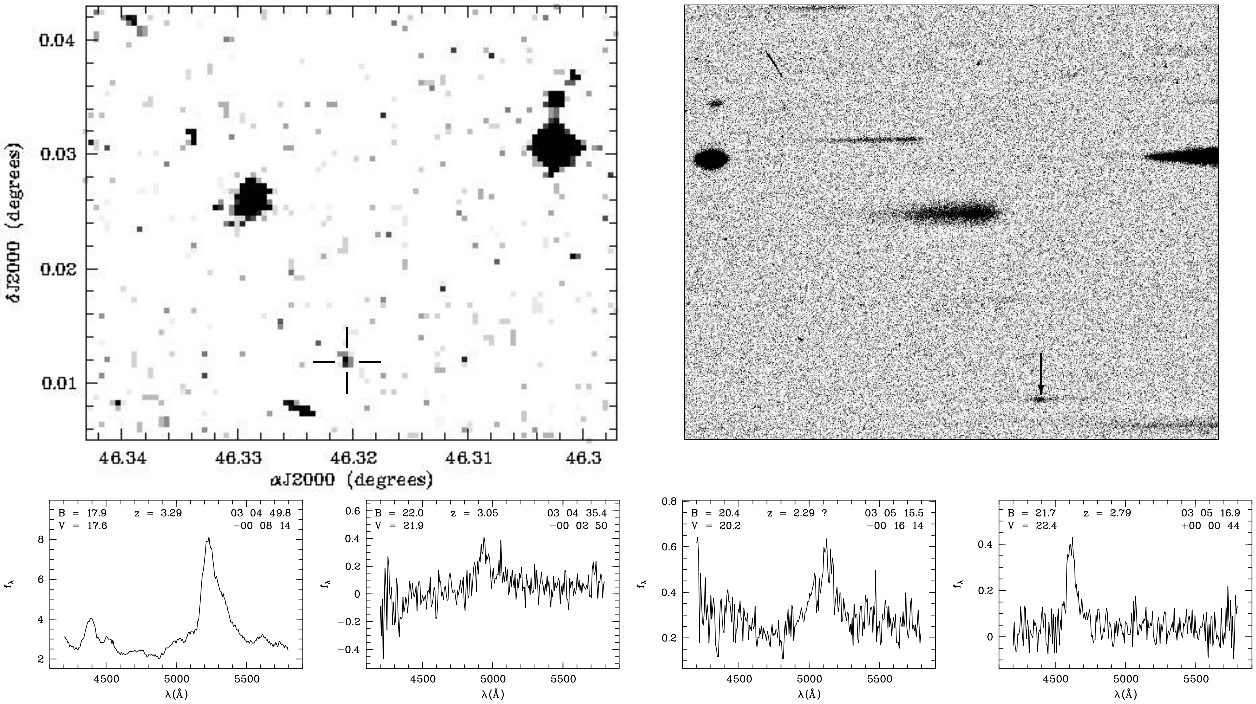

Fig. 4.1. Discovery of the two quasar candidates. The upper left panel shows a 2.8′ × 2.3′ DSS1 image of the sky region around the faint QSO 03027−0010 marked with a cross. The upper right panel displays the corresponding region of the slitless WFI *B* exposures (0° rotation, 1800 s stacked observations). The emission line of QSO 03027−0010 is clearly visible (arrow). The lower panels show the combined and calibrated slitless spectra of $z > 2$ quasars found on the total 25′ × 33′ field with their DSS1 position, redshift and magnitude estimates (from left to right: Q 0302−003, QSO 03020−0014, QSO 03027−0027 and QSO 03027−0010).

against the FORS2 He/Ne/Ar/HgCd arc lamps and spectrophotometrically calibrated against the HST standard stars Feige 110 and GD 108. Data reduction was performed with standard IRAF tasks. The spectra were optimally extracted using the algorithm introduced by Horne (1986). Table 4.1 summarizes our spectroscopic follow-up observations.

Figure 4.2 shows the calibrated spectra of the two candidates. Both are confirmed to be quasars at redshifts correctly estimated in the slitless spectra. Since the quality of our FORS2 aquisition images is superior to the DSS image, we refined the QSO positions (see Table 5.1) and denote these as QSO 03027−0010 and QSO 03027−0027 in the following, according to IAU conventions.

There is a strong associated absorption line system in the spectrum of QSO 03027−0010 at $z_{\rm abs} = 2.804 \pm 0.001$ visible in Lyα, N v and C iv. A C iv system is present at $z_{\rm abs} = 2.696$ that is also visible in Si iv and that corresponds to a strong Lyα absorption line in the Lyα forest. Moreover, a Mg ii absorber may be present at $z_{\rm abs} = 0.750$.

QSO 03027−0027 shows a strong metal line system at $z_{\rm abs} = 2.115$, easily detectable in Mg ii, C iv, Si iv and C ii. Another weaker C iv system may be present at $z_{\rm abs} = 2.243$.

Table 4.2 shows our quasar redshift determination based on all detectable emission lines. The S/N of both spectra generally prevents a clear detection of low-ionization lines, such as O i+Si ii or O iii]. The redshift measurement based on the Mg ii line in QSO 03027−0027 is inaccurate due to the decreasing resolving power of the grism at the longest recordable wavelengths. Consequently, the redshifts have to be measured in high-ionization lines which suffer from systematic blueshifts (Gaskell 1982; Tytler & Fan 1992; McIntosh et al. 1999). The measurements in the spectrum of QSO 03027−0010 are further affected by the associated absorption system. Having these caveats in mind, we adopt a redshift of $z = 2.290 \pm 0.002$ for QSO 03027−0027 and a redshift of $z = 2.808 \pm 0.004$ for QSO 03027−0010.

Apparent magnitudes of both quasars were derived based on the available spectrophotometry, yielding $V = 21.7$ for QSO 03027−0010 and $V = 19.9$ for QSO 03027−0027.

4.2.3. Continuum and redshift of Q 0302−003

In order to be able to use the FORS2 spectrum of Q 0302−003 for measuring its transmission properties in the H i Lyα forest region, we had to obtain a working estimate of the continuum. This was established by fitting a cubic spline to selected high-transmission regions of the data, using the DIPSO software under Starlink [1]. Due to the low resolution of the spectrum, the absorption lines are heavily blended. We checked our continuum fit for systematic errors using line lists from high-resolution spectra published by Hu et al. (1995) from Keck HIRES data and by Kim et al. (2002) from VLT UVES data. The list from Hu et al. (1995) covers the redshift range $2.627 \leq z \leq 3.110$, whereas the list from Kim et al. (2002) extends between $2.957 \leq z \leq 3.235$. The two line lists were used to create artificial Lyα forest spectra which were subsequently convolved with the line spread function of the FORS2 600B grism and rebinned to 1.5 Å/pixel. The result was an excellent correspondence (r.m.s. error ∼ 3%) between our data and the simulated spectra, indicating that our fit did not grossly underestimate the true continuum. The only regions where our continuum estimate is significantly too low by ∼ 8% are the wavelength range largely devoid of Lyα absorption from ∼ 5050 Å to

---

[1] The authors acknowledge the data analysis facilities provided by the Starlink Project which is run by CCLRC on behalf of PPARC.

Table 4.1. Observing log for the spectroscopic follow-up.

Object	α (J2000)	δ (J2000)	Night	Grism	Slit	Exposure	Airmass	Seeing
QSO 03027−0010	$03^h05^m16\overset{s}{.}80$	$+00°00'45\overset{''}{.}1$	17 Nov 2004	300V	$1\overset{''}{.}0$	600 s	1.10	$0\overset{''}{.}9$
QSO 03027−0027	$03^h05^m15\overset{s}{.}62$	$-00°16'14\overset{''}{.}4$	17 Nov 2004	300V	$1\overset{''}{.}0$	300 s	1.10	$0\overset{''}{.}7$
Q 0302−003	$03^h04^m49\overset{s}{.}71$	$-00°08'13\overset{''}{.}0$	19 Nov 2004	600B	$1\overset{''}{.}0$	1800 s	1.18	$\lesssim 1\overset{''}{.}9$

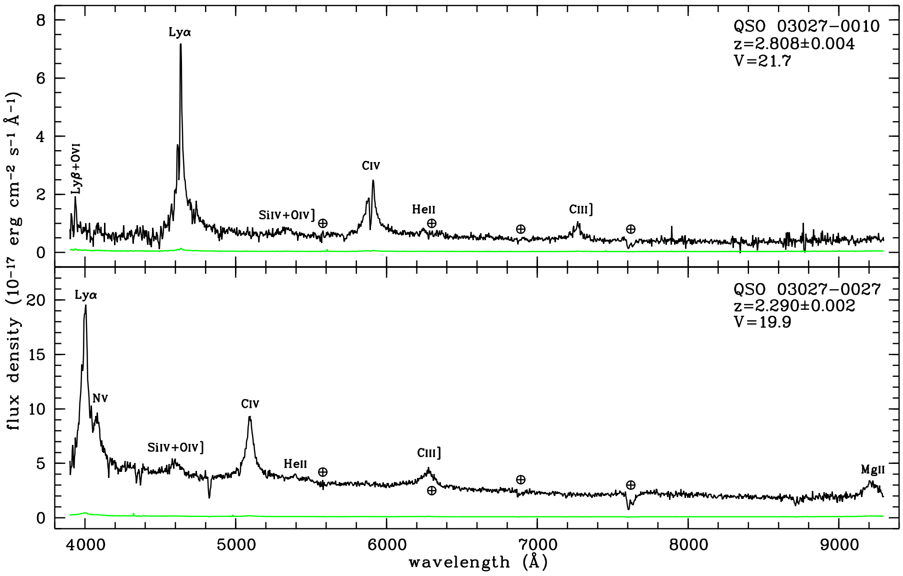

Fig. 4.2. VLT/FORS2 spectra of the two discovered QSOs. The spectra are shown in black lines together with their corresponding 1σ noise arrays (green/gray lines). Detected emission lines and major atmospheric artifacts are indicated.

Table 4.2. Redshift determination of the two newly discovered QSOs.

Emission line	QSO 03027−0010 λ [Å]	z	QSO 03027−0027 λ [Å]	z
Lyβ+O VI	3936 ± 5	2.810 ± 0.005	–	–
Lyα	4627 ± 7	2.806 ± 0.006	4004 ± 3	2.294 ± 0.003
N V	–	–	4081 ± 3	2.291 ± 0.003
Si IV+O IV]	5335 ± 10	2.812 ± 0.007	4598 ± 8	2.284 ± 0.006
C IV	5896 ± 11	2.806 ± 0.007	5095 ± 2	2.289 ± 0.001
He II	6244 ± 3	2.806 ± 0.002	5393 ± 3	2.288 ± 0.002
C III]	7268 ± 4	2.808 ± 0.002	6278 ± 5	2.289 ± 0.003
Mg II	–	–	9223 ± 15	2.296 ± 0.005

~ 5100 Å, known as the Dobrzycki & Bechtold void (Dobrzycki & Bechtold 1991a) and a small region at ~ 4480 Å already in the line wing of the Lyβ+O VI line of Q 0302−003 where continuum fitting becomes complicated.

We also checked the line lists of Hu et al. (1995) and Kim et al. (2002) for metal line contamination of the H I Lyα forest. Only a few identified systems contaminate the Lyα forest. These are narrow lines with low column densities, which are heavily blended with H I lines at our low resolution. The absorption by metals is therefore negligible and we will treat the whole absorption in the spectral range of the H I Lyα forest as genuine H I Lyα absorption.

Our FORS2 spectrum of Q 0302−003 covers the wavelength range from the UV cutoff to ~6350 Å and has a S/N of ~ 75 in the quasar continuum, so we can measure the positions of the lines Lyβ+O VI, Lyα, N V, O I+Si II, C II and Si IV+O IV]. We base our redshift measurement on the low-ionization lines O I+Si II and C II, which should yield the best possible estimate of the systemic redshift. We get a redshift of $z = 3.285 \pm 0.001$ for the O I+Si II line and a redshift of $z = 3.284 \pm 0.001$ for the C II line, which is consistent with the value of 3.286 originally obtained by Sargent et al. (1989). But we note that their value was based on the Lyα and the C IV emission line.

The sky region around Q 0302−003 was targeted by SDSS, and Q 0302−003 was observed spectroscopically. We checked the SDSS DR3 database for the spectroscopic redshift of Q 0302−003 and found the redshift to be too high, $z_{\mathrm{SDSS}} \simeq 3.295 \pm 0.001$. Given this large offset of $\Delta z = 0.009$, we obtained the SDSS spectrum of Q 0302−003 from the SDSS data archive and recovered the redshift values for the low-ionization lines O I+Si II ($z = 3.286 \pm 0.002$) and C II ($z = 3.284 \pm 0.002$). We conclude that the SDSS redshift assignment for Q 0302−003 is incorrect and adopt a redshift of $z = 3.285$ for this quasar in the following.

4.2.4. HST/STIS data

Q 0302−003 was one of the few high-redshift quasars observed successfully in the He II Lyα forest below 303.78 Å rest frame wavelength with HST and its *Space Telescope Imaging Spectrograph* at a resolution of 1.8 Å (Heap et al. 2000, hereafter refered to as H00). We retrieved these data from the HST archive and re-reduced them using CALSTIS v2.13 distributed with IRAF. As in the reduction by H00, we adjusted the background subtraction windows in order to correct for the spatial variability of the STIS MAMA1 detector background. We adopt their flux normalization with a power law $f_\nu \propto \nu^{-\alpha}$ with $\alpha = 2$, yielding $f_\lambda = \text{const.} \simeq 2.1 \times 10^{-16}\,\mathrm{erg\,cm^{-2}\,s^{-1}\,Hz^{-1}}$. The spectral index of 2 is consistent with the composite QSO EUV spectral index of ~ 1.8 by Telfer et al. (2002).

4.2.5. Quasars in the vicinity of Q 0302−003

Table 4.3 tabulates all 6 known quasars at $z > 2$ within a radius $< 30'$ around Q 0302−003. Their distribution in red-

Table 4.3. Known $z > 2$ foreground quasars within 30′ of Q 0302−003 ($z = 3.285$). We list positions, redshifts, V magnitudes, projected angular distances ϑ from Q 0302−003, and the corresponding transverse proper distances $d_\perp(z)$ at the emission epoch of each foreground quasar.

QSO	Abbr.	α (J2000)	δ (J2000)	z	V	ϑ [′]	$d_\perp$ [Mpc]	discovery paper
QSO 03022−0023	F	$03^{\mathrm{h}}04^{\mathrm{m}}45\overset{\mathrm{s}}{.}94$	$-00^\circ11'38\overset{''}{.}2$	2.142	22.5	3.55	1.77	Jakobsen et al. (2003)
QSO 03027−0027	E	$03^{\mathrm{h}}05^{\mathrm{m}}15\overset{\mathrm{s}}{.}62$	$-00^\circ16'14\overset{''}{.}4$	2.290	19.9	10.31	5.08	this paper
QSO 03027−0010	B	$03^{\mathrm{h}}05^{\mathrm{m}}16\overset{\mathrm{s}}{.}80$	$+00^\circ00'45\overset{''}{.}1$	2.808	21.7	11.24	5.29	this paper
Q 0302-D113	D	$03^{\mathrm{h}}04^{\mathrm{m}}30\overset{\mathrm{s}}{.}33$	$-00^\circ08'11\overset{''}{.}4$	2.920	24.3	4.85	2.26	Steidel et al. (2003)
QSO 03020−0014	A	$03^{\mathrm{h}}04^{\mathrm{m}}35\overset{\mathrm{s}}{.}37$	$-00^\circ02'50\overset{''}{.}9$	3.050	20.5	6.46	2.97	Jakobsen et al. (2003)
Q 0301−005	C	$03^{\mathrm{h}}03^{\mathrm{m}}41\overset{\mathrm{s}}{.}05$	$-00^\circ23'21\overset{''}{.}8$	3.231	17.8	22.89	10.34	Barbieri & Cristiani (1986)

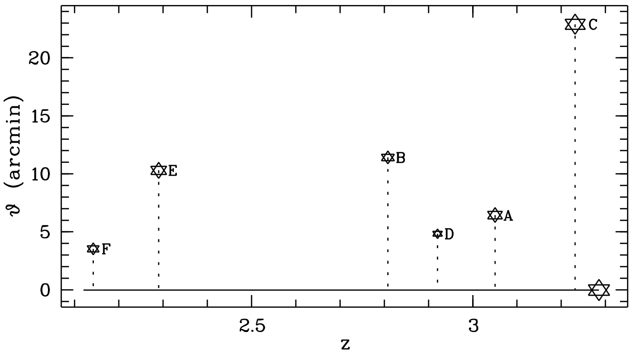

Fig. 4.3. Distribution of the foreground quasars from Table 4.3 with respect to Q 0302−003. Symbol size indicates apparent optical magnitude.

shift and separation from the central line of sight is shown in Fig. 4.3. In addition to the QSOs discovered or rediscovered in our survey, we found two further quasars listed by Véron-Cetty & Véron (2003). Spectra for these QSOs were retrieved from public archives, in order to measure the emission redshifts as consistently as possible. For the sake of clarity, we will use a simplified nomenclature in the following and denote the foreground QSOs by the letters A . . . F as indicated in Table 4.3.

Q 0301−005 (QSO C) is a bright QSO known since long. It was observed by SDSS and we obtained its spectrum from the SDSS data archive. Previous redshift determinations were based on high-ionization lines (Sargent et al. 1989), so its redshift of $z = 3.223$ measured by Sargent et al. (1989) may have been underestimated. The SDSS spectrum of this QSO has sufficient S/N to measure the low-ionization lines O i+Si ii and C ii, yielding a redshift of $z = 3.231$ for this object in agreement with the SDSS redshift assignment. Note the large shift of $\Delta z = 0.008$ with respect to the measurement based on high-ionization lines.

The two quasars discovered by Jakobsen et al. (2003, hereafter refered to as J03) have spectra taken with FORS1 in the ESO/VLT Science Archive. We performed an independent reduction and give here a refined redshift (redshift uncertainty 0.002) and the magnitude for QSO 03022−0023 (QSO F). With $V = 22.5$ it is too faint to be detected in our slitless spectroscopic survey material. Our estimate of redshift and redshift error for QSO 03020−0014 (QSO A) agrees with the values given in J03.

Q 0302-D113 (QSO D) was published by Steidel et al. (2003) after the compilation of the Véron-Cetty & Véron (2003) catalog. No spectrum is available for this very faint ($R \simeq 24.6$) object. Its V magnitude in Table 4.3 is estimated from R.

4.3. No visible H i transverse proximity effect

We first conducted a simple visual search for locally enhanced transmission of the H i Lyman forest at the location of the foreground quasars. Figure 4.4 displays our low-resolution transmission spectrum of Q 0302−003, together with the effective locations of the foreground quasars projected into the forest. The proximity effect manifests itself as a statistical increase in Lyα forest transmission near a quasar. Already a quick examination of Fig. 4.4 shows that there are at least no obvious H i voids located at any of the foreground quasars that could be revealed by visual inspection, with the possible exception of QSO A which is located very close to a local transmission maximum. There is no such correlation for any of the other QSOs. There is, however, a significant increase of Lyα forest transmission towards the Lyα line of the central QSO Q 0302−003 itself.

Considering the luminosities of the foreground QSOs and their projected angular distances from the central line of sight, this lack of a transverse proximity effect in H i is no real surprise. We computed the parameter

$$\omega(z) = \sum_{j=1}^{n} \frac{f_{\nu_{\mathrm{LL}},j}}{4\pi J_\nu(z)} \frac{\left(1+z'_j\right)^{-\alpha_j+1}}{\left(1+z_j\right)} \left(\frac{\alpha_{J_\nu}+3}{\alpha_j+3}\right)\left(\frac{d_L\left(z_j,0\right)}{d_L\left(z_j,z\right)}\right)^2 \tag{4.1}$$

which is the ratio between the summed photoionization rates of n quasars at redshifts z_j with a rest frame Lyman limit flux $f_{\nu_{\mathrm{LL}},j}$, penetrating the absorber at redshift z and the overall UV background with Lyman-limit intensity J_ν. $d_L\left(z_j,0\right)$ is the luminosity distance of QSO j, and $d_L\left(z_j,z\right)$ is its luminosity distance as seen at the absorber; the redshift of the quasar as seen at the absorber is z'_j (Liske 2000). Thus, $\omega\left(z_{\mathrm{em}}\right)$ characterizes the expected strength of the transverse proximity effect signature at a given QSO redshift along the line of sight: A highly significant effect would require $\omega\left(z_{\mathrm{em}}\right) \gg 1$, i.e. a UV radiation field dominated by the local source.

We fixed the UV background at 1 ryd to $J_\nu = 7 \times 10^{-22}$ erg cm^{-2} s^{-1} Hz^{-1} sr^{-1} (Scott et al. 2000) and assumed it to be constant over the relevant redshift range $2 < z < 3.285$ with a power-law shape $J_\nu \propto \nu^{-\alpha_{J_\nu}}$ and $\alpha_{J_\nu} = 1.5$. The quasar Lyman limit fluxes were estimated from the available spectra by fitting a power law $f_\nu \propto \nu^{-\alpha}$ to the quasar continuum redward of the Lyα emission line, excluding the emission lines. Table 4.4 lists the resulting spectral indices and the Lyman limit fluxes for the quasars. For QSO D there was no spectrum available and we estimated its Lyman limit flux from its R magnitude assuming a power law index $\alpha = 0.5$.

In all cases except for Q 0302−003 itself we find peak ω values significantly below unity. The highest value is reached by the very luminous QSO C, for which Dobrzycki & Bechtold

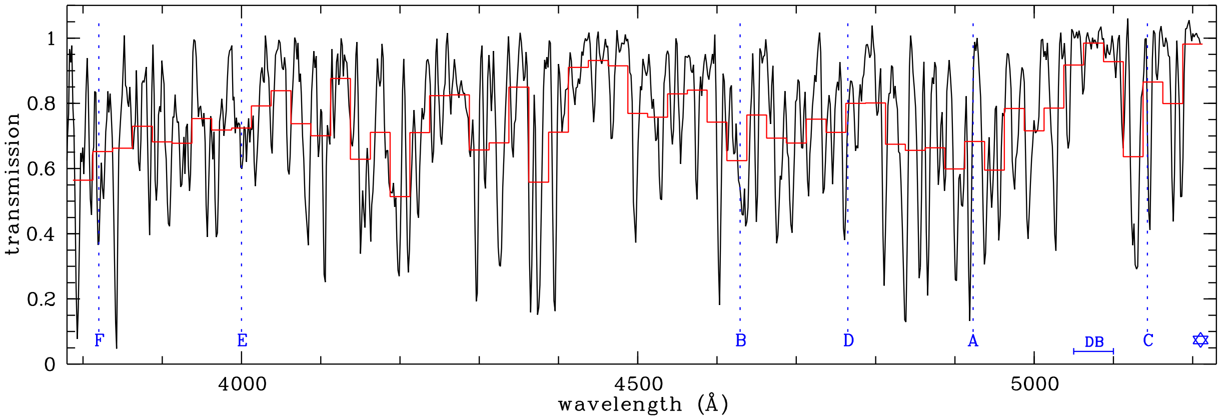

Fig. 4.4. Transmission spectrum of the H I Lyα & Lyβ forest of Q 0302−003. The spectrum is shown in black from 3780 Å to 5210 Å (corresponding to the Lyα emission peak of Q 0302−003). Letters and vertical dotted lines mark the foreground quasars from Table 4.3 projected into the forest. We also indicated the background quasar Q 0302−003 by a star symbol and the void identified by Dobrzycki & Bechtold (1991a) (DB). The binned line is the average transmission in 25 Å bins.

Table 4.4. Rest frame Lyman limit fluxes of Q 0302−003 and all nearby QSOs. A power law $f_\nu \propto \nu^{-\alpha}$ is fitted to all quasars with an available spectrum. $f_{\nu_{\rm LL}}$ is the extrapolated Lyman limit flux in the QSO rest frame and $\omega(z_{\rm em})$ is the resulting predicted strength of the transverse proximity effect (see text).

QSO	Abbr.	α	$f_{\nu_{\rm LL}}$ [μJy]	$\omega(z_{\rm em})$
QSO 03022−0023	F	1.12 ± 0.06	2 ± 4	0.073
QSO 03027−0027	E	0.67 ± 0.02	22 ± 17	0.121
QSO 03027−0010	B	0.88 ± 0.02	4 ± 4	0.035
QSO 0302-D113	D		0.3 ± 0.3	0.028
QSO 03020−0014	A	1.42 ± 0.01	10 ± 7	0.253
Q 0301−005	C	0.90 ± 0.01	136 ± 89	0.776
Q 0302−003	★	0.50 ± 0.01	222 ± 124	∞

(1991a) proposed that it might cause the large void at $z \sim 3.17$. While the redshift offset between this void and QSO C at $z = 3.231$ may still be explained by anisotropic emission, the small $\omega(z_{\rm em})$ value implies that this quasar would have to be implausibly bright in the direction of the void (Dobrzycki & Bechtold 1991b). Note that due to their small redshift difference, Q 0302−003 and QSO C have similar impact at $z \simeq 3.231$. The $\omega(z_{\rm em})$ value of QSO C is therefore the sum of the contributions from these two sources. The small projected proximity effect zone of QSO C merges with the onset of the much larger line of sight proximity effect zone caused by Q 0302−003 itself. The refined redshift of QSO C implies an even larger offset between quasar and void; together with the modest value of ω it follows that the Dobrzycki & Bechtold (1991a) void is very unlikely related to the ionizing radiation from QSO C. This statement will be reinforced below in Sect. 4.5.

For all other QSOs the ω values are even much smaller. Consequently, as long as one assumes roughly isotropic radiation, these QSOs should leave no individually detectable traces of a transverse proximity effect. This also holds for QSO A. Its matching redshift with a small H I void could therefore be just a coincidence, especially when considering the large number of similar features in the spectrum. Nevertheless, the combined evidence from H I and He II forests suggests that this region does indeed receive a substantial amount of hard QSO radiation (H00, J03).

4.4. Fluctuations in the He II Lyman forest

Now we turn to the He II Lyα absorption observed with STIS on HST in the redshift range $2.76 < z < 3.285$ by H00. Figure 4.5 compares the transmission spectra of the He II and H I Lyα absorption towards Q 0302−003 as a function of redshift. The main features are labeled following H00.

There are only three confined regions of significantly non-zero transmission in the He II spectrum. Firstly, the redshift range from $z = 3.22$ up to the emission redshift of Q 0302−003 of $z_{\rm em} = 3.285$ displays strongly enhanced transparency, presumably through a strong line of sight proximity effect created by a Strömgren sphere in an IGM where He II is still not reionized to He III (Hogan et al. 1997, H00). The luminous QSO C is located within the extent of this zone, albeit near its low-redshift end.

Second, there is a prominent transmission feature at $3.043 < z < 3.063$ (‘void A’). H00 speculated that this was likely to be created by a nearby AGN. J03 found the closely coinciding quasar QSO 03020−0014 (QSO A) and argued that this QSO most likely was responsible for the void, although they invoked some modest degree of anisotropic radiation in order to explain an apparent shift between the QSO at $z = 3.050 \pm 0.003$ and their stated peak of void A at $z = 3.056$. From our measurement the peak of void A is at redshift $z = 3.052$ which is perfectly consistent with the QSO being located symmetric to the void.

The third transmission window is a considerably wider region at $z \lesssim 2.87$ (‘region B’). The S/N per pixel in the STIS data is low, but the transmission nearly continuously exceeds the noise. Region B is located at the low-redshift end of the STIS spectrum and the detector sensitivity strongly decreases towards the cutoff at $z \sim 2.76$, but it is likely that we see the onset of a proper He II Lyα forest. This interpretation is supported by the large extent of this region with inherent substructure and a spectral hardening of the radiation field in region B found by H00.

QSO B falls into the redshift range of region B, but that region is much too broad to allow for a close connection between this quasar and the overall enhancement of transparency. However, we notice that while the H I forest near QSO B actually shows significant absorption there is no corresponding depression in the He II forest as would be expected for a roughly constant column density ratio. We tentatively conclude that this

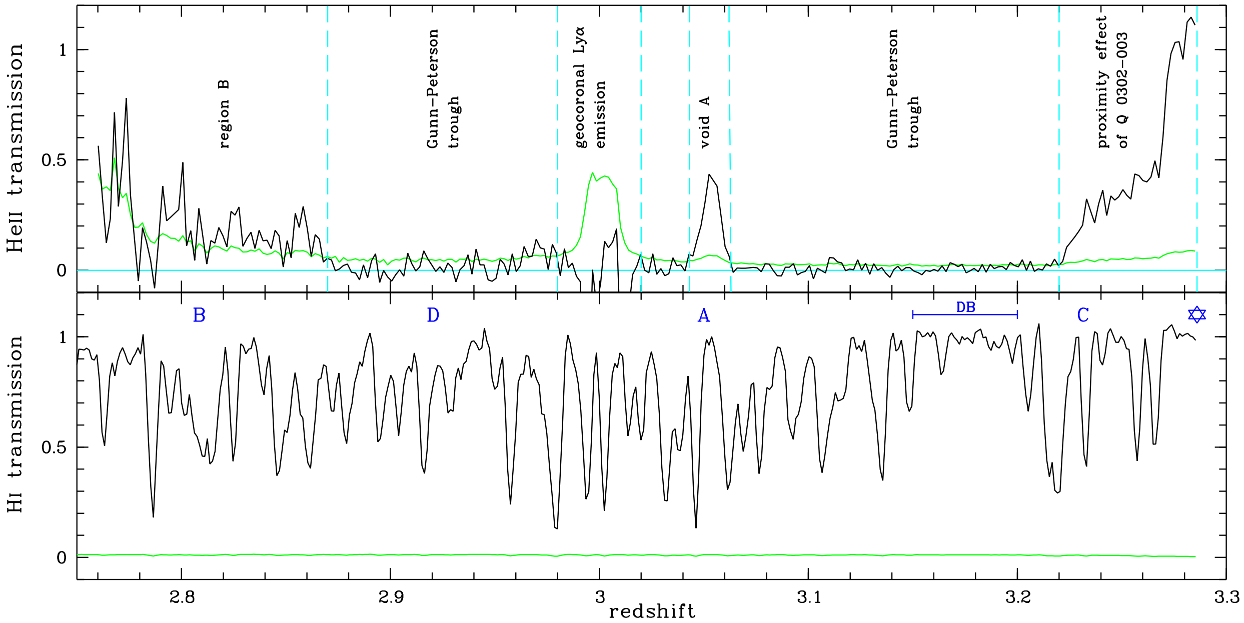

Fig. 4.5. Comparison of the He ii and the H i Lyα absorption spectrum towards Q 0302−003. Upper panel: Transmission in He ii Lyα vs. redshift from the HST/STIS data obtained by H00. The green/gray curve shows the 1σ uncertainty per pixel. The horizontal line denotes the zero flux level. Vertical dashed lines divide the spectrum into several labeled regions of interest (see text). The lower panel displays the corresponding section of our FORS2 H i Lyα transmission spectrum. Quasar and void locations are marked as in Fig. 4.4.

ratio may change significantly near QSO B, possibly indicating the radiative influence of the quasar.

4.5. The spectral hardness of the UV radiation field

4.5.1. Diagnostics

A key parameter to study the radiative influence of a given quasar on the IGM is the relative hardness of the UV radiation ionizing the intergalactic matter. There are several established ways to express this hardness. If the shape of the ionizing continuum is known, the spectral softness parameter is defined as the ratio between the ionization rates of H i and He ii,

$$S = \frac{\Gamma_{\mathrm{H\,I}}}{\Gamma_{\mathrm{He\,II}}} \simeq 4^{\alpha+1} \tag{4.2}$$

with α as the relevant spectral index, $f_\nu \propto \nu^{-\alpha}$. More indirectly, the hardness can be described by the ratio η of the column densities of He ii and H i at given z,

$$\eta = \frac{N_{\mathrm{He\,II}}}{N_{\mathrm{H\,I}}}. \tag{4.3}$$

This quantity is theoretically predicted to be $\lesssim 100$ for a hard ionizing field with mostly quasars acting as ionizing sources, and $\gtrsim 100$ for a soft radiation field that is dominated by galaxies (Haardt & Madau 1996; Fardal et al. 1998); typically, $S \simeq 2.3\eta$ if H i and He ii are highly ionized. Unfortunately it is hard to measure η directly, because of the limited spectral resolution of the FUV spectrographs aboard HST. Only for the two lines of sight towards HE 2347−4342 and HS 1700+6416, FUSE spectra of sufficient resolution have allowed direct measurements of He ii column densities and η (Kriss et al. 2001; Zheng et al. 2004b; Shull et al. 2004; Reimers et al. 2004), revealing fluctuations of η on very small scales of $\Delta z \approx 10^{-3}$, indicating the presence of hard and soft photoionizing sources whose radiation is filtered through the cosmic web.

At lower resolution a technique has been applied that allows one to at least roughly estimate η. Using accurately measured H i column densities from optical spectroscopy, one assumes a value for η, generates the ensuing He ii spectrum, degrades it to the actual resolution of the UV spectrum and compares the simulation with the data (Reimers et al. 1997; Hogan et al. 1997; Anderson et al. 1999; Heap et al. 2000; Smette et al. 2002). These studies showed consistently and in agreement with the higher resolution FUSE results that η significantly fluctuates over the entire redshift range covered by a given line of sight. On this basis H00 predicted that void A in Q 0302−003 had to be created by a QSO because only a small value of $\eta \sim 50$ could reproduce the STIS spectrum in this region, whereas outside of it η was much larger. Subsequently J03 discovered QSO A almost exactly at the predicted redshift.

An alternative to the above procedure is given by evaluating the ratio R of the effective optical depths of He ii and H i,

$$R \equiv \frac{\tau_{\mathrm{eff,He\,II}}}{\tau_{\mathrm{eff,H\,I}}}, \tag{4.4}$$

which has the same overall characteristics as η, but is resolution-independent. High (small) values of R will be obtained if the He ii absorption is high (small) compared to H i, indicating a soft (hard) photoionizing field.

We now want to investigate fluctuations of η in other parts of the Q 0302−003 spectrum, notably in region B. Our approach is therefore reverse to that of H00 and J03, in that we have now specific redshifts given by quasars, and we are interested in the behaviour of η at these redshifts. However, we first need to consider the question of how much these results depend on unresolved weak Lyman forest lines.

4.5.2. Unresolved weak H i forest lines

For given H i column density, the He ii absorption is typically much stronger than the corresponding H i absorption ($\eta \gg 1$).

He II can therefore be traced in absorbers with $\log N_{\mathrm{H\,I}} \lesssim 12$, where the more diffuse component of the IGM sets in – effectively a shallow Gunn-Peterson trough (e.g. Songaila et al. 1995; Fardal et al. 1998). This IGM component is very hard to account for in the H I forest because its detection relies on small shallow excursions of the data from the assumed quasar continuum that can easily get lost in the fitting process. Almost every quasar continuum in high-resolution data is defined locally, so one typically does not account for this low-density IGM component. This poses a fundamental problem when trying to estimate the spectral hardness of the UV radiation field by comparing the absorption in H I and He II. The derived values for η and R will be systematically overestimated when the true H I absorption is underestimated.

The best approach to account for the additional undetected H I absorption is by resolving the He II absorption into discrete lines and using the He II forest to predict the low end of the H I column density distribution (Kriss et al. 2001; Zheng et al. 2004b). This option is available only for two quasar lines of sight with FUSE data.

Other possibilities are to use analytic approximations to calculate the mean Lyα forest absorption arising from these lines (Møller & Jakobsen 1990; Zuo 1993; Madau 1995) or to simulate their impact with empirically established distribution laws. Noting that the line lists of Hu et al. (1995) and Kim et al. (2002) become grossly incomplete below $\log N_{\mathrm{H\,I}} \simeq 12$, we estimated the contribution of $9 \leq \log N_{\mathrm{H\,I}} \leq 12$ systems to the total absorption. This yields a lower limit on τ_{GP} from completely undetected absorption lines. We assumed a power law-shape column density distribution function with slope $\beta = 1.5$ and used the empirical redshift distribution parameterization from Kim et al. (2002). From both simulation and analytic approximation we obtained an effective optical depth of $\tau_{\mathrm{eff}} \simeq 0.02$ for this column density range.

A suitable correction has to be higher than this lower limit due to the partial incompleteness of the line lists at $\log N_{\mathrm{H\,I}} \lesssim 13$. H00 generated weak forest lines with $9 \leq \log N_{\mathrm{H\,I}} \leq 13$ by extrapolating the distribution functions from Kim et al. (1997), resulting in an estimate of $\tau_{\mathrm{GP}} \simeq 0.06$. Our best-guess value is somewhat lower than this; based on exploring various parameterizations of the distribution functions for the range $12 \leq \log N_{\mathrm{H\,I}} \leq 13$, we adopted an overall $\tau_{\mathrm{GP}} \simeq 0.04$.

We applied this correction over the whole redshift range of interest by multipying our FORS2 transmission spectrum by a factor $\langle T_{\mathrm{H\,I,GP}}\rangle = 0.96$. The main source of uncertainty of both used approaches lies certainly in the extrapolation of the column density distribution to below the validated range. However, this is not a major problem for our study because we are primarily interested in spatial fluctuations of R and η rather than absolute values.

The additional absorption in He II Lyα that arises from the cloud population not observed in H I can be easily calculated. These absorbers are optically thin both in H I and He II, so that

$$\langle T_{\mathrm{He\,II,GP}}\rangle = \langle T_{\mathrm{H\,I,GP}}\rangle^{\eta/4}\,. \tag{4.5}$$

Applying the H I transmission correction factor gives a global He II transmission correction as a function of η. Simulated He II spectra created from incomplete H I line lists have to be multiplied by $\langle T_{\mathrm{He\,II,GP}}\rangle$. Since the depth of the shallow H I Gunn-Peterson trough is not exactly known, a degeneracy in the hardness parameter η arises due to the strong dependence of the η value fitting the data on the assumed $\langle T_{\mathrm{H\,I,GP}}\rangle$. From Fig. 4.6 we find that all simulated He II spectra except those with very low ($\eta \simeq 1$) or very high assumed η depend strongly on the value of $\langle T_{\mathrm{H\,I,GP}}\rangle$. Any study based on low-resolution He II spectra will therefore be plagued by the ambiguity that different η values will fit the data, depending on the adopted correction for low-column density material. The best-fitting η will overestimate (underestimate) the true value if $\langle T_{\mathrm{H\,I,GP}}\rangle$ is set too high (low). As a consequence of this degeneracy, the spectral hardness values derived from low-resolution He II data have an uncertain absolute scale. However, any indications for fluctuations in the fitting η values along the line of sight due to a changing hardness of the ionizing field will remain valid, unless the shallow Gunn-Peterson trough correction itself fluctuates with a similar rate.

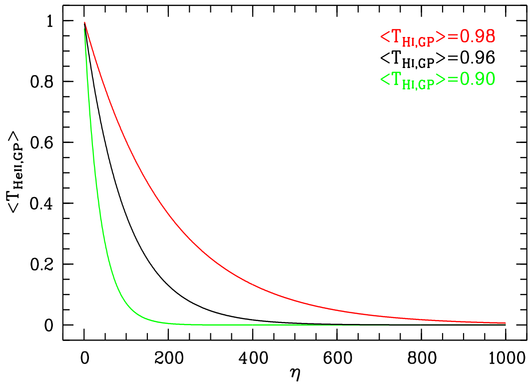

Fig. 4.6. $\langle T_{\mathrm{He\,II,GP}}\rangle$ vs. η for different $\langle T_{\mathrm{H\,I,GP}}\rangle$. In the range of physical η values, the He II transmission correction is strongly dependent on $\langle T_{\mathrm{H\,I,GP}}\rangle$.

4.5.3. The fluctuating optical depth ratio

In order to apply the above defined hardness indicator R, we binned the STIS spectrum and the FORS2 spectrum of Q 0302−003 into aligned redshift bins of common size. For the STIS spectrum we adopted the wavelength resolution of $\Delta\lambda \simeq 1.8$ Å as estimated by H00 and binned both transmission spectra into $\Delta z = 0.006$ bins starting at $z = 2.76$ up to the emission redshift of Q 0302−003 at $z = 3.285$. This rebinning implies that one has to deal with original flux bins that only partly overlap with the new bins. We adopted the method from Telfer et al. (2002), who weighted each original flux by the extent of the overlap with the new bin. The errors were computed accordingly.

The optical depth ratio $R = \ln\langle T_{\mathrm{He\,II}}\rangle / \ln\langle T_{\mathrm{H\,I}}\rangle$ would obtain unphysical values if $\langle T\rangle \leq 0$ or $\langle T\rangle \geq 1$. In our case only the He II spectrum is affected. Two $\langle T_{\mathrm{He\,II}}\rangle \geq 1$ bins near Q 0302−003 are contaminated by its blue He II emission line wing. Due to their location in the proximity effect zone, we estimate $\langle T_{\mathrm{He\,II}}\rangle \gtrsim 0.9$, corresponding to upper limits on R. Values with $\langle T_{\mathrm{He\,II}}\rangle \leq 0$ have been replaced by their errors, yielding upper limits on $\langle T_{\mathrm{He\,II}}\rangle$ and lower limits on R. The region $2.98 < z < 3.02$ is excluded because of the contamination from the geocoronal Lyα emission line in the STIS spectrum. Error bars for R were computed by propagating the transmission errors.

The result for all created redshift bins is shown in Fig. 4.7. One clearly sees a large variation in R, ranging from values of a few to $\gtrsim 50$, indicating substantial spectral fluctuations in the UV radiation field. Most interestingly, R reaches a local minimum near every quasar along the line of sight, as expected for

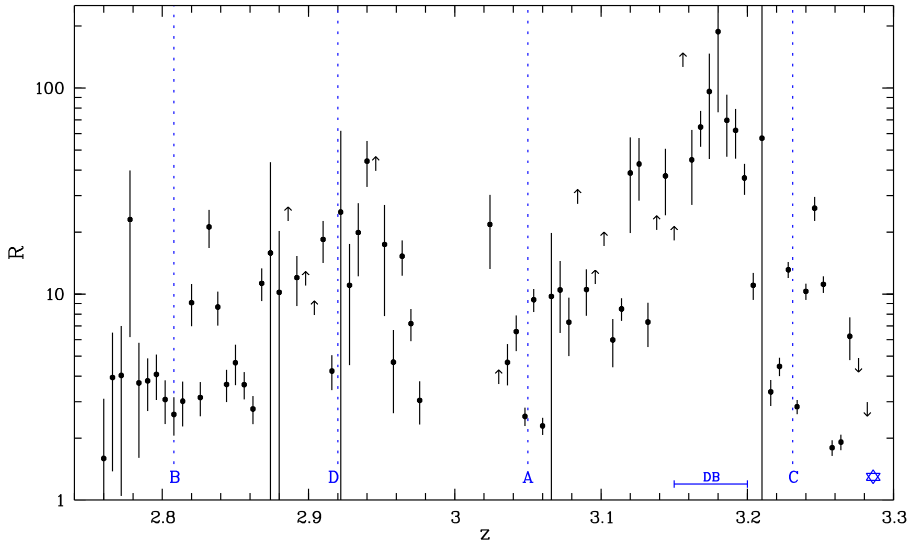

Fig. 4.7. Ratio of effective optical depths R vs. redshift z. Arrows indicate upper and lower limits. Quasar and void locations are marked as in Fig. 4.4. Note that R reaches small values near every quasar along the line of sight. There is a distinctive local minimum in R at the redshift of QSO B.

hard UV sources. Specifically, $R \simeq 3$ near all known quasars in the field except maybe QSO D, for which we have only a single bin at $z = 2.916$ with a small value of $R \simeq 4$. Notice that $R \simeq 3$ also close to Q 0302−003 itself, and again so at the redshift of QSO C.

In order to estimate the statistical significance to find a local $R \lesssim 3$ minimum near the foreground quasars we performed Monte Carlo simulations. By randomly distributing quasars over the considered redshift range we estimate from 10000 simulations a probability of $\sim 9.3\%$ that a single quasar falls into a redshift bin that corresponds to a local R minimum at $\log(R) < 0.5$. Since three foreground quasars (QSO A, B and C) fall in such a minimum, the probability to find this constellation by chance is $< 0.1\%$.

Figure 4.7 shows also that the radiation field in the Dobrzycki & Bechtold (1991a) H I void appears to be very soft, as already observed by H00. The errors are substantial, however, because throughout the void there is still a Gunn-Peterson trough seen in He II, with only very weak absorption in H I. There is a clear trend of higher R values when approaching the approximate center of the void at $z \simeq 3.175$, reaching up to $R \sim 200$.

Finally we note that in Fig. 4.7 there are three narrow redshift regions at $z = 2.778$, $z = 2.832$ and $z = 2.940$ where the local radiation field seems to be quite soft with $R \gtrsim 20$. From Fig. 4.5 we see that these high R values correspond to small H I voids. Such a correlation has been observed already in the high-resolution studies with FUSE towards HE 2347−4342 (Kriss et al. 2001; Shull et al. 2004) and may indicate the contribution of star-forming galaxies to the UV background or quasar radiation that has been filtered and softened by radiative transfer through the cosmic web. The HST data for Q 0302−003 are insufficient to assess this in any detail.

4.5.4. The fluctuating column density ratio

We now turn to the more indirect approach of estimating η through comparing the predicted with the observed He II absorption. We used the H I line lists of Hu et al. (1995) and Kim et al. (2002), which jointly cover the redshift range accessible with STIS in He II Lyα. The Hu et al. (1995) list covers the range $2.627 \leq z \leq 3.110$, where the QSOs B, D, and A are located, whereas the list from Kim et al. (2002) extends between $2.957 \leq z \leq 3.235$, including QSOs A and C, the H I void by Dobrzycki & Bechtold (1991a). Only a small part of the line of sight proximity effect zone of Q 0302−003 itself is covered.

We simulated the Voigt profiles of the He II Lyα transition by assuming pure non-thermal broadening of the lines ($b_{\mathrm{He\,II}} = b_{\mathrm{H\,I}}$) and a constant value for η along the line of sight that was used to convert the observed $N_{\mathrm{H\,I}}$ into $N_{\mathrm{He\,II}}$. Non-thermal broadening found in simulations can be either due to turbulent motions of the gas or the differential Hubble flow, with the latter being dominant for the low-column density forest (Zhang et al. 1995, 1998; Hernquist et al. 1996; Weinberg et al. 1997; Bryan et al. 1999). Additionally Zheng et al. (2004b) presented observational evidence for $b_{\mathrm{He\,II}} \simeq b_{\mathrm{H\,I}}$. We then applied the He II transmission correction factor for undetected material in H I $\langle T_{\mathrm{He\,II,GP}} \rangle \simeq 0.96^{\eta/4}$. We performed the simulations for a range of η values from 15 to 3000. Finally, we degraded the resolution of the He II transmission spectrum to the actual STIS resolution by convolving it with a Gaussian line spread function of 1.8 Å FWHM and rebinning the spectrum to the STIS pixel size of 0.6 Å.

The results for four representative values of η are shown in Fig. 4.8 as the difference between the observed and the simulated spectrum, where positive (negative) deviations from zero indicate that η has to be smaller (higher) than the assumed η of the curve. One can clearly see that different values of η match to different redshift regions, so the hardness of the ionizing radiation field has to fluctuate along the line of sight. Remarkably, the spectral regions around most of the quasars are best reproduced by low η values, which are typical of quasars (Haardt & Madau 1996; Fardal et al. 1998).

The onset of the line-of-sight proximity effect region of Q 0302−003 is reproduced with $\eta \sim 50$. H00 analyzed the proximity effect zone of Q 0302−003 in detail and found that η strongly decreases when approaching Q 0302−003. Thus, in the proximity effect zone of Q 0302−003 hard radiation is present that is softened with increasing distance to the quasar.

In the nearby H I void found by Dobrzycki & Bechtold (1991a), a physical underdensity or a very soft radiation field with $\eta \gtrsim 350$ is required, as already noted by H00. Such high η values are inconsistent with quasars as main ionizing sources. Furthermore, neither the survey by J03 nor our survey did reveal previously unknown quasars close to the void. As discussed in Sect. 4.3 above, QSO C is presumably not capable of creat-

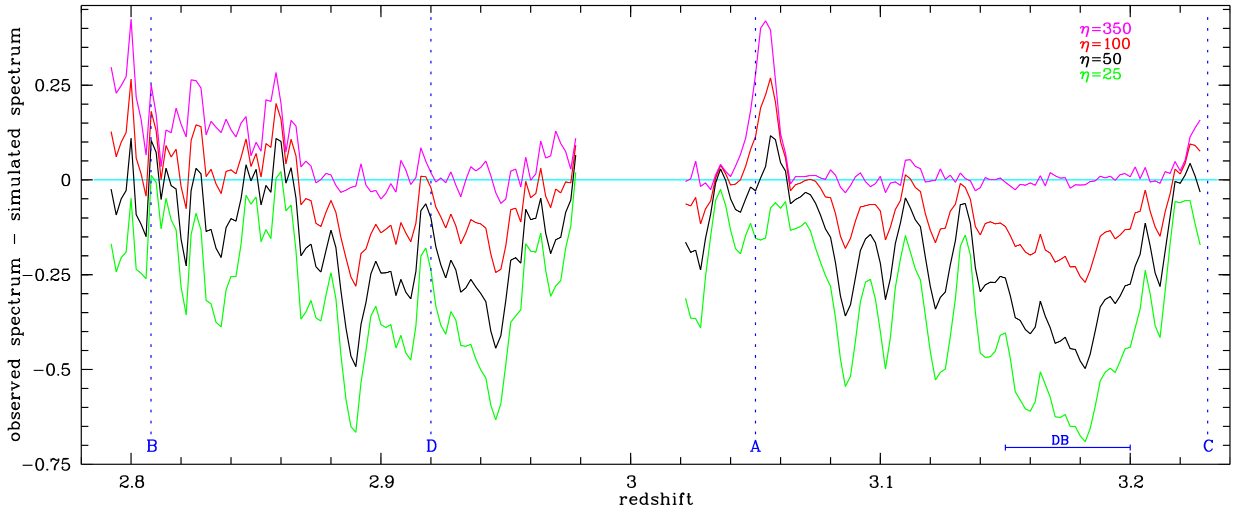

Fig. 4.8. Observed vs. predicted He ii Lyα absorption, in differential representation (observed minus predicted). Different values for η were used for the simulations (see text). The part of the spectrum with $z \leq 2.98$ was simulated using the H i line list by Hu et al. (1995), whereas the H i line list by Kim et al. (2002) was used at $z \geq 3.02$. The spectral region contaminated by geocoronal Lyα emission is not shown. Quasar and void locations are marked as in Fig. 4.4. Positive (negative) deviations from zero indicate that η has to be smaller (higher) than the assumed η of the curve.

ing the void. There is also no large overdensity of LBGs observed in the redshift range of the void that might photoionize the H i (Adelberger et al. 2003). Most likely, this void is a large-scale structure feature and not one created by local photoionizing sources.

J03 associated QSO A with void A mainly by showing that such an association has a very small probability of chance occurrence, and that the luminosity of QSO A is high enough to account for the void. Figure 4.8 shows clearly that most parts of void A can be fitted with $25 \lesssim \eta \lesssim 50$, which clearly favours a transverse proximity effect from a quasar.

Region B is quite crowded, and in Fig. 4.9 we present an enlarged view of Fig. 4.8 for this redshift range. The best-fit value of η fluctuates between $\eta \sim 100$ and ~ 25 on scales comparable to the spectral resolution of the STIS data. This overall hardening of the metagalactic UV radiation field compared to the soft radiation field in the Gunn-Peterson trough can probably be attributed to the progressing He ii reionization and the onset of a proper He ii Lyman forest (Zheng et al. 2004b).

Notably, $\eta \simeq 25$ is reached only in two points, one of which precisely concides with the redshift where our newly discovered QSO B is located. This match is very unlikely to be a chance occurence; it is much more plausible to assume that hard radiation from QSO B intercepts the line of sight towards Q 0302−003 at this point.

Steidel et al. (2003) found two LBGs at angular distances of $\vartheta = 3\overset{\prime}{.}04$ and $\vartheta = 4\overset{\prime}{.}33$ from Q 0302−003 near the redshift of QSO B, at $z = 2.805$ and $z = 2.811$ (also indicated in Fig. 4.9). While the H i Lyman continuum escape fraction of LBGs is still debated (Steidel et al. 2001; Giallongo et al. 2002; Fernández-Soto et al. 2003; Shapley et al. 2003), the number of He ii ionizing photons produced is at most a few per cent of the number of photons exceeding the H i Lyman edge according to current evolutionary synthesis models of starburst galaxies (Leitherer et al. 1999; Smith et al. 2002; Schaerer 2003). We therefore rule out the possibility that these two LBGs supply the hard photons required for the inferred η minimum.

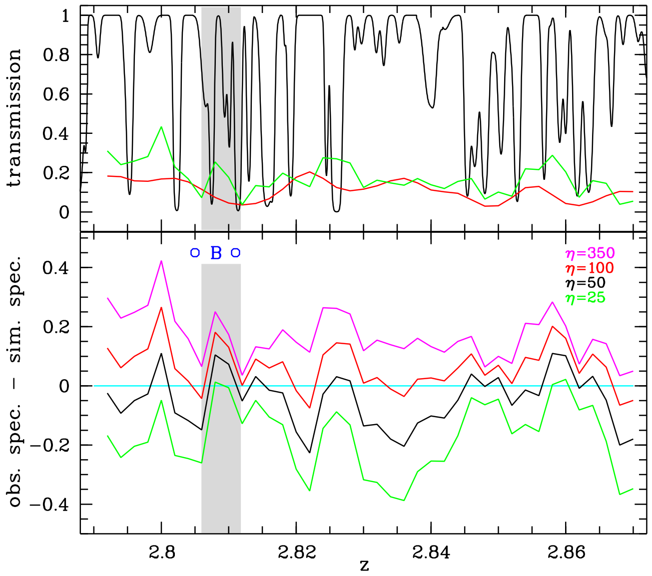

Fig. 4.9. Close-up of region B ($z < 2.87$). The upper panel shows the H i forest spectrum of Q 0302−003 reconstructed from the line list by Hu et al. (1995) (black), the He ii transmission (green/light gray) and the simulated STIS spectrum for $\eta = 100$ (red/dark gray). The lower panel shows the fluctuating spectral hardness in this region (close-up of Fig. 4.8). The letter marks the foreground quasar QSO 03027−0010 (QSO B) at $z = 2.808$. Circles indicate the two nearby LBGs found by Steidel et al. (2003). In the gray-shaded redshift range $2.806 \leq z \leq 2.812$, η =25–50 provides the best fit.

The situation is less clear for the weak QSO D also discovered by Steidel et al. (2003). At the redshift of this QSO, the overall appearance of the He ii forest is that of a completely opaque Gunn-Peterson trough, probably reflecting a still partly neutral He ii component of the IGM. This region is well described with $\eta \sim 350$ (Fig. 4.8). However, we see also that Fig. 4.8 suggests a drop down to $\eta \sim 100$ again at exactly the redshift of a QSO near the line of sight. This corresponds to a small spike of excess flux in the Gunn-Peterson trough (see Fig. 4.5) which is formally still consistent with the noise level. While we therefore cannot really claim to have detected another case of the transverse proximity effect, we cannot exclude it either, and the coincidence is certainly suggestive.

4.6. Discussion

Within the redshift range covered by the STIS data on the He II forest of Q 0302−003, five QSOs are known in or along the line of sight. Only one of these, the central quasar Q 0302−003 itself, shows unambiguous evidence for a proximity effect in H I. There is a possible small void near QSO A, but this could just as well be due to the overall distribution of H I material along the line of sight. At the redshifts of all three other QSOs, the transmission of the H I Lyman forest in the line of sight towards Q 0302−003 seems to be rather below average. Our estimated UV luminosities of these QSOs confirm that a classical transverse proximity effect is not really expected.

Considering the STIS UV spectra of the He II Lyman forest region instead, this picture does not change dramatically. Only in one case, at the redshift of QSO A, we see a clear 'He II void', which in fact led to the discovery of the QSO (H00, J03). For QSO B and maybe also for QSO D we find nonzero He II transmissions, but these certainly do not qualify as voids in their own right. A similar case holds for QSO C (see Fig. 4.5), where however a confusion with the line of sight proximity effect zone of Q 0302−003 complicates the situation.

Only by combining H I and He II transmission properties, the radiative imprints of the QSOs along the line of sight become clearly separated from large scale fluctuations of the distribution of matter. This is particularly prominent for region B and QSO B, where the H I forest of Q 0302−003 shows in fact a complex of enhanced H I absorption, possibly even associated with the QSO in form of a large scale structure filament (Fig. 4.9). Eleven absorbers with $\log N_{\mathrm{H\,I}} > 13$ reside in the redshift range $2.80 < z < 2.82$, four of them between the projected positions of the LBGs at $z = 2.805$ and $z = 2.811$. Assuming an average spectral hardness in this redshift regime ($\eta \sim 100$), one expects strong corresponding He II absorption arising from these absorbers even at the low resolution of STIS (Fig. 4.9). Instead, we see that the He II forest remains transparent at this redshift, however with nothing that could be interpreted as a 'void'. Both spectral hardness estimators R and the best-fit η, on the other hand, show a clearly pronounced extremum at precisely the correct redshift, in excellent agreement with the easier to interpret cases of QSO A and Q 0302−003. Thus, the most likely reasons for the different appearance of the He II transmission portions near QSO A (He II void) and QSO B (no void) in spite of a similar inferred hardness are different intrinsic densities of the overionized regions (small H I void vs. filament) combined with the progressing He II reionization with lower fluctuations of the He II transmission and the spectral hardness at lower redshift. The same effect, though much less significant, can be seen for QSO D.

Even for QSO C there might be a similar imprint onto the Q 0302−003 line of sight. Given the UV luminosity of Q 0302−003, the He III zone in the line of sight is surprisingly large, especially if the He II abundance in the surrounding IGM was still high. A possible additional contributor of hard ionizing photons could be the very luminous QSO C, intercepting the low-z end of the proximity effect region of Q 0302−003. Figures 4.7 and 4.8 provide evidence for a very hard radiation field at just the redshift of QSO C which then, towards Q 0302−003, becomes somewhat softer again before finally hardening in the inner proximity effect zone. We suggest that the He II void at $z > 3.22$ is really generated by the combined actions of a transverse proximity effect of QSO C and a line of sight effect of Q 0302−003.

We conclude that there is strong evidence for a *transverse proximity effect in spectral hardness* occuring in several incidences along the line of sight towards Q 0302−003. While individual η fluctuations might still be regarded as coincidental, and possibly due to the crude diagnostics used, local minima of R and η are in fact found at exactly the redshifts of all five relevant QSOs, indicating a UV radiation field significantly enhanced due to a local hard source. Notice that because of the low overall UV background at 4 ryd, the proximity effect zone in spectral hardness is considerably larger than that of the conventional H I proximity effect. For QSO B, it reaches over ~ 5 Mpc, and for the luminous QSO C it may even bridge more than 10 Mpc.

Besides the continuum placement and the background subtraction, the main source of uncertainty in our assessment of R and η is the correction for weak unresolved H I lines, the 'shallow H I Gunn-Peterson trough' created by the quasi-diffuse component in the IGM. Small changes in the adopted correction lead to large changes in the best-fit η, as η is very sensitive to small H I column densities. The same is true for the optical depth ratio R, which is very sensitive at high H I transmission values. This degeneracy affects the inferred R and η values as such, but the observed *fluctuations* and their correlation with the redshifts of known quasars are largely unaffected. Furthermore, the range of our inferred η values ($25 \lesssim \eta \lesssim 350$) is generally believed to be typical for the conditions in the IGM at $z \sim 3$.

A very interesting, though highly speculative observation concerns the relation between the strength of the 'spectral hardness proximity effect' and the UV spectral slope of the QSO in question. QSO A is about 1 mag brighter in V than QSO B, and it is also somewhat closer to the central line of sight. On the other hand, the inferred η is even slightly lower at the redshift of QSO B than in void A. Adopting the continuum slopes given in Table 4.4 and boldly extrapolating towards 4 ryd, we predict values of the spectral softness of $S \simeq 29$ for QSO A and $S \simeq 10$ for QSO B; thus, the latter QSO is expected to be even *brighter* at the He II ionizing limit than the former. The higher η values are therefore inferred near QSO A which has the softer spectrum, whereas lower η values fit the data near QSO B which has the harder spectrum.

4.7. A lower limit on the quasar lifetime

Both incarnations of the proximity effect allow a lower limit on the quasar lifetime t_{q}, since photons from a quasar need a certain time to propagate to the point of their absorption in the IGM. The observation of the line-of-sight proximity effect in the Lyα *forest* yields only lower limits based on the typical equilibrium timescale of Lyα absorbers of $\simeq 10^4$ yr (e.g. Bajtlik et al. 1988), mainly because the line-of-sight proximity effect observed in a line forest is a statistical effect. However, in a mostly neutral medium, there exists the sharp observable boundary that defines the radius of the Strömgren sphere around the quasar. So far, this has been observed in H I Lyα towards SDSS J1030+0524 at $z = 6.28$ (Pentericci et al. 2002) and in He II Lyα towards Q 0302−003 (Hogan et al. 1997) and PKS 1935−692 (Anderson et al. 1999). Simple modelling of the zone inside the Strömgren sphere yields $t_{\mathrm{q}} \gtrsim 13$ Myr (Pentericci et al. 2002) and $t_{\mathrm{q}} \gtrsim 40$ Myr (Hogan et al. 1997).

In the case of the transverse proximity effect one cannot measure the extent of the proximity effect zone, neither in a line forest nor in a Gunn-Peterson trough, since the proximity effect zone is intersected by another line of sight by chance. The

Table 4.5. Minimum lifetimes $\Delta t' = d_\perp/c$ for all foreground quasars of Q 0302−003 with an indication of the transverse proximity effect.

QSO	Abbr.	z	$d_\perp$ [Mpc]	$\Delta t'$ [Myr]
QSO 03027−0010	B	2.808	5.29	17
QSO 0302-D113	D	2.920	2.26	7
QSO 03020−0014	A	3.050	2.97	9
Q 0301−005	C	3.231	10.34	34

emission epoch of the ionizing photons of the source in the direction of the background line of sight cannot be observed, since these photons have to be emitted prior to our observations. So the transverse proper distance $d_\perp$ between the two lines of sight at the emission redshift of the foreground quasar has to serve as an approximation for the expanding distance between the source and the emitted photons. Due to the expansion of the universe between the emission and the absorption of the photons, the inferred light travel time $\Delta t' = d_\perp/c$ is larger than the actual light travel time Δt, but usually the correction for expansion is very small.

We have argued in the previous section that the QSOs A–D show at least an indication for the transverse proximity effect in the line of sight towards Q 0302−003. Assuming a correspondence between the known foreground quasars and He III zones around them having low η, we can infer their minimum total quasar lifetimes listed in Table 4.5. These are all consistent with the estimates based on the proximity effect (Srianand 1997; Hogan et al. 1997; Anderson et al. 1999; Pentericci et al. 2002, J03) and theoretical arguments (Martini 2004 and references therein). Due to the high sensitivity of the spectral hardness we are able to constrain the quasar lifetime for a sample of quasars forming a close group on the sky, yielding minimum quasar lifetimes in the range $\Delta t' \gtrsim 10$–30 Myr.

4.8. Conclusions

The transverse proximity effect in quasar spectra has so far mostly been associated with the notion of voids in the H I Lyman forest, created by the overionized zones around quasars near the line of sight. It has always been clear, however, that true voids due to large scale structure and apparent voids due to the proximity effect would be essentially indistinguishable on an individual basis. This problem holds also for the He II Lyman forest that has now become accessible for a small number of high-redshift QSOs.

We argue in this study that spectral hardness indicators provide an efficient way to discriminate between large scale structure and proximity effect. The line of sight proximity effect towards Q 0302−003 and the transverse proximity effect due to QSO 03020−0014 (dubbed 'QSO A' in this paper) were already discussed by Heap et al. (2000) and Jakobsen et al. (2003) and are, since the discovery of QSO A, clear-cut cases where both the optical depth ratio and the hardness parameter η show pronounced minima close to the quasars. We investigated the H I and He II absorption properties at redshifts near our newly discovered QSO 03027−0010 ('QSO B'), and also near the other known QSOs close to the line of sight. In each single case we find evidence for a link between spectral hardness and the presence of a nearby quasar.

Thus, the relative UV hardness is a sensitive *physical* quantity to search for individual sources of the metagalactic UV radiation field beyond the simple detection of associations between quasars and voids. Quasars and voids may be unrelated, whereas the spectral hardness is related to the spectral energy distributions of the ionizing sources. In particular, a void will not occur if the quasar overionizes an intrinsically overdense region. The spectral hardness may break this density degeneracy that affects studies of the proximity effect (Loeb & Eisenstein 1995; Schirber et al. 2004; Rollinde et al. 2005). At least for QSO B, this case of an overdense region is apparently applicable.

The excellent match between the measured QSO redshifts and the inferred minima of $\eta(z)$ imply that there is essentially no need to invoke strongly anisotropic radiation for any of the quasars in question. This is in stark contrast to the situation for the H I proximity effect where anisotropy or even beaming has repeatedly been claimed (Dobrzycki & Bechtold 1991a; Crotts 1989; Møller & Kjærgaard 1992; Schirber et al. 2004). It is likely that true large scale structure in the Lyman forest has contributed to mask the intrinsic transverse proximity effect in several of these cases.

The redshift range of $2.7 \lesssim z < 3.2$ studied in the line of sight towards Q 0302−003 is of very high interest in the context of studying the putative reionization epoch of He II. We have shown that one can determine the sources that ionize this line of sight, even at low resolution. Near the low-redshift end of the covered spectral range, there are clear indications for a transition from He III bubbles in the IGM towards a more or less fully ionized He III IGM where also the overall UV background is dominated by QSO radiation. Our estimates of η in this redshift range are fully compatible with this concept. Even then, local sources of very hard radiation such as QSO B can significantly modify the UV background over distances of several Mpc. It would be highly desirable to be able to study these processes at higher spectral resolution. Unfortunately, Q 0302−003 is too faint for observations with the *Far Ultraviolet Spectroscopic Explorer*, and the only perspective for significantly improved data lies with the Cosmic Origins Spectrograph to be installed on HST.

Acknowledgements. Based on observations collected at the European Southern Observatory, Chile (Proposals 070.A-0425 and 074.A-0273). Data collected under Proposal 068.A-0194 was obtained from the ESO Science Archive. Based on observations made with the NASA/ESA Hubble Space Telescope, obtained from the data archive at the Space Telescope Institute. STScI is operated by the association of Universities for Research in Astronomy, Inc. under the NASA contract NAS 5-26555.

We thank the staff of the ESO observatories La Silla and Paranal for their professional assistance in obtaining the optical data discussed in this paper. We are grateful to Aldo Dall'Aglio for providing his code to simulate absorption line spectra from a given line list. GW acknowledges support by a HWP grant from the state of Brandenburg, Germany.

Funding for the creation and distribution of the SDSS Archive has been provided by the Alfred P. Sloan Foundation, the Participating Institutions, the National Aeronautics and Space Administration, the National Science Foundation, the U.S. Department of Energy, the Japanese Monbukagakusho, and the Max Planck Society. The SDSS Web site is http://www.sdss.org/. The SDSS is managed by the Astrophysical Research Consortium (ARC) for the Participating Institutions. The Participating Institutions are The University of Chicago, Fermilab, the Institute for Advanced Study, the Japan Participation Group, The Johns Hopkins University, the Korean Scientist Group, Los Alamos National Laboratory, the Max-Planck-Institute for Astronomy (MPIA), the Max-Planck-Institute for Astrophysics (MPA), New Mexico State University, University of Pittsburgh, University of Portsmouth, Princeton University, the United States Naval Observatory, and the University of Washington.

References

Adelberger, K. L., Steidel, C. C., Shapley, A. E., & Pettini, M. 2003, ApJ, 584, 45

Anderson, S. F., Hogan, C. J., Williams, B. F., & Carswell, R. F. 1999, AJ, 117, 56

Bajtlik, S., Duncan, R. C., & Ostriker, J. P. 1988, ApJ, 327, 570
Barbieri, C. & Cristiani, S. 1986, A&AS, 63, 1
Bryan, G. L., Machacek, M., Anninos, P., & Norman, M. L. 1999, ApJ, 517, 13
Croft, R. A. C. 2004, ApJ, 610, 642
Croft, R. A. C., Weinberg, D. H., Pettini, M., Hernquist, L., & Katz, N. 1999, ApJ, 520, 1
Crotts, A. P. S. 1989, ApJ, 336, 550
Crotts, A. P. S. & Fang, Y. 1998, ApJ, 502, 16
Davidsen, A. F., Kriss, G. A., & Zheng, W. 1996, Nat, 380, 47
Dobrzycki, A. & Bechtold, J. 1991a, ApJ, 377, L69
Dobrzycki, A. & Bechtold, J. 1991b, in ASP Conf. Ser. 21: The Space Distribution of Quasars, 272
Fardal, M. A., Giroux, M. L., & Shull, J. M. 1998, AJ, 115, 2206
Fardal, M. A. & Shull, J. M. 1993, ApJ, 415, 524
Fernández-Soto, A., Barcons, X., Carballo, R., & Webb, J. K. 1995, MNRAS, 277, 235
Fernández-Soto, A., Lanzetta, K. M., & Chen, H.-W. 2003, MNRAS, 342, 1215
Gaskell, C. M. 1982, ApJ, 263, 79
Giallongo, E., Cristiani, S., D'Odorico, S., & Fontana, A. 2002, ApJ, 568, L9
Gunn, J. E. & Peterson, B. A. 1965, ApJ, 142, 1633
Haardt, F. & Madau, P. 1996, ApJ, 461, 20
Heap, S. R., Williger, G. M., Smette, A., et al. 2000, ApJ, 534, 69
Hernquist, L., Katz, N., Weinberg, D. H., & Miralda-Escudé, J. 1996, ApJ, 457, L51
Hogan, C. J., Anderson, S. F., & Rugers, M. H. 1997, AJ, 113, 1495
Horne, K. 1986, PASP, 98, 609
Hu, E. M., Kim, T.-S., Cowie, L. L., & Songaila, A. 1995, AJ, 110, 1526
Jakobsen, P., Boksenberg, A., Deharveng, J. M., et al. 1994, Nat, 370, 35
Jakobsen, P., Jansen, R. A., Wagner, S., & Reimers, D. 2003, A&A, 397, 891
Kim, T.-S., Carswell, R. F., Cristiani, S., D'Odorico, S., & Giallongo, E. 2002, MNRAS, 335, 555
Kim, T.-S., Hu, E. M., Cowie, L. L., & Songaila, A. 1997, AJ, 114, 1
Kriss, G. A., Shull, J. M., Oegerle, W., et al. 2001, Sci, 293, 1112
Leitherer, C., Schaerer, D., Goldader, J. D., et al. 1999, ApJS, 123, 3
Liske, J. 2000, MNRAS, 319, 557
Liske, J. & Williger, G. M. 2001, MNRAS, 328, 653
Loeb, A. & Eisenstein, D. J. 1995, ApJ, 448, 17
Madau, P. 1995, ApJ, 441, 18
Martini, P. 2004, in Carnegie Observatories Astrophysics Series Vol. 1: Coevolution of Black Holes and Galaxies, ed. L. C. Ho (Cambridge University Press), 170
McDonald, P., Seljak, U., Cen, R., Bode, P., & Ostriker, J. P. 2005, MNRAS, 360, 1471
McIntosh, D. H., Rix, H.-W., Rieke, M. J., & Foltz, C. B. 1999, ApJ, 517, L73
Meiksin, A. & White, M. 2004, MNRAS, 350, 1107
Møller, P. & Jakobsen, P. 1990, A&A, 228, 299
Møller, P. & Kjærgaard, P. 1992, A&A, 258, 234
Pentericci, L., Fan, X., Rix, H.-W., et al. 2002, AJ, 123, 2151
Reimers, D., Fechner, C., Hagen, H.-J., et al. 2005, A&A, 442, 63
Reimers, D., Fechner, C., Kriss, G., et al. 2004, astro-ph/0410588
Reimers, D., Köhler, S., Wisotzki, L., et al. 1997, A&A, 327, 890
Ricotti, M., Gnedin, N. Y., & Shull, J. M. 2000, ApJ, 534, 41
Rollinde, E., Srianand, R., Theuns, T., Petitjean, P., & Chand, H. 2005, MNRAS, 361, 1015
Sargent, W. L. W., Steidel, C. C., & Boksenberg, A. 1989, ApJS, 69, 703
Schaerer, D. 2003, A&A, 397, 527
Schaye, J., Theuns, T., Rauch, M., Efstathiou, G., & Sargent, W. L. W. 2000, MNRAS, 318, 817
Schirber, M., Miralda-Escudé, J., & McDonald, P. 2004, ApJ, 610, 105
Scott, J., Bechtold, J., Dobrzycki, A., & Kulkarni, V. P. 2000, ApJS, 130, 67
Shapley, A. E., Steidel, C. C., Pettini, M., & Adelberger, K. L. 2003, ApJ, 588, 65
Shull, J. M., Tumlinson, J., Giroux, M. L., Kriss, G. A., & Reimers, D. 2004, ApJ, 600, 570
Smette, A., Heap, S. R., Williger, G. M., et al. 2002, ApJ, 564, 542
Smith, L. J., Norris, R. P. F., & Crowther, P. A. 2002, MNRAS, 337, 1309
Songaila, A., Hu, E. M., & Cowie, L. L. 1995, Nat, 375, 124
Srianand, R. 1997, ApJ, 478, 511
Steidel, C. C., Adelberger, K. L., Shapley, A. E., et al. 2003, ApJ, 592, 728
Steidel, C. C., Pettini, M., & Adelberger, K. L. 2001, ApJ, 546, 665
Telfer, R. C., Zheng, W., Kriss, G. A., & Davidsen, A. F. 2002, ApJ, 565, 773
Theuns, T., Zharoubi, S., Kim, T.-S., Tzanavaris, P., & Carswell, R. F. 2002, MNRAS, 332, 367
Tytler, D. & Fan, X. 1992, ApJS, 79, 1
Véron-Cetty, M.-P. & Véron, P. 2003, A&A, 412, 399
Weinberg, D. H., Hernquist, L., Katz, N., Croft, R., & Miralda-Escudé, J. 1997, in Proceedings of the 13th IAP Astrophysics Colloquium: Structure and Evolution of the Intergalactic Medium from QSO Absorption Line Systems, ed. P. Petitjean & S. Charlot (Paris: Editions Frontières), 133
Wisotzki, L., Selman, F., & Gilliotte, A. 2001, The Messenger, 104, 8
Zhang, Y., Anninos, P., & Norman, M. L. 1995, ApJ, 453, L57
Zhang, Y., Meiksin, A., Anninos, P., & Norman, M. L. 1998, ApJ, 495, 63
Zheng, W., Chiu, K., Anderson, S. F., et al. 2004a, AJ, 127, 656
Zheng, W., Kriss, G. A., Deharveng, J.-M., et al. 2004b, ApJ, 605, 631
Zuo, L. 1992, MNRAS, 258, 36
Zuo, L. 1993, A&A, 278, 343

Chapter 5

The transverse proximity effect in spectral hardness on the line of sight towards HE 2347−4342[⋆]

G. Worseck[1], C. Fechner[2,3], L. Wisotzki[1], and A. Dall'Aglio[1]

[1] Astrophysikalisches Institut Potsdam, An der Sternwarte 16, 14482 Potsdam, Germany
[2] Hamburger Sternwarte, Universität Hamburg, Gojenbergsweg 112, 21029 Hamburg, Germany
[3] Universität Potsdam, Am Neuen Palais 10, 14469 Potsdam, Germany

ABSTRACT

We report the discovery of 14 quasars in the vicinity of HE 2347−4342, one of the two quasars whose intergalactic He ɪɪ forest has been resolved with FUSE. By analysing the H ɪ and the He ɪɪ opacity variations separately, no transverse proximity effect is detected near three foreground quasars of HE 2347−4342: QSO J23503−4328 ($z = 2.282$, $\vartheta = 3\overset{\prime}{.}59$), QSO J23500−4319 ($z = 2.302$, $\vartheta = 8\overset{\prime}{.}77$) and QSO J23495−4338 ($z = 2.690$, $\vartheta = 16\overset{\prime}{.}28$). This is primarily due to line contamination and overdensities probably created by large-scale structure. By comparing the H ɪ absorption and the corresponding He ɪɪ absorption, we estimated the fluctuating spectral shape of the extragalactic UV radiation field along this line of sight. We find that the UV spectral shape near HE 2347−4342 and in the projected vicinity of the three foreground quasars is statistically harder than expected from UV background models dominated by quasars. In addition, we find three highly ionised metal line systems near the quasars. However, they do not yield further constraints on the shape of the ionising field. We conclude that the foreground quasars show a transverse proximity effect that is detectable as a local hardening of the UV radiation field, although the evidence is strongest for QSO J23495−4338. Thus, the relative spectral hardness traces the proximity effect also in overdense regions prohibiting the traditional detection in the H ɪ forest. Furthermore, we emphasise that softening of quasar radiation by radiative transfer in the intergalactic medium is important to understand the observed spectral shape variations. From the transverse proximity effect of QSO J23495−4338 we obtain a lower limit on the quasar lifetime of ~ 25 Myr.

5.1. Introduction

After reionisation the intergalactic medium (IGM) is kept highly photoionised by the metagalactic UV radiation field generated by the overall population of quasars and star-forming galaxies (e.g. Haardt & Madau 1996; Fardal et al. 1998; Bianchi et al. 2001; Sokasian et al. 2003). The intensity and spectral shape of the UV background determines the ionisation state of the observable elements in the IGM. In particular, the remaining fraction of intergalactic neutral hydrogen and singly ionised helium is responsible for the Lyα forest of H ɪ and He ɪɪ.

On lines of sight passing near quasars the IGM will be statistically more ionised due to the local enhancement of the UV flux that should result in a statistically higher IGM transmission ('void') in the QSO's vicinity (Fardal & Shull 1993; Croft 2004; McDonald et al. 2005). This so-called proximity effect has been found with high statistical significance on lines of sight towards luminous quasars (e.g. Bajtlik et al. 1988; Giallongo et al. 1996; Scott et al. 2000). On the other hand, a transverse proximity effect created by foreground ionising sources nearby the line of sight has not been clearly detected in the H ɪ forest, except the recent detection at $z = 5.70$ by Gallerani et al. (2007). While two large H ɪ voids have been claimed to be due to the transverse proximity effect by Dobrzycki & Bechtold (1991a, however see Dobrzycki & Bechtold 1991b) and Srianand (1997), other studies find at best marginal evidence (Fernández-Soto et al. 1995; Liske & Williger 2001), and most attempts resulted in non-detections (Crotts 1989; Møller & Kjærgaard 1992; Crotts & Fang 1998; Schirber et al. 2004; Croft 2004). This has led to explanations involving the systematic effects of anisotropic radiation, quasar variability (Schirber et al. 2004), intrinsic overdensities (Loeb & Eisenstein 1995; Rollinde et al. 2005; Hennawi & Prochaska 2007; Guimarães et al. 2007) and finite quasar lifetimes (Croft 2004).

Intergalactic He ɪɪ Lyα absorption ($\lambda_{\mathrm{rest}} = 303.7822$ Å) can be studied only towards the few quasars at $z > 2$ whose far UV flux is not extinguished by intervening Lyman limit systems (Picard & Jakobsen 1993; Jakobsen 1998). Of the six quasars successfully observed so far, the lines of sight towards HE 2347−4342 ($z = 2.885$) and HS 1700+6416 ($z = 2.736$) probe the post-reionisation era of He ɪɪ with an emerging He ɪɪ forest that has been resolved with FUSE (Kriss et al. 2001; Shull et al. 2004; Zheng et al. 2004; Fechner et al. 2006; Fechner & Reimers 2007a).

In a highly ionised IGM a comparison of the H ɪ with the corresponding He ɪɪ absorption yields an estimate of the spectral shape of the UV radiation field due to the different ionisation thresholds of both species. The amount of He ɪɪ compared to H ɪ gives a measure of the spectral softness, generally expressed via the column density ratio $\eta = N_{\mathrm{He\,II}}/N_{\mathrm{H\,I}}$. Typically, $\eta \lesssim 100$ indicates a hard radiation field generated by the surrounding quasar population, whereas $\eta \gtrsim 100$ requires a significant contribution of star-forming galaxies or heavily softened quasar radiation (e.g. Haardt & Madau 1996; Fardal et al. 1998; Haardt & Madau 2001).

[⋆] This chapter is published in *Astronomy & Astrophysics*, 2007, 473, 805.

The recent FUSE observations of the He II Lyα forest revealed large η fluctuations ($1 \lesssim \eta \lesssim 1000$) on small scales of $0.001 \lesssim \Delta z \lesssim 0.03$ with a median $\eta \simeq 80$–100. Apart from scatter due to the low-quality He II data at $S/N \sim 5$ (Fechner et al. 2006; Liu et al. 2006) and possible systematic errors due to the generally assumed line broadening mechanism (Fechner & Reimers 2007a), several physical reasons for these η variations have been proposed. A combination of local density variations (Miralda-Escudé et al. 2000), radiative transfer effects (Maselli & Ferrara 2005; Tittley & Meiksin 2006) and local differences in the properties of quasars may be responsible for the fluctuations. In particular, at any given point in the IGM at $z > 2$ only a few quasars with a range of spectral indices (Telfer et al. 2002; Scott et al. 2004) contribute to the UV background at $h\nu \geq 54.4$ eV (Bolton et al. 2006).

Already low-resolution He II spectra obtained with HST indicate a fluctuating radiation field, which has been interpreted as the onset of He II reionisation in Strömgren spheres around hard He II photoionising sources along or near the line of sight (Reimers et al. 1997; Heap et al. 2000; Smette et al. 2002). Jakobsen et al. (2003) found a quasar coinciding with the prominent He II void at $z = 3.05$ towards Q 0302−003, thereby presenting the first clear case of a transverse proximity effect. In Worseck & Wisotzki (2006), hereafter Paper I, we revealed the transverse proximity effect as a systematic increase in spectral hardness around all four known foreground quasars along this line of sight. This suggests that a hard radiation field is a sensitive probe of the transverse proximity effect even if there is no associated void in the H I forest, either because of the weakness of the effect, or because of large-scale structure.

Along the line of sight towards HE 2347−4342 several He II voids have been claimed to be due to nearby unknown AGN (Smette et al. 2002). Likewise, some forest regions with a detected hard radiation field may correspond to proximity effect zones of putative foreground quasars (Fechner & Reimers 2007a). Here we report on results from a slitless spectroscopic quasar survey in the vicinity of HE 2347−4342 and on spectral shape fluctuations of the UV radiation field probably caused by foreground quasars towards the sightline of HE 2347−4342. The paper is structured as follows. Sect. 5.2 presents the observations and the supplementary data employed for the paper. Although we do not detect any transverse proximity effect in the H I forest (Sect. 5.3), the fluctuating UV spectral shape along the line of sight indicates a hard radiation field in the projected vicinity of the foreground quasars (Sect. 5.4). In Sect. 5.5 we study three nearby metal line systems which could further constrain the ionising field. We interpret the statistically significant excesses of hard radiation as being due to the transverse proximity effect (Sect. 5.6). We present our conclusions in Sect. 5.7. Throughout the paper we adopt a flat cosmological model with $\Omega_{\mathrm{m}} = 0.3$, $\Omega_\Lambda = 0.7$ and $H_0 = 70\,\mathrm{km\,s^{-1}\,Mpc^{-1}}$.

5.2. Observations and data reduction

5.2.1. Search for QSO candidates near HE 2347−4342

In October 2002 we observed a $25' \times 33'$ field centred on HE 2347−4342 ($z = 2.885$) with the ESO Wide Field Imager (WFI, Baade et al. 1999) at the ESO/MPI 2.2 m Telescope (La Silla) in its slitless spectroscopic mode (Wisotzki et al. 2001) as part of a survey for faint quasars in the vicinity of established high-redshift quasars. A short summary of the survey is given in Paper I; a detailed description will follow in a separate paper.

A semi-automated search for emission line objects among the slitless spectra of the ∼ 1400 detected objects in the field resulted in 10 prime quasar candidates.

5.2.2. Spectroscopic follow-up

Follow-up spectroscopy of these 10 quasar candidates was obtained with the Focal Reducer/Low Dispersion Spectrograph 2 (FORS2, Appenzeller et al. 1998) on ESO VLT UT1/Antu in Visitor Mode on November 17 and 19, 2004 under variable seeing but clear conditions. The spectra were taken either with the 300V grism or the 600B grism and a $1''$ slit kept at the parallactic angle, resulting in a spectral resolution of ∼ 10 Å *FWHM* and ∼ 4.5 Å *FWHM*, respectively. No order separation filter was employed, leading to possible order overlap at $\lambda > 6600$ Å in the spectra taken with the 300V grism. Exposure times were adjusted to yield $S/N \sim 20$ in the quasar continuum. The spectra were calibrated in wavelength against the FORS2 He/Ne/Ar/HgCd arc lamps and spectrophotometrically calibrated against the HST standard stars Feige 110 and GD 108. Data reduction was performed with standard IRAF tasks using the optimal extraction algorithm by Horne (1986). Figure 5.1 shows the spectra of the quasars together with 4 quasars from another survey (Sect. 5.2.3). Table 5.1 summarises our spectroscopic follow-up observations.

5.2.3. Additional quasars

We checked the ESO Science Archive for additional quasars in the vicinity of HE 2347−4342 and found several unpublished quasars from a deeper slitless spectroscopic survey using the ESO VLT, the results of which (on the field of Q 0302−003) are described in Jakobsen et al. (2003). We obtained their follow-up spectra of quasars surrounding HE 2347−4342 from the archive and publish them here in agreement with P. Jakobsen. In the course of their survey FORS1 spectra of 10 candidates were taken with the 300V grism crossed with the GG435 order separation filter and a $1''$ slit, calibrated against the standards LTT 7987 and GD 50. Seven of their candidates are actually quasars, of which 3 were also found independently by our survey. The remaining 4 quasars are beyond our redshift-dependent magnitude limit. The FORS1 spectra of the 4 additional quasars are displayed in Fig. 5.1 and listed separately in Table 5.1. According to the quasar catalogue by Véron-Cetty & Véron (2006) there are no other previously known quasars within a radius $< 30'$ around HE 2347−4342.

5.2.4. Redshifts and magnitudes

Redshifts of the 14 quasars were determined by taking every detectable emission line into account. Line peaks were measured by eye and errors were estimated taking into account the S/N of the lines, line asymmetries and the presence of absorption systems. The quasar redshifts were derived by weighting the measurements of detected lines. Since high-ionisation lines suffer from systematic blueshifts with respect to the systemic redshift (Gaskell 1982; Tytler & Fan 1992; McIntosh et al. 1999), a higher weight was given to low-ionisation lines. Obviously blueshifted lines were discarded. Redshift errors were estimated from the redshift differences of the remaining lines and their estimated errors.

The 14 discovered quasars lie in the broad redshift range $0.720 \leq z \leq 3.542$. Fig. 5.2 shows their angular separations with

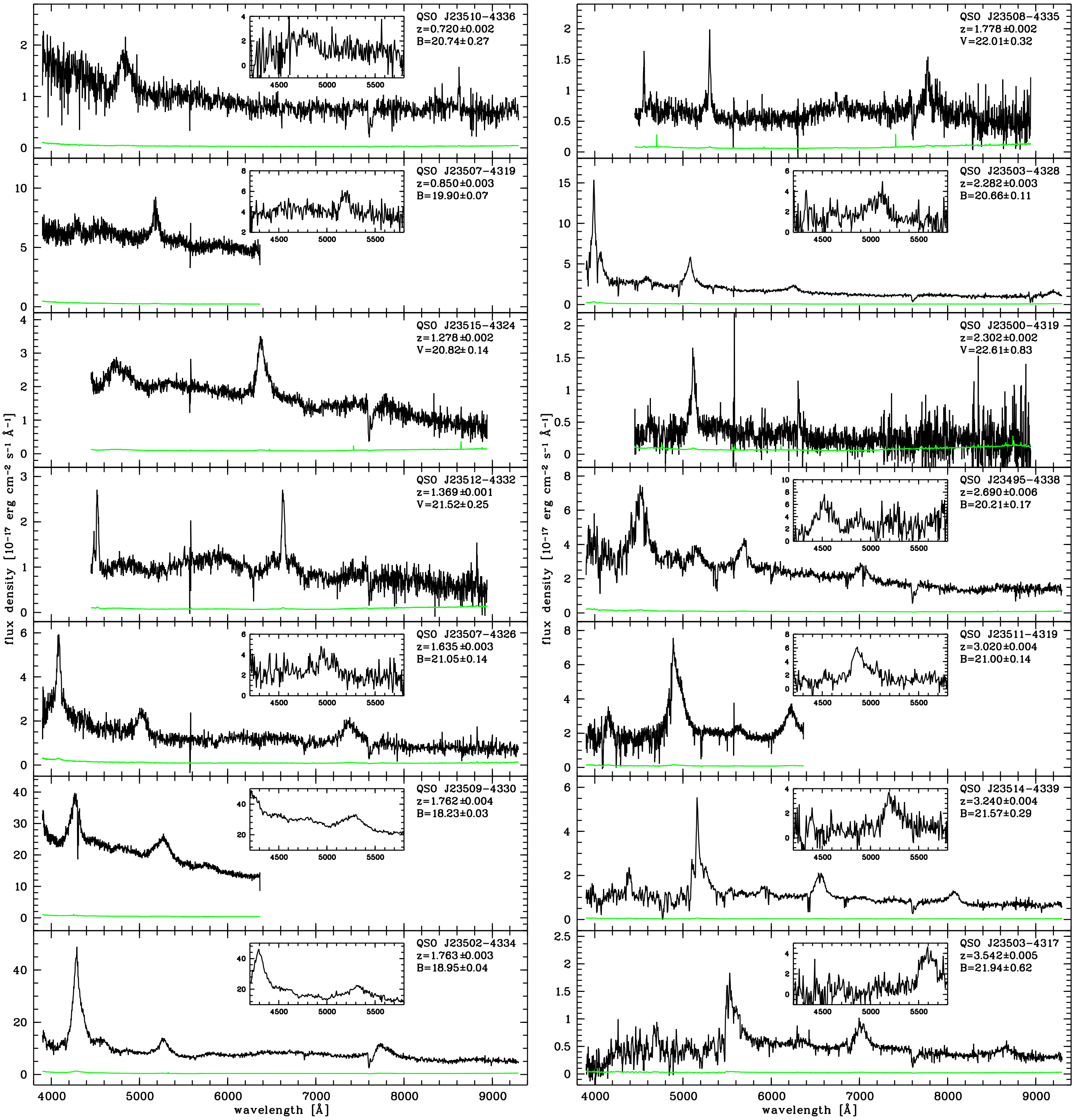

Fig. 5.1. VLT/FORS spectra of quasars in the vicinity of HE 2347−4342. The spectra are shown in black together with their 1σ noise arrays (green/grey lines). The small inserts show the corresponding discovery spectra from our slitless survey in the same units.

respect to HE 2347−4342. We find three background quasars to HE 2347−4342 and we identify a pair of bright quasars at $z \simeq 1.763$ separated by 7ꞌ.8. Three foreground quasars (labelled A–C in Table 5.1 and Fig. 5.2) are located in the redshift range to study the transverse proximity effect. Table 5.2 provides the redshift measurements for the detected emission lines in their spectra. The redshift of QSO J23503−4328 was based on Lyα and C iv. The measurement of the Mg ii is uncertain because of the decline of the resolving power of the 300V grism towards the red, but yields a slightly higher redshift than the adopted one. For QSO J23500−4319 we measured a consistent redshift from the C iv and the C iii] line. The redshift measurement of QSO J23495−4338 was difficult due to several metal absorption line systems of which only two Mg ii systems at $z = 0.921$ and $z = 1.518$ could be identified. In particular, Fe ii absorption from the $z = 0.912$ system hampered a redshift measurement of the Lyα line. The C iv and the C iii] lines show unidentified absorption features. Thus, the redshift of QSO J23495−4338 is heavily weighted towards the very noisy low-ionisation lines O i+Si ii and C ii. However, redshift uncertainties of the foreground quasars do not significantly affect our results.

Table 5.1. Quasars observed near the line of sight of HE 2347−4342. The first 10 listed quasars have been found in our survey, the remaining 4 quasars result from the previously unpublished survey by P. Jakobsen. Quasar magnitudes are B and V magnitudes for our survey and Jakobsen's survey, respectively.

Object	α (J2000)	δ (J2000)	z	Magnitude	Night	Grism	Exposure	Airmass	Seeing	Abbr.
QSO J23510−4336	$23^{\rm h}51^{\rm m}05\overset{\rm s}{.}50$	$-43^{\circ}36'57\overset{''}{.}2$	0.720 ± 0.002	20.74 ± 0.27	19 Nov 2004	300V	1200 s	1.30	$1\overset{''}{.}3$	
QSO J23507−4319	$23^{\rm h}50^{\rm m}44\overset{\rm s}{.}97$	$-43^{\circ}19'26\overset{''}{.}0$	0.850 ± 0.003	19.90 ± 0.07	17 Nov 2004	600B	360 s	1.28	$0\overset{''}{.}7$	
QSO J23507−4326	$23^{\rm h}50^{\rm m}45\overset{\rm s}{.}39$	$-43^{\circ}26'37\overset{''}{.}0$	1.635 ± 0.003	21.05 ± 0.14	17 Nov 2004	300V	200 s	1.23	$1\overset{''}{.}0$	
QSO J23509−4330	$23^{\rm h}50^{\rm m}54\overset{\rm s}{.}80$	$-43^{\circ}30'42\overset{''}{.}2$	1.762 ± 0.004	18.23 ± 0.03	17 Nov 2004	600B	300 s	1.08	$0\overset{''}{.}7$	
QSO J23502−4334	$23^{\rm h}50^{\rm m}16\overset{\rm s}{.}18$	$-43^{\circ}34'14\overset{''}{.}7$	1.763 ± 0.003	18.95 ± 0.04	17 Nov 2004	300V	60 s	1.18	$0\overset{''}{.}7$	
QSO J23503−4328	$23^{\rm h}50^{\rm m}21\overset{\rm s}{.}55$	$-43^{\circ}28'43\overset{''}{.}7$	2.282 ± 0.003	20.66 ± 0.11	17 Nov 2004	300V	400 s	1.20	$0\overset{''}{.}7$	A
QSO J23495−4338	$23^{\rm h}49^{\rm m}34\overset{\rm s}{.}53$	$-43^{\circ}38'08\overset{''}{.}7$	2.690 ± 0.006	20.21 ± 0.17	19 Nov 2004	300V	360 s	1.13	$1\overset{''}{.}2$	C
QSO J23511−4319	$23^{\rm h}51^{\rm m}09\overset{\rm s}{.}44$	$-43^{\circ}19'41\overset{''}{.}6$	3.020 ± 0.004	21.00 ± 0.14	17 Nov 2004	600B	1000 s	1.09	$1\overset{''}{.}1$	
QSO J23514−4339	$23^{\rm h}51^{\rm m}25\overset{\rm s}{.}54$	$-43^{\circ}39'02\overset{''}{.}9$	3.240 ± 0.004	21.57 ± 0.29	17 Nov 2004	300V	1400 s	1.14	$1\overset{''}{.}2$	
QSO J23503−4317	$23^{\rm h}50^{\rm m}21\overset{\rm s}{.}94$	$-43^{\circ}17'30\overset{''}{.}0$	3.542 ± 0.005	21.94 ± 0.62	19 Nov 2004	300V	1800 s	1.23	$1\overset{''}{.}2$	
						600B	1800 s	1.33	$1\overset{''}{.}2$	
QSO J23515−4324	$23^{\rm h}51^{\rm m}33\overset{\rm s}{.}05$	$-43^{\circ}24'45\overset{''}{.}2$	1.278 ± 0.002	20.82 ± 0.14	06 Oct 2002	300V	900 s	1.24	$0\overset{''}{.}7$	
QSO J23512−4332	$23^{\rm h}51^{\rm m}15\overset{\rm s}{.}18$	$-43^{\circ}32'34\overset{''}{.}3$	1.369 ± 0.001	21.52 ± 0.25	06 Oct 2002	300V	900 s	1.18	$0\overset{''}{.}7$	
QSO J23508−4335	$23^{\rm h}50^{\rm m}52\overset{\rm s}{.}91$	$-43^{\circ}35'06\overset{''}{.}8$	1.778 ± 0.002	22.01 ± 0.32	06 Oct 2002	300V	900 s	1.11	$0\overset{''}{.}9$	
QSO J23500−4319	$23^{\rm h}50^{\rm m}00\overset{\rm s}{.}28$	$-43^{\circ}19'46\overset{''}{.}1$	2.302 ± 0.002	22.61 ± 0.83	06 Oct 2002	300V	900 s	2.37	$0\overset{''}{.}8$	B

Table 5.2. Detected emission lines and redshifts of QSOs A–C.

Object	Emission line	$\lambda_{\rm obs}$ [Å]	z
QSO J23503−4328	Lyα	3989 ± 4	2.281 ± 0.003
	N V	4070 ± 8	2.282 ± 0.006
	Si IV+O IV]	4585 ± 8	2.276 ± 0.006
	C IV	5082 ± 4	2.281 ± 0.003
	C III]	6253 ± 7	2.276 ± 0.004
	Mg II	9196 ± 12	2.286 ± 0.004
			2.282 ± 0.003
QSO J23500−4319	Si IV+O IV]	4613 ± 6	2.296 ± 0.004
	C IV	5115 ± 3	2.302 ± 0.002
	C III]	6305 ± 2	2.303 ± 0.001
			2.302 ± 0.002
QSO J23495−4338	Lyα	4513 ± 10	2.712 ± 0.008
	O I+Si II	4823 ± 10	2.694 ± 0.008
	C II	4930 ± 10	2.692 ± 0.007
	Si IV+O IV]	5135 ± 15	2.669 ± 0.011
	C IV	5691 ± 10	2.674 ± 0.006
	C III]	7028 ± 10	2.682 ± 0.005
			2.690 ± 0.006

Apparent magnitudes were derived from target aquisition images photometrically calibrated against the standard star fields PG 2213−006 or Mark A (Landolt 1992). Unfortunately the aquisition exposures of the faintest quasars were too short to determine their magnitudes accurately. Magnitudes derived from integration of the spectra are consistent with the photometric ones after correcting for slit losses.

We note that QSO J23507−4326 is variable. This quasar has been detected in both slitless surveys and had $V \simeq 20.3$ in October 2001, $V \simeq 20.7$ in October 2002 and $V \simeq 21.0$ in November 2004. We were able to discover this quasar in its bright phase while missing the slightly fainter quasar QSO J23515−4324 detected only in the survey by P. Jakobsen.

5.2.5. Optical spectra of HE 2347−4342

From the ESO Science Archive we retrieved the optical spectra of HE 2347−4342 taken with UVES at VLT UT2/Kueyen in the Large Programme "The Cosmic Evolution of the Intergalactic Medium" (Bergeron et al. 2004). Data reduction was performed using the UVES pipeline provided by ESO (Ballester et al. 2000). The vacuum-barycentric corrected co-added spectra yield a $S/N \sim 100$ in the Lyα forest at $R \sim 45000$. The spectrum was normalised in the covered wavelength range $3000 \lesssim \lambda \lesssim 10000$ Å using a cubic spline interpolation algorithm.

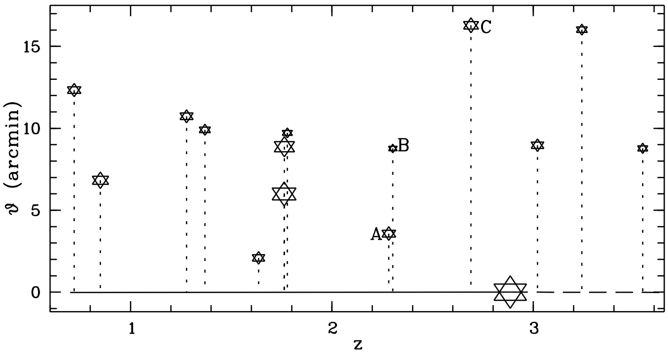

Fig. 5.2. Distribution of separation angles ϑ vs. redshift z of the quasars from Table 5.1 with respect to HE 2347−4342. Symbol size indicates apparent optical magnitude.

5.2.6. Far-UV spectra of HE 2347−4342

HE 2347−4342 is one of the two high-redshift quasars observed successfully in the He II Lyα forest below 303.7822 Å rest frame wavelength with the Far Ultraviolet Spectroscopic Explorer (FUSE) at a resolution of $R \sim 20000$, although at a $S/N \lesssim 5$ (Kriss et al. 2001; Zheng et al. 2004). G. Kriss and W. Zheng kindly provided the reduced FUSE spectrum of HE 2347−4342 described in Zheng et al. (2004). We adopted their flux normalisation with a power law $f_\lambda = 3.3 \times 10^{-15} \left(\lambda/1000\text{Å}\right)^{-2.4}$ erg cm^{-2} s^{-1} Å^{-1} reddened by the Cardelli et al. (1989) extinction curve assuming $E(B-V) = 0.014$ (Schlegel et al. 1998).

5.3. The Lyα forest near the foreground quasars

Aiming to detect the transverse proximity effect as an underdensity ('void') in the Lyα forest towards HE 2347−4342 we examined the forest regions in the projected vicinity of the three foreground quasars labelled A–C in Table 5.1. The H I forest of HE 2347−4342 has been analysed in several studies, e.g. by Zheng et al. (2004) and Fechner & Reimers (2007a), hereafter called Z04 and FR07, respectively. Since the line list from FR07 is limited to $z > 2.29$, T.-S. Kim (priv. comm.) kindly provided

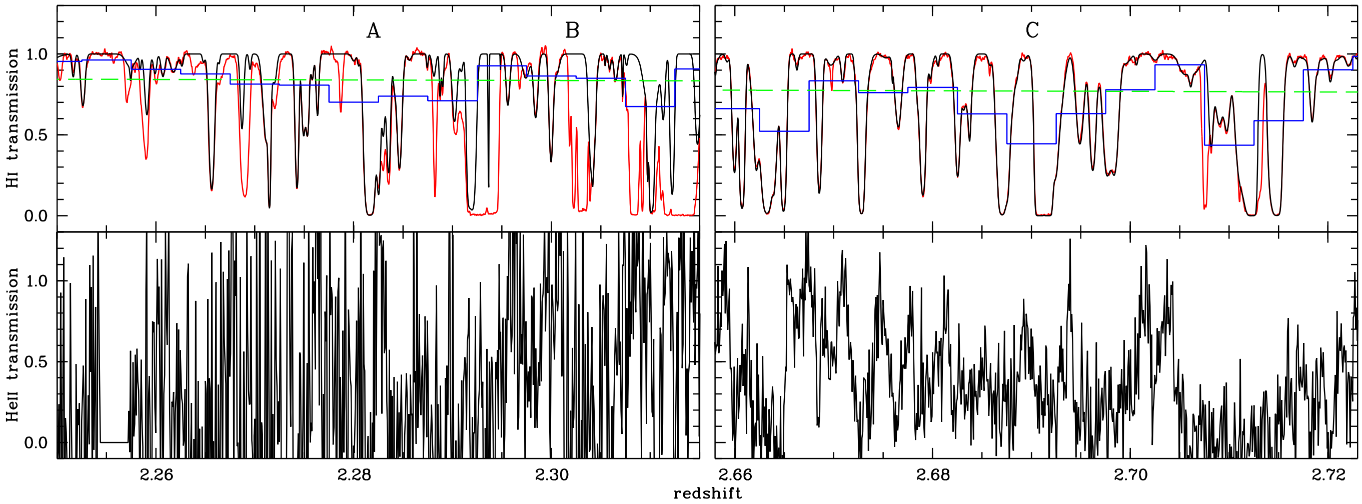

Fig. 5.3. The Lyα forest of HE 2347−4342 in the vicinity of the foreground quasars A–C from Table 5.1. The upper panels show the normalised optical spectrum of HE 2347−4342 including Lyβ and metal lines (red/grey) and the H I Lyα transmission obtained from the line list by T.-S. Kim (black). The binned line shows the mean H I Lyα transmission in $\Delta z = 0.005$ bins towards HE 2347−4342, whereas the dashed green/grey line indicates the expected mean transmission $\langle T\rangle^{\rm exp}$. The lower panels display the corresponding He II transmission from the FUSE spectrum.

an independent line list including the lower redshift Lyα forest ($z > 1.79$). Both line lists agree very well in their overlapping redshift range $2.29 < z < 2.89$.

Figure 5.3 displays the H I and the He II forest regions near the foreground quasars A–C. The H I Lyα forest is contaminated by metals. In particular at $z < 2.332$ there is severe contamination due to the O VI absorption of the associated system of HE 2347−4342 (Fechner et al. 2004). Because the strong O VI absorption overlaps with the projected positions of QSO A and QSO B it is very difficult to obtain a well-determined H I line sample in this region. Furthermore, there is Lyβ absorption of H I and He II at $z < 2.294$. We also overplot in Fig. 5.3 the mean H I Lyα transmission in $\Delta z = 0.005$ bins obtained from T.-S. Kim's line list and the generally expected mean transmission over several lines of sight $\langle T\rangle^{\rm exp} = {\rm e}^{-\tau_{\rm eff}^{\rm exp}}$ with $\tau_{\rm eff}^{\rm exp} = 0.0032\,(1+z)^{3.37}$ (Kim et al. 2002).

We do not detect a significant void near the three foreground quasars, neither in the H I forest nor in the He II forest. In the vicinity of QSO A and QSO B, even a careful decontamination of the optical spectrum does not reveal a significant H I underdensity. Instead, the transmission is fluctuating around the mean. Due to the poor quality of the FUSE data in this region ($S/N \lesssim 2$) and the He II Lyβ absorption from higher redshifts, a simple search for He II voids near QSO A and QSO B is impossible. In the vicinity of QSO C the H I Lyα absorption is slightly higher than on average. There is a small void at $z \simeq 2.702$ that can be identified in the forests of both species. The probability of chance occurrence of such small underdensities is high, so linking this void to QSO C seems unjustified. However, note that the He II absorption in the vicinity of QSO C ($z \sim 2.69$) is lower than at $z \sim 2.71$ in spite of the same H I absorption. This points to fluctuations in the spectral shape of the ionising radiation near the quasar (Sect. 5.4.3).

Given the luminosities and distances of our foreground quasars to the sightline of HE 2347−4342, could we expect to detect the transverse proximity effect as voids in the H I forest? As in Paper I, we modelled the impact of the foreground quasars on the line of sight towards HE 2347−4342 with the parameter

$$\omega(z) = \sum_{j=1}^{n} \frac{f_{\nu_{\rm LL},j}}{4\pi J_\nu(z)} \frac{\left(1+z'_j\right)^{-\alpha_j+1}}{\left(1+z_j\right)} \left(\frac{\alpha_{J_\nu}+3}{\alpha_j+3}\right)\left(\frac{d_L\left(z_j,0\right)}{d_L\left(z_j,z\right)}\right)^2 \qquad (5.1)$$

which is the ratio between the summed photoionisation rates of n quasars at redshifts z_j with rest frame Lyman limit fluxes $f_{\nu_{\rm LL},j}$, penetrating the absorber at redshift z and the overall UV background with Lyman limit intensity J_ν. $d_L(z_j,0)$ is the luminosity distance of QSO j, and $d_L(z_j,z)$ is its luminosity distance as seen at the absorber; the redshift of the quasar as seen at the absorber is z'_j (Liske 2000). A value $\omega \gg 1$ predicts a highly significant proximity effect.

We assumed a constant UV background at 1 ryd of $J_\nu = 7\times10^{-22}\,{\rm erg\,cm^{-2}\,s^{-1}\,Hz^{-1}\,sr^{-1}}$ (Scott et al. 2000) with a power-law shape $J_\nu \propto \nu^{-\alpha_{J_\nu}}$ and $\alpha_{J_\nu} = 1.8$. The quasar Lyman limit fluxes were estimated from the spectra by fitting a power law $f_\nu \propto \nu^{-\alpha}$ to the quasar continuum redward of the Lyα emission line, excluding the emission lines. The spectra were scaled to yield the measured photometric magnitudes. Table 5.3 lists the resulting spectral indices, the H I Lyman limit fluxes, and the transverse distances.

The combined effects of QSOs A and B result in a peak $\omega_{\rm max} \simeq 0.89$, while QSO C yields $\omega_{\rm max} \simeq 0.11$. So we expect only a weak signature of the transverse proximity effect that can be easily diluted by small-scale transmission fluctuations around $\langle T\rangle^{\rm exp}$. Thus, the apparent lack of a transverse proximity effect in the H I forest is no surprise.

We can also roughly estimate the amplitude of the proximity effect in the He II forest. Extrapolating the power laws (QSOs and background) above 4 ryd at $\eta = 50$ (Haardt & Madau 1996, hereafter HM96) we get $\omega_{\rm max} \simeq 20$ near QSO A and $\omega_{\rm max} \simeq 2$ near QSO C. A softer background would result in higher values of ω, whereas absorption of ionising photons in the He II forest would decrease ω. However, due to the arising He II Lyβ forest and the low S/N in the FUSE data near QSOs A and B, even high ω values do not necessarily result in a visible He II void. In the direct vicinity of QSO C the He II data is not saturated, but shows no clear void structure either. We will show in the following sections that the spectral shape of the radiation field

Table 5.3. Rest frame Lyman limit fluxes of foreground QSOs. A power law $f_\nu \propto \nu^{-\alpha}$ is fitted to the QSO continua and $f_{\nu_{\mathrm{LL}}}$ is the extrapolated H I Lyman limit flux in the QSO rest frame. $d_\perp(z)$ denotes the transverse proper distance to the line of sight towards HE 2347−4342.

QSO	Abbr.	z	α	$f_{\nu_{\mathrm{LL}}}$ [μJy]	$d_\perp(z)$ [Mpc]
QSO J23503−4328	A	2.282	0.21	16	1.76
QSO J23500−4319	B	2.302	0.84	1	4.33
QSO J23495−4338	C	2.690	0.24	29	7.75

is a more sensitive indicator of the transverse proximity effect than the detection of voids in the forests.

5.4. The fluctuating shape of the UV radiation field towards HE 2347−4342

5.4.1. Diagnostics

If both hydrogen and helium are highly ionised in the IGM with roughly primordial abundances, the column density ratio $\eta = N_{\mathrm{He\,II}}/N_{\mathrm{H\,I}}$ indicates the softness of the UV radiation field impinging on the absorbers. Theoretically, η can be derived numerically via photoionisation models of the IGM with an adopted population of ionising sources. At the redshifts of interest, $50 \lesssim \eta \lesssim 100$ is predicted for a UV background generated by quasars (HM96; Fardal et al. 1998), whereas higher values indicate a contribution of star-forming galaxies (e.g. Haardt & Madau 2001, hereafter HM01).

The He II forest has been resolved with FUSE towards HE 2347−4342 and HS 1700+6416, allowing a direct estimation of η by fitting the absorption lines (Kriss et al. 2001; Zheng et al. 2004; Fechner et al. 2006, FR07). Due to the low S/N and the strong line blending in the He II forest the He II lines have to be fitted with absorber redshifts and Doppler parameters fixed from the fitting of the H I data of much higher quality. Generally, pure non-thermal line broadening ($b_{\mathrm{He\,II}} = b_{\mathrm{H\,I}}$) is assumed (however, see FR07 and Sect. 5.6 below). The He II forest towards HE 2347−4342 was fitted independently by Z04 and FR07. In the following, we rely on the line fitting results from FR07, which at any rate are consistent with those obtained by Z04 in the redshift ranges near the quasars.

All current studies indicate that η is strongly fluctuating on very small scales in the range $1 \lesssim \eta \lesssim 1000$. The median column density ratio towards HE 2347−4342 is $\eta \simeq 62$ (Z04), whereas Fechner et al. (2006) find a higher value of $\eta \simeq 85$ towards HS 1700+6416. Both studies find evidence for an evolution of η towards smaller values at lower redshifts. However, only part of the scatter in η is due to redshift evolution and statistical errors, so the spectral shape of the UV radiation field has to fluctuate (FR07). Although the analyses of both available lines of sight give consistent results, cosmic variance may bias the derived median η and its evolution. This is of particular interest for our study, since we want to reveal local excesses of low η near the quasars with respect to the median (Sect. 5.4.3). Clearly, more lines of sight with He II absorption would be required to yield tighter constraints on the redshift evolution of η.

The detailed results of visual line fitting may be subjective and may depend on the used fitting software. In particular, ambiguities in the decomposition of blended H I lines can affect the derived η values (Fechner & Reimers 2007b). Therefore we also analyse the UV spectral shape variations using the ratio of the effective optical depths

$$R = \frac{\tau_{\mathrm{eff,He\,II}}}{\tau_{\mathrm{eff,H\,I}}}. \tag{5.2}$$

As introduced in Paper I, this parameter is a resolution-independent estimator of the spectral shape of the UV radiation field with small (high) R values indicating hard (soft) radiation on a certain redshift scale Δz. Shull et al. (2004) followed a similar approach by taking $\eta \simeq 4\tau_{\mathrm{He\,II}}/\tau_{\mathrm{H\,I}}$ for a restricted τ range on scales of $\Delta z = 1.6 \times 10^{-4}$ and $\Delta z = 6.6 \times 10^{-4}$. However, this scaling relation between τ and η is only valid at the centre of an absorption line (Miralda-Escudé 1993). The column density ratio is defined per absorption line and not as a continuous quantity, whereas R can be defined on any scale. While R and η are correlated (see below), there is no simple conversion between R and η and the correlation will depend on the adopted redshift scale of R.

5.4.2. Fluctuations in R and η along the line of sight

We obtained $R(z)$ by binning both normalised Lyα forest spectra of H I and He II into aligned redshift bins of $\Delta z = 0.005$ in the range $2.3325 < z < 2.8975$ and computed $R = \ln\langle T_{\mathrm{He\,II}}\rangle / \ln\langle T_{\mathrm{H\,I}}\rangle$ with the mean transmission $\langle T_{\mathrm{He\,II}}\rangle$ and $\langle T_{\mathrm{H\,I}}\rangle$. The choice of the redshift binning scale was motivated by the typical scale of η fluctuations $0.001 \lesssim \Delta z \lesssim 0.03$ (Kriss et al. 2001, FR07). We adopted the binning procedure by Telfer et al. (2002) in order to deal with original flux bins that only partly overlap with the new bins. The errors were computed accordingly. Due to the high absorption and the low S/N of the He II data we occasionally encountered unphysical values $\langle T_{\mathrm{He\,II}}\rangle \leq 0$. These were replaced by their errors, yielding lower limits on R. We mostly neglected the usually small metal contamination in the computation of $\langle T_{\mathrm{H\,I}}\rangle$ in the Lyα forest because the errors in R are dominated by the low S/N and the more uncertain continuum level of the He II spectrum. The FUSE data in the redshift bins at $z = 2.375$, 2.380, 2.730, 2.735, 2.845 and 2.850 are contaminated by galactic H_2 absorption, so no R measurement on the full scale of $\Delta z = 0.005$ can be performed there.

At $2.29 \lesssim z_{\mathrm{Ly}\alpha} \lesssim 2.33$ the H I Lyα forest is severely contaminated by O VI from the associated system of HE 2347−4342 (Fechner et al. 2004). Furthermore, the Lyβ forest of both species emerges at $z_{\mathrm{Ly}\alpha} < 2.294$. Because this excess absorption would bias the direct estimation of R in the spectra, we tried to decontaminate the forests at $z < 2.332$. $\langle T_{\mathrm{H\,I}}\rangle$ was computed from the H I Lyα forest reconstructed from the line list by T.-S. Kim (Sect. 5.3). The corresponding $\langle T_{\mathrm{He\,II}}\rangle$ was obtained after dividing the FUSE data by the simulated Lyβ absorption of the lines at higher redshift. Since the decontamination depends on the validity of the He II line parameters as well as on the completeness of the H I line list in the complex region contaminated by O VI, the derived R values at $z < 2.332$ have to be regarded as rough estimates.

The resulting $R(z)$ is shown in the upper panel of Fig. 5.4. The optical depth ratio strongly fluctuates around its median value $R \simeq 4.8$ obtained for uncontaminated redshift bins, indicating spectral fluctuations in the UV radiation field. We also show in Fig. 5.4 the median $\eta(z)$ on the same redshift bins based on the line fitting results in FR07. Also the median η strongly fluctuates with a slight trend of an increase with redshift (Z04). Clearly, the data is inconsistent with a spatially uniform UV background, but the median $\eta \simeq 70$ of the line sample is consistent with quasar-dominated models of the UV background. A comparison of $R(z)$ and $\eta(z)$ reveals that both quantities are

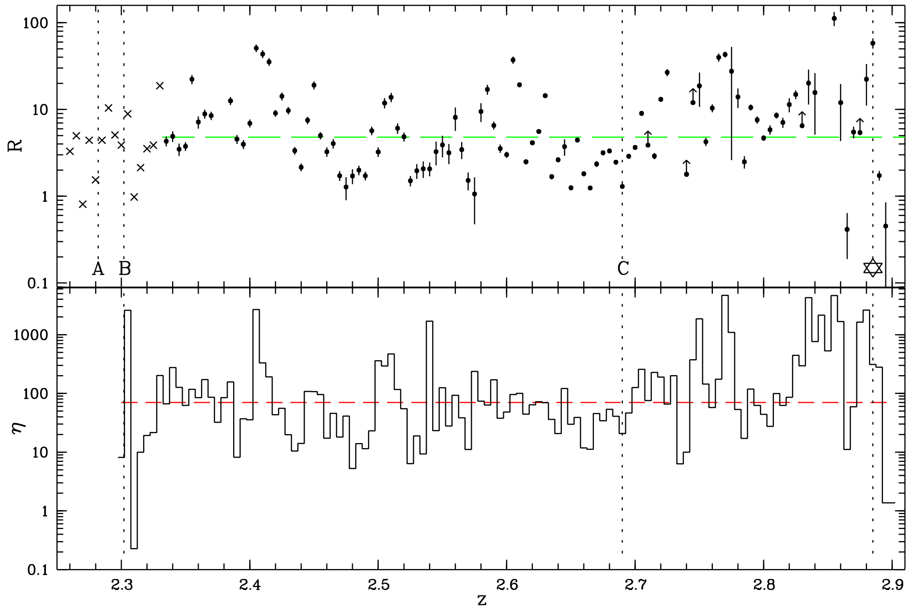

Fig. 5.4. The fluctuating spectral shape of the UV background towards HE 2347−4342. The upper panel shows the ratio of effective optical depths R vs. redshift z in $\Delta z = 0.005$ bins. Data points at $z < 2.332$ (crosses) have been decontaminated from O VI and Lyβ absorption (see text). Foreground quasars are marked with letters and vertical dotted lines as well as HE 2347−4342 (star symbol). The dashed line indicates the median $R \simeq 4.8$ obtained at $z > 2.332$ in uncontaminated bins. The lower panel shows the median η from FR07 in the same redshift bins. The dashed line indicates the median $\eta \simeq 70$ of the line sample.

correlated. The Spearman rank order correlation coefficient is $r_S = 0.67$ with a probability of no correlation $P_S = 6 \times 10^{-15}$.

There is a scatter in the relation between R and η, which is due to noise in the He II data and due to the fact that R is a spectral softness indicator that is smoothed in redshift. Therefore, in addition to the UV spectral shape, R will depend on the density fluctuations of the Lyα forest on the adopted scale. In order to estimate the scatter in R due to these density fluctuations, we simulated H I and He II Lyα forest spectra. We generated 100 H I forests with the same overall redshift evolution of $\tau^{\rm exp}_{\rm eff,H\,I} = 0.0032\,(1+z)^{3.37}$ (Kim et al. 2002) based on the empirical line distribution functions in redshift z, column density $N_{\rm H\,I}$ and Doppler parameter $b_{\rm H\,I}$ (e.g. Kim et al. 2001). We modelled each forest as a composition of lines with Voigt profiles using the approximation by Tepper-García (2006). The spectral resolution ($R \sim 42000$) and quality ($S/N \sim 100$) closely matches the optical data of HE 2347−4342. The corresponding He II forests were generated at FUSE resolution with a $S/N = 4$ for four constant values of $\eta = 10$, 20, 50 and 100. We assumed pure non-thermal broadening of the lines. Then we computed R at $2 \le z \le 3$ on our adopted scale $\Delta z = 0.005$, yielding 20000 R measurements for each considered η. For convenience we took out the general redshift dependence of $\tau_{\rm eff,H\,I}$ via dividing by the expected effective optical depth $\tau^{\rm exp}_{\rm eff,H\,I}$, so

$$D = \frac{\tau_{\rm eff,H\,I}}{\tau^{\rm exp}_{\rm eff,H\,I}} \qquad (5.3)$$

is a measure of H I overdensity ($D > 1$) or underdensity ($D < 1$).

In Fig. 5.5 we show the relation $R(D)$ obtained from the Monte Carlo simulations and compare it to the distribution observed towards HE 2347−4342. The simulated $R(D)$ can be fitted reasonably with a 3rd order polynomial in logarithmic space, yielding a general decrease of R with D for every η. The root-mean-square scatter increases from 0.13 dex for $\eta = 10$ to 0.18 dex for $\eta = 100$. At $D \gtrsim 3$ the $R(D)$ distribution flattens due to saturation of high-column density absorbers on the flat part of the curve of growth. The flattening causes substantial overlap between the simulated R distributions at $D \gtrsim 5$, making R increasingly insensitive to the underlying η. However, at $D \lesssim 3$ hard radiation and soft radiation can be reasonably well distinguished. We also overplot the measured $R(D)$ towards HE 2347−4342 in Fig. 5.5. The observed distribution is inconsistent with a constant η, but the majority of values falls into the modelled η range. While many high R values indicate $\eta > 100$, values with $R \lesssim 2$ correspond to $\eta \lesssim 20$ at $D \lesssim 3$. Thus, the very low R values always indicate a hard radiation field up to moderate overdensities. As we will see in the next section, the saturation effect probably does not play a role in relating a hard radiation field to the nearby quasars.

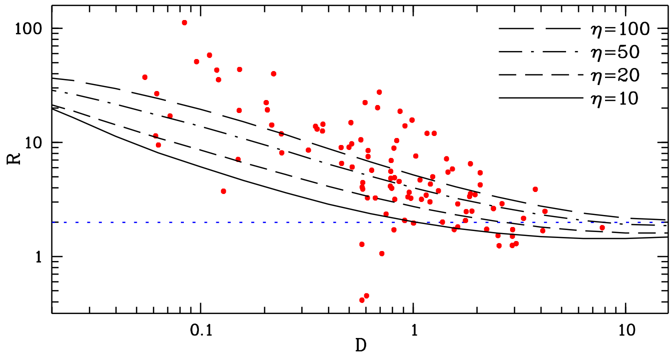

Fig. 5.5. Dependence of R on $D = \tau_{\rm eff,H\,I}/\tau^{\rm exp}_{\rm eff,H\,I}$ for different simulated values of η. The curves indicate the polynomial fits to the simulated distributions in logarithmic space. Filled circles represent the measured $R(D)$ towards HE 2347−4342 in uncontaminated bins at $z > 2.332$. The horizontal dotted line denotes $R = 2$.

5.4.3. The UV radiation field near the quasars

We now investigate in greater detail the spectral shape of the UV radiation field near the four quasars with available data on R and η: the background quasar HE 2347−4342 and the foreground QSOs A–C. Due to the small number of comparison values derived from only two lines of sight, we will adopt $\eta = 100$ as a characteristic value for the overall UV background at $z > 2.6$ (HE 2347−4342, QSO C) and a value of $\eta = 50$ at $z \sim 2.3$ (QSOs A and B). The former value is close to the median $\eta = 102$ obtained by Fechner et al. (2006) at $2.58 < z < 2.75$ towards HS 1700+6416, whereas the latter η value accounts for the probable evolution of η with redshift. Furthermore, we will compare the η values in the vicinity of the quasars to models of the UV background.

HE 2347−4342

A close inspection of Fig. 5.4 reveals a strongly fluctuating radiation field near HE 2347−4342 with some very small, but also high R values. Also the column density ratio shows large fluctuations ($1 \lesssim \eta \lesssim 1000$) with six $\eta \lesssim 10$ absorbers out of the 20 absorbers at $z > 2.86$. These strong variations of the spectral shape are likely due to radiative transfer effects in the associated absorption system causing an apparent lack of the proximity effect of HE 2347−4342 (Reimers et al. 1997). The high He II column densities of the associated system may soften the quasar radiation with increasing distance and Fig. 5.4 supports this interpretation. Due to the probable strong softening of the hard quasar radiation on small scales, the relative spectral hardness near HE 2347−4342 is only revealed by individual low η values instead of robust median values. However, also the highly ionised metal species of the associated system (Fechner et al. 2004) favour the presence of hard QSO radiation. Thus we conclude that despite the lack of a radiation-induced void near HE 2347−4342, its impact onto the IGM can be detected via the relative spectral hardness of the UV radiation field. The three $R < 2$ values near HE 2347−4342 have $D < 3$, so they are probably not affected by saturation.

QSOs A and B

If our decontamination of the Lyα forests near the two $z \sim 2.3$ QSOs A and B is correct, R should reflect UV spectral shape variations also in that region. Indeed, the redshift bin at $z = 2.280$ next to QSO A ($z = 2.282$) is a local R minimum with $R \simeq 1.5$. At $z = 2.270$ we find $R \simeq 0.8$. At the redshift of QSO B ($z = 2.302$) the radiation field is quite soft, but we note a low $R \sim 1$ at $z = 2.310$. We obtain $D < 3$ for the four $R \lesssim 2$ values near QSO A and QSO B, so saturation is not relevant, and the low R values correspond to low η values.

The measured η values in this redshift region are presented in Fig. 5.6. The error bars are only indicative, since blended line components are not independent and the He II column densities are derived with constraints from the H I forest. Lower limits on η result from features detected in He II but not in H I. Due to ambiguities in the line profile decomposition at the H I detection limit and the present low quality of the He II data it is hard to judge the reality of most of these added components (Fechner & Reimers 2007b). Nevertheless, since η for adjacent lines may be not independent due to line blending, we must include the lower limits in the analysis. At $z < 2.294$ the fitting of He II lines becomes unreliable due to the arising Lyβ forest. Therefore, no direct estimates of η can be obtained in the immediate vicinity of QSO A. Furthermore, the H I line sample may be incomplete or the line parameters may be not well constrained due to blending with the O VI of the associated system of HE 2347−4342.

Considering these caveats, the median $\eta \simeq 19$ obtained for the values at $z < 2.332$ shown in Fig. 5.6 is only an estimate. Nevertheless, this is much lower than the typical values $\eta \sim 50$ found at $z \sim 2.3$ towards HS 1700+6416 (Fechner et al. 2006). Moreover, it is also lower than at slightly higher redshifts towards HE 2347−4342. For instance, the median η increases to $\eta = 79$ in the redshift range $2.35 \leq z \leq 2.40$. This is inconsistent with the smooth redshift evolution of η on large scales inferred by Z04 and Fechner et al. (2006) for both available sightlines. Thus, we infer an excess of hard radiation in the vicinity of QSO A and QSO B. The most extreme η values are located in the projected vicinity of QSO B, with 6 lines reaching $\eta < 1$. If estimated correctly, these low η values require local hard sources and cannot be generated by the diffuse UV background. Both foreground quasars could be responsible for the hard radiation field because of similar light travel times to the probably affected absorbers ($t_A \simeq 2t_B$).

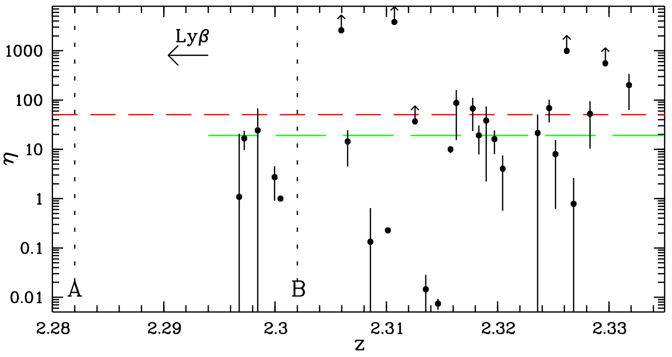

Fig. 5.6. Column density ratio η vs. redshift z in the vicinity of QSO A and QSO B. The long (short) dashed line indicates the median $\eta \simeq 19$ in this redshift range ($\eta = 50$ for a UV background generated by quasars). At $z < 2.294$ the He II Lyβ forest sets in.

QSO C

Since metal contamination of the H I forest is small in the projected vicinity of QSO C (Fig. 5.3), the UV spectral shape is better constrained here than near QSO A and QSO B. From Fig. 5.4 we note a local R minimum ($R \simeq 1.3$) that exactly coincides with the redshift of QSO C ($z = 2.690$). At higher redshifts R rises, possibly indicating a softer ionising field. However, at $2.63 \lesssim z \lesssim 2.695$ the optical depth ratio is continuously below the median with $R < 2$ in five redshift bins. Due to the H I overdensities near QSO C, all $R < 2$ values have $D > 1$, but only the bin at $z = 2.635$ has $D \simeq 4$, so the remaining ones may still indicate low column density ratios η.

Figure 5.7 displays the η values from FR07 in the redshift range $2.63 < z < 2.73$ in the projected vicinity of QSO C. For comparison, we also indicate $\eta = 100$ that is consistent with the median $\eta = 102$ towards HS 1700+6416 in this redshift range (Fechner et al. 2006). While the data generally shows strong fluctuations around the median over the whole covered redshift range (Z04; Fechner et al. 2006), there is an apparent excess of small η values near QSO C indicating a predominantly hard radiation field. From the data, a median $\eta \simeq 46$ is obtained at $2.63 < z < 2.73$ including the lower limits on η. The median η near QSO C is lower than the median η towards HS 1700+6416 by a factor of two and also slightly lower than the η obtained for spatially uniform UV backgrounds generated by quasars. The relative agreement of the median η near QSO C and hard versions of quasar UV background models may result from the softening of the quasar radiation by the IGM at the large proper distances $d \gtrsim 7.75$ Mpc considered here (Table 5.3). This will be further explored in Sect. 5.6.2. The larger contrast between the median η near QSO C and the median η towards HS 1700+6416 yields stronger evidence for a local hardening of the UV radiation near QSO C. However,

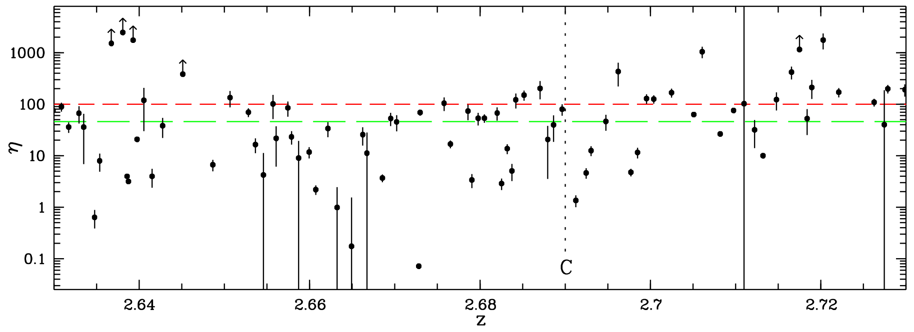

Fig. 5.7. Column density ratio η vs. redshift z in the vicinity of QSO C. The short dashed line denotes $\eta = 100$ that is consistent with the median $\eta \simeq 102$ obtained in the range $2.58 < z < 2.75$ towards HS 1700+6416 (Fechner et al. 2006). The long dashed line indicates the median $\eta \simeq 46$ obtained for the shown η values ($2.63 < z < 2.73$).

this comparison value derived from the single additional line of sight tracing this redshift range may be biased itself.

Near QSO C the column density ratio still fluctuates and is not homogeneously low as naively expected. We also note an apparent offset of the low η region near QSO C towards lower redshift due to fewer absorbers with low η at $z > 2.69$. While some of the fluctuations can be explained by uncertainties to recover η reliably from the present data, the very low $\eta \leq 10$ values ($\simeq 24\%$ of the data in Fig. 5.7) are likely intrinsically low. These η values are in conflict with a homogeneous diffuse UV background, and are likely affected by a local hard source. In Sect. 5.6.4 we will estimate the error budget of η by Monte Carlo simulations.

If QSO C creates a fluctuation in the spectral shape of the UV background, the distance between the quasar and the line of sight implies a light travel time of $t = 25$ Myr. The low (high) redshift end of the region shown in Fig. 5.7 corresponds to a light travel time of 64 Myr (44 Myr). Since these light travel times are comparable, we argue that it is important to consider not only the immediate projected vicinity of QSO C to be affected by the proximity effect (see also Fig. 5.10 below).

In summary, both spectral shape indicators R and η indicate a predominantly hard UV radiation field near all four known quasars in this field. Many η values in the projected vicinity of the quasars indicate a harder radiation than expected even for model UV backgrounds of quasars alone. This points to a transverse proximity effect detectable via the relative spectral hardness. However, there are other locations along the line of sight with an inferred hard radiation field, but without an associated quasar, most notably the regions at $z \sim 2.48$ and $z \sim 2.53$ (Fig. 5.4). Before discussing these in detail (Sect. 5.6.3), we search for additional evidence for hard radiation near the foreground quasars by analysing nearby metal line systems.

5.5. Constraints from metal line systems

Observed metal line systems provide an additional tool to constrain the spectral shape of the ionising radiation. Since photoionisation modelling depends on several free parameters, appropriate systems should preferably show many different ionic species. Fechner et al. (2004) analysed the associated metal line system of HE 2347−4342 and found evidence for a hard quasar spectral energy distribution at the absorbers with highest velocities that are probably closest to the quasar. Their large He II column densities probably shield the other absorbers which are better modelled with a softer radiation field. The results by Fechner et al. (2004) are consistent with the more direct hardness estimators R and η near HE 2347−4342 (Sect. 5.4.3).

In the spectrum of HE 2347−4342 an intervening metal line system is detected at $z = 2.7119$ which is close to the redshift of QSO C ($\Delta z = 0.022$) at a proper distance of $d \simeq 10.0$ Mpc. At $z = 2.2753$ there is another system showing multiple components of C IV and N V as well as only weak H I absorption ($N_{\mathrm{H\,I}} < 10^{13.7}\,\mathrm{cm}^{-2}$). The presence of N V and weak H I features with associated metal absorption are characteristic of intrinsic absorption systems exposed to hard radiation. Due to the small proper distance to QSO A ($d \simeq 3.1$ Mpc) this system is probably illuminated by the radiation of the close-by quasar. A third suitable metal line system at $z = 2.3132$ is closer to QSO B ($d \simeq 6.1$ Mpc) than to QSO A ($d \simeq 12.0$ Mpc). But since QSO A is much brighter than QSO B (Table 5.3), the metal line system at $z = 2.3132$ might be affected by both quasars. Due to their small relative velocities with respect to the quasars of $< 3000\,\mathrm{km\,s}^{-1}$ the systems are likely associated to the quasars (e.g. Weymann et al. 1981).

In order to construct CLOUDY models (Ferland et al. 1998, version 05.07) we assumed a single-phase medium, i.e. all observed ions arise from the same gas phase, as well as a solar abundance pattern (Asplund et al. 2005) at a constant metallicity throughout the system. Furthermore, we assumed pure photoionisation and neglected a possible contribution of collisional ionisation. The absorbers were modelled as distinct, plane-parallel slabs of constant density testing different ionising spectra.

5.5.1. The system at $z = 2.275$ near QSO A

The system at $z = 2.2753$ shows seven components of C IV and N V along with unsaturated features of H I (Fig. 5.8). The absorber densities are constrained by the C IV/N V ratio. For the HM01 background scaled to yield $\log J_{\mathrm{b}} = -21.15$ at the H I Lyman limit (Scott et al. 2000), we derive densities in the range $10^{-4.38}$ to $10^{-3.35}\,\mathrm{cm}^{-3}$ at a metallicity of ~ 0.6 solar. The estimated absorber sizes are ~ 5 kpc or even smaller, where the sizes are computed according to $N_{\mathrm{H}} = n_{\mathrm{H}} l$ with the absorbing path length l. With an additional contribution by QSO A, modelled as a power law with $\alpha = 0.21$ and H I Lyman limit intensity $\log J_{\mathrm{q}} = -21.9$ at the location of the absorber, we obtain an even higher metallicity of ~ 11 times solar. Densities in the range $10^{-2.95}$ to $10^{-2.01}\,\mathrm{cm}^{-3}$ are found leading to very small absorbers of $\lesssim 10$ pc.

Both models lead to unusually high metallicities and very small absorber sizes. However, Schaye et al. (2007) recently reported on a large population of compact high-metallicity absorbers. Using the HM01 background they found typical sizes of ~ 100 pc and densities of $10^{-3.5}\,\mathrm{cm}^{-3}$ for absorbers with nearly solar or even super-solar metallicities. In fact, this system is part of the sample by Schaye et al. (2007).

Since the system exhibits only a few different species, it is impossible to discriminate between the soft and the hard radiation model. In principle, both models lead to a consistent de-

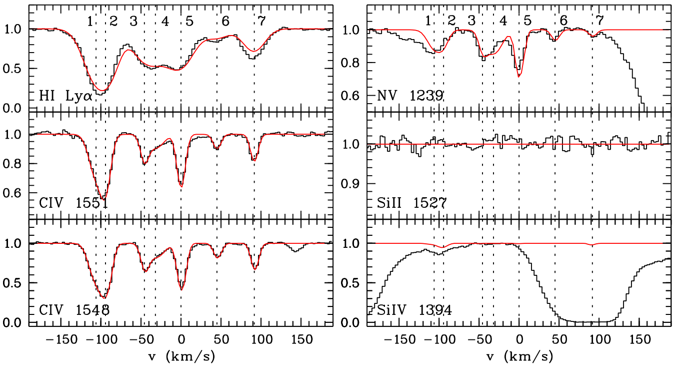

Fig. 5.8. Metal line system at $z = 2.2753$ towards HE 2347−4342. The displayed profiles assume the rescaled HM01 background. Zero velocity corresponds to $z = 2.2753$.

Table 5.4. Measured column densities of the metal line system at $z = 2.2753$. Several components of H I remain unresolved.

#	$v\,[\mathrm{km\,s^{-1}}]$	H I	C IV	N V
1	−106.2	13.634 ± 0.005	13.25 ± 0.59	12.70 ± 0.27
2	−94.3		13.26 ± 0.57	12.40 ± 0.42
3	−45.8	13.319 ± 0.015	12.76 ± 0.39	12.43 ± 0.14
4	−32.0		12.80 ± 0.40	12.88 ± 0.06
5	0.0	13.232 ± 0.019	13.17 ± 0.03	12.94 ± 0.02
6	44.8	12.604 ± 0.020	12.51 ± 0.09	12.21 ± 0.05
7	91.5	13.042 ± 0.007	12.79 ± 0.05	11.98 ± 0.11

scription of the observed metal lines. The soft HM01 UV background yields $\eta \sim 170$ for the modelled absorbers, whereas the model including the hard radiation of QSO A leads to $\eta \sim 10$. Recall that the He II forest cannot be used to measure η directly due to blending with Lyβ features and very low S/N.

5.5.2. The systems near QSO B and QSO C

The systems at $z = 2.3132$ and $z = 2.7119$ are located near QSO B and QSO C, respectively. Only few ions are observed and some of them may even be blended. Therefore, no significant conclusions based on CLOUDY models can be drawn. Using the column density estimates we find that the system at $z = 2.7119$ close to QSO C exhibiting C IV and O VI can be described consistently with a HM01+QSO background. Models assuming a quasar flux of $\log J_{\mathrm{q}} \gtrsim -22.5$ seen by the absorber yield $\eta \lesssim 40$, consistent with the direct measurements from the He II forest. However, the metal transitions alone do not provide strong constraints.

The system at $z = 2.3132$ shows C IV in six components along with Si IV and Si III. The Lyman series of this system suffers from severe blending preventing a reliable estimation of the H I column density. Therefore metallicities and absorber sizes cannot be estimated. Adopting our column density estimates we infer that this system can be reasonably modelled with or without a specific quasar contribution.

5.6. Discussion

5.6.1. The transverse proximity effect in spectral hardness

Fourteen quasars have been found in the vicinity of HE 2347−4342 of which three are located in the usable part of the H I Lyα forest towards HE 2347−4342. No H I underdensity is detected near these foreground quasars even when correcting for contamination by the O VI absorption from the associated system of HE 2347−4342. An estimate of the predicted effect confirms that even if existing, the classical proximity effect is probably too weak to be detected on this line of sight due to the high UV background at 1 ryd and small-scale variance in the H I transmission (Sect. 5.3).

However, the analysis of the spectral shape of the UV radiation field near the foreground quasars yields a markedly different result. The spectral shape is fluctuating, but it is predominantly hard near HE 2347−4342 and the known foreground quasars. Close to QSO C, both estimators R and η are consistent with a significantly harder radiation field than on average. There is a sharp R minimum located precisely at the redshift of the quasar, but embedded in a broader region of low R values statistically consistent with a hard radiation field of $\eta \lesssim 10$ (Fig. 5.4). The column density ratio η is also lower than on average and indicates a harder radiation field than obtained for quasar-dominated models of the UV background (Fig. 5.7). Because of line blending, only one of the three metal line systems detected near the foreground quasars can be used to estimate the shape of the ionising field. The metal line system at $z = 2.275$ can be described reasonably by the HM01 background with or without a local ionising component by QSO A. The He II forest does not provide independent constraints for this absorber. Line blending prevents an unambiguous detection of O VI at $z = 2.712$, leaving the shape of the ionising field poorly constrained without taking into account the He II forest. Thus, the systems show highly ionised metal species, but our attempts to identify a local quasar radiation component towards them remain inconclusive.

The most probable sources for the hard radiation field at $z \sim 2.30$ and $z \sim 2.69$ towards HE 2347−4342 are the nearby foreground quasars. In particular, the absorbers with $\eta \lesssim 10$ have to be located in the vicinity of an AGN, since the filtering of quasar radiation over large distances results in $\eta \gtrsim 50$. Also star-forming galaxies close to the line of sight cannot yield the low η values, since they are unable to produce significant numbers of photons at $h\nu > 54.4$ eV (Leitherer et al. 1999; Smith et al. 2002; Schaerer 2003). We conclude that there is evidence for a transverse proximity effect of QSO C detectable via the relative spectral hardness. There are also indications that QSO A and QSO B show the same effect, although contamination adds uncertainty to the spectral shape variations in their projected vicinity.

Given these incidences of a hard radiation field near the quasars, how do these results relate to those of Paper I, in which we investigated the line of sight towards Q 0302−003? Both lines of sight show He II absorption and on both lines of sight we find evidence for a predominantly hard radiation field near the quasars in the background and the foreground. However, the decrease of η near quasars towards Q 0302−003 appears to be much smoother than towards HE 2347−4342.

There are several reasons for the lack of small-scale spectral shape variations on the line of sight to Q 0302−003. First, the low-resolution STIS spectrum of Q 0302−003 does not resolve the He II lines and limits the visible scale of fluctuations to $\Delta z \gtrsim 0.006$ (Paper I). Much smaller scales can be probed in the resolved He II forest of HE 2347−4342, but the fitting of blended noisy He II features may result in artificial η variations. We will discuss the uncertainties of η below (Sect. 5.6.4). Second, Q 0302−003 ($z = 3.285$) probes higher redshifts, where the He II fraction in the IGM is significantly higher and the inferred radiation field is very soft ($\eta \sim 350$ in the Gunn-Peterson trough). Therefore, the impact of a hard source on the spectral shape is likely to be more pronounced than at lower redshifts after the end of He II reionisation, where η of the UV background gradually decreases.

5.6.2. The decrease of η near QSO C

We now investigate quantitatively whether the foreground quasars are capable of creating a hardness fluctuation on the sightline towards HE 2347−4342. Unfortunately, since only one quasar is located in an uncontaminated region of the Lyα forests, we can present sufficient evidence only for QSO C. For the other two quasars the data is too sparse and contamination adds uncertainty to the derived η, but in principle QSO A should also show a strong effect, because its Lyman limit flux penetrating the line of sight is ~ 8 times higher than the one of QSO C.

Heap et al. (2000) and Smette et al. (2002) presented simple models of the decrease of η in front of a quasar taking into account the absorption of ionising photons by the IGM. In a highly photoionised IGM with helium mass fraction $Y \simeq 0.24$ and temperature $T \simeq 2 \times 10^4$ K we have

$$\eta \simeq \frac{Y}{4\,(1-Y)}\frac{\alpha_{\mathrm{He\,II}}}{\alpha_{\mathrm{H\,I}}}\frac{\Gamma_{\mathrm{H\,I}}}{\Gamma_{\mathrm{He\,II}}} \simeq 0.42\frac{\Gamma_{\mathrm{H\,I}}}{\Gamma_{\mathrm{He\,II}}}, \tag{5.4}$$

where Γ_i and α_i are the photoionisation rate and the radiative recombination coefficient for species i (Fardal et al. 1998). The photoionisation rate is $\Gamma_i = \Gamma_{i,\mathrm{b}} + \Gamma_{i,\mathrm{q}}$ with a contribution of the background and the quasar. The contribution of the quasar to the photoionisation rate of species i at the jth absorber in front of it ($z_j > z_{j+1}$) is

$$\begin{aligned}\Gamma_{i,\mathrm{q}}(z_j) \;=\;& \frac{\sigma_i f_{\nu,i}}{h(1+z_\mathrm{q})}\left(\frac{1+z_\mathrm{q}}{1+z_j}\right)^{-\alpha+1}\left(\frac{d_\mathrm{L}(z_\mathrm{q},0)}{d_\mathrm{L}(z_\mathrm{q},z_j)}\right)^2 \\ & \times \int_1^\infty x^{-\alpha-4}\exp\left(-\sum_{k=1}^{j-1} N_{i,k}\sigma_i x^{-3}\left(\frac{1+z_k}{1+z_j}\right)^{-3}\right)\mathrm{d}x\end{aligned} \tag{5.5}$$

with the photoionisation cross section at the Lyman limit σ_i, the observed Lyman limit flux $f_{\nu,i}$ and $x = \nu/\nu_i$ with the Lyman limit frequency ν_i. Extrapolating the power law continuum flux to the He II Lyman limit yields $f_{\nu,\mathrm{He\,II}} = f_{\nu,\mathrm{H\,I}}4^{-\alpha}$. With the spectral index α from Table 5.3 we obtain $\eta_\mathrm{min} \simeq 2.3$ for QSO C.

We simulated $\eta(z)$ for a set of 1000 Monte Carlo Lyα forest spectra generated with the procedure discussed in Sect. 5.4.2. We assumed $\Gamma_{\mathrm{H\,I,b}} = 1.75 \times 10^{-12}\ \mathrm{s}^{-1}$ corresponding to the UV background from Sect. 5.3 and $\eta_\mathrm{b} = 100$, which agrees with the median η towards HS 1700+6416 in the redshift range under consideration (Fechner et al. 2006). The intervening absorbers successively block the quasar flux. Especially, every absorber with $\log N_{\mathrm{H\,I}} > 15.8$ will truncate the quasar flux at $h\nu > 4$ ryd due to a He II Lyman limit system, leading to an abrupt softening of the radiation field.

Figure 5.9 presents the simulated decrease of the median η approaching QSO C assuming a constant quasar luminosity, isotropic radiation and an infinite quasar lifetime together with the upper and lower percentiles of the η distribution obtained in bins of proper distance $\Delta d = 2$ Mpc. The spread in the simulated η is due to line-of-sight differences in the absorber properties. Since we consider the transverse proximity effect, we are limited to a proper distance $d \gtrsim 7.75$ Mpc (Table 5.3). The model agrees reasonably with the median η of the data obtained in concentric rings around the quasar. As expected, individual η values strongly deviate from this simple model due to the assumptions of the quasar properties (constant luminosity and spectral index, isotropic radiation) and due to the unknown real distribution of absorbers in transverse direction. Recently, Hennawi & Prochaska (2007) found evidence for excess small-scale clustering of high-column density systems in transverse direction to quasar sightlines. In Sect. 5.4.3 we found indications that the η distribution around QSO C is not symmetric, which could be due to such anisotropic shielding. However, this does not imply an intrinsic anisotropy due to the unknown matter distribution around the quasar and the large uncertainties in individual η values. Moreover, the line-of-sight variance at a constant $\eta = 100$ is too small to explain the large observed spread of the η values. Clearly, a self-consistent explanation of the small-scale η fluctuations would require hydrodynamical simulations of cosmological radiative transfer in order to investigate possible shielding effects and the statistical distribution of η values near quasars. While there is recent progress in case of the UV background (Sokasian et al. 2003; Croft 2004; Maselli & Ferrara 2005; Bolton et al. 2006), a proper treatment of three-dimensional radiative transfer in the IGM around a quasar is still in its infancy. However, our simplified approach suggests that QSO C is capable of changing the spectral shape of the UV radiation field by the right order of magnitude to explain the low η values in its vicinity. Also a variation in the sizes and the centres of the bins chosen for Fig. 5.9 does not drastically change the indicated excess of low η at $d \lesssim 14$ Mpc. Figure 5.9 also shows very clearly that the sphere of influence for the transverse proximity effect is not limited to the immediate vicinity of the quasar.

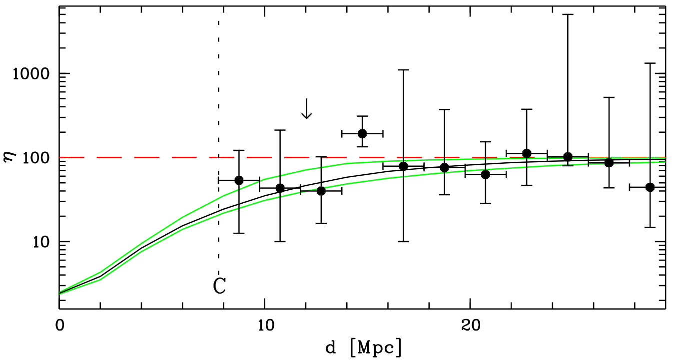

Fig. 5.9. Column density ratio η vs. proper distance d. The black full line shows the modelled decrease of the median η approaching QSO C with respect to the ambient $\eta_\mathrm{b} = 100$ (dashed line). Green/grey lines mark the upper and lower quartiles of the simulated η distribution in bins of $\Delta d = 2$ Mpc. QSO C is located at 7.75 Mpc. Filled circles show the median η from FR07 in concentric rings of $\Delta d = 2$ Mpc around the quasar. Error bars are the quartile distances to the median. The arrow marks the metal line system at $z = 2.7122$ at $d = 12.03$ Mpc.

Figure 5.10 shows a two-dimensional cut in comoving space near QSO C in the plane spanned by both lines of sight. The minimum separation of both lines of sight corresponds to a light travel time of $\simeq 25.2$ Myr, but the lifetime of QSO C could be $\gtrsim 40$ Myr due to the low η values at larger distances. The fluctuations of the UV spectral shape could be explained by shadowing of the hard QSO radiation by unknown intervening structures between both lines of sight.

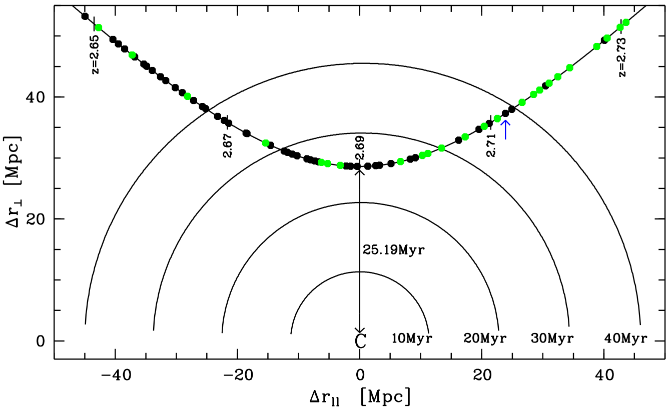

Fig. 5.10. Transverse comoving separation $\Delta r_\perp$ vs. line-of-sight comoving separation $\Delta r_\parallel$ with respect to QSO C. Black (green/grey) points denote absorbers with $\eta < 100$ ($\eta \geq 100$) on the line of sight towards HE 2347−4342 (curved line) with indicated redshifts. The arrow points to the metal line system at $z = 2.712$. The half circles show the distance travelled by light emitted at the indicated times prior to our observation. The minimum light travel time between the two lines of sight is 25.19 Myr.

5.6.3. Other regions with an inferred hard UV radiation field

In Fig. 5.4 we note two additional regions at $z \sim 2.48$ and $z \sim 2.53$ where R is prominently small and where there is no nearby quasar. Also the fitted $\eta(z)$ shows very low values apparently unrelated to a known foreground quasar. Figure 5.11 displays the redshift distribution of the $\eta \leq 10$ subsample. The low η values are clustered with two peaks near the foreground quasars, but also at $z \sim 2.40$, $z \sim 2.48$ and $z \sim 2.53$. At the first glance the existence of such regions seems to undermine the relation between the foreground quasars and a low η in their vicinity. However, there are several plausible explanations for the remaining low η values:

1. *Unknown quasars:* We can conclude from Paper I that the quasars responsible for hardness fluctuations may be very faint (like Q 0302-D113 in Paper I) or may reside at large distances (Q 0301−005 in Paper I). QSO C is located near the edge of our survey area centred on HE 2347−4342, so other quasars capable of influencing the UV spectral shape might be located outside the field of view. Moreover, in order to sample the full quasar luminosity domain ($M_B \leq -23$) at $z \sim 2.5$ our survey is still too shallow by ∼ 1 magnitude. Therefore, a larger and/or deeper survey around HE 2347−4342 is desirable.
2. *Quasar lifetime:* Assuming that quasars are long-lived and radiate isotropically, every statistically significant low η fluctuation should be due to a nearby quasar. On the other hand, short-lived quasars will not be correlated with a hard radiation field due to the light travel time from the quasar to the background line of sight. Quasar lifetimes are poorly constrained by observations to $1 \lesssim t_\mathrm{q} \lesssim 100$ Myr (Martini 2004). This could be short enough to create relic light echoes from extinct quasars. The comoving space density of quasars with $M_B < -23$ at $z \simeq 2.5$ is $\simeq 3.7 \times 10^{-6}$ Mpc^{-3} (Wolf et al. 2003) resulting in an average proper separation of ∼ 18.5 Mpc between two lines of sight. This translates into a light travel time of ∼ 60 Myr which is of the same order as the quasar lifetime. So it is quite possible that some quasars have already turned off, but their hard radiation is still present.

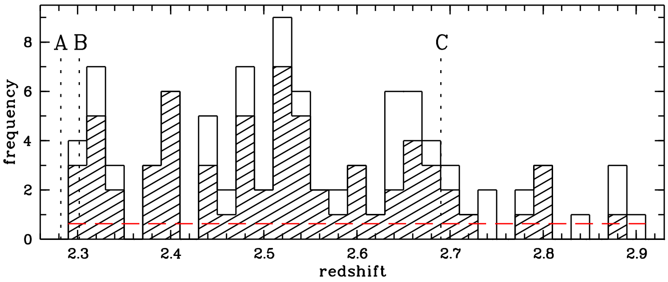

Fig. 5.11. Redshift distribution of low-η absorbers. The open (hashed) histogram shows all ($N_\mathrm{H\,I} \leq 10^{14}$ cm^{-2}) absorbers with $\eta \leq 10$. Letters and dotted lines mark foreground quasars. The horizontal dashed line denotes the estimated average number of absorbers scattered from $\eta = 80$ to $\eta \leq 10$ ($\simeq 0.64$ per bin).

3. *Obscured quasars:* Anisotropic emission of type I quasars may lead to redshift offsets between regions with an inferred hard radiation field and quasars close to the line of sight. In the extreme case the putative quasar radiates in transverse direction, but is obscured on our line of sight (type II quasar). The space density of type II AGN at $z > 2$ is very uncertain due to the challenging optical follow-up that limits the survey completeness (e.g. Barger et al. 2003; Szokoly et al. 2004; Krumpe et al. 2007). Thus, the fraction of obscured AGN at high redshift is highly debated (Akylas et al. 2006; Treister & Urry 2006), but may well equal that of type I AGN in the luminosity range of interest (Ueda et al. 2003).

We believe that a combination of the above effects is responsible for the loose correlation between low η values and active quasars. In particular, at $z \sim 2.4$ we infer a hard radiation field in a H I void (FR07), which may have been created by a luminous quasar that is unlikely to be missed by our survey ($V \lesssim 22$).

In Fig. 5.11 we also indicate the error level due to inaccurate line fitting and noise in the He II data (dashed line) obtained from simulated data (see below). The low number of η values scattered from a simulated $\eta = 80$ to $\eta \leq 10$ implies that the overdensities of such small η values are statistically significant. Constraining the sample to lines with $\log(N_\mathrm{H\,I}) < 14$ due to a possible bias caused by thermal broadening does not remove the significant clusters of lines with small η.

5.6.4. Uncertainties in the spectral hardness

Our findings are likely to be affected by random errors and possibly also by systematic errors mostly related to the He II data. The poor quality of the FUSE spectrum of HE 2347−4342 ($S/N \lesssim 5$) contributes to the fluctuations in η even if the η value was constant (Fechner et al. 2006, see also below). The optical depth ratio R should be less affected by noise, since it is an average over a broader redshift range $\Delta z = 0.005$. The low S/N and the generally high absorption at $\eta \gg 1$ provide uncertainty for the continuum determination in the He II spectrum. The extrapolated reddened power law is certainly an approximation.

Although the η fitting results from FR07 are broadly consistent with those of Z04 and agree well in the regions near the foreground quasars, there are substantial differences in some redshift ranges. This is probably due to the combined effects of low He II data quality, different data analysis software and ambiguities in the deblending of lines. At present, η cannot be reliably determined at individual absorbers unless metal transitions provide further constraints.

In order to assess the random scatter in η due to the low S/N He II data and ambiguities in the line deblending of both species, we again used Monte Carlo simulations. Ten H I Lyα forest spectra were generated in the range $2 < z < 3$ via the Monte Carlo procedure outlined in Sect. 5.4.2. The resolution $R \sim 42000$ and $S/N = 100$ closely resembles the optical data of HE 2347−4342. We also generated the corresponding He II forests at FUSE resolution and $S/N = 4$. We assumed pure non-thermal line broadening and $\eta = 80$. Voigt profiles were automatically fitted to the H I spectra using AUTOVP [1] (Davé et al. 1997). The He II spectra were then automatically fitted with redshifts z and non-thermal Doppler parameters $b_{\mathrm{H\,I}}$ fixed from the fitted H I line lists, yielding 7565 simulated η values. On average the recovered η is slightly higher than the simulated one (median $\eta \simeq 89$) with a large spread ($0 < \eta \lesssim 8000$), but only 285 lines have $\eta \leq 10$. Thus, we estimate a probability $P \simeq 3.8\%$ that η is scattered randomly from $\eta = 80$ to $\eta \leq 10$ if the assumption of non-thermal broadening is correct. Note that this probability is likely an upper limit due to the fact that only H I Lyα was used to obtain the line parameters, which results in large error bars for saturated lines on the flat part of the curve of growth. In the real data, these errors were avoided by fitting unsaturated higher orders of the Lyman series wherever possible.

In the line sample by FR07, 94 out of the 526 absorbers have $\eta \leq 10$, whereas our simulation implies that only ~ 20 are expected to be randomly scattered to $\eta \leq 10$ if η was constant. Thus, the major part of the scatter of η in the data is due to real fluctuations in the UV spectral shape. The majority of the low $\eta \leq 10$ values is inconsistent with $\eta \geq 80$, so they indicate a hard radiation field in spite of the low S/N in the He II data. Yet, due to the large intrinsic scatter obtained from the simulations, individual η values hardly trace the variations of the UV spectral shape. Local spatial averages should be more reliable (FR07). Since the transverse proximity effect zones always extend over some redshift range, this requirement is fulfilled and *on average* we reveal a harder radiation field than expected.

Concerning the high tail of the simulated distribution at $\eta = 80$, $\sim 15\%$ of the lines are returned with $\eta \gtrsim 200$. This may indicate that a fraction of the observed high η values is still consistent with a substantially harder radiation field, underlining that single η values poorly constrain the spectral shape.

Possibly, some η values are systematically too low due to the assumption of non-thermal broadening ($b_{\mathrm{He\,II}} = b_{\mathrm{H\,I}}$) when fitting the He II forest. FR07 found that this leads to underestimated η values at $N_{\mathrm{H\,I}} \gtrsim 10^{13}$ cm^{-2} if the lines are in fact thermally broadened ($b_{\mathrm{He\,II}} = 0.5 b_{\mathrm{H\,I}}$). Non-thermal broadening is caused by turbulent gas motions or the differential Hubble flow, with the latter affecting in particular the low-column density forest. Thermal broadening becomes important in collapsed structures at high column densities. In simulations of the Lyα forest, non-thermal broadening has been found to dominate (Zhang et al. 1995, 1998; Hernquist et al. 1996; Weinberg et al. 1997; Bolton et al. 2006; Liu et al. 2006). This has been confirmed observationally for the low-column density forest (Z04; Rauch et al. 2005). On the other hand, eight out of eleven absorbers with $N_{\mathrm{H\,I}} > 10^{14}$ cm^{-2} in the vicinity of QSO C have $\eta \leq 10$ (Fig. 5.7). Although the column density ratio of these absorbers could be underestimated due to an unknown contribution of thermal broadening, the statistical evidence for a hard radiation field is based on the vast majority of low-column density lines. The median η obtained in this region does not increase significantly after excluding the suspected lines (~ 53 vs. ~ 40). This is still much lower than the median $\eta \sim 100$ towards HS 1700+6416 in this redshift range (Fechner et al. 2006). Therefore, it is unlikely that our results are biased due to the assumed line broadening.

5.7. Conclusions

Traditionally, the transverse proximity effect of a quasar has been claimed to be detectable as a radiation-induced void in the H I Lyα forest. But due to several systematic effects like quasar variability, finite quasar lifetime, intrinsic overdensities around quasars, or anisotropic radiation, most searches yielded negative results (e.g. Schirber et al. 2004; Croft 2004).

In this paper, we have analysed the fluctuating spectral shape of the UV background in the projected vicinity of the three foreground quasars QSO J23503−4328, QSO J23500−4319 and QSO J23495−4338 (dubbed QSO A, B and C) on the line of sight towards HE 2347−4342 ($z = 2.885$). By comparing the H I absorption and the corresponding He II absorption, we have presented evidence for a statistical excess of hard UV radiation near the foreground quasars. However, due to contamination of the forests near QSO A ($z = 2.282$) and QSO B ($z = 2.302$), the evidence is strongest for QSO C ($z = 2.690$). We interpret these indicators for an excess of hard radiation near the foreground quasars as a manifestation of the transverse proximity effect. A simple model indicates that the foreground quasars are capable of generating the observed hard radiation over the observed distances of several Mpc. Furthermore, we tried to model the ionising radiation field of three metal line systems close to the foreground quasars. Two of those are strongly affected by line blending and do not allow for reliable photoionisation models. The remaining system can be modelled reasonably with or without a contribution by a local quasar. Future larger samples of highly ionised unblended metal systems near foreground quasars may provide evidence for local hardness fluctuations.

In Worseck & Wisotzki (2006) we revealed the transverse proximity effect as a systematic local hardness fluctuation around four foreground quasars near Q 0302−003 and pointed out that the relative UV spectral hardness is a sensitive physical indicator of the proximity effect over distances of several Mpc. In this study we are able to confirm this on a second line of sight. Evidently, small-scale transmission fluctuations in the H I forest can dilute the small predicted signature of the effect. However, the hard spectral shape of the UV radiation field still indicates the transverse proximity effect despite the H I density fluctuations. Thus, we confirm our previous result that the spectral hardness breaks the density degeneracy that affects the traditional searches for the proximity effect. Moreover, the predicted transverse proximity effect of the quasars in the H I forest is weak due to the high UV background at 1 ryd. Still the UV spectral shape is able to discriminate local UV sources independent of the amplitude of the UV background.

Bolton et al. (2006) find that the large UV spectral shape fluctuations in the IGM are likely due to the small number of quasars contributing to the He II ionisation rate at any given point, whereas the H I ionisation rate is rather homogeneous due to the probable contribution of star-forming galaxies (e.g. Bianchi et al. 2001; Sokasian et al. 2003; Shapley et al. 2006). Our findings confirm the picture that AGN create the hard part of the intergalactic UV radiation field. If the quasar is active long enough, its hard radiation field can be observed penetrating a background line of sight. It is also likely that light echoes from already extinguished quasars are responsible for some locations

---

[1] http://ursa.as.arizona.edu/~rad/autovp.tar

of hard radiation without an associated quasar. The transverse proximity effect of QSO C implies a minimum quasar lifetime of ∼ 25 Myr (probably even ∼ 40 Myr), providing additional constraints to more indirect estimates (e.g. Martini 2004, and references therein).

However, the UV radiation field near the foreground quasars is not homogeneously hard as naively expected, but still shows fluctuations. Apart from substantial measurement uncertainties, the unknown density structure around the quasar could shield the ionising radiation in some directions, maybe even preferentially in transverse direction to the line of sight (Hennawi & Prochaska 2007). Thus, radiative transfer effects may become important to explain a fluctuating UV spectral shape in the presence of a nearby quasar. Large-scale simulations of cosmological radiative transfer with discrete ionising sources are required to adress these issues in detail.

Moreover, the He II forest has been resolved so far only towards two quasars at a very low $S/N \lesssim 5$. While the low data quality primarily creates uncertainties in the spectral shape on small spatial scales, large scales could be affected by cosmic variance. Thus, the general redshift evolution of the UV spectral shape is not well known and estimates obtained from single lines of sight may well be biased by local sources.

Acknowledgements. Based on observations collected at the European Southern Observatory, Chile (Proposals 070.A-0425 and 074.A-0273). Data collected under Proposals 068.A-0194, 070.A-0376 and 166.A-0106 was obtained from the ESO Science Archive. We thank the staff of the ESO observatories La Silla and Paranal for their professional assistance in obtaining the optical data discussed in this paper. We are grateful to Peter Jakobsen for agreeing to publish the quasars from his survey. We thank Gerard Kriss and Wei Zheng for providing the reduced FUSE spectrum of HE 2347−4342. Tae-Sun Kim kindly supplied an additional line list of HE 2347−4342. GW and ADA acknowledge support by a HWP grant from the state of Brandenburg, Germany. CF is supported by the Deutsche Forschungsgemeinschaft under RE 353/49-1. We thank the anonymous referee for helpful comments.

References

Akylas, A., Georgantopoulos, I., Georgakakis, A., Kitsionas, S., & Hatziminaoglou, E. 2006, A&A, 459, 693
Appenzeller, I., Fricke, K., Furtig, W., et al. 1998, The Messenger, 94, 1
Asplund, M., Grevesse, N., & Sauval, A. J. 2005, in ASP Conf. Ser. 336: Cosmic Abundances as Records of Stellar Evolution and Nucleosynthesis, 25, astro–ph/0410214
Baade, D., Meisenheimer, K., Iwert, O., et al. 1999, The Messenger, 95, 15
Bajtlik, S., Duncan, R. C., & Ostriker, J. P. 1988, ApJ, 327, 570
Ballester, P., Mondigliani, A., Boitquin, O., et al. 2000, The Messenger, 101, 31
Barger, A. J., Cowie, L. L., Capak, P., et al. 2003, AJ, 126, 632
Bergeron, J., Petitjean, P., Aracil, B., et al. 2004, The Messenger, 118, 40
Bianchi, S., Cristiani, S., & Kim, T.-S. 2001, A&A, 376, 1
Bolton, J. S., Haehnelt, M. G., Viel, M., & Carswell, R. F. 2006, MNRAS, 366, 1378
Cardelli, J. A., Clayton, G. C., & Mathis, J. S. 1989, ApJ, 345, 245
Croft, R. A. C. 2004, ApJ, 610, 642
Crotts, A. P. S. 1989, ApJ, 336, 550
Crotts, A. P. S. & Fang, Y. 1998, ApJ, 502, 16
Davé, R., Hernquist, L., Weinberg, D. H., & Katz, N. 1997, ApJ, 477, 21
Dobrzycki, A. & Bechtold, J. 1991a, ApJ, 377, L69
Dobrzycki, A. & Bechtold, J. 1991b, in ASP Conf. Ser. 21: The Space Distribution of Quasars, 272
Fardal, M. A., Giroux, M. L., & Shull, J. M. 1998, AJ, 115, 2206
Fardal, M. A. & Shull, J. M. 1993, ApJ, 415, 524
Fechner, C., Baade, R., & Reimers, D. 2004, A&A, 418, 857
Fechner, C. & Reimers, D. 2007a, A&A, 461, 847
Fechner, C. & Reimers, D. 2007b, A&A, 463, 69
Fechner, C., Reimers, D., Kriss, G. A., et al. 2006, A&A, 455, 91
Ferland, G. J., Korista, K. T., Verner, D. A., et al. 1998, PASP, 110, 761
Fernández-Soto, A., Barcons, X., Carballo, R., & Webb, J. K. 1995, MNRAS, 277, 235
Gallerani, S., Ferrara, A., Fan, X., & Roy Choudhury, T. 2007, MNRAS, submitted, arXiv:0706.1053
Gaskell, C. M. 1982, ApJ, 263, 79
Giallongo, E., Cristiani, S., D'Odorico, S., Fontana, A., & Savaglio, S. 1996, ApJ, 466, 46
Guimarães, R., Petitjean, P., Rollinde, E., et al. 2007, MNRAS, 377, 657
Haardt, F. & Madau, P. 1996, ApJ, 461, 20
Haardt, F. & Madau, P. 2001, in Clusters of Galaxies and the High Redshift Universe Observed in X-rays, ed. D. M. Neumann & J. T. T. Van, 64
Heap, S. R., Williger, G. M., Smette, A., et al. 2000, ApJ, 534, 69
Hennawi, J. F. & Prochaska, J. X. 2007, ApJ, 655, 735
Hernquist, L., Katz, N., Weinberg, D. H., & Miralda-Escudé, J. 1996, ApJ, 457, L51
Horne, K. 1986, PASP, 98, 609
Jakobsen, P. 1998, A&A, 335, 876
Jakobsen, P., Jansen, R. A., Wagner, S., & Reimers, D. 2003, A&A, 397, 891
Kim, T.-S., Carswell, R. F., Cristiani, S., D'Odorico, S., & Giallongo, E. 2002, MNRAS, 335, 555
Kim, T.-S., Cristiani, S., & D'Odorico, S. 2001, A&A, 373, 757
Kriss, G. A., Shull, J. M., Oegerle, W., et al. 2001, Sci, 293, 1112
Krumpe, M., Lamer, G., Schwope, A. D., et al. 2007, A&A, 466, 41
Landolt, A. U. 1992, AJ, 104, 340
Leitherer, C., Schaerer, D., Goldader, J. D., et al. 1999, ApJS, 123, 3
Liske, J. 2000, MNRAS, 319, 557
Liske, J. & Williger, G. M. 2001, MNRAS, 328, 653
Liu, J., Jamkhedkar, P., Zheng, W., Feng, L.-L., & Fang, L.-Z. 2006, ApJ, 645, 861
Loeb, A. & Eisenstein, D. J. 1995, ApJ, 448, 17
Martini, P. 2004, in Carnegie Observatories Astrophysics Series Vol. 1: Coevolution of Black Holes and Galaxies, ed. L. C. Ho (Cambridge University Press), 170
Maselli, A. & Ferrara, A. 2005, MNRAS, 364, 1429
McDonald, P., Seljak, U., Cen, R., Bode, P., & Ostriker, J. P. 2005, MNRAS, 360, 1471
McIntosh, D. H., Rix, H.-W., Rieke, M. J., & Foltz, C. B. 1999, ApJ, 517, L73
Miralda-Escudé, J. 1993, MNRAS, 262, 273
Miralda-Escudé, J., Haehnelt, M., & Rees, M. J. 2000, ApJ, 530, 1
Møller, P. & Kjærgaard, P. 1992, A&A, 258, 234
Picard, A. & Jakobsen, P. 1993, A&A, 276, 331
Rauch, M., Becker, G. D., Viel, M., et al. 2005, ApJ, 632, 58
Reimers, D., Köhler, S., Wisotzki, L., et al. 1997, A&A, 327, 890
Rollinde, E., Srianand, R., Theuns, T., Petitjean, P., & Chand, H. 2005, MNRAS, 361, 1015
Schaerer, D. 2003, A&A, 397, 527
Schaye, J., Carswell, R. F., & Kim, T.-S. 2007, MNRAS, submitted, astro-ph/0701761
Schirber, M., Miralda-Escudé, J., & McDonald, P. 2004, ApJ, 610, 105
Schlegel, D. J., Finkbeiner, D. P., & Davis, M. 1998, ApJ, 500, 525
Scott, J., Bechtold, J., Dobrzycki, A., & Kulkarni, V. P. 2000, ApJS, 130, 67
Scott, J., Kriss, G. A., Brotherton, M., et al. 2004, ApJ, 615, 135
Shapley, A. E., Steidel, C. C., Pettini, M., Adelberger, K. L., & Erb, D. K. 2006, ApJ, 651, 688
Shull, J. M., Tumlinson, J., Giroux, M. L., Kriss, G. A., & Reimers, D. 2004, ApJ, 600, 570
Smette, A., Heap, S. R., Williger, G. M., et al. 2002, ApJ, 564, 542
Smith, L. J., Norris, R. P. F., & Crowther, P. A. 2002, MNRAS, 337, 1309
Sokasian, A., Abel, T., & Hernquist, L. 2003, MNRAS, 340, 473
Srianand, R. 1997, ApJ, 478, 511
Szokoly, G. P., Bergeron, J., Hasinger, G., et al. 2004, ApJS, 155, 271
Telfer, R. C., Zheng, W., Kriss, G. A., & Davidsen, A. F. 2002, ApJ, 565, 773
Tepper-García, T. 2006, MNRAS, 369, 2025
Tittley, E. R. & Meiksin, A. 2006, astro-ph/0605317
Treister, E. & Urry, C. M. 2006, ApJ, 652, L79
Tytler, D. & Fan, X. 1992, ApJS, 79, 1
Ueda, Y., Akiyama, M., Ohta, K., & Miyaji, T. 2003, ApJ, 598, 886
Véron-Cetty, M.-P. & Véron, P. 2006, A&A, 455, 773
Weinberg, D. H., Hernquist, L., Katz, N., Croft, R., & Miralda-Escudé, J. 1997, in Proceedings of the 13th IAP Astrophysics Colloquium: Structure and Evolution of the Intergalactic Medium from QSO Absorption Line Systems, ed. P. Petitjean & S. Charlot (Paris: Editions Frontières), 133
Weymann, R. J., Carswell, R. F., & Smith, M. G. 1981, ARA&A, 19, 41
Wisotzki, L., Selman, F., & Gilliotte, A. 2001, The Messenger, 104, 8
Wolf, C., Wisotzki, L., Borch, A., et al. 2003, A&A, 408, 499
Worseck, G. & Wisotzki, L. 2006, A&A, 450, 495
Zhang, Y., Anninos, P., & Norman, M. L. 1995, ApJ, 453, L57
Zhang, Y., Meiksin, A., Anninos, P., & Norman, M. L. 1998, ApJ, 495, 63
Zheng, W., Kriss, G. A., Deharveng, J.-M., et al. 2004, ApJ, 605, 631

Chapter 6

Conclusions and Outlook[⋆]

G. Worseck

6.1. Summary

In this work we have searched for new quasar groups around well-studied high-redshift quasars and used them to investigate the transverse proximity effect. The main results can be summarised as follows:

- **A slitless survey for faint quasars:**
  We performed a CCD-based slitless spectroscopic survey for faint $V \lesssim 22$ quasars on $18 \sim 26.'2 \times 33.'5$ fields centred on bright quasars. We developed software to optimally extract slitless spectroscopic grism data accounting for contaminating spectral orders in the field of view. We proved that a ~ 1 h total exposure time with a slitless spectrograph on a 2 m-class telescope probes $V \sim 22$ sources whose spectra are recorded with a continuum signal-to-noise ratio $S/N \sim 1$. Sources with strong emission lines can be detected well beyond this limit. We have shown that a deep slitless spectroscopic quasar survey can be performed with a nowadays small 2 m-class telescope, comparing well with previous studies at higher demanded 4–5 m telescopes.

- **New groups of high-redshift quasars:**
  Having centred our survey fields on 18 $2.76 < z < 4.69$ quasars we established new groups of quasars at angular distances $\vartheta \lesssim 15'$ around these bright quasars that have been extensively observed with the UV-Visual Echelle Spectrograph (UVES) at the Very Large Telescope. From the 169 previously unknown quasar candidates detected among the ~ 29000 slitless spectra we selected 81 potential $z > 1.7$ quasars for spectroscopic follow-up and confirmed 80 of them. 64 of the confirmed quasars reside in the redshift range of interest to us ($1.7 < z < 3.6$).
  Excluding the central quasars, our survey has increased the number of known $z > 1.7$ quasars in these fields by a factor ~ 5. The 13 previously known $z \gtrsim 1.7$ quasars at $V \lesssim 22$ were readily rediscovered by our survey as well as the central quasars and several low-redshift quasars. The number of confirmed $z > 1.7$ quasars around the central quasars ranges from one on the field of Q 1209+0919 to nine on the field of Q 0347−383. We even discovered a comparatively bright $B \simeq 19.3$ quasar at $z = 2.709$ in the sky region around Q 2139−4434 that had been extensively surveyed already (e.g. Hawkins 2000; Francis et al. 2004) with 26 previously known $z > 1.7$ quasars within a radius $< 30'$ around Q 2139−4434. For most of the central quasars our survey has provided the first projected neighbouring quasars.
  In a targeted survey limited by observing time for candidate confirmation, a high survey efficiency is more important than survey completeness. The high success rate of the spectroscopic follow-up implies that most of the remaining candidates are quasars as well.

- **The apparent absence of the transverse proximity effect in the H I Lyα forest:**
  In background quasar spectra of our quasar groups we searched for a systematically decreased H I Lyα forest absorption near every suitable foreground quasar in order to reveal the transverse proximity effect. We characterised the statistical distribution of the H I Lyα effective optical depth via Monte Carlo simulations in order to quantify the significance of effective optical depth fluctuations in the Lyα forest. The observed quasar pairs show no sign of the transverse proximity effect as a systematic underdensity, neither at the low resolution of FORS nor at the high resolution of UVES. In contrast, by treating the simulated data in the same way as the observed data we found that if the effect was present at its predicted strength, it should have been marginally detectable at the 1–2σ level.
  Systematic effects of quasar variability, quasar anisotropy and in particular intrinsic overdensities near the quasars are likely to cause the apparent lack of the transverse proximity effect. However, since a clear signature of the effect was predicted only for three quasar pairs, definite conclusions require larger samples of close projected quasar pairs. We estimate that $\gtrsim 5$ medium-resolution spectra of background sightlines close to foreground quasars are necessary to statistically establish the effect, provided that the UV radiation field of the foreground quasars exceeds the UV background by a factor of $\gtrsim 3$ and the adverse systematic effects can be ignored. However, if quasars reside in overdense regions, any weak predicted signature of the transverse proximity effect will be masked by the intrinsic density fluctuations in the intergalactic medium.

- **The first detections of the transverse proximity effect in spectral hardness:**
  Two background quasar sightlines in our sample show intergalactic He II absorption. Comparing this to the corresponding H I absorption yields an estimate of the spectral shape of the ambient UV radiation field. A hard radiation field corresponds to low inferred column density ratios $\eta = N_{\mathrm{He\,II}}/N_{\mathrm{H\,I}}$. We analysed the UV spectral shape fluctuations near the foreground quasars along these two lines of sight and found it to be systematically harder near the quasars than on average.

The hard radiation field near the background quasars is already known. Heap et al. (2000) inferred the hard radiation field near Q 0302−003 via comparing the Lyα forest absorption of H I and He II. Fechner et al. (2004) analysed the complex associated metal line system of HE 2347−4342 and found that the most of the absorbers require a hard radiation field. We found evidence for a hard radiation field near all seven foreground quasars along these two sightlines. We interpret this as the transverse proximity effect detected as a local UV spectral hardness fluctuation.

Correlating foreground quasars and the inferred UV spectral shape along the line of sight towards Q 0302−003 we found a harder radiation field near the four accessible foreground quasars. In the direct vicinity of the quasars η is consistent with values of 25–100, whereas the regions with trough-like He II absorption require $\eta \gtrsim 200$. At least three of the foreground quasars are located well outside the proximity effect zone of Q 0302−003, so that the transverse proximity effect can be disentangled from the line-of-sight effect.

For the line of sight towards HE 2347−4342 we used the η measurements by Fechner & Reimers (2007) as well as flux statistics to reveal a harder radiation field near three foreground quasars (median $\eta \sim 20$–50) than in general (median $\eta \sim 80$–100). In the vicinity of the quasars the column density ratio still shows large fluctuations on small scales that are probably caused by radiative transfer effects in the intergalactic medium. Additionally, due to systematic and statistical errors single η values poorly trace the spectral shape of the radiation field. However, on average the radiation field near the quasars is harder than far away from them, suggesting a local influence of the quasars in transverse direction to the line of sight.

- **A physical measure of the transverse proximity effect:**
  Using only the H I Lyα forest, no transverse proximity effect of these seven quasars was detected. Neither it was predicted to be very strong. In fact, in some cases the H I Lyα absorption is higher than on average, suggesting the presence of local overdensities around the foreground quasars that mask a transverse proximity effect. We found that the UV spectral shape traces the transverse proximity effect even in overdense regions or at large distances where it is not predicted to be significant in the H I forest. Moreover, due to the hard spectral energy distribution of quasars compared to inactive galaxies, a harder radiation field near quasars is expected. Thus, the spectral hardness is a sensitive physical measure of the transverse proximity effect that is able to break the overdensity degeneracy that affects the traditional search for the transverse proximity effect.

- **Lower limits on the quasar lifetime:**
  Our detection of the transverse proximity effect implies lower limits on the quasar lifetime of $t_{\rm Q} \gtrsim 10$–30 Myr depending on the separation between the quasar and the background sightline. These are consistent with other more indirect estimates (e.g. Martini 2004).

6.2. Future prospects

Our findings provide several opportunities for further investigations of the proximity effect and the three-dimensional distribution of the cosmic web:

- **Transverse proximity effect in spectral hardness from He II absorption:**
  We have revealed the transverse proximity effect in spectral hardness towards two of the six currently known sightlines with intergalactic He II absorption. Whereas two of the remaining sightlines are not useful because of lacking data quality (SDSS J2346−0016 at $z = 3.50$, Zheng et al. 2004) or a low-redshift intervening DLA truncating the far-UV flux (PKS 1935−692 at $z = 3.18$, Anderson et al. 1999) the surroundings of the other two (QSO 1157+3143 at $z \simeq 3.0$ studied by Reimers et al. (2005) and HS 1700+6416 at $z = 2.72$ studied by Fechner et al. (2006)) could be surveyed for quasars that might correspond to incidences of a hard radiation field. In particular, since the He II forest has been resolved by FUSE towards HS 1700+6416, quasars nearby this sightline could shed further light on the UV spectral shape variations induced by local sources. However, the limited number of sightlines with observable He II absorption clearly limits our so far successful approach to reveal the transverse proximity effect.
  In the near future, the Cosmic Origins Spectrograph (COS) to be installed on the Hubble Space Telescope (HST) will provide He II absorption spectra of UV-transparent quasars that are too faint to be observed with the Far-Ultraviolet Spectroscopic Explorer (FUSE). A cross-correlation of quasar catalogues with UV imaging source catalogues from the Galaxy Evolution Explorer (GALEX) will yield the targets whose far-UV flux is likely unabsorbed. These new sightlines will provide new opportunities to characterise the fluctuating shape of the UV background and to correlate them with known sources.

- **Transverse proximity effect in spectral hardness from metal line systems:**
  Alternatively, photoionisation modelling of metal line systems could provide constraints on the spectral shape of the ionising field. In Chapter 5 we have performed such an analyis for three metal line systems near the three foreground quasars, but our results were ambiguous. Unblended transitions of several ions are needed to constrain the spectral shape. Therefore, suitable metal line systems might be rare. However, quasars likely reside in overdense regions which are likely metal-enriched. Thus, metal line systems near quasars might frequently occur. In fact, many quasars show associated metal absorption systems along their lines of sight. We have shown in Chapter 5 that the metal line systems near the foreground quasars of HE 2347−4342 also fulfill the usual definition of associated systems in terms of relative velocity.
  Shortly before this work was finished, Gonçalves et al. (2007) published a study on highly ionised metal absorption systems near foreground quasars towards the quasar triplet KP76, KP77 and KP78 at $z \simeq 2.5$ separated by 2–3′ on the sky. The traditional line counting approach did not yield evidence for a transverse proximity effect in this well-studied triplet (Crotts & Fang 1998). This illustrates that metal line systems have the potential to reveal the transverse proximity effect in spectral hardness.

- **The overdense quasar environment:**
  The Lyα forest absorption near the quasar traces the baryonic structure in a probably overdense region. Absorption statistics of the Lyα forest on background sightlines near

foreground quasars can be used to map the average forest absorption in the quasar vicinity (Croft 2004; Hennawi et al. 2006). With an independent estimate of the UV background it is possible to disentangle the proximity effect from the intrinsic density structure near the quasar (Rollinde et al. 2005; Guimarães et al. 2007). In this way Faucher-Giguère et al. (2007) and Kim & Croft (2007) have proposed to estimate the average mass of a quasar host halo from the line-of-sight proximity effect and the transverse proximity effect, respectively.

- **Transverse correlations in the intergalactic medium:**
  The quasar groups discovered in our survey can be used to study the intergalactic matter in three dimensions, either by correlating metal absorption systems observed at small velocity separations towards paired sightlines (e.g. Williger et al. 1996; Dinshaw & Impey 1996) or by correlating the Lyα forest absorption (e.g. Williger et al. 2000; Rollinde et al. 2003; Coppolani et al. 2006; D'Odorico et al. 2006). The low-resolution FORS spectra presented in this work clearly lack the resolution and the S/N to do this, although they might be used to facilitate the inversion the Lyα forest to infer the its large-scale topology (Pichon et al. 2001). Moreover, a correlation of metal line absorption would benefit from an extended wavelength coverage.
  With the upcoming X-shooter spectrograph at the VLT these goals can be accomplished. X-shooter will enable medium-resolution ($R \sim 4500$) spectroscopy of faint $V \lesssim 22$ quasars from the atmospheric UV cutoff to the H band in a single exposure. This spectrograph has the resolution, wavelength coverage and throughput to perform follow-up studies of the intergalactic medium towards the newly discovered quasar groups presented in this work. Of course, similar medium-resolution spectrographs on other telescopes (e.g. ESI at Keck) can be used as well. The central lines of sight of our groups have already been observed at high resolution with UVES and medium-resolution spectra of the quasars presented herein will certainly be gathered in the near future.

References

Anderson, S. F., Hogan, C. J., Williams, B. F., & Carswell, R. F. 1999, AJ, 117, 56
Coppolani, F., Petitjean, P., Stoehr, F., et al. 2006, MNRAS, 370, 1804
Croft, R. A. C. 2004, ApJ, 610, 642
Crotts, A. P. S. & Fang, Y. 1998, ApJ, 502, 16
Dinshaw, N. & Impey, C. D. 1996, ApJ, 458, 73
D'Odorico, V., Viel, M., Saitta, F., et al. 2006, MNRAS, 372, 1333
Faucher-Giguère, C.-A., Lidz, A., Zaldarriaga, M., & Hernquist, L. 2007, ApJ,submitted, astro-ph/0701042
Fechner, C., Baade, R., & Reimers, D. 2004, A&A, 418, 857
Fechner, C. & Reimers, D. 2007, A&A, 461, 847
Fechner, C., Reimers, D., Kriss, G. A., et al. 2006, A&A, 455, 91
Francis, P. J., Palunas, P., Teplitz, H. I., Williger, G. M., & Woodgate, B. E. 2004, ApJ, 614, 75
Gonçalves, T. S., Steidel, C. C., & Pettini, M. 2007, ApJ, in press, arXiv:0711.4113
Guimarães, R., Petitjean, P., Rollinde, E., et al. 2007, MNRAS, 377, 657
Hawkins, M. R. S. 2000, A&AS, 143, 465
Heap, S. R., Williger, G. M., Smette, A., et al. 2000, ApJ, 534, 69
Hennawi, J. F., Prochaska, J. X., Burles, S., et al. 2006, ApJ, 651, 61
Kim, Y.-R. & Croft, R. 2007, MNRAS,submitted, astro-ph/0701012
Martini, P. 2004, in Carnegie Observatories Astrophysics Series Vol. 1: Coevolution of Black Holes and Galaxies, ed. L. C. Ho (Cambridge University Press), 170
Pichon, C., Vergely, J. L., Rollinde, E., Colombi, S., & Petitjean, P. 2001, MNRAS, 326, 597
Reimers, D., Fechner, C., Hagen, H.-J., et al. 2005, A&A, 442, 63
Rollinde, E., Petitjean, P., Pichon, C., et al. 2003, MNRAS, 341, 1279
Rollinde, E., Srianand, R., Theuns, T., Petitjean, P., & Chand, H. 2005, MNRAS, 361, 1015
Williger, G. M., Hazard, C., Baldwin, J. A., & McMahon, R. G. 1996, ApJS, 104, 145
Williger, G. M., Smette, A., Hazard, C., Baldwin, J. A., & McMahon, R. G. 2000, ApJ, 532, 77
Zheng, W., Chiu, K., Anderson, S. F., et al. 2004, AJ, 127, 656

Appendix A

Theory of the transverse proximity effect in a flat Λ universe

ABSTRACT

We derive the necessary equations of the ionisation model introduced by Bajtlik et al. (1988) for the new concordance model with pressureless matter and a cosmological constant. The publications so far considered the Einstein-de Sitter model. We also introduce modifications of the ionisation model due to absorption of ionising radiation along the line of sight. A simple analytic expression for the maximum ω parameter is derived.

A.1. Photoionisation equilibrium

After reionisation the low-density intergalactic medium is kept highly photoionised by the intergalactic UV radiation field. If the intensity of the UV radiation field is approximately constant in time, the intergalactic medium is in photoionisation equilibrium. Consider a pure hydrogen cloud, having a particle number density n, in ionisation equilibrium with the ambient background of UV photons with intensity $J_{\nu,\mathrm{b}}$. The ionisation equilibrium is written as

$$n_{\mathrm{H\,II}}\alpha_{\mathrm{A}}\left(T\right) n_{e,\mathrm{f}} = n_{\mathrm{H\,I}}\Gamma_{\mathrm{b}}, \tag{A.1}$$

where $n_{\mathrm{H\,I}}$ and $n_{\mathrm{H\,II}}$ are the particle number densities of H I and H II, $n_{e,\mathrm{f}}$ is the free-electron density, $\alpha_{\mathrm{A}}(T)$ is the case A recombination coefficient and Γ_{b} is the photoionisation rate due to the UV background, given as

$$\Gamma_{\mathrm{b}} = \int_{\nu_{\mathrm{LL}}}^{\infty} \frac{4\pi J_{\nu,\mathrm{b}}\left(\nu\right)}{h\nu}\,\sigma\left(\nu\right)\mathrm{d}\nu, \tag{A.2}$$

with the Lyman limit frequency ν_{LL} and the photoionisation cross section $\sigma(\nu)$. For hydrogen-like ions we have $\sigma(\nu) = \sigma_{\mathrm{LL}}\left(\nu/\nu_{\mathrm{LL}}\right)^{-3}$. For hydrogen the photoionisation cross section at the Lyman limit is $\sigma_{\mathrm{LL}} = 6.33 \times 10^{-18}$ cm^2. Case A recombination generally applies if the cloud is optically thin in the lines of the Lyman series and all direct recombination photons escape the cloud. For H I $\alpha_{\mathrm{A}}(T) \simeq 2.51 \times 10^{-13} T_{4.3}^{-0.76}$ cm^{-3} s^{-1} at the typical temperatures encountered in the intergalactic medium $T_{4.3} = T/(10^{4.3}\ \mathrm{K}) \simeq 1$ (Fardal et al. 1998). Equation (A.1) is also valid for the column density $N_{\mathrm{H\,I}}$, the projected particle number density along the line of sight to Earth.

A.2. Additional discrete UV sources

In the vicinity of a UV source, such as a luminous quasar, the ionisation rate is locally enhanced so that the ionisation equilibrium changes to

$$n'_{\mathrm{H\,II}}\alpha_{\mathrm{A}}\left(T'\right) n'_{e,\mathrm{f}} = n'_{\mathrm{H\,I}}\left(\Gamma_{\mathrm{b}} + \Gamma_{\mathrm{q}}\right) \tag{A.3}$$

with the local contribution $\Gamma_{\mathrm{q}} = \sum_{j=1}^{m}\Gamma_{\mathrm{q},j}$ by m quasars.

Under the assumption that the additional photoheating due to the quasars is weak and considering the weak temperature dependence of α_{A} we have $\alpha_{\mathrm{A}}(T') \simeq \alpha_{\mathrm{A}}(T)$. Assuming further a pure hydrogen cloud with $n_{e,\mathrm{f}} = n_{\mathrm{H\,II}}$ and considering particle conservation in the absorber we get

$$n_{\mathrm{H\,I}}\Gamma_{\mathrm{b}} \simeq n'_{\mathrm{H\,I}}\left(\Gamma_{\mathrm{b}} + \Gamma_{\mathrm{q}}\right)\left(1 + \frac{n'_{\mathrm{H\,I}}}{n'_{\mathrm{H\,II}}} - \frac{n_{\mathrm{H\,I}}}{n'_{\mathrm{H\,II}}}\right)^{2}. \tag{A.4}$$

Since the hydrogen in the intergalactic medium is highly ionised with $n'_{\mathrm{H\,I}}/n'_{\mathrm{H\,II}} \ll 1$ and $n_{\mathrm{H\,I}}/n'_{\mathrm{H\,II}} \ll 1$, the neutral hydrogen density near the UV source is simply reduced to

$$n'_{\mathrm{H\,I}} \simeq n_{\mathrm{H\,I}}\frac{\Gamma_{\mathrm{b}}}{\Gamma_{\mathrm{b}} + \Gamma_{\mathrm{q}}} = \frac{n_{\mathrm{H\,I}}}{1+\omega} \tag{A.5}$$

with the ratio of the ionisation rates of the local sources and the background

$$\omega = \frac{\Gamma_{\mathrm{q}}}{\Gamma_{\mathrm{b}}}. \tag{A.6}$$

Similarly we can write for the column density

$$N_{\mathrm{H\,I}} = \frac{N_{\mathrm{H\,I},\infty}}{1+\omega} \tag{A.7}$$

where $N_{\mathrm{H\,I},\infty}$ is the column density that would have been observed if the quasar was at infinite distance. Thus, a parameter $\omega \gg 1$ predicts a strong proximity effect.

A.3. The ratio of ionisation rates ω

The ionisation rates of the local quasars and the background depend on redshift (distance). The ionisation rate of the jth quasar is

$$\Gamma_{\mathrm{q},j}(z) = \int_{\nu_{\mathrm{LL}}}^{\infty} \frac{f_{\nu,j}(\nu, z)}{h\nu} \sigma(\nu)\, \mathrm{d}\nu. \tag{A.8}$$

If we consider the quasar luminosity $L_{\nu,j}$ to be constant the quasar flux density $f_{\nu,j}(\nu, z)$ at redshift z at frequency ν in the absorber's rest frame can be written as

$$f_{\nu,j}(\nu, z) = \frac{L_{\nu,j}\left(\nu\left(1 + z'_j\right)\right)}{4\pi d_L^2\left(z_j, z\right)} \left(1 + z'_j\right) \tag{A.9}$$

Here $d_L\left(z_j, z\right)$ and z'_j are the luminosity distance and the redshift of quasar j at today's redshift z_j in the absorber's rest frame at redshift z. The quasar luminosity is linked to the today's flux density $f_{\nu,j}(\nu_{\mathrm{obs}}, 0)$ via

$$L_{\nu,j}\left(\nu\left(1 + z'_j\right)\right) = \frac{4\pi d_L^2\left(z_j, 0\right)}{1 + z_j} f_{\nu,j}\left(\nu\left(\frac{1 + z'_j}{1 + z_j}\right), 0\right) \tag{A.10}$$

with the frequency $\nu_{\mathrm{obs}} = \nu\left(\frac{1+z'_j}{1+z_j}\right)$ that is observed today. Inserting (A.10) into (A.9) we get

$$f_{\nu,j}(\nu, z) = f_{\nu,j}\left(\nu\left(\frac{1 + z'_j}{1 + z_j}\right), 0\right)\left(\frac{1 + z'_j}{1 + z_j}\right)\left(\frac{d_L\left(z_j, 0\right)}{d_L\left(z_j, z\right)}\right)^2. \tag{A.11}$$

The bandwidth term in (A.9) and (A.10) is usually ignored because $z'_j \simeq 0$. Only Liske & Williger (2001) take it into account.

The quasar flux density above the Lyman limit in the quasar rest frame is not directly accessible due to the absorption of the quasar's UV flux in the Lyα forest. It is usually obtained by extrapolating the unabsorbed quasar continuum redward of the Lyα emission line to the Lyman limit. Considering that the quasar continuum can be approximated by a power law $f_{\nu,j} \propto \nu^{-\alpha_j}$ the quasar flux density becomes

$$f_{\nu,j}(\nu, z) = f_{\nu,j}\left(\frac{\nu_{\mathrm{LL}}}{1 + z_j}, 0\right)\left(\frac{\nu}{\nu_{\mathrm{LL}}}\right)^{-\alpha_j} \frac{\left(1 + z'_j\right)^{-\alpha_j+1}}{1 + z_j} \left(\frac{d_L\left(z_j, 0\right)}{d_L\left(z_j, z\right)}\right)^2. \tag{A.12}$$

After inserting (A.11) into (A.8) and integrating for $\alpha_j > -3$ the ionisation rate at redshift z of quasar j is

$$\Gamma_{\mathrm{q},j}(z) = \frac{\sigma_{\mathrm{LL}}}{h\left(\alpha_j + 3\right)} f_{\nu,j}\left(\frac{\nu_{\mathrm{LL}}}{1 + z_j}, 0\right) \frac{\left(1 + z'_j\right)^{-\alpha_j+1}}{1 + z_j} \left(\frac{d_L\left(z_j, 0\right)}{d_L\left(z_j, z\right)}\right)^2. \tag{A.13}$$

If the UV background intensity is a power law in frequency $J_{\nu,\mathrm{b}} \propto \nu^{-\alpha_{J_\nu}}$ then

$$\Gamma_{\mathrm{b}}(z) = \frac{4\pi\sigma_{\mathrm{LL}}}{h\left(\alpha_{J_\nu} + 3\right)} J_{\nu_{\mathrm{LL}}}(z) \tag{A.14}$$

for $\alpha_{J_\nu} > -3$ with the Lyman limit intensity $J_{\nu_{\mathrm{LL}}}(z)$. With this approximation the ratio of ionisation rates becomes a flux ratio

$$\omega(z) = \sum_{j=1}^{m} \frac{f_{\nu,j}\left(\frac{\nu_{\mathrm{LL}}}{1+z_j}, 0\right)}{4\pi J_{\nu_{\mathrm{LL}}}(z)} \left(\frac{\alpha_{J_\nu} + 3}{\alpha_j + 3}\right) \frac{\left(1 + z'_j\right)^{-\alpha_j+1}}{1 + z_j} \left(\frac{d_L\left(z_j, 0\right)}{d_L\left(z_j, z\right)}\right)^2. \tag{A.15}$$

From the above equation the original version calculated by Bajtlik et al. (1988) can be obtained by setting $z'_j = 0$ and $\alpha_{J_\nu} > -3 = \alpha_j$ for a single quasar for an assumed Einstein-de Sitter model (see below).

A.4. Redshifts and luminosity distances

The redshift z' and the luminosity distances $d_L\left(z_j, 0\right)$ and $d_L\left(z_j, z\right)$ in eq. (A.15) still have to be calculated to obtain ω. To do this, different levels of complexity are involved for the line-of-sight proximity effect and the transverse proximity effect, respectively.

A.4.1. Line-of-sight proximity effect

On the line of sight the redshift z' of the quasar as observed at the absorber can be easily obtained by

$$1 + z' = \frac{1 + z_j}{1 + z} \tag{A.16}$$

The luminosity distance $d_L\left(z_j, z\right)$ can be generalised from the standard expression for the luminosity distance that we derive today $d_L\left(z_j, 0\right)$ as

$$d_L\left(z_j, z\right) = (1 + z')\, a\,(z)\, r\left(z_j, z\right) \tag{A.17}$$

with the scale factor $a(z) = 1/\,(1 + z)$ and the comoving distance $r(z_j, z)$ between the quasar and the absorber. The luminosity distance depends on the assumed cosmological model. It will be given here for the Einstein-de Sitter universe that is considered in most publications on the proximity effect and for the present concordance model: a flat universe with matter and a cosmological constant.

Einstein-de Sitter universe

In the Einstein-de Sitter universe the luminosity distances are

$$d_L\left(z_j, 0\right) = \frac{2c}{H_0}\left(1 + z_j - \sqrt{1 + z_j}\right) \tag{A.18}$$

and

$$d_L\left(z_j, z\right) = \frac{2c}{H(z)}\left(1 + z' - \sqrt{1 + z'}\right) = \frac{2c}{H_0\,(1 + z)^{3/2}}\left(\frac{1 + z_j}{1 + z} - \sqrt{\frac{1 + z_j}{1 + z}}\right) \tag{A.19}$$

with the Hubble constant H_0 and the speed of light c.

Λ-universe

In a flat Λ-universe with matter density parameter Ω_m and positive density parameter of the cosmological constant Ω_Λ the luminosity distance

$$d_L\left(z_j, 0\right) = (1 + z)\,\frac{c}{H_0}\int_0^{z_j}\frac{\mathrm{d}z''}{\sqrt{\Omega_\mathrm{m}\,(1 + z'')^3 + \Omega_\Lambda}} \tag{A.20}$$

can be generalised to

$$d_L\left(z_j, z\right) = (1 + z')\,\frac{c}{H(z)}\int_0^{z'}\frac{\mathrm{d}z''}{\sqrt{\Omega_\mathrm{m}(z)\,(1 + z'')^3 + \Omega_\Lambda(z)}} \tag{A.21}$$

with the scaled Hubble parameter

$$H\,(z) = H_0\sqrt{\Omega_\mathrm{m}\,(1 + z)^3 + \Omega_\Lambda} \tag{A.22}$$

and the scaled density parameters

$$\Omega_\mathrm{m}\,(z) = \frac{\Omega_\mathrm{m}\,(1 + z)^3}{\Omega_\mathrm{m}\,(1 + z)^3 + \Omega_\Lambda} \tag{A.23}$$

$$\Omega_\Lambda\,(z) = 1 - \Omega_\mathrm{m}\,(z)\,. \tag{A.24}$$

Thus we have for the luminosity distance in case of the line-of-sight proximity effect

$$d_L\left(z_j, z\right) = \left(\frac{1 + z_j}{1 + z}\right)\frac{c}{H_0\sqrt{\Omega_\mathrm{m}\,(1 + z)^3 + \Omega_\Lambda}}\int_0^{\frac{1+z_j}{1+z}-1}\frac{\mathrm{d}z''}{\sqrt{\frac{\Omega_\mathrm{m}(1+z)^3}{\Omega_\mathrm{m}(1+z)^3+\Omega_\Lambda}\left((1 + z'')^3 - 1\right) + 1}}\,. \tag{A.25}$$

Most previous studies of the proximity effect used the Einstein-de Sitter model that yields an analytic formula for the impact parameter ω. Phillipps et al. (2002) studied the impact of cosmological models on the proximity effect and the derived UV background intensity. However, they apparently did not scale the density parameters according to (A.23) and (A.24). Fortunately, they limited their discussion to an empty universe and the Einstein-de Sitter model, leaving their results unaffected.

A.4.2. Transverse proximity effect

The generalised luminosity distance (A.17) still applies and the comoving distance $r(z_j, z)$ is given by the Euclidean cosine rule that is valid in a flat universe (e.g. Peacock 1999)

$$r\left(z_j, z\right) = \sqrt{r^2\left(z_j\right) + r^2(z) - 2r\left(z_j\right) r(z) \cos\vartheta} \tag{A.26}$$

where we have introduced the separation angle ϑ between the background line of sight and the foreground quasar at z_j. However, it is hard to calculate z'.

Einstein-de Sitter universe

Liske (2000) presented a closed solution to get z' for all homogeneous zero-pressure Friedmann cosmologies without a cosmological constant. Hence, the solution for the Einstein-de Sitter universe is

$$z' = \frac{2P^2}{\left(1/2 - 2P^2\right)^2}\left(\frac{3}{2} - 2P^2 + \frac{1}{2P}\right) \tag{A.27}$$

with

$$P^2 = \frac{1}{4\left(1 + z_j\right)}\left(P_+^2 \sin^2\frac{\vartheta}{2} + P_-^2 \cos^2\frac{\vartheta}{2}\right), \tag{A.28}$$

$$P_+ = 2\sqrt{\left(1 + z_j\right)(1 + z)} - \sqrt{1 + z_j} - \sqrt{1 + z} \tag{A.29}$$

and

$$P_- = \sqrt{1 + z_j} - \sqrt{1 + z}. \tag{A.30}$$

With equations (A.26), (A.27) and the comoving distance $r(z) = \frac{2c}{H_0}\left(1 - 1/\sqrt{1 + z}\right)$ the luminosity distance $d_L\left(z_j, z\right)$ (A.17) is fully specified.

Λ-universe

Since z' does not have a closed form in cosmological models with a cosmological constant, the proper distance integral of the quasar as seen from the absorber has to be inverted numerically. We have

$$\frac{r\left(z_j, z\right)}{1 + z} = \frac{c}{H_0\sqrt{\Omega_\mathrm{m}(1 + z)^3 + \Omega_\Lambda}} \int_0^{z'} \frac{\mathrm{d}z''}{\sqrt{\frac{\Omega_\mathrm{m}(1+z)^3}{\Omega_\mathrm{m}(1+z)^3+\Omega_\Lambda}\left(\left(1 + z''\right)^3 - 1\right) + 1}}, \tag{A.31}$$

where the transverse comoving distance is given by (A.26) and only z' is unknown. Again the luminosity distance can be obtained via (A.17).

A.5. Attenuation of ionising radiation in the intergalactic medium

So far we have assumed that the ionising radiation of the local quasars is not absorbed by the intergalactic medium. The ratio of ionisation rates ω (A.15) is strictly valid only in empty space. Since the intergalactic medium is mostly optically thin in H I at the redshifts under consideration, the expected attenuation is small. However, the effective optical depth of the IGM in He II at the same redshifts is much larger, so attenuation might be significant. Accurate column densities are required to calculate the absorption. Because the transverse structures between two close-by sightlines in the IGM remain unknown, such calculations are limited to the line-of-sight proximity effect. An extension to the transverse proximity effect requires the assumption of spatial symmetry around the quasar. Heap et al. (2000) modelled the absorption of ionising quasar radiation on the line of sight. In principle, their calculations should be consistent with the ones carried out below, but we noted some confusion in their notation. Therefore, we verified their results independently. Smette et al. (2002) extended the absorption model to the transverse proximity effect, which, however, is limited to sources at very small distances to the background line of sight since they assumed that the radiation of the foreground sources penetrate the same absorbers that are observed on the line of sight.

Consider a series of m intergalactic absorbers at $z_1, \cdots, z_m$ with column densities $N_1, \cdots, N_m$ in front of a quasar at redshift z_q ($z_\mathrm{q} > z_1 > \cdots > z_m$). Let the absorber be composed of fully ionised particles and hydrogen-like ions, in particular H I and He II. The unabsorbed flux density of a quasar that penetrates a specific point in the IGM is given by eq. (A.12). Thus, the quasar flux density impinging on the 1st absorber $f_\nu^\mathrm{in}(\nu, z_1)$ is simply this unattenuated flux. The quasar flux density escaping the 1st absorber is

$$f_\nu^\mathrm{out}(\nu, z_1) = f_\nu^\mathrm{in}(\nu, z_1) e^{-\tau_1(\nu)} = f_\nu^\mathrm{in}(\nu, z_1) e^{-N_1\sigma_\mathrm{LL}(\nu/\nu_\mathrm{LL})^{-3}} \tag{A.32}$$

for absorber rest-frame frequencies $\nu \geq \nu_{\mathrm{LL}}$. The flux density that penetrates the jth absorber is the product of the unabsorbed flux density and the frequency-dependent attenuation by the foreground absorbers corrected for additional redshift between them

$$\begin{aligned} f_\nu^{\mathrm{in}}(\nu, z_j) &= f_\nu\left(\frac{\nu_{\mathrm{LL}}}{1+z_{\mathrm{q}}}, 0\right)\left(\frac{\nu}{\nu_{\mathrm{LL}}}\right)^{-\alpha_{\mathrm{q}}}\left(\frac{1+z_{\mathrm{q}}}{1+z_j}\right)^{-\alpha_{\mathrm{q}}+1}\frac{1}{1+z_{\mathrm{q}}}\left(\frac{d_L\left(z_{\mathrm{q}},0\right)}{d_L\left(z_{\mathrm{q}},z_j\right)}\right)^2 \\ &\times\exp\left[-\sum_{k=1}^{j-1} N_k\sigma_{\mathrm{LL}}\left(\frac{\nu(1+z_k)}{\nu_{\mathrm{LL}}(1+z_j)}\right)^{-3}\right]. \end{aligned} \tag{A.33}$$

Equation (A.8) gives the quasar ionisation rate

$$\Gamma_{\mathrm{q}}(z_j) = \frac{\sigma_{\mathrm{LL}} f_\nu\left(\frac{\nu_{\mathrm{LL}}}{1+z_{z_{\mathrm{q}}}}, 0\right)}{h\left(1+z_{\mathrm{q}}\right)}\left(\frac{1+z_{\mathrm{q}}}{1+z_j}\right)^{-\alpha_{\mathrm{q}}+1}\left(\frac{d_L\left(z_{\mathrm{q}},0\right)}{d_L\left(z_{\mathrm{q}},z_j\right)}\right)^2\int_1^\infty x^{-\alpha_{\mathrm{q}}-4}\exp\left[-\sum_{k=1}^{j-1}N_k\sigma_{\mathrm{LL}}x^{-3}\left(\frac{1+z_k}{1+z_j}\right)^{-3}\right]\mathrm{d}x \tag{A.34}$$

with the frequency ratio $x = \nu/\nu_{\mathrm{LL}}$.

The attenuation of the quasar flux in the He II forest softens the ionising spectrum of the quasar. The spectral shape of the UV background is given by the softness parameter $S_{\mathrm{b}} = \Gamma_{\mathrm{b,H\,I}}/\Gamma_{\mathrm{b,He\,II}}$ or the column density ratio $\eta_{\mathrm{b}} = N_{\mathrm{He\,II}}/N_{\mathrm{H\,I}} \simeq 0.42 S_{\mathrm{b}}$ if both species are highly photoionised (Fardal et al. 1998). Assuming that η_{b} is known we can estimate the change of η as a function of distance to the observed background quasar. In the vicinity of the quasar we have

$$\eta = \eta_{\mathrm{b}}\left(\frac{1+\omega_{\mathrm{H\,I}}}{1+\omega_{\mathrm{He\,II}}}\right) \tag{A.35}$$

with the ratios of ionisation rates of quasar (eq. (A.34)) and background for both species.

A.6. The maximum ratio of ionisation rates

A simple estimate of the predicted impact of a quasar at redshift z_{q} onto its surroundings can be obtained by considering its maximum ratio of ionisation rates $\omega_{\max} = \omega(z_{\mathrm{q}})$. For a foreground quasar the luminosity distance between two lines of sight at redshift z_{q} becomes

$$d_L(z_{\mathrm{q}}, z_{\mathrm{q}}) = \left(\frac{1+z'}{1+z_{\mathrm{q}}}\right) r(z_{\mathrm{q}}, 0)\sqrt{2-2\cos\vartheta}, \tag{A.36}$$

where we have used equations (A.17) and (A.26). In conjunction with eq. (A.15) the maximum ω parameter is

$$\omega_{\max} = \frac{f_\nu\left(\frac{\nu_{\mathrm{LL}}}{1+z_{\mathrm{q}}}, 0\right)}{4\pi J_{\nu_{\mathrm{LL}}}\left(z_{\mathrm{q}}\right)}\left(\frac{\alpha_{J_\nu}+3}{\alpha_{\mathrm{q}}+3}\right)\frac{\left(1+z'_{\mathrm{q}}\right)^{-\alpha_{\mathrm{q}}-1}\left(1+z_{\mathrm{q}}\right)^3}{(2-2\cos\vartheta)}. \tag{A.37}$$

The maximum ω is almost independent on the cosmological model because z'_{q} is similar and very small in any model, so that it can be safely neglected for small sightline separations. Furthermore, for the small angles of interest here $\cos\vartheta \simeq 1 - \vartheta^2/2$. Thus, we obtain the simple expression

$$\omega_{\max} \simeq \frac{f_\nu\left(\frac{\nu_{\mathrm{LL}}}{1+z_{\mathrm{q}}}, 0\right)}{4\pi J_{\nu_{\mathrm{LL}}}\left(z_{\mathrm{q}}\right)}\left(\frac{\alpha_{J_\nu}+3}{\alpha_{\mathrm{q}}+3}\right)\frac{\left(1+z_{\mathrm{q}}\right)^3}{\vartheta^2} \tag{A.38}$$

that does not require any numerical integral inversion.

A.7. Observable signatures in the Lyman forest

The reduction in the column densites of the lines due to the proximity effect has a direct consequence on the observables of the Lyman forest. If we assume that all lines above a certain column density threshold $N_{\mathrm{thresh},\infty}$ can be detected far from the quasar, the lines close to this threshold will not be observable near the quasar because they drop below the detection threshold, which changes near the quasar to $N_{\mathrm{thresh}} = N_{\mathrm{thresh},\infty}(1+\omega)$. Therefore the line number density generally evolving with redshift far from the quasar as

$$\frac{\mathrm{d}\mathcal{N}_\infty}{\mathrm{d}z} = A\,(1+z)^\gamma \tag{A.39}$$

changes to

$$\frac{\mathrm{d}\mathcal{N}}{\mathrm{d}z} = \frac{\mathrm{d}\mathcal{N}_\infty}{\mathrm{d}z}\frac{\mathrm{d}\mathcal{N}}{\mathrm{d}\mathcal{N}_\infty} = A\,(1+z)^\gamma\,(1+\omega)^{1-\beta} \tag{A.40}$$

for a power law column density distribution $\mathrm{d}\mathcal{N}/\mathrm{d}N \propto N^{-\beta}$ (Bajtlik et al. 1988).

Most published works focus on the reduction of the line density near the quasar in order to reveal the proximity effect. However, only the weakest lines will become undetectable, whereas the others become systematically weakened but remain in the line sample. An alternative approach uses the average absorption in the forest, given by the effective optical depth

$$\tau_{\mathrm{eff},\infty} = B\,(1+z)^{\gamma+1} \tag{A.41}$$

(Zuo 1993) if all lines evolve with redshift as a power law (A.39). B is a proportionality constant. For the effective optical depth in presence of a nearby quasar one can write similarly to equation (A.40)

$$\tau_{\mathrm{eff}} = \tau_{\mathrm{eff},\infty}\,(1+\omega)^{1-\beta} = B\,(1+z)^{\gamma+1}\,(1+\omega)^{1-\beta} \tag{A.42}$$

(Liske & Williger 2001). Observationally, the effective optical depth can be easily determined also at low resolution without having to define a line sample. However, the column density distribution has to be taken from high-resolution spectra.

References

Bajtlik, S., Duncan, R. C., & Ostriker, J. P. 1988, ApJ, 327, 570
Fardal, M. A., Giroux, M. L., & Shull, J. M. 1998, AJ, 115, 2206
Heap, S. R., Williger, G. M., Smette, A., et al. 2000, ApJ, 534, 69
Liske, J. 2000, MNRAS, 319, 557
Liske, J. & Williger, G. M. 2001, MNRAS, 328, 653
Peacock, J. A. 1999, Cosmological Physics (Cambridge University Press)
Phillipps, S., Horleston, N. J., & White, A. C. 2002, MNRAS, 336, 587
Smette, A., Heap, S. R., Williger, G. M., et al. 2002, ApJ, 564, 542
Zuo, L. 1993, A&A, 278, 343

Appendix B

Atlas of slitless WFI spectra of objects with emission lines

B.1. WFI spectra of rediscovered quasars in the survey fields

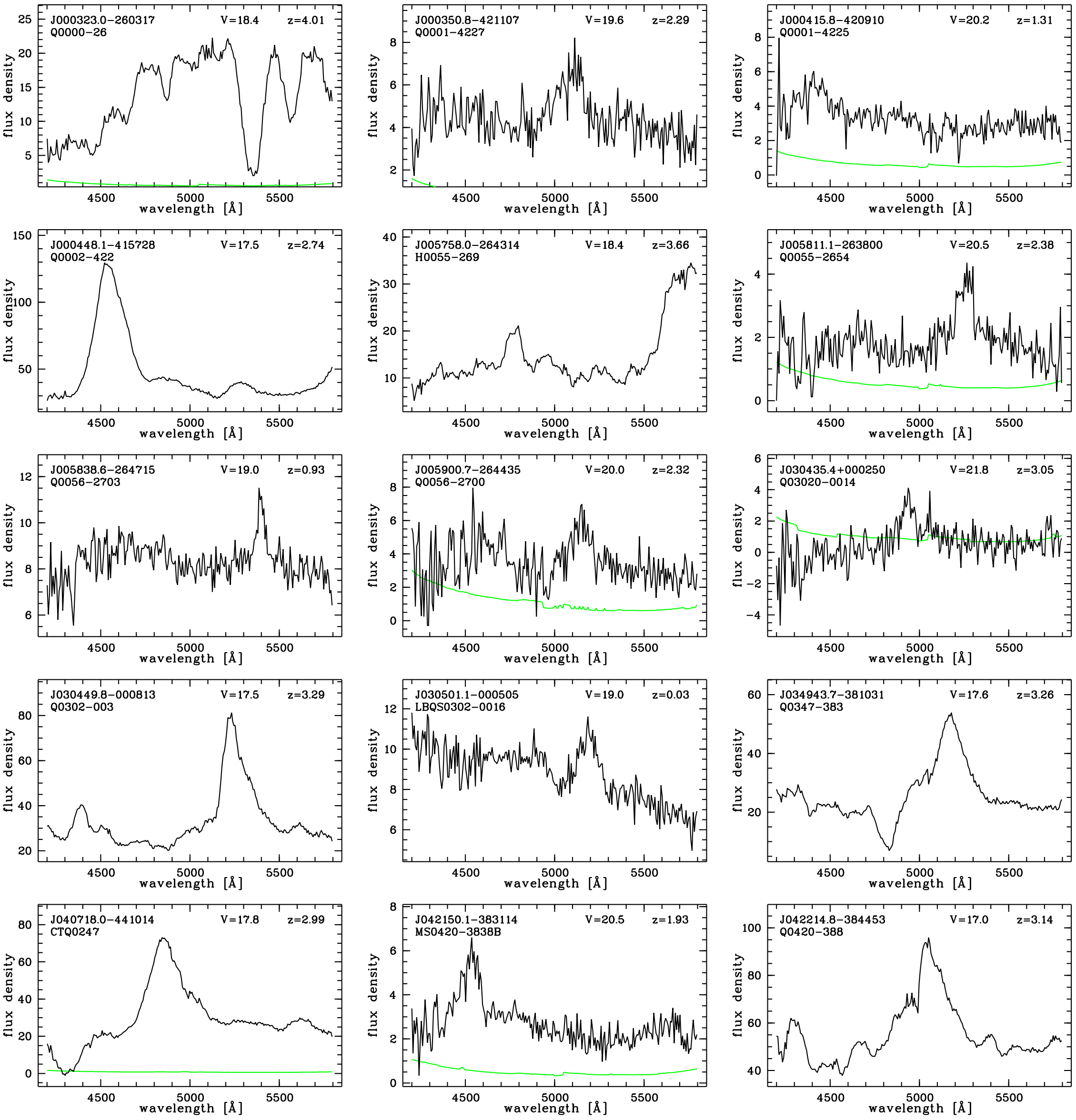

Fig. B.1. RA-ordered list of slitless WFI spectra (black) and 1σ noise arrays (in green/grey at low S/N) of 38 rediscovered quasars and AGN in the survey fields. The (approximate) flux densities are given in 10^{-17} erg cm^{-2} s^{-1} Å^{-1}. Labelled are the celestial coordinates (format: `HHMMSS.S±DDMMSS`, J2000), the quasar name, its redshift measured in the WFI spectrum and the integrated V magnitude. Q 0000−26 is automatically detected due to the DLAs in the forest.

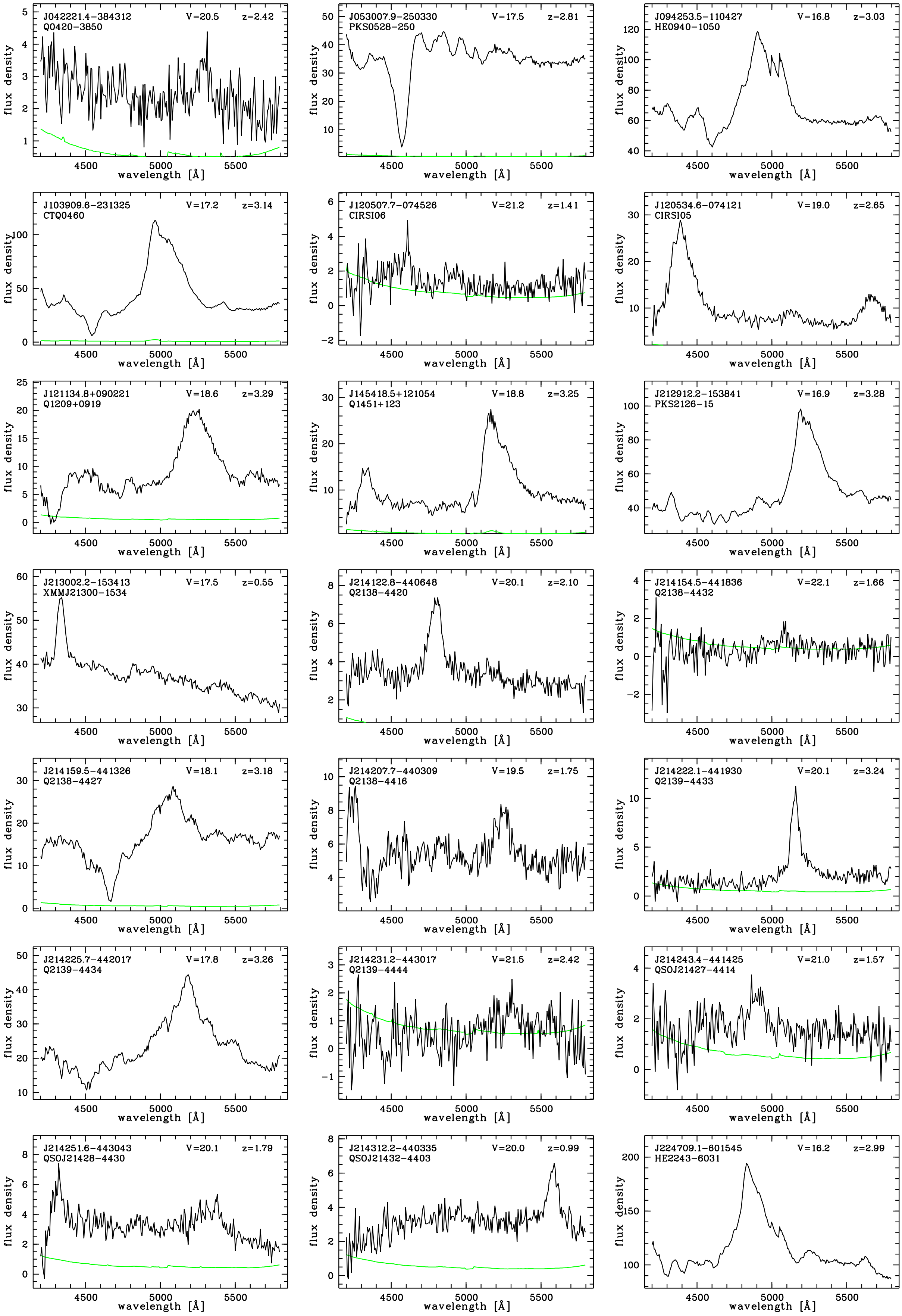

Fig. B.1. continued.

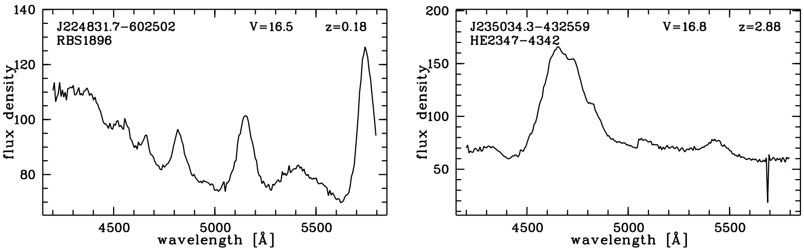

Fig. B.1. continued.

B.2. WFI spectra of previously unknown quasar candidates included in the follow-up with FORS2

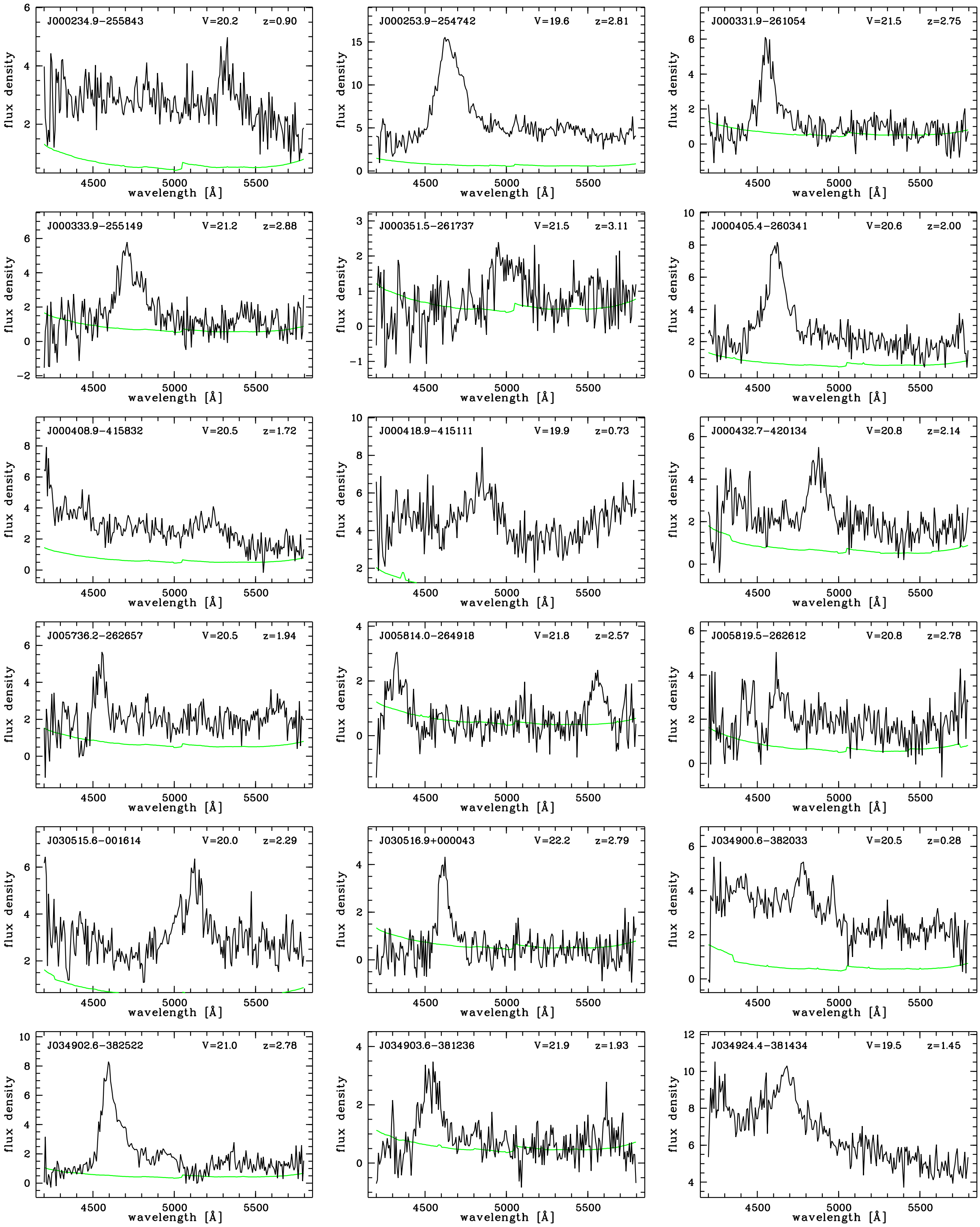

Fig. B.2. RA-ordered list of slitless WFI spectra of the 81 previously unknown quasar candidates included in the follow-up with FORS2. The spectra are shown in black together with their 1σ noise arrays (green/grey) if the S/N is low. The (approximate) flux densities are given in 10^{-17} erg cm^{-2} s^{-1} Å^{-1}. Labelled are the celestial coordinates (format: `HHMMSS.S±DDMMSS`, J2000), the integrated V magnitude and the redshift measured in the WFI spectrum knowing the actual redshift from the FORS2 spectrum. Based on the FORS2 spectra all objects except J 034900.6−382033 were confirmed as quasars.

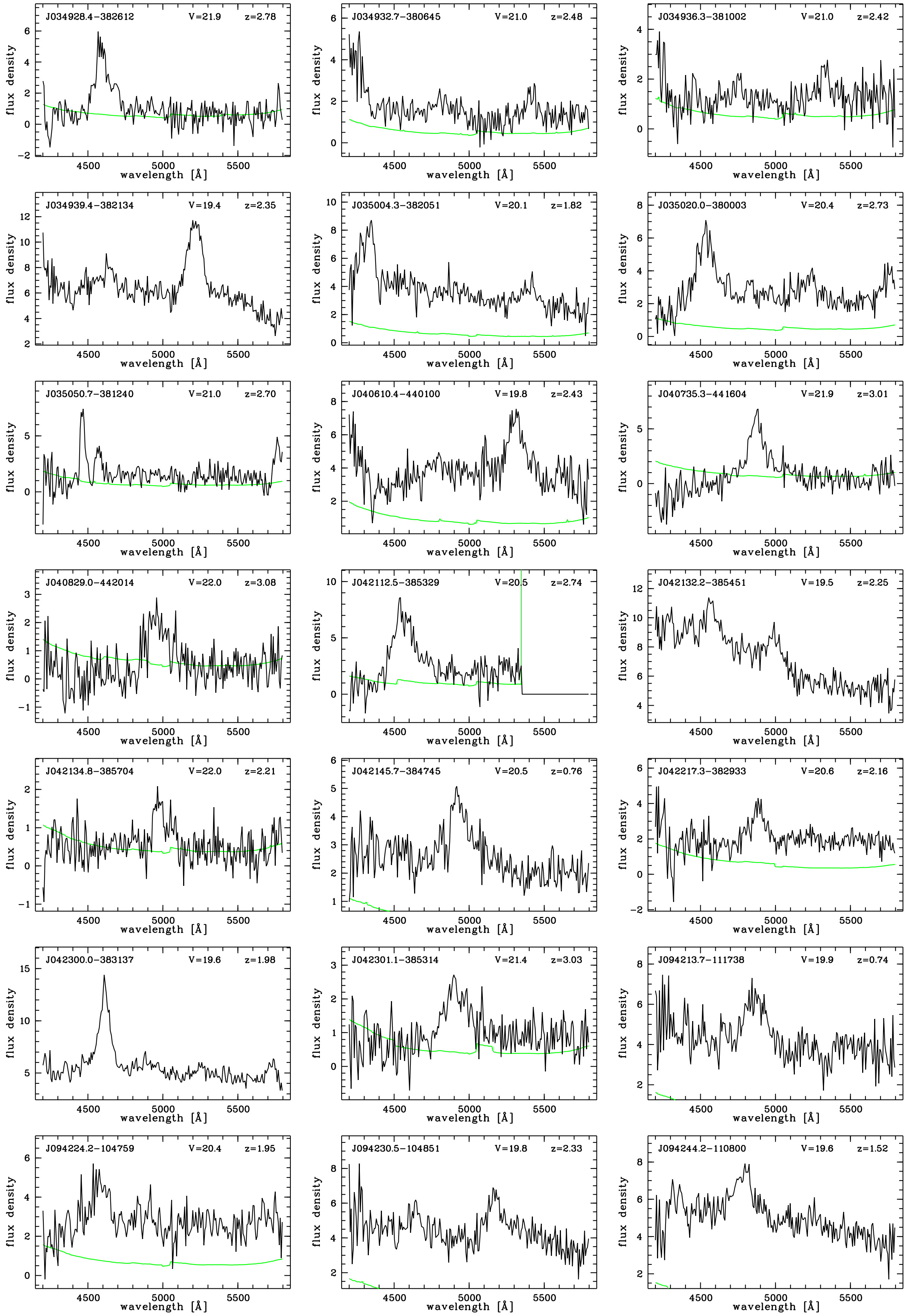

Fig. B.2. continued.

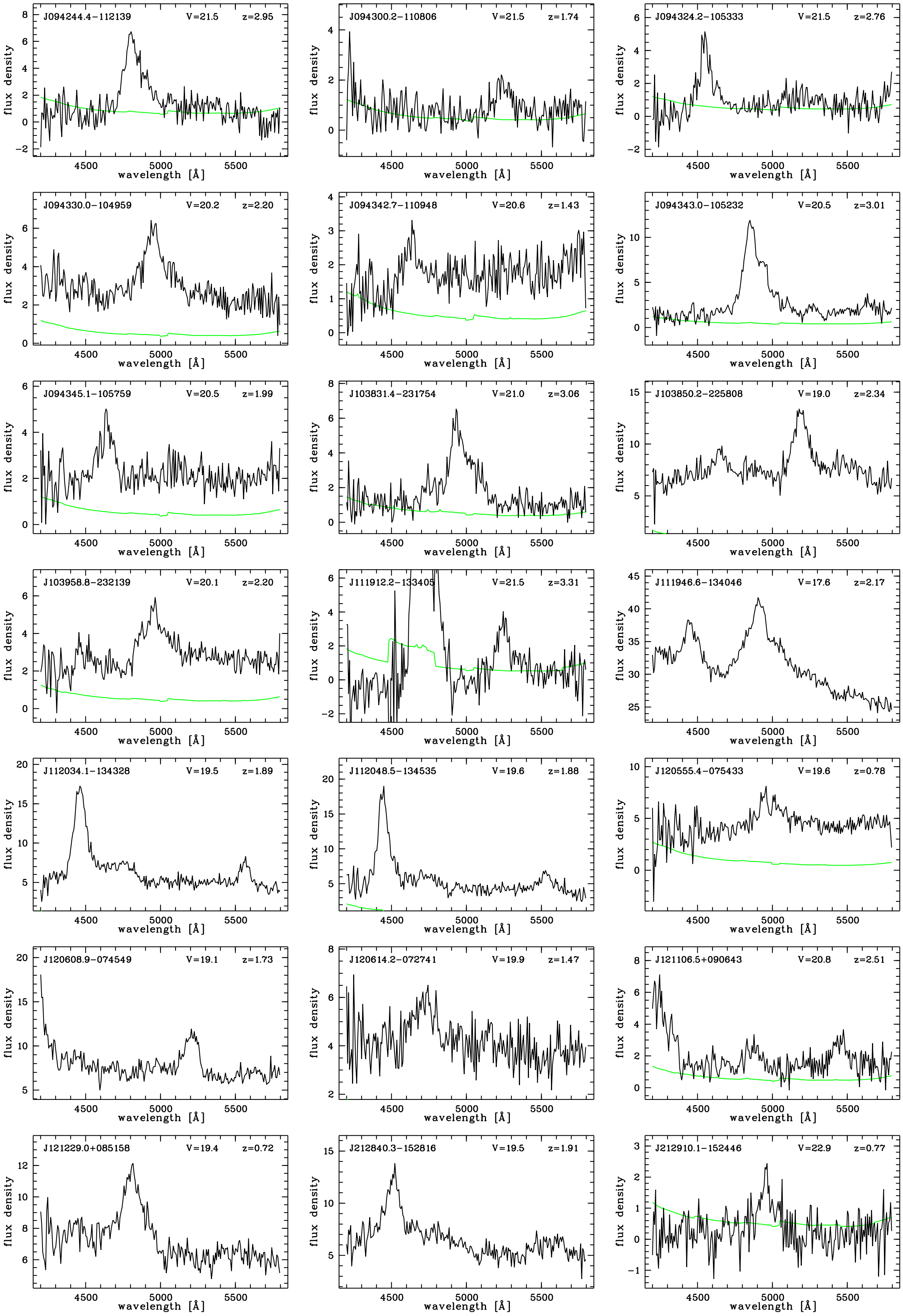

Fig. B.2. continued. Note that the blue part of the spectrum of QSO J11192−1334 is contaminated by zero-order residuals. Due to its location at the edge of the field of view it is recorded only at one WFI rotation angle.

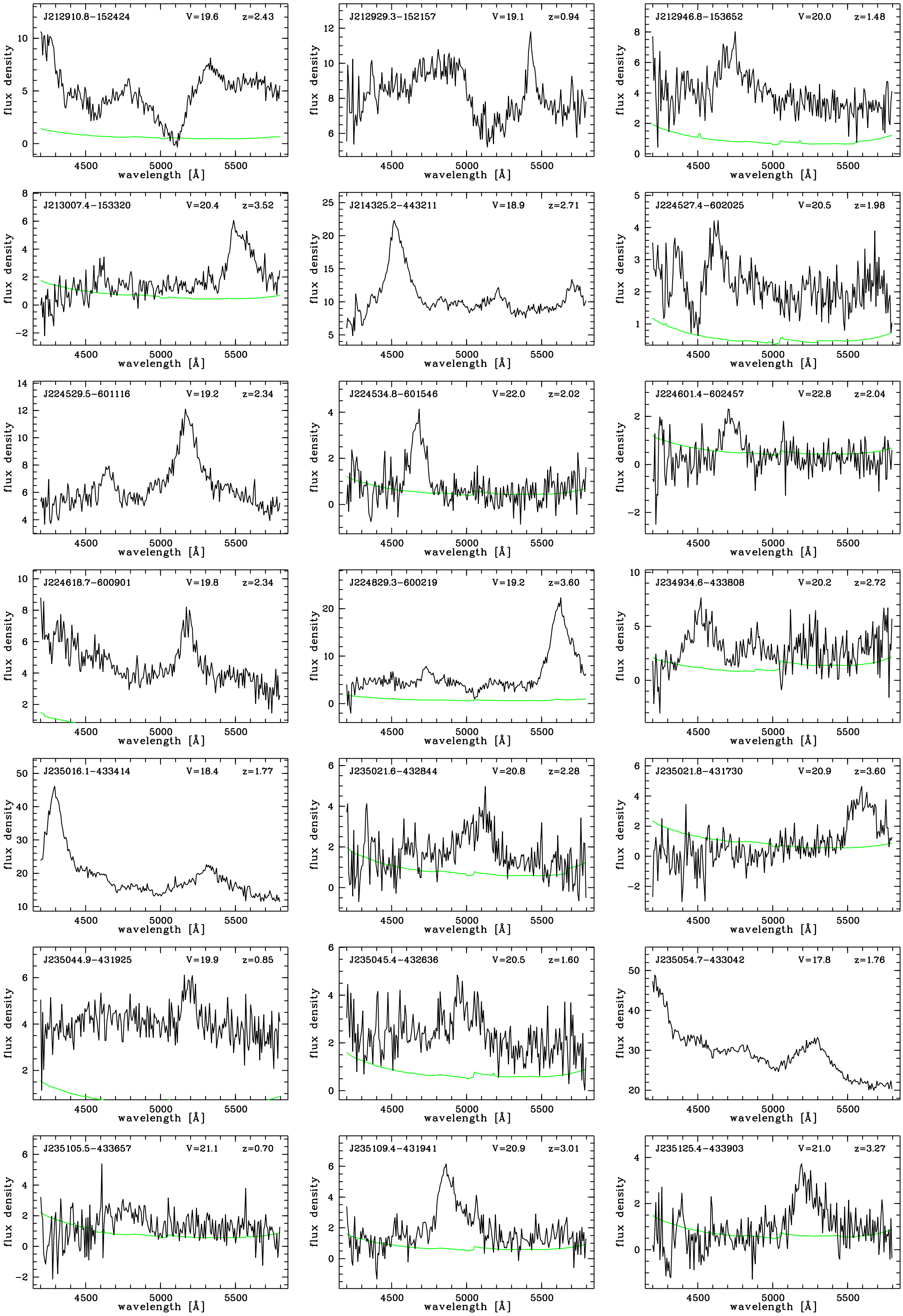

Fig. B.2. continued.

B.3. WFI spectra of remaining unknown quasar candidates without follow-up spectra

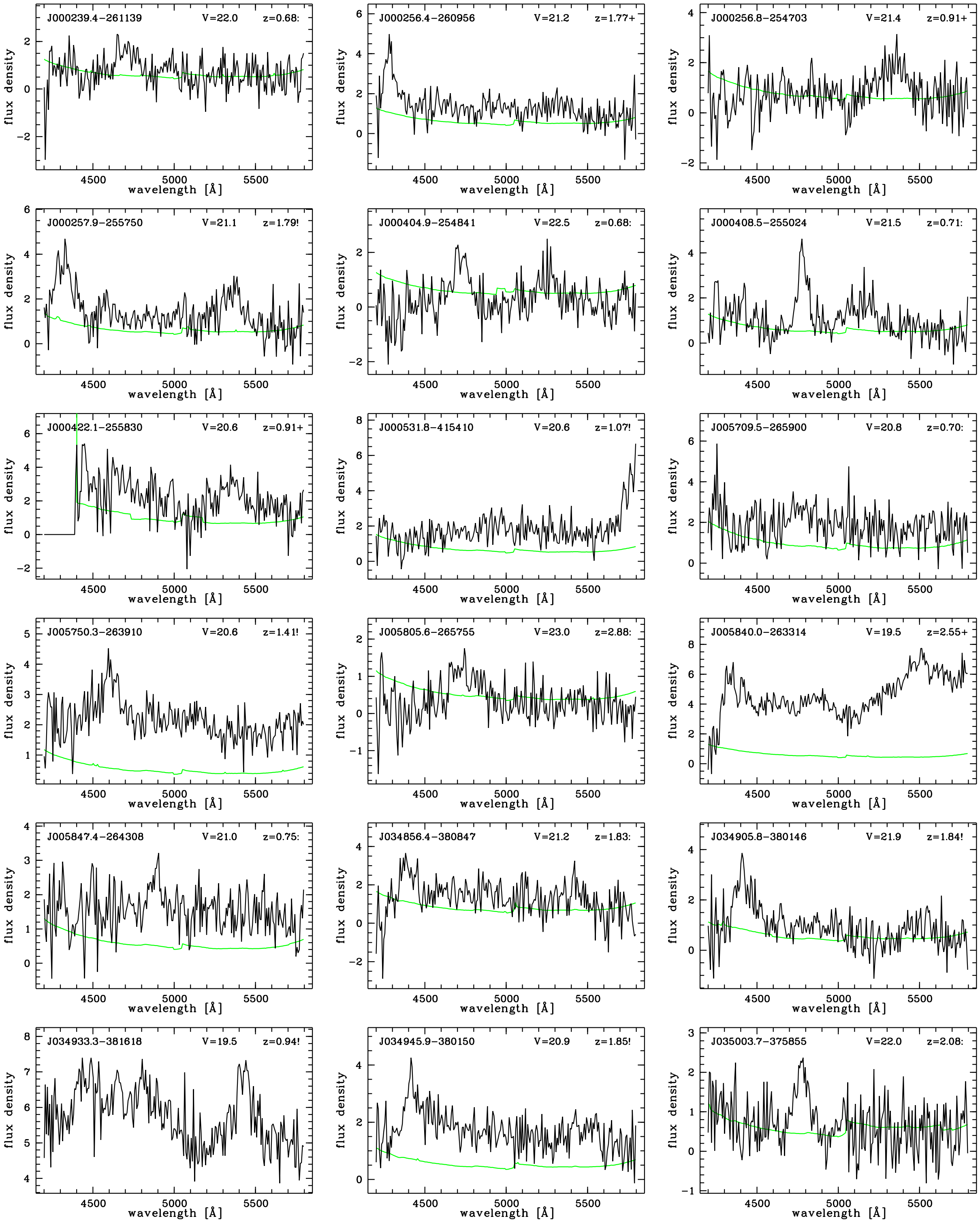

Fig. B.3. RA-ordered list of slitless WFI spectra of 88 unknown quasar candidates without follow-up spectra. The spectra are shown in black together with their 1σ noise arrays (green/grey) if the S/N is low. The (approximate) flux densities are given in 10^{-17} erg cm^{-2} s^{-1} Å^{-1}. Labelled are the celestial coordinates (format: `HHMMSS.S±DDMMSS`, J2000), the integrated V magnitude and the estimated redshift. Ambiguous redshifts guessed from a single emission line are marked by a colon. Plus signs mark rather robust redshift estimates. Exclamation marks stand for secure redshifts based on the shape of a single line or the detection of two lines either in the principal spectral range 4200 Å$\leq \lambda \leq$5800 Å or the R band spectra if available. J005840.0−263314 is a prominent BAL QSO.

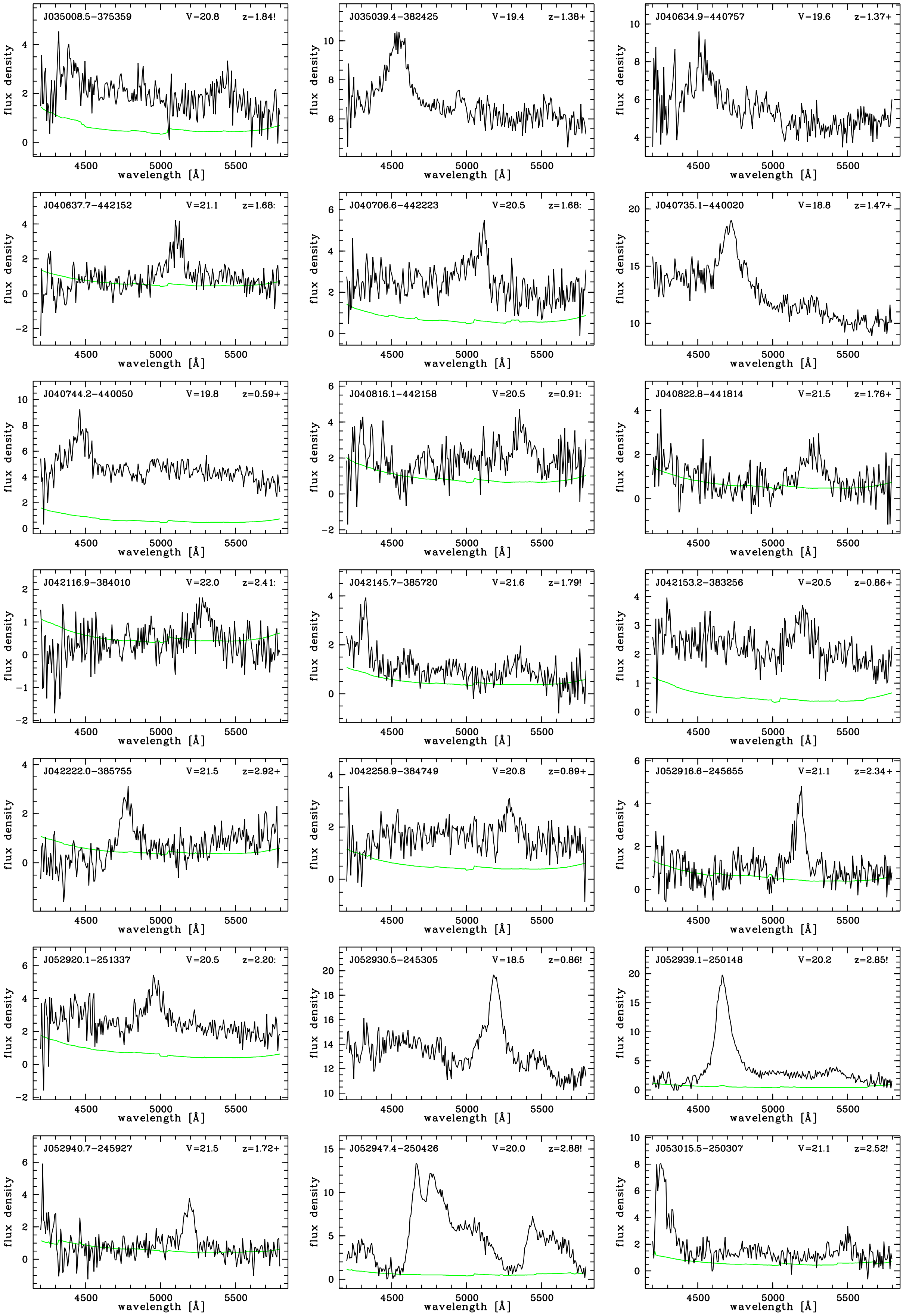

Fig. B.3. continued. Note that the field of PKS 0528−250 with 7 bona fide quasar candidates was not included in the follow-up campaign with FORS2.

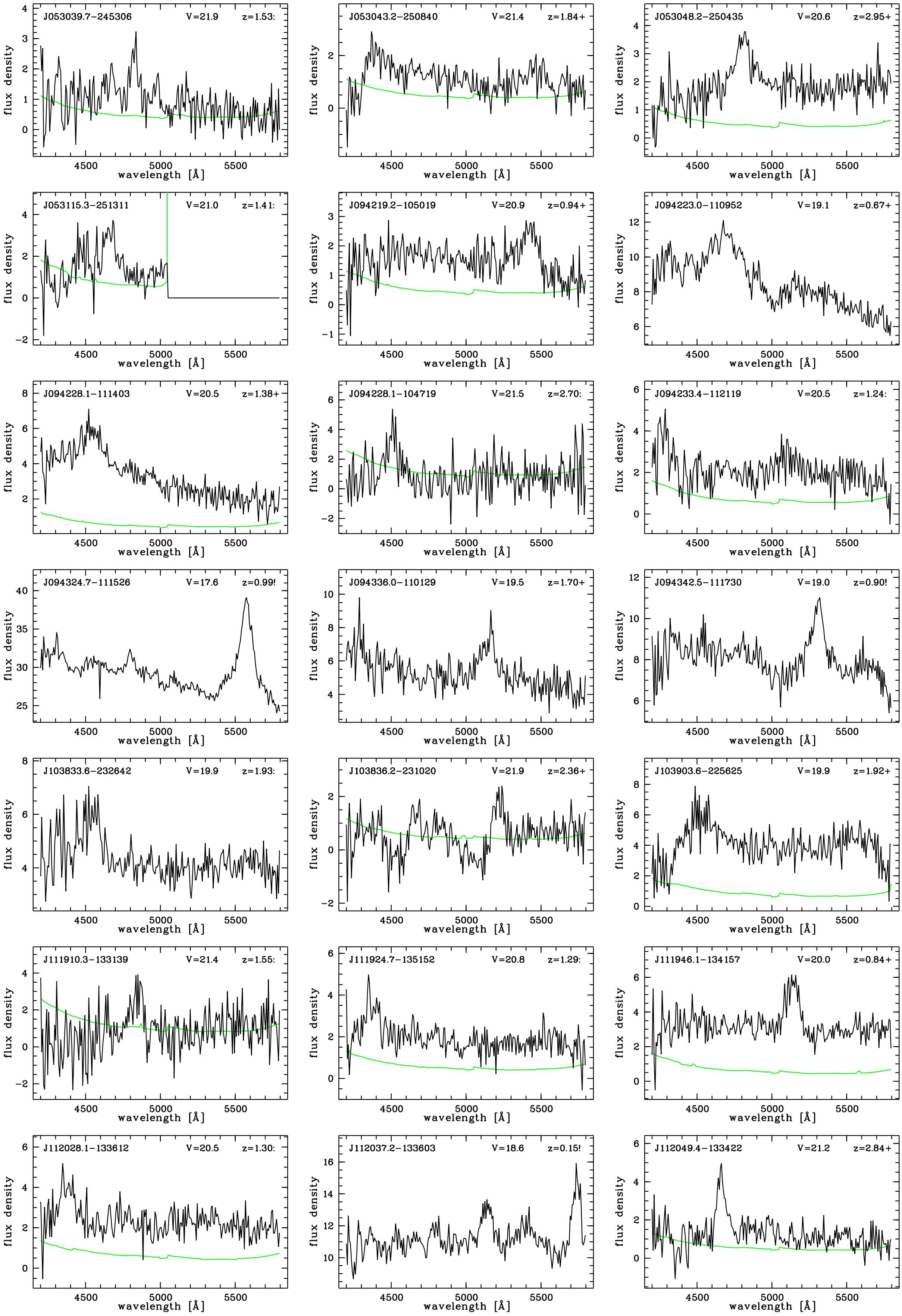

Fig. B.3. continued.

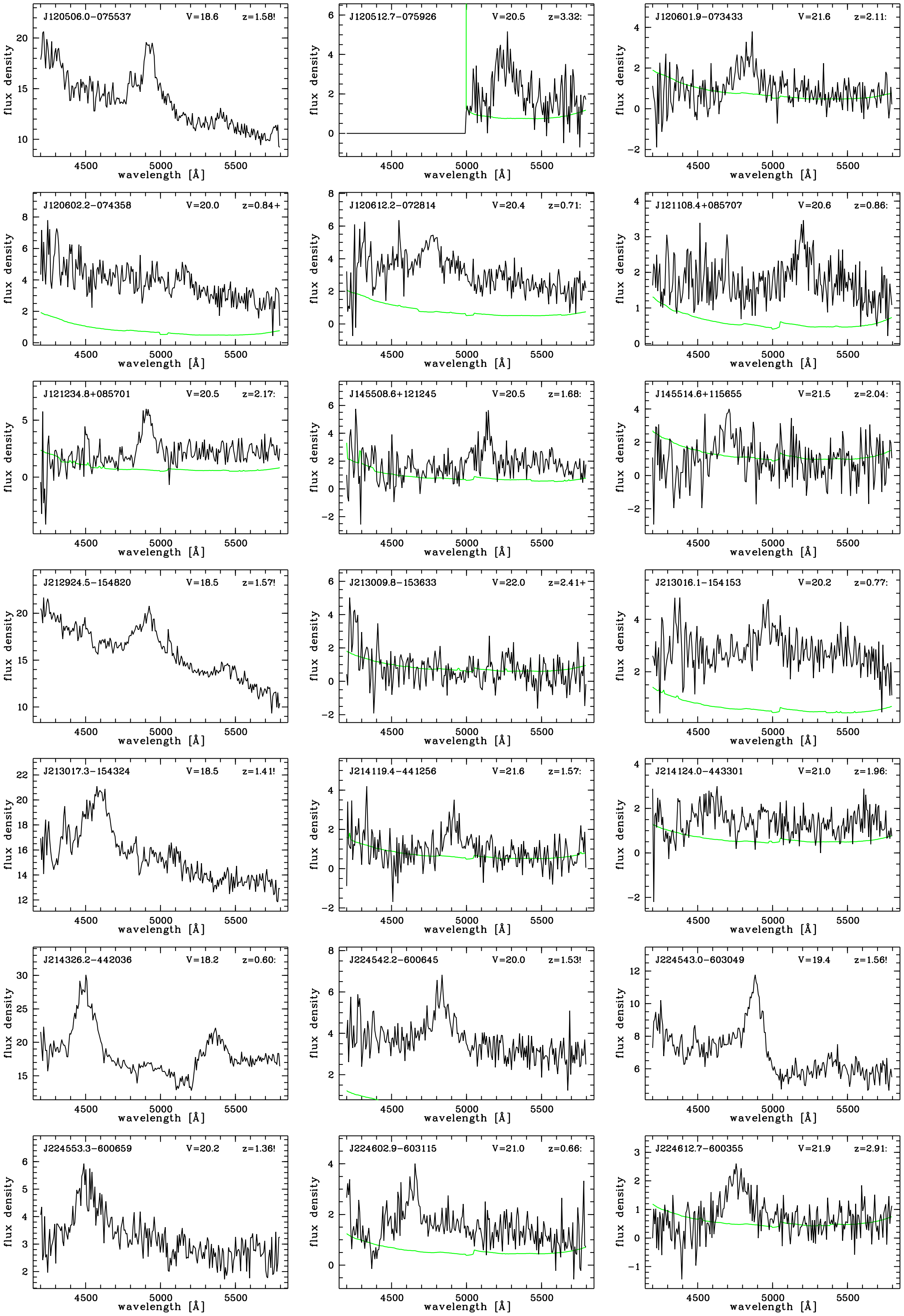

Fig. B.3. continued. The spectrum of J214326.2−442036 might be contaminated by a nearby galaxy. Francis et al. (2004) list J214124.0−443301 as a quasar candidate with uncertain redshift, whereas they identified J214119.4−441256 as a galaxy at $z = 0.062$ which is not supported by the slitless WFI spectrum.

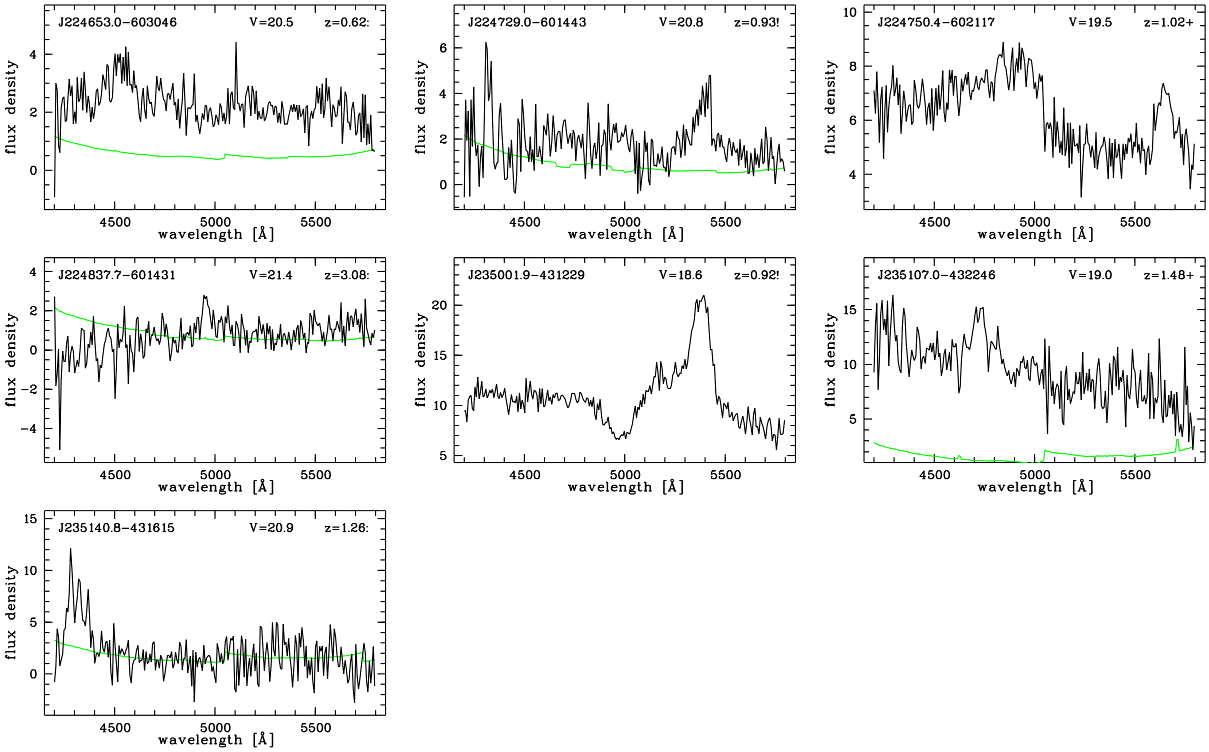

Fig. B.3. continued.

B.4. WFI spectra of likely emission line galaxies

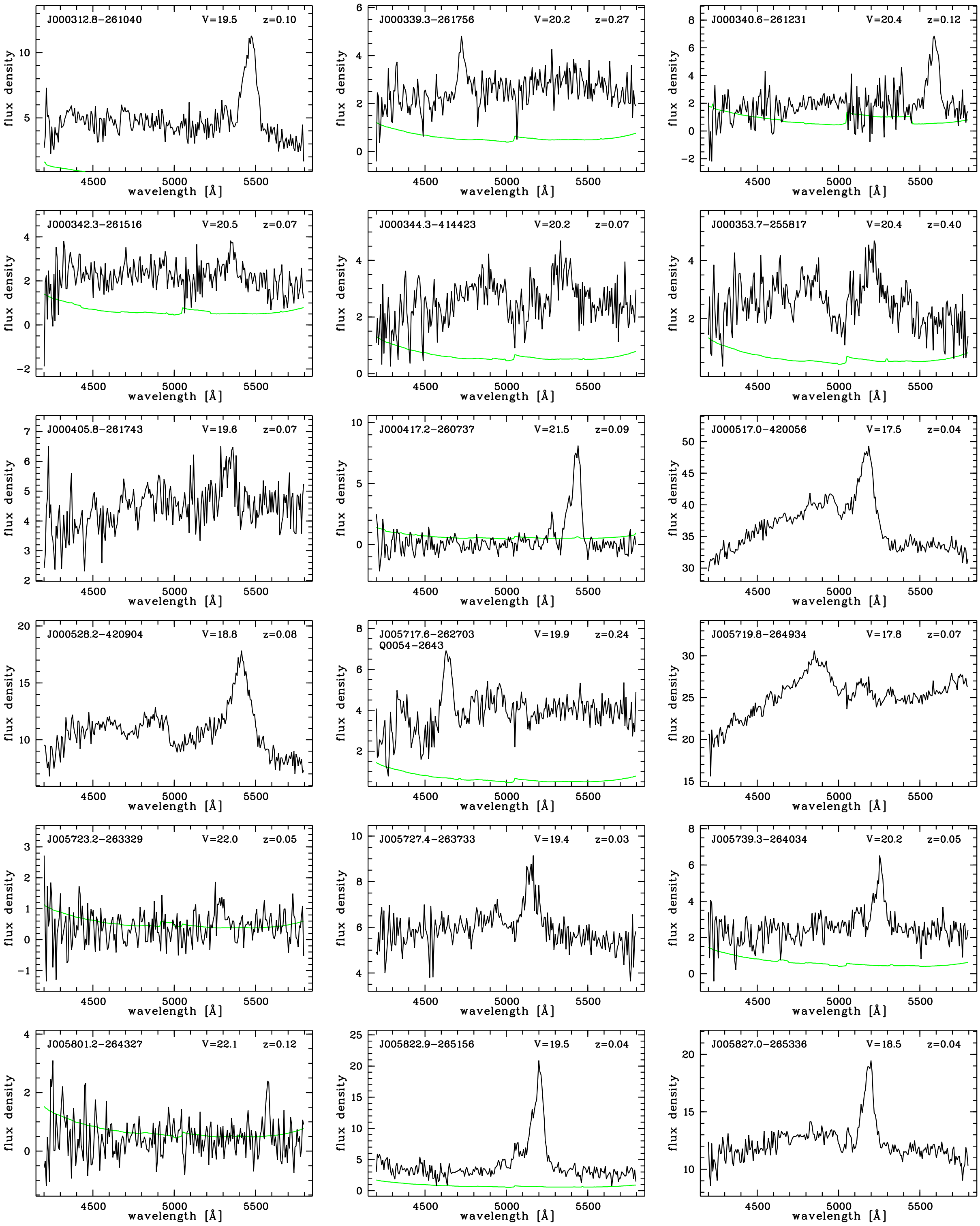

Fig. B.4. RA-ordered list of slitless WFI spectra of 145 objects classified as emission line galaxies (known and unknown). None of these objects was included in the follow-up observations. The spectra are shown in black together with their 1σ noise arrays (green/grey) if the S/N is low. The (approximate) flux densities are given in 10^{-17} erg cm^{-2} s^{-1} Å^{-1}. Labelled are the celestial coordinates (format: `HHMMSS.S±DDMMSS`, J2000), the integrated V magnitude and the estimated redshift. In most of the cases the classification is easy due to the asymmetric appearance of the blended [O III] doublet and the nearby Hβ line. Some galaxies have weak [O III] emission and a visible 4000 Å break at the blue end of the spectrum. Also [O II] emission is easily identified. Due to the very low seeing-dependent resolution the sample is likely contaminated by low-redshift AGN. Moreover, due to the lack of Hα in the spectral range this sample of star-forming galaxies is likely incomplete.

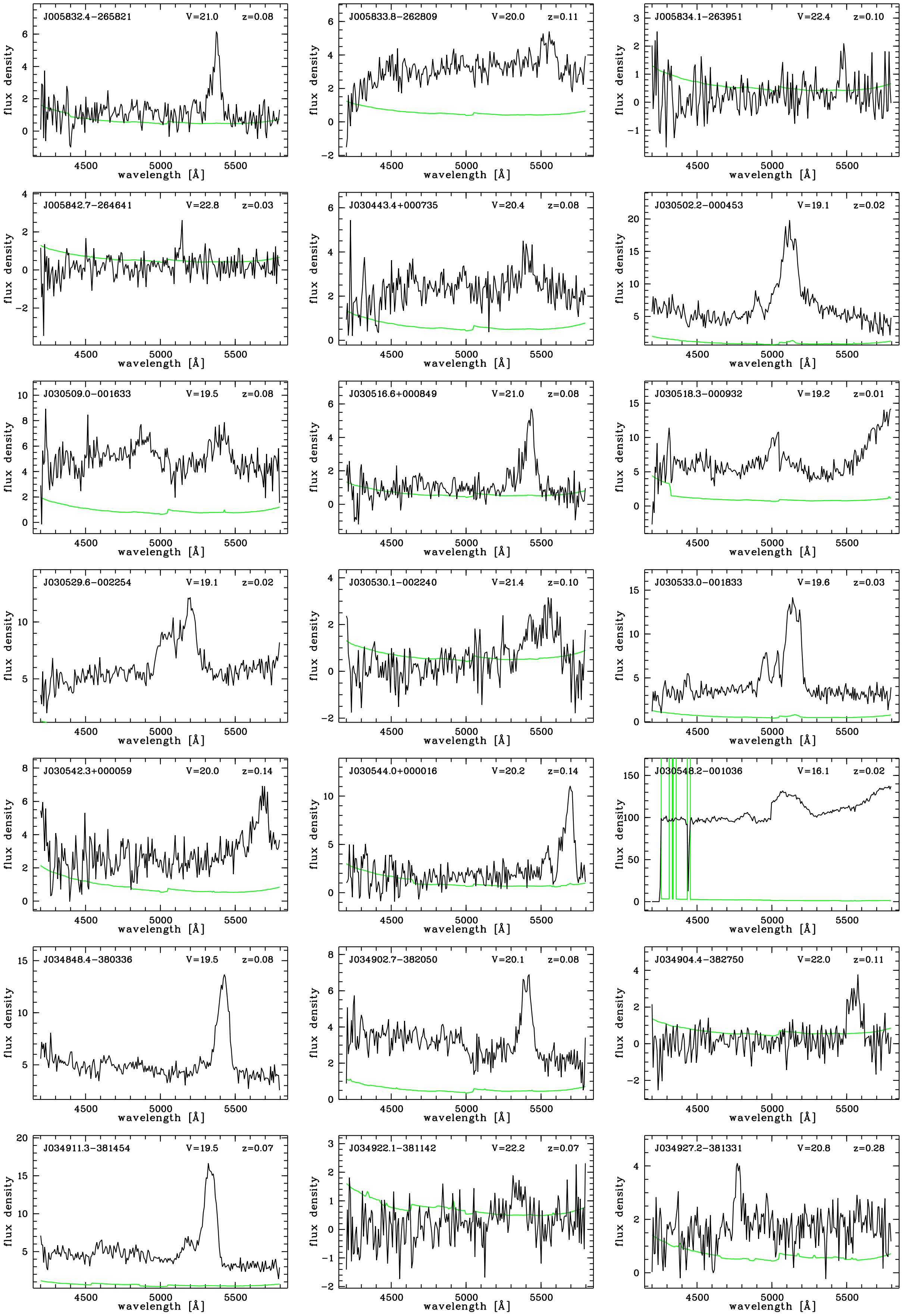

Fig. B.4. continued.

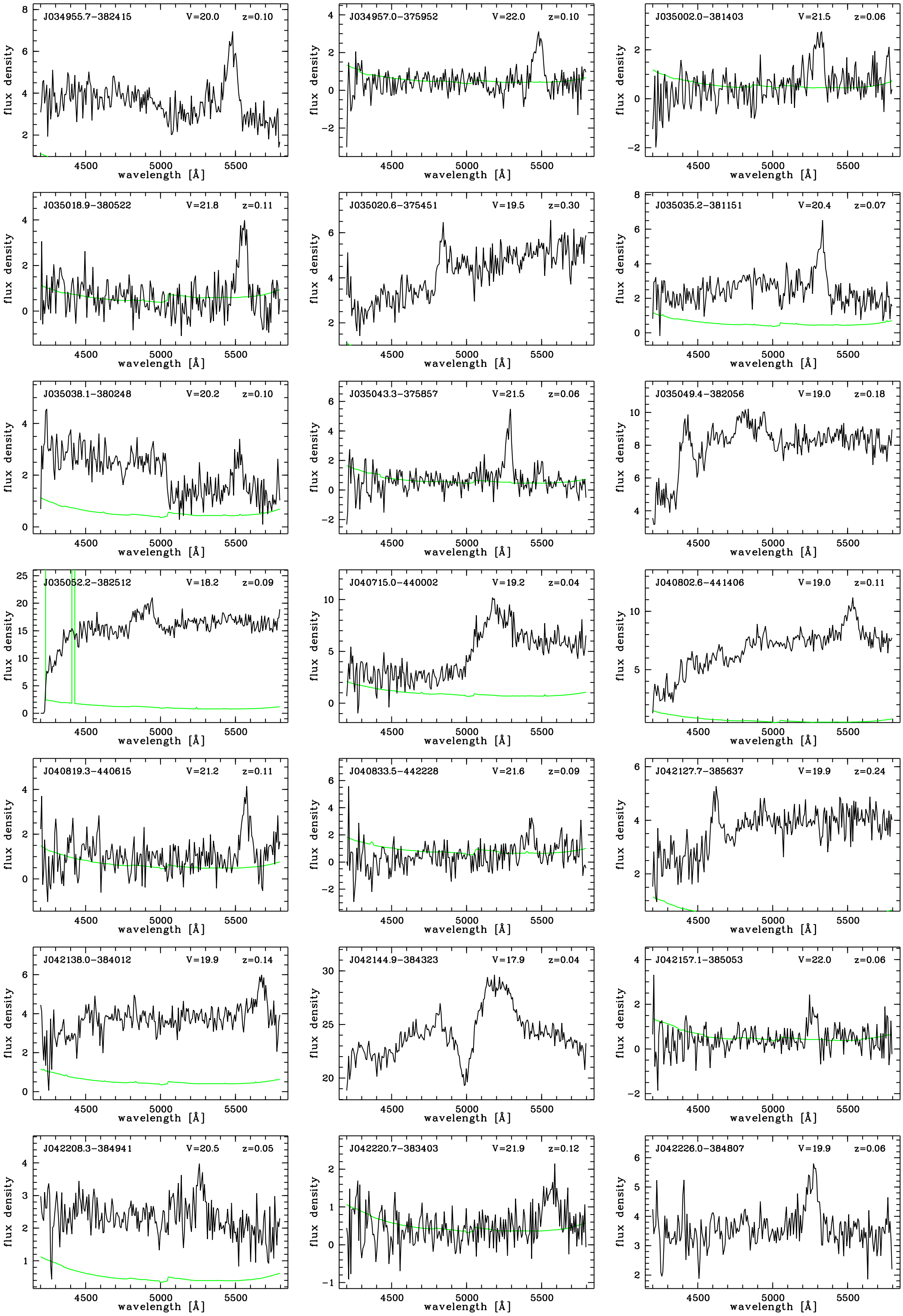

Fig. B.4. continued.

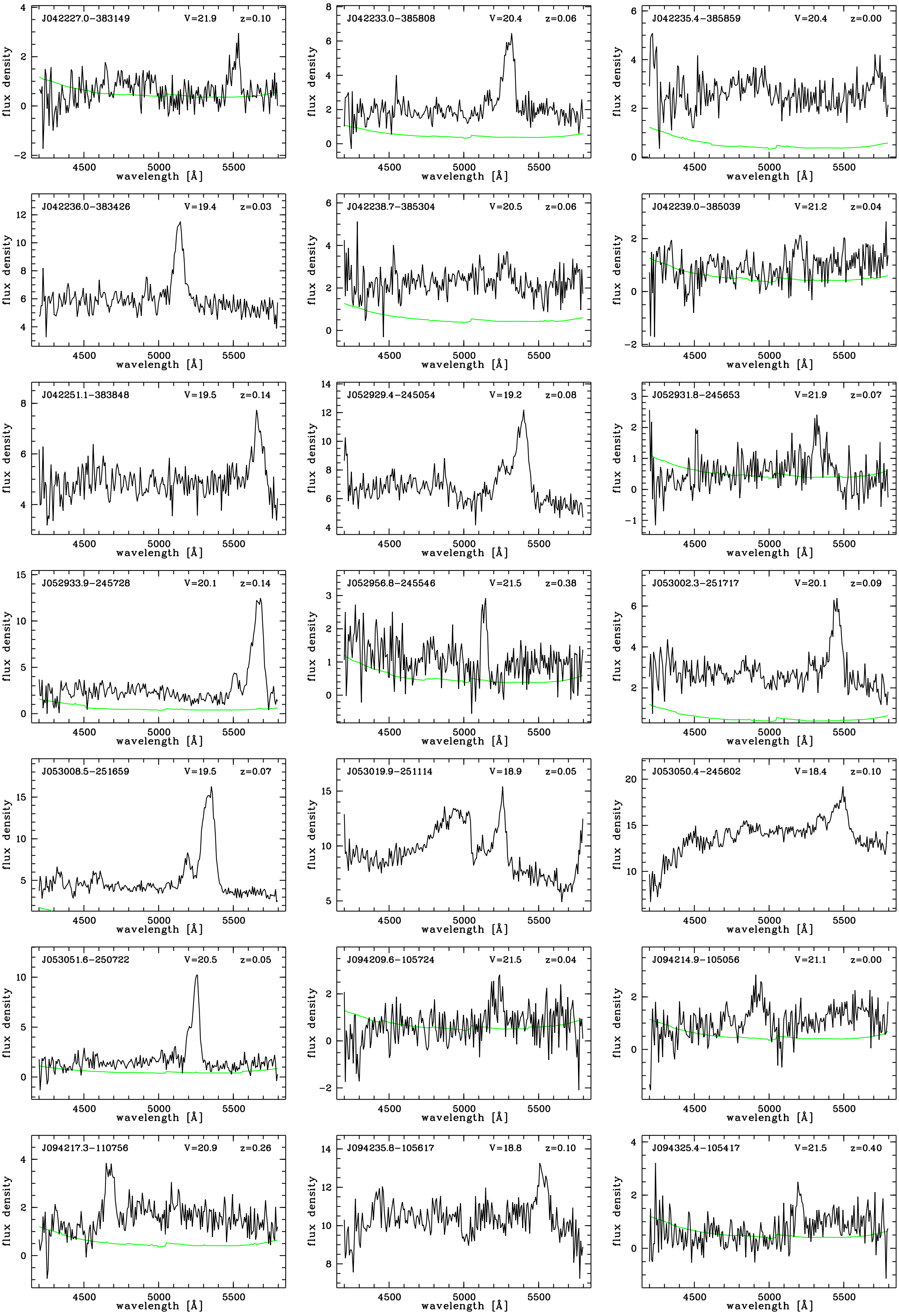

Fig. B.4. continued. The spectrum of J053019.9−251114 is contaminated.

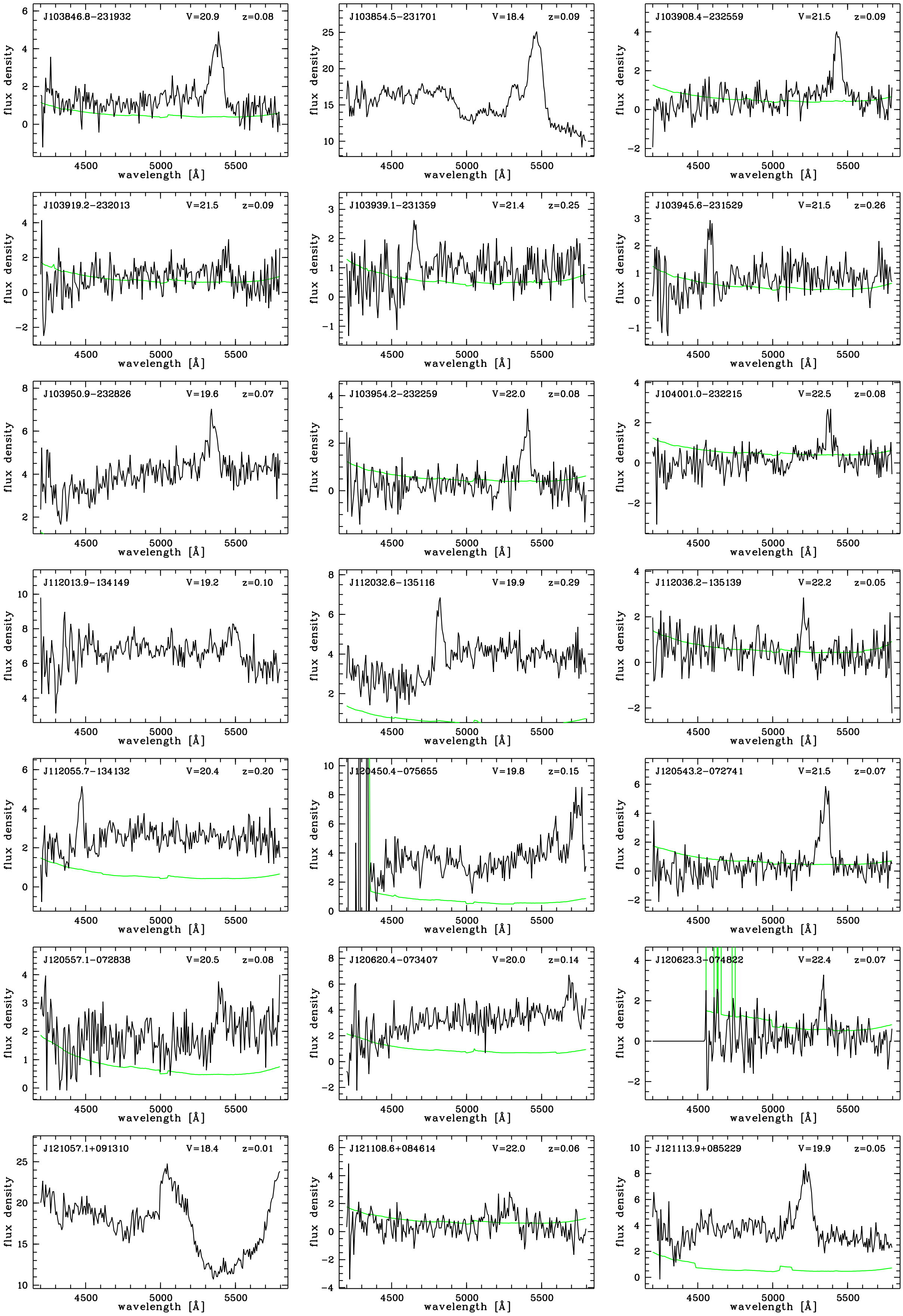

Fig. B.4. continued.

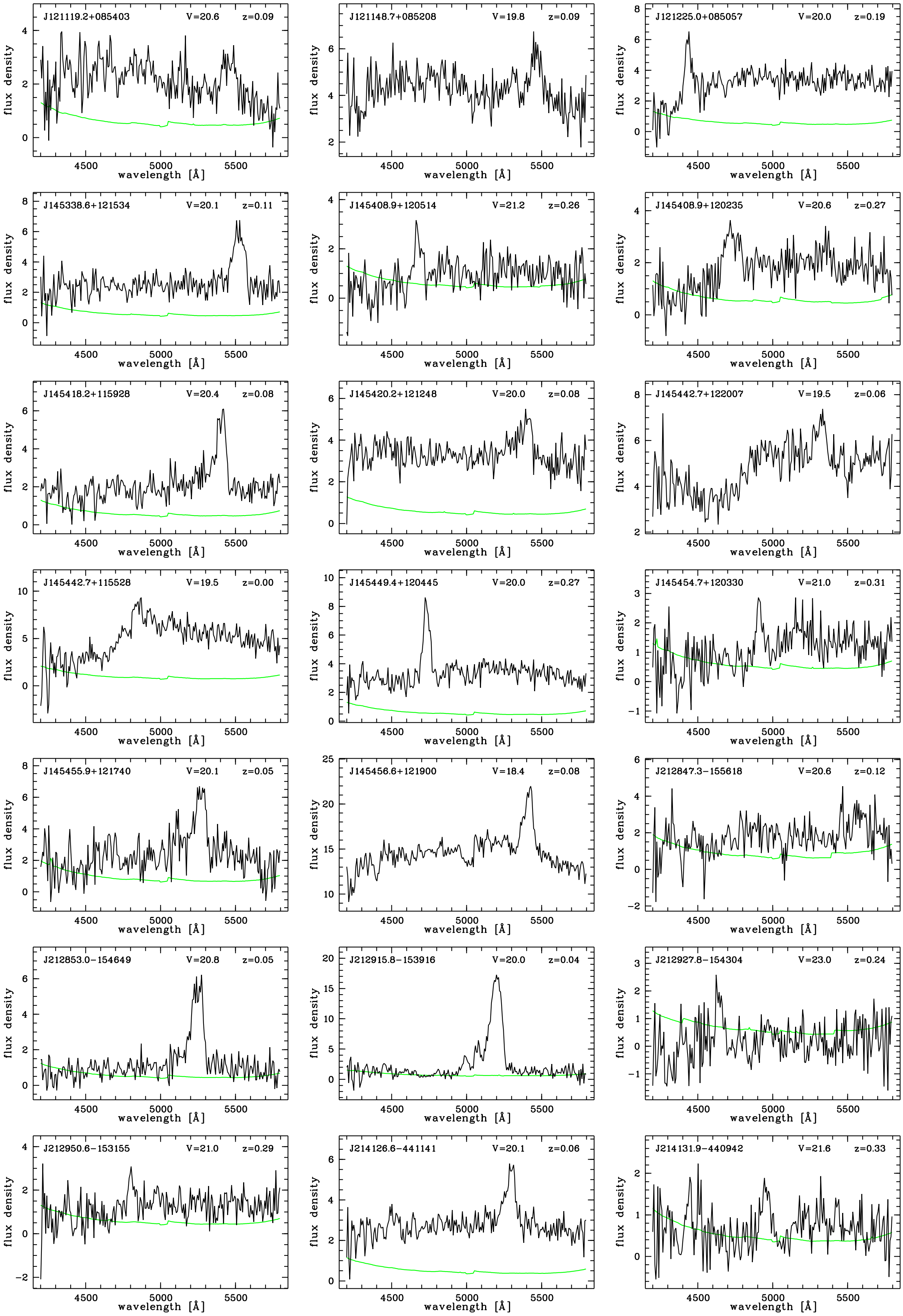

Fig. B.4. continued.

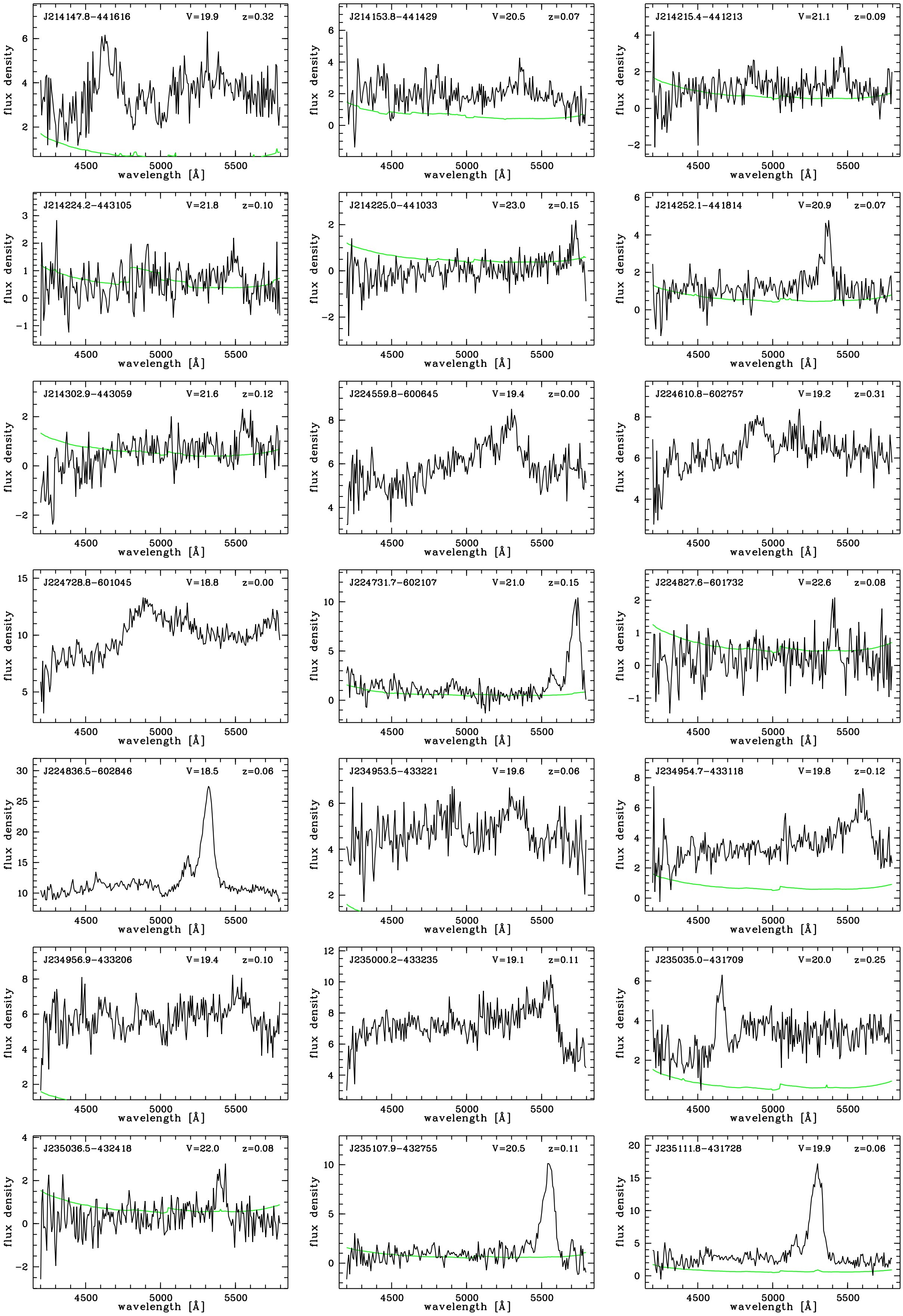

Fig. B.4. continued.

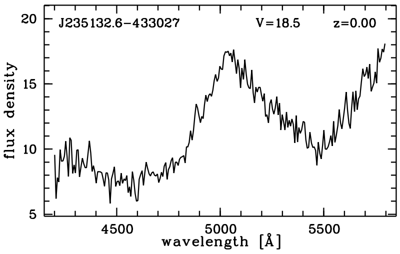

Fig. B.4. continued.

Appendix C

FORS2 redshift measurements of candidates included in the follow-up

Table C.1. Measured emission lines of newly discovered quasars in the vicinity of Q 0000−26.

Object	Emission line	$\lambda_{\rm rest}$ [Å]	$\lambda_{\rm obs}$ [Å]	z	comments
QSO J00025−2558	Mg II	2798.75	5275 ± 7	0.885 ± 0.003	
	Hβ	4862.68	9180 ± 7	0.888 ± 0.001	
				0.887 ± 0.002	
QSO J00040−2603	Lyα	1215.67	3649 ± 4	2.002 ± 0.003	
	Si IV+O IV]	1399.41	4180 ± 20	1.987 ± 0.014	noisy
	C IV	1549.06	4653 ± 8	2.004 ± 0.005	absorption, asymmetric
	C III]	1908.73	5730 ± 8	2.002 ± 0.004	
				2.002 ± 0.003	
QSO J00035−2610	Lyβ+O VI	1033.03	3891 ± 10	2.767 ± 0.010	forest absorption
	Lyα	1215.67	4585 ± 4	2.772 ± 0.003	
	N V	1240.14	4684 ± 6	2.777 ± 0.005	
	O I+Si II	1305.59	4903 ± 12	2.755 ± 0.010	noisy
	Si IV+O IV]	1399.41	5278 ± 15	2.772 ± 0.011	noisy
	C IV	1549.06	5837 ± 4	2.768 ± 0.003	
				2.771 ± 0.003	
QSO J00028−2547	Lyα	1215.67	4636 ± 5	2.814 ± 0.004	
	N V	1240.14	4725 ± 10	2.810 ± 0.008	blended with Lyα
	Si IV+O IV]	1399.41	5325 ± 15	2.805 ± 0.011	noisy, broad line
	C IV	1549.06	5902 ± 6	2.810 ± 0.004	
				2.812 ± 0.004	
QSO J00035−2551	Lyα	1215.67	4714 ± 4	2.878 ± 0.003	
	O I+Si II	1305.59	5053 ± 10	2.870 ± 0.008	noisy
	C II	1335.30	5173 ± 6	2.874 ± 0.004	noisy
	Si IV+O IV]	1399.41	5417 ± 9	2.871 ± 0.006	
	C IV	1549.06	5985 ± 8	2.864 ± 0.005	absorption
				2.875 ± 0.004	
QSO J00038−2617	Lyα	1215.67	4952 ± 4	3.073 ± 0.003	
	N V	1240.14	5042 ± 10	3.066 ± 0.008	blended with Lyα, noisy
	Si IV+O IV]	1399.41	5699 ± 15	3.072 ± 0.011	noisy
	C IV	1549.06	6277 ± 9	3.052 ± 0.006	
	C III]	1908.73	7774 ± 15	3.073 ± 0.008	noisy
				3.073 ± 0.003	

Table C.2. Measured emission lines of newly discovered quasars in the vicinity of Q 0002−422.

Object	Emission line	$\lambda_{\rm rest}$ [Å]	$\lambda_{\rm obs}$ [Å]	z	comments
QSO J00043−4151	Mg II	2798.75	4878 ± 3	0.743 ± 0.001	
	Hβ	4862.68	8477 ± 6	0.743 ± 0.001	
	[O III]	4960.30	8637 ± 5	0.741 ± 0.001	
	[O III]	5008.24	8731 ± 3	0.743 ± 0.001	
				0.743 ± 0.001	
QSO J00041−4158	C IV	1549.06	4215 ± 3	1.721 ± 0.002	
	C III]	1908.73	5176 ± 5	1.712 ± 0.003	
				1.720 ± 0.004	
QSO J00045−4201	Lyα	1215.67	3838 ± 2	2.157 ± 0.002	
	Si IV+O IV]	1399.41	4413 ± 8	2.153 ± 0.006	noisy
	C IV	1549.06	4889 ± 3	2.156 ± 0.002	
	C III]	1908.73	6025 ± 10	2.157 ± 0.005	noisy
				2.157 ± 0.002	

Table C.3. Measured emission lines of newly discovered quasars in the vicinity of H 0055−269.

Object	Emission line	$\lambda_{\rm rest}$ [Å]	$\lambda_{\rm obs}$ [Å]	z	comments
QSO J00576−2626	C IV	1549.06	4549 ± 8	1.937 ± 0.005	absorption
	C III]	1908.73	5617 ± 8	1.943 ± 0.004	sky residuals
	Mg II	2798.75	8270 ± 10	1.955 ± 0.004	noisy
				1.942 ± 0.004	
QSO J00582−2649	Lyα	1215.67	4345 ± 4	2.574 ± 0.003	
	O I+Si II	1305.59	4661 ± 4	2.570 ± 0.003	noisy
	Si IV+O IV]	1399.41	4996 ± 12	2.570 ± 0.009	noisy
	C IV	1549.06	5534 ± 4	2.572 ± 0.003	
	C III]	1908.73	6800 ± 7	2.563 ± 0.004	
				2.572 ± 0.003	
QSO J00583−2626	Lyα	1215.67	4570 ± 20	2.759 ± 0.016	strong absorption
	Si IV+O IV]	1399.41	5190 ± 15	2.709 ± 0.011	
	C IV	1549.06	5761 ± 10	2.719 ± 0.006	
	C III]	1908.73	7107 ± 10	2.723 ± 0.005	asymmetric
				2.720 ± 0.006	

Table C.4. Measured emission lines of newly discovered quasars in the vicinity of Q 0302−003.

Object	Emission line	$\lambda_{\rm rest}$ [Å]	$\lambda_{\rm obs}$ [Å]	z	comments
QSO J03052−0016	Lyα	1215.67	4004 ± 3	2.294 ± 0.003	
	N V	1240.14	4081 ± 3	2.291 ± 0.003	
	Si IV+O IV]	1399.41	4598 ± 8	2.284 ± 0.006	
	C IV	1549.06	5095 ± 2	2.289 ± 0.001	
	He II	1640.42	5393 ± 3	2.288 ± 0.002	
	C III]	1908.73	6278 ± 5	2.289 ± 0.003	
	Mg II	2798.75	9223 ± 15	2.296 ± 0.005	
				2.290 ± 0.002	
QSO J03052+0000	Lyβ+O VI	1033.03	3936 ± 5	2.810 ± 0.005	forest absorption
	Lyα	1215.67	4627 ± 7	2.806 ± 0.006	associated absorption
	Si IV+O IV]	1399.41	5335 ± 10	2.812 ± 0.007	
	C IV	1549.06	5896 ± 11	2.806 ± 0.007	associated absorption
	He II	1640.42	6244 ± 3	2.806 ± 0.002	
	C III]	1908.73	7268 ± 4	2.808 ± 0.002	
				2.808 ± 0.004	

Table C.5. Measured emission lines of quasars and emission line galaxies in the vicinity of Q 0347−383.

Object	Emission line	$\lambda_{\rm rest}$ [Å]	$\lambda_{\rm obs}$ [Å]	z	comments
J03490−3820	[O II]	3728.48	4790 ± 1	0.2847 ± 0.0002	
	Hβ	4862.68	6248 ± 1	0.2849 ± 0.0002	
	[O III]	4960.30	6374 ± 1	0.2850 ± 0.0002	
	[O III]	5008.24	6434 ± 1	0.2847 ± 0.0002	
	[N II]	6549.85	8415 ± 1	0.2848 ± 0.0002	
	Hα	6564.61	8435 ± 1	0.2849 ± 0.0002	
	[N II]	6585.28	8460 ± 1	0.2847 ± 0.0002	
	[S II]	6718.29	8631 ± 1	0.2847 ± 0.0001	
	[S II]	6732.67	8651 ± 1	0.2849 ± 0.0001	
				0.2848 ± 0.0001	Emission line galaxy
QSO J03494−3814	C IV	1549.06	3826 ± 4	1.470 ± 0.003	
	C III]	1908.73	4717 ± 4	1.471 ± 0.002	
	Mg II	2798.75	6927 ± 4	1.475 ± 0.001	telluric absorption
				1.471 ± 0.002	
QSO J03500−3820	Si IV+O IV]	1399.41	3936 ± 10	1.813 ± 0.007	
	C IV	1549.06	4366 ± 4	1.818 ± 0.003	
	C III]	1908.73	5380 ± 5	1.819 ± 0.003	
	Mg II	2798.75	7889 ± 7	1.819 ± 0.003	
				1.819 ± 0.002	
QSO J03490−3812	Si IV+O IV]	1399.41	4122 ± 7	1.946 ± 0.005	
	C IV	1549.06	4562 ± 8	1.945 ± 0.005	absorption
	C III]	1908.73	5611 ± 4	1.940 ± 0.002	
	Mg II	2798.75	8244 ± 8	1.946 ± 0.003	
				1.945 ± 0.003	
QSO J03496−3821	Lyα	1215.67	4075 ± 2	2.352 ± 0.002	
	N V	1240.14	4158 ± 6	2.353 ± 0.005	blended with Lyα
	O I+Si II	1305.59	4364 ± 5	2.343 ± 0.004	absorption
	C II	1335.30	4471 ± 5	2.348 ± 0.004	noisy
	Si IV+O IV]	1399.41	4678 ± 8	2.343 ± 0.006	
	C IV	1549.06	5189 ± 3	2.350 ± 0.002	
	He II	1640.42	5489 ± 9	2.346 ± 0.005	noisy
				2.351 ± 0.003	
QSO J03496−3810	Lyα	1215.67	4170 ± 3	2.430 ± 0.002	absorption
	N V	1240.14	4260 ± 5	2.435 ± 0.004	blended with Lyα, absorption
	O I+Si II	1305.59	4483 ± 4	2.434 ± 0.003	absorption
	C II	1335.30	4587 ± 6	2.435 ± 0.004	noisy, absorption
	Si IV+O IV]	1399.41	4802 ± 10	2.431 ± 0.007	asymmetric
	C IV	1549.06	5311 ± 3	2.429 ± 0.002	absorption
				2.433 ± 0.003	
QSO J03495−3806	Lyα	1215.67	4226 ± 2	2.476 ± 0.002	
	N V	1240.14	4315 ± 6	2.479 ± 0.005	blended with Lyα
	Si IV+O IV]	1399.41	4859 ± 8	2.472 ± 0.006	
	C IV	1549.06	5380 ± 3	2.473 ± 0.002	
				2.475 ± 0.003	
QSO J03508−3812	Lyβ+O VI	1033.03			Broad Absorption Line QSO
	Lyα	1215.67			Broad Absorption Line QSO
	N V	1240.14			Broad Absorption Line QSO
	Si IV+O IV]	1399.41			Broad Absorption Line QSO
	C IV	1549.06			Broad Absorption Line QSO
	He II	1640.42	6064 ± 6	2.700 ± 0.004	
	C III]	1908.73	7071 ± 3	2.705 ± 0.002	
				2.705 ± 0.003	
QSO J03503−3800	Lyα	1215.67	4554 ± 3	2.746 ± 0.002	absorption
	O I+Si II	1305.59	4877 ± 6	2.735 ± 0.005	
	C II	1335.30	4986 ± 6	2.734 ± 0.004	
	Si IV+O IV]	1399.41	5224 ± 5	2.733 ± 0.004	
	C IV	1549.06	5760 ± 4	2.718 ± 0.003	absorption
				2.734 ± 0.003	

Table C.5. continued.

Object	Emission line	$\lambda_{\rm rest}$ [Å]	$\lambda_{\rm obs}$ [Å]	z	comments
QSO J03490−3825	Lyβ+O VI	1033.03	3895 ± 10	2.770 ± 0.010	associated absorption
	Lyα	1215.67	4587 ± 5	2.773 ± 0.004	associated absorption
	N V	1240.14	4688 ± 5	2.780 ± 0.004	blended with Lyα, associated absorption
	O I+Si II	1305.59	4930 ± 5	2.776 ± 0.004	absorption
	C II	1335.30	5044 ± 5	2.777 ± 0.004	absorption
	Si IV+O IV]	1399.41	5286 ± 10	2.777 ± 0.007	associated absorption
	C IV	1549.06	5850 ± 5	2.776 ± 0.003	associated absorption
	He II	1640.42	6180 ± 4	2.767 ± 0.002	noisy, blueshifted
				2.777 ± 0.003	
QSO J03494−3826	Lyβ+O VI	1033.03	3918 ± 6	2.793 ± 0.006	forest absorption
	Lyα	1215.67	4598 ± 2	2.782 ± 0.002	
	N V	1240.14	4700 ± 8	2.790 ± 0.006	blended with Lyα
	O I+Si II	1305.59	4934 ± 5	2.779 ± 0.004	
	C II	1335.30	5048 ± 4	2.780 ± 0.003	
	Si IV+O IV]	1399.41	5288 ± 7	2.779 ± 0.005	
	C IV	1549.06	5859 ± 3	2.782 ± 0.002	
				2.782 ± 0.002	

Table C.6. Measured emission lines of newly discovered quasars in the vicinity of CTQ 0247.

Object	Emission line	$\lambda_{\rm rest}$ [Å]	$\lambda_{\rm obs}$ [Å]	z	comments
QSO J04061−4401	Lyα	1215.67	4160 ± 15	2.422 ± 0.012	strong absorption systems
	Si IV+O IV]	1399.41	4728 ± 15	2.379 ± 0.011	strong absorption systems
	C IV	1549.06	5238 ± 10	2.381 ± 0.006	strong absorption systems
				2.410 ± 0.020	
QSO J04075−4416	Lyβ+O VI	1033.03	4163 ± 10	3.030 ± 0.010	forest absorption
	Lyα	1215.67	4904 ± 3	3.034 ± 0.002	absorption
	N V	1240.14	5013 ± 4	3.042 ± 0.003	blended with Lyα
	O I+Si II	1305.59	5262 ± 9	3.030 ± 0.007	noisy
	Si IV+O IV]	1399.41	5623 ± 8	3.018 ± 0.006	noisy
	C IV	1549.06	6250 ± 6	3.035 ± 0.004	absorption
				3.034 ± 0.003	
QSO J04084−4420	Lyβ+O VI	1033.03	4192 ± 9	3.058 ± 0.009	forest absorption
	Lyα	1215.67	4962 ± 4	3.082 ± 0.003	
	N V	1240.14	5056 ± 6	3.077 ± 0.005	blended with Lyα
	O I+Si II	1305.59	5330 ± 8	3.082 ± 0.006	noisy
	C II	1335.30	5442 ± 10	3.075 ± 0.007	noisy
	Si IV+O IV]	1399.41	5697 ± 10	3.071 ± 0.007	noisy
	C IV	1549.06	6315 ± 5	3.077 ± 0.003	
				3.080 ± 0.004	

Table C.7. Measured emission lines of newly discovered quasars in the vicinity of Q 0420−388.

Object	Emission line	$\lambda_{\rm rest}$ [Å]	$\lambda_{\rm obs}$ [Å]	z	comments
QSO J04217−3847	Mg II	2798.75	4957 ± 6	0.771 ± 0.002	
				0.771 ± 0.002	
QSO J04229−3831	Lyα	1215.67	3636 ± 8	1.991 ± 0.007	associated absorption
	Si IV+O IV]	1399.41	4178 ± 8	1.986 ± 0.006	
	C IV	1549.06	4633 ± 7	1.991 ± 0.005	associated absorption
	C III]	1908.73	5708 ± 4	1.990 ± 0.002	
				1.990 ± 0.002	
QSO J04222−3829	Lyα	1215.67	3850 ± 6	2.167 ± 0.005	absorption
	Si IV+O IV]	1399.41	4433 ± 11	2.168 ± 0.008	
	C IV	1549.06	4906 ± 6	2.167 ± 0.004	
	C III]	1908.73	6049 ± 10	2.169 ± 0.005	
	Mg II	2798.75	8870 ± 20	2.169 ± 0.007	noisy
				2.168 ± 0.003	
QSO J04215−3857	Lyα	1215.67	3932 ± 10	2.234 ± 0.008	
	Si IV+O IV]	1399.41	4519 ± 12	2.229 ± 0.009	
	C IV	1549.06	5004 ± 7	2.230 ± 0.005	absorption
	C III]	1908.73	6176 ± 4	2.236 ± 0.002	
	Mg II	2798.75	9046 ± 12	2.232 ± 0.004	noisy
				2.235 ± 0.003	
QSO J04215−3854	Lyα	1215.67	4010 ± 12	2.299 ± 0.010	broad line, absorption
	Si IV+O IV]	1399.41	4584 ± 15	2.276 ± 0.011	
	C IV	1549.06	5060 ± 15	2.266 ± 0.010	broad line, absorption
	C III]	1908.73	6224 ± 12	2.261 ± 0.006	broad line
				2.270 ± 0.010	
QSO J04212−3853	Lyα	1215.67	4526 ± 4	2.723 ± 0.003	
	N V	1240.14	4613 ± 8	2.720 ± 0.006	blended with Lyα
	O I+Si II	1305.59	4862 ± 7	2.724 ± 0.005	
	C II	1335.30	4977 ± 10	2.727 ± 0.007	absorption
	Si IV+O IV]	1399.41	5207 ± 10	2.721 ± 0.007	
	C IV	1549.06	5768 ± 4	2.717 ± 0.003	
				2.723 ± 0.003	
QSO J04230−3853	Lyα	1215.67	4930 ± 10	3.055 ± 0.008	absorption
	Si IV+O IV]	1399.41	5648 ± 10	3.036 ± 0.007	
	C IV	1549.06	6260 ± 6	3.041 ± 0.004	
	C III]	1908.73	7720 ± 20	3.045 ± 0.010	telluric absorption
				3.042 ± 0.005	

Table C.8. Measured emission lines of newly discovered quasars in the vicinity of HE 0940−1050.

Object	Emission line	$\lambda_{\rm rest}$ [Å]	$\lambda_{\rm obs}$ [Å]	z	comments
QSO J09422−1117	Mg II	2798.75	4873 ± 7	0.741 ± 0.003	
				0.741 ± 0.003	
QSO J09437−1109	C IV	1549.06	3800 ± 10	1.453 ± 0.006	narrow line, associated absorption
	C III]	1908.73	4688 ± 6	1.456 ± 0.003	narrow line
	C II]	2326.44	5720 ± 8	1.459 ± 0.003	strong line
	[Ne IV]	2423.83	5947 ± 3	1.454 ± 0.001	strong line
	Mg II	2798.75	6875 ± 6	1.456 ± 0.002	narrow, associated absorption
				1.456 ± 0.002	
QSO J09427−1108	C IV	1549.06	3911 ± 10	1.525 ± 0.006	asymmetric
	C III]	1908.73	4804 ± 8	1.517 ± 0.004	
				1.517 ± 0.004	

Table C.8. continued.

Object	Emission line	$\lambda_{\rm rest}$ [Å]	$\lambda_{\rm obs}$ [Å]	z	comments
QSO J09430−1108	Si iv+O iv]	1399.41	3830 ± 30	1.737 ± 0.021	break in spectrum at $\lambda < 3750$ Å
	C iv	1549.06	4239 ± 9	1.736 ± 0.006	associated absorption
	C iii]	1908.73	5210 ± 9	1.730 ± 0.005	
	Mg ii	2798.75	7665 ± 12	1.739 ± 0.004	telluric absorption
	N iii]	1750.26	4780 ± 6	1.731 ± 0.003	
				1.730 ± 0.003	
QSO J09424−1047	Si iv+O iv]	1399.41	4160 ± 15	1.973 ± 0.011	
	C iv	1549.06	4601 ± 6	1.970 ± 0.004	
	C iii]	1908.73	5670 ± 8	1.971 ± 0.004	
	Mg ii	2798.75	8335 ± 10	1.978 ± 0.004	
				1.971 ± 0.003	
QSO J09437−1057	Lyα	1215.67	3682 ± 10	2.029 ± 0.008	noisy
	Si iv+O iv]	1399.41	4140 ± 15	1.958 ± 0.011	blueshifted
	C iv	1549.06	4686 ± 4	2.025 ± 0.003	
	C iii]	1908.73	5769 ± 12	2.022 ± 0.006	
	Mg ii	2798.75	8460 ± 15	2.023 ± 0.005	
				2.023 ± 0.004	
QSO J09435−1049	Lyα	1215.67	3911 ± 3	2.217 ± 0.002	broad line
	N v	1240.14	3990 ± 10	2.217 ± 0.008	blended with Lyα, absorption
	Si iv+O iv]	1399.41	4500 ± 8	2.216 ± 0.006	broad line
	C iv	1549.06	4979 ± 5	2.214 ± 0.003	broad line
	C iii]	1908.73	6129 ± 6	2.211 ± 0.003	broad line
				2.216 ± 0.003	
QSO J09425−1048	Lyα	1215.67	4042 ± 6	2.325 ± 0.005	absorption
	C ii	1335.30	4458 ± 9	2.339 ± 0.007	very noisy
	Si iv+O iv]	1399.41	4662 ± 10	2.331 ± 0.007	
	C iv	1549.06	5141 ± 8	2.319 ± 0.005	absorption
				2.325 ± 0.005	
QSO J09434−1053	Lyβ+O vi	1033.03	3885 ± 20	2.761 ± 0.019	forest absorption
	Lyα	1215.67	4571 ± 4	2.760 ± 0.003	
	N v	1240.14	4669 ± 10	2.765 ± 0.008	blended with Lyα
	Si iv+O iv]	1399.41	5255 ± 10	2.755 ± 0.007	
	C iv	1549.06	5825 ± 4	2.760 ± 0.003	
	C iii]	1908.73	7170 ± 6	2.756 ± 0.003	
				2.760 ± 0.003	
QSO J09427−1121	Lyβ+O vi	1033.03	4070 ± 10	2.940 ± 0.010	forest absorption
	Lyα	1215.67	4824 ± 3	2.968 ± 0.002	absorption
	N v	1240.14	4917 ± 10	2.965 ± 0.008	blended with Lyα, absorption
	O i+Si ii	1305.59	5171 ± 4	2.961 ± 0.003	absorption
	C ii	1335.30	5301 ± 7	2.970 ± 0.005	noisy
	Si iv+O iv]	1399.41	5533 ± 8	2.954 ± 0.006	
	C iv	1549.06	6139 ± 4	2.963 ± 0.003	
				2.963 ± 0.003	
QSO J09437−1052	Lyβ+O vi	1033.03	4130 ± 10	2.998 ± 0.010	forest absorption
	Lyα	1215.67	4885 ± 3	3.018 ± 0.002	absorption
	N v	1240.14	4983 ± 10	3.018 ± 0.008	blended with Lyα
	S ii	1262.59	5076 ± 8	3.020 ± 0.006	
	O i+Si ii	1305.59	5240 ± 4	3.014 ± 0.003	
	C ii	1335.30	5368 ± 6	3.020 ± 0.004	noisy
	Si iv+O iv]	1399.41	5614 ± 8	3.012 ± 0.006	
	C iv	1549.06	6215 ± 6	3.012 ± 0.004	asymmetric
				3.018 ± 0.003	

Table C.9. Measured emission lines of newly discovered quasars in the vicinity of CTQ 0460.

Object	Emission line	$\lambda_{\rm rest}$ [Å]	$\lambda_{\rm obs}$ [Å]	z	comments
QSO J10399−2321	Lyα	1215.67	3910 ± 15	2.216 ± 0.012	associated absorption
	N V	1240.14	3986 ± 15	2.214 ± 0.012	associated absorption
	Si IV+O IV]	1399.41	4498 ± 10	2.214 ± 0.007	
	C IV	1549.06	4975 ± 15	2.212 ± 0.010	associated absorption
	C III]	1908.73	6138 ± 8	2.216 ± 0.004	broad line
				2.216 ± 0.004	
QSO J10388−2258	Lyα	1215.67	4044 ± 6	2.327 ± 0.005	absorption
	N V	1240.14	4120 ± 10	2.322 ± 0.008	absorption
	O I+Si II	1305.59	4342 ± 5	2.326 ± 0.004	
	C II	1335.30	4441 ± 7	2.326 ± 0.005	noisy
	Si IV+O IV]	1399.41	4650 ± 10	2.323 ± 0.007	
	C IV	1549.06	5147 ± 5	2.323 ± 0.003	
				2.326 ± 0.003	
QSO J10385−2317	Lyβ+O VI	1033.03	4237 ± 15	3.102 ± 0.015	forest absorption
	Lyα	1215.67	4976 ± 8	3.093 ± 0.007	absorption
	N V	1240.14	5067 ± 20	3.086 ± 0.016	absorption, blended with Lyα
	O I+Si II	1305.59	5342 ± 10	3.092 ± 0.008	absorption, noisy
	C II	1335.30	5475 ± 7	3.100 ± 0.005	noisy
	Si IV+O IV]	1399.41	5723 ± 10	3.090 ± 0.007	
	C IV	1549.06	6340 ± 10	3.093 ± 0.006	line not fully in spectral range
				3.099 ± 0.004	

Table C.10. Measured emission lines of newly discovered quasars in the vicinity of BR 1117−1329.

Object	Emission line	$\lambda_{\rm rest}$ [Å]	$\lambda_{\rm obs}$ [Å]	z	comments
QSO J11208−1345	C IV	1549.06	4483 ± 3	1.894 ± 0.002	
	C III]	1908.73	5520 ± 7	1.892 ± 0.004	
	Mg II	2798.75	8095 ± 8	1.892 ± 0.003	
				1.893 ± 0.002	
QSO J11205−1343	Si IV+O IV]	1399.41	4072 ± 10	1.910 ± 0.007	
	C IV	1549.06	4509 ± 3	1.911 ± 0.002	
	C III]	1908.73	5554 ± 5	1.910 ± 0.003	
	Mg II	2798.75	8141 ± 5	1.909 ± 0.002	
				1.910 ± 0.002	
QSO J11197−1340	Lyα	1215.67	3925 ± 15	2.229 ± 0.012	broad line, associated absorption?
	C II	1335.30	4300 ± 6	2.220 ± 0.004	
	Si IV+O IV]	1399.41	4489 ± 15	2.208 ± 0.011	
	C IV	1549.06	4953 ± 10	2.197 ± 0.006	absorption, asymmetric, blueshifted
	C III]	1908.73	6120 ± 15	2.206 ± 0.008	broad line
				2.220 ± 0.004	
QSO J11192−1334	Lyα	1215.67	5178 ± 15	3.259 ± 0.012	associated absorption
	Si IV+O IV]	1399.41	5966 ± 15	3.263 ± 0.011	associated absorption
	C IV	1549.06	6580 ± 15	3.248 ± 0.010	associated absorption
	He II	1640.42	6970 ± 10	3.249 ± 0.006	
	O III]	1663.48	7078 ± 10	3.255 ± 0.006	
	C III]	1908.73	8116 ± 9	3.252 ± 0.005	
				3.252 ± 0.005	

Table C.11. Measured emission lines of newly discovered quasars in the vicinity of BR 1202−0725.

Object	Emission line	$\lambda_{\rm rest}$ [Å]	$\lambda_{\rm obs}$ [Å]	z	comments
QSO J12059−0754	Mg II	2798.75	4963 ± 3	0.773 ± 0.001	
				0.773 ± 0.001	
QSO J12062−0727	C IV	1549.06	3840 ± 15	1.479 ± 0.010	spectral break at $\lambda \lesssim 3750$ Å
	C III]	1908.73	4730 ± 20	1.478 ± 0.010	
	Mg II	2798.75	6932 ± 15	1.477 ± 0.005	
				1.478 ± 0.003	
QSO J12061−0745	C IV	1549.06	4227 ± 3	1.729 ± 0.002	
	C III]	1908.73	5212 ± 4	1.731 ± 0.002	
				1.730 ± 0.002	

Table C.12. Measured emission lines of newly discovered quasars in the vicinity of Q 1209+0919.

Object	Emission line	$\lambda_{\rm rest}$ [Å]	$\lambda_{\rm obs}$ [Å]	z	comments
QSO J12124+0851	Mg II	2798.75	4838 ± 7	0.729 ± 0.003	
				0.729 ± 0.003	
QSO J12111+0906	Lyα	1215.67	4300 ± 8	2.537 ± 0.007	absorption
	O I+Si II	1305.59	4615 ± 5	2.535 ± 0.004	
	C II	1335.30	4719 ± 3	2.534 ± 0.002	
	Si IV+O IV]	1399.41	4936 ± 10	2.527 ± 0.007	
	C IV	1549.06	5474 ± 7	2.534 ± 0.005	asymmetric
				2.534 ± 0.002	

Table C.13. Measured emission lines of newly discovered quasars in the vicinity of PKS 2126−15.

Object	Emission line	$\lambda_{\rm rest}$ [Å]	$\lambda_{\rm obs}$ [Å]	z	comments
QSO J21294−1521	Mg II	2798.75	4423 ± 2	0.580 ± 0.001	spectral break at $\lambda \lesssim 3750$ Å
				0.580 ± 0.001	
QSO J21291−1524A	Mg II	2798.75	4988 ± 3	0.782 ± 0.001	
	Hβ	4862.68	8646 ± 15	0.778 ± 0.003	noisy, sky residuals
				0.782 ± 0.001	
QSO J21297−1536	C IV	1549.06	3889 ± 10	1.511 ± 0.006	spectral break
	C III]	1908.73	4789 ± 10	1.509 ± 0.005	
	Mg II	2798.75	7023 ± 15	1.509 ± 0.005	
				1.509 ± 0.003	
QSO J21286−1528	Si IV+O IV]	1399.41	4075 ± 20	1.912 ± 0.014	noisy
	C IV	1549.06	4519 ± 6	1.917 ± 0.004	
	C III]	1908.73	5581 ± 8	1.924 ± 0.004	
	Mg II	2798.75	8203 ± 10	1.931 ± 0.004	
				1.925 ± 0.005	
QSO J21291−1524B	Lyα	1215.67	4230 ± 30	2.480 ± 0.025	Broad Absorption Line QSO
	C IV	1549.06	5300 ± 30	2.421 ± 0.019	velocity structure of BAL components indicates blueshift of C IV
				2.480 ± 0.030	
QSO J21301−1533	Lyβ+O VI	1033.03	4635 ± 15	3.487 ± 0.015	forest absorption
	Lyα	1215.67	5455 ± 5	3.487 ± 0.004	strong absorption systems
	N V	1240.14	5560 ± 10	3.483 ± 0.008	blended with Lyα
	O I+Si II	1305.59	5863 ± 10	3.491 ± 0.008	asymmetric
	C II	1335.30	5993 ± 10	3.488 ± 0.007	very noisy
	Si IV+O IV]	1399.41	6257 ± 15	3.471 ± 0.011	noisy, absorption
				3.487 ± 0.003	

Table C.14. Measured emission lines of newly discovered quasars in the vicinity of Q 2139−4434.

Object	Emission line	$\lambda_{\rm rest}$ [Å]	$\lambda_{\rm obs}$ [Å]	z	comments
QSO J21413−4406	Lyα	1215.67	3780 ± 7	2.109 ± 0.006	associated absorption?
(KNOWN)	N v	1240.14	3852 ± 15	2.106 ± 0.012	blended with Lyα, associated absorption?
	Si iv+O iv]	1399.41	4339 ± 15	2.101 ± 0.011	
	C iv	1549.06	4803 ± 7	2.101 ± 0.005	asymmetric
	C iii]	1908.73	5930 ± 8	2.107 ± 0.004	
	Mg ii	2798.75	8703 ± 10	2.110 ± 0.004	noisy, sky residuals
				2.107 ± 0.003	
QSO J21425−4430	Lyα	1215.67	4123 ± 40	2.392 ± 0.033	strong associated absorption, narrow line
(KNOWN)	C iv	1549.06	5253 ± 15	2.391 ± 0.010	strong associated system
	C iii]	1908.73	6436 ± 12	2.372 ± 0.006	noisy
				2.372 ± 0.006	
QSO J21434−4432	Lyα	1215.67	4517 ± 8	2.716 ± 0.007	absorption
	N v	1240.14	4598 ± 15	2.708 ± 0.012	blended with Lyα, absorption
	O i+Si ii	1305.59	4812 ± 7	2.709 ± 0.005	
	C ii	1335.30	4952 ± 12	2.709 ± 0.009	noisy
	Si iv+O iv]	1399.41	5182 ± 10	2.703 ± 0.007	
	C iv	1549.06	5725 ± 5	2.696 ± 0.003	
				2.709 ± 0.004	
QSO J21423−4419	Lyβ+O vi	1033.03	4368 ± 20	3.228 ± 0.019	forest absorption
(KNOWN)	Lyα	1215.67	5139 ± 3	3.227 ± 0.002	
	N v	1240.14	5239 ± 6	3.225 ± 0.005	absorption?, double peak?
	O i+Si ii	1305.59	5516 ± 4	3.225 ± 0.003	
	C ii	1335.30	5645 ± 2	3.228 ± 0.001	
	Si iv+O iv]	1399.41	5908 ± 15	3.222 ± 0.011	absorption?, double peak?
				3.228 ± 0.002	

Table C.15. Measured emission lines of newly discovered quasars in the vicinity of HE 2243−6031.

Object	Emission line	$\lambda_{\rm rest}$ [Å]	$\lambda_{\rm obs}$ [Å]	z	comments
QSO J22454−6020	C iv	1549.06	4622 ± 20	1.984 ± 0.013	associated absorption
	C iii]	1908.73	5733 ± 20	2.004 ± 0.010	extremely weak, noisy
	Mg ii	2798.75	8347 ± 15	1.982 ± 0.005	weak, noisy
				1.984 ± 0.015	
QSO J22455−6015	Lyα	1215.67	3689 ± 4	2.035 ± 0.003	
	Si iv+O iv]	1399.41	4265 ± 10	2.048 ± 0.007	noisy
	C iv	1549.06	4700 ± 5	2.034 ± 0.003	
	C iii]	1908.73	5795 ± 7	2.036 ± 0.004	
	Mg ii	2798.75	8500 ± 8	2.037 ± 0.003	
				2.036 ± 0.002	
QSO J22460−6024	Lyα	1215.67	3692 ± 10	2.037 ± 0.008	noisy, associated absorption
	Si iv+O iv]	1399.41	4256 ± 15	2.041 ± 0.011	noisy
	C iv	1549.06	4717 ± 10	2.045 ± 0.006	associated absorption
	C iii]	1908.73	5805 ± 6	2.041 ± 0.003	
	Mg ii	2798.75	8515 ± 10	2.042 ± 0.004	
				2.041 ± 0.003	
QSO J22454−6011	Lyα	1215.67	4038 ± 4	2.322 ± 0.003	absorption
	N v	1240.14	4119 ± 10	2.321 ± 0.008	blended with Lyα
	O i+Si ii	1305.59	4347 ± 7	2.330 ± 0.005	noisy
	C ii	1335.30	4439 ± 7	2.324 ± 0.005	noisy
	Si iv+O iv]	1399.41	4653 ± 9	2.325 ± 0.006	
	C iv	1549.06	5148 ± 5	2.323 ± 0.003	
				2.324 ± 0.003	
QSO J22463−6009	Lyα	1215.67	4047 ± 2	2.329 ± 0.002	
	N v	1240.14	4133 ± 5	2.333 ± 0.004	blended with Lyα
	O i+Si ii	1305.59	4333 ± 9	2.318 ± 0.007	noisy
	Si iv+O iv]	1399.41	4651 ± 9	2.324 ± 0.006	
	C iv	1549.06	5156 ± 3	2.328 ± 0.002	
				2.329 ± 0.003	
QSO J22484−6002	Lyβ+O vi	1033.03	4742 ± 9	3.590 ± 0.009	forest absorption
	Lyα	1215.67	5570 ± 6	3.582 ± 0.005	associated Lyman limit system
	N v	1240.14	5688 ± 5	3.587 ± 0.004	blended with Lyα
	O i+Si ii	1305.59	5988 ± 3	3.586 ± 0.002	
				3.586 ± 0.002	

Table C.16. Measured emission lines of newly discovered quasars in the vicinity of HE 2347−4342.

Object	Emission line	$\lambda_{\rm rest}$ [Å]	$\lambda_{\rm obs}$ [Å]	z	comments
QSO J23510−4336	Mg II	2798.75	4807 ± 10	0.718 ± 0.004	asymmetric
	[O III]	5008.24	8624 ± 2	0.722 ± 0.001	
				0.720 ± 0.002	
QSO J23507−4319	C II]	2326.44	4294 ± 6	0.846 ± 0.003	
	Mg II	2798.75	5182 ± 5	0.852 ± 0.002	noisy, absorption?
				0.850 ± 0.003	
QSO J23507−4326	C IV	1549.06	4083 ± 3	1.636 ± 0.002	
	C III]	1908.73	5026 ± 6	1.633 ± 0.003	
	Mg II	2798.75	7370 ± 10	1.633 ± 0.004	
				1.635 ± 0.003	
QSO J23509−4330	C IV	1549.06	4271 ± 4	1.757 ± 0.003	absorption system redward of line peak indicates blueshift
	C III]	1908.73	5271 ± 8	1.762 ± 0.004	broad
				1.762 ± 0.004	
QSO J23502−4334	Si IV+O IV]	1399.41	3878 ± 9	1.771 ± 0.006	
	C IV	1549.06	4290 ± 5	1.769 ± 0.003	asymmetric
	C III]	1908.73	5273 ± 5	1.763 ± 0.003	
	Mg II	2798.75	7730 ± 10	1.762 ± 0.004	telluric absorption
				1.763 ± 0.003	
QSO J23503−4328	Lyα	1215.67	3989 ± 4	2.281 ± 0.003	
	N V	1240.14	4070 ± 8	2.282 ± 0.006	blended with Lyα, absorption
	Si IV+O IV]	1399.41	4585 ± 8	2.276 ± 0.006	
	C IV	1549.06	5082 ± 4	2.281 ± 0.003	asymmetric
	C III]	1908.73	6253 ± 7	2.276 ± 0.004	
	Mg II	2798.75	9196 ± 12	2.286 ± 0.004	
				2.282 ± 0.003	
QSO J23495−4338	Lyα	1215.67	4513 ± 10	2.712 ± 0.008	absorption
	O I+Si II	1305.59	4823 ± 10	2.694 ± 0.008	noisy, absorption
	C II	1335.30	4930 ± 10	2.692 ± 0.007	noisy, absorption
	Si IV+O IV]	1399.41	5135 ± 15	2.669 ± 0.011	absorption
	C IV	1549.06	5691 ± 10	2.674 ± 0.006	absorption, blueshift
	C III]	1908.73	7028 ± 10	2.682 ± 0.005	absorption
				2.690 ± 0.006	
QSO J23511−4319	Lyβ+O VI	1033.03	4154 ± 10	3.021 ± 0.010	forest absorption
	Lyα	1215.67	4889 ± 4	3.022 ± 0.003	
	Si IV+O IV]	1399.41	5622 ± 9	3.017 ± 0.006	noisy
	C IV	1549.06	6223 ± 7	3.017 ± 0.005	broad
				3.020 ± 0.004	
QSO J23514−4339	Lyβ+O VI	1033.03	4389 ± 9	3.249 ± 0.009	forest absorption
	Lyα	1215.67	5159 ± 6	3.244 ± 0.005	associated absorption
	O I+Si II	1305.59	5538 ± 10	3.242 ± 0.008	noisy, absorption system
	C II	1335.30	5664 ± 8	3.242 ± 0.006	very noisy
	Si IV+O IV]	1399.41	5925 ± 10	3.234 ± 0.007	absorption
	C IV	1549.06	6553 ± 10	3.230 ± 0.006	associated absorption
	C III]	1908.73	8077 ± 7	3.232 ± 0.004	
				3.240 ± 0.004	
QSO J23503−4317	Lyβ+O VI	1033.03	4689 ± 10	3.539 ± 0.010	forest absorption
	Lyα	1215.67	5529 ± 10	3.548 ± 0.008	associated absorption
	O I+Si II	1305.59	5940 ± 10	3.550 ± 0.008	noisy
	Si IV+O IV]	1399.41	6300 ± 15	3.502 ± 0.011	weak, sky residuals
	C IV	1549.06	7022 ± 12	3.533 ± 0.008	associated absorption
	C III]	1908.73	8669 ± 8	3.542 ± 0.004	
				3.542 ± 0.005	

Appendix D

FORS spectra of newly discovered quasars and quasar field distributions

Quasars and quasar candidates near Q 0000−26

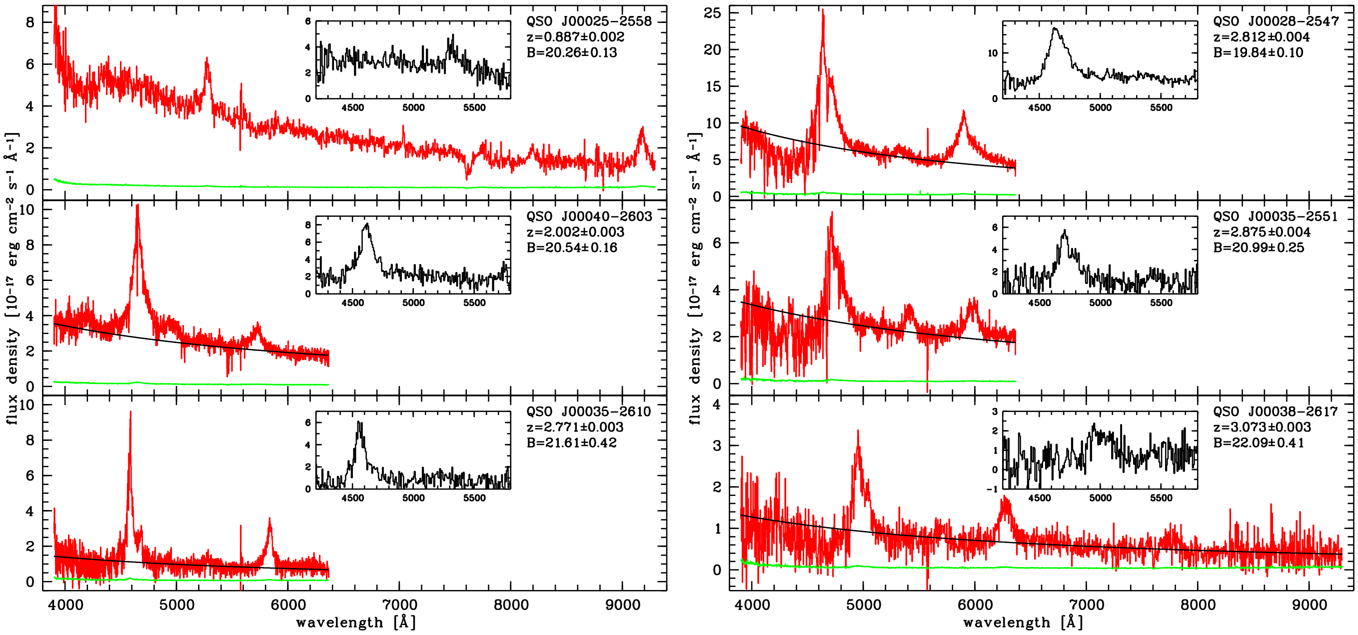

Fig. D.1. VLT/FORS2 spectra of newly discovered quasars in the vicinity of Q 0000−26. The extinction-corrected spectra are shown in red/dark grey together with their 1σ noise arrays (green/light grey). The spectra have been scaled to yield the measured photometric *B* magnitudes before correcting them for Galactic extinction. For quasars at $z > 1.7$ power law fits to the continua redward of Lyα are overplotted in black. The small inserts show the slitless WFI spectra of the quasars in the same units.

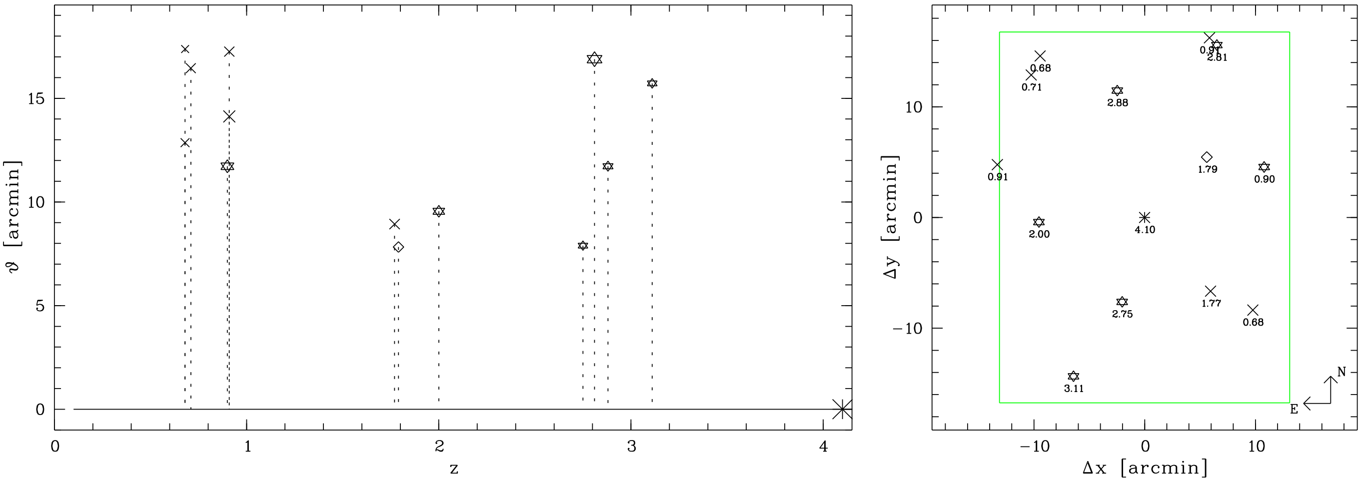

Fig. D.2. *Left:* Angular distribution of quasars and quasar candidates with respect to the central quasar Q 0000−26 as a function of redshift. Asterisks and star symbols mark known quasars and newly discovered confirmed quasars, respectively. Apart from the central quasar only rediscovered known quasars are shown (inside surveyed field, brighter than $V \simeq 22$, emission line in the observed wavelength range). Lozenges (crosses) show remaining WFI quasar candidates with secure (estimated) redshifts. Symbol size indicates apparent optical magnitude. All redshifts have been measured in the slitless WFI spectra ($\sigma_z \lesssim 0.03$). *Right:* Quasar distribution on the sky centred on Q 0000−26 with indicated redshifts. The green/grey rectangle marks the nominal contiguous slitless WFI field of view ($26.'2 \times 33.'5$) without rotating the instrument, for simplicity centred on Q 0000−26. Due to slight offsets of the field centres with respect to the central quasar and the instrument rotation for half of the exposure time some detected quasars may be located outside the nominal field of view.

Quasars and quasar candidates near Q 0002−422

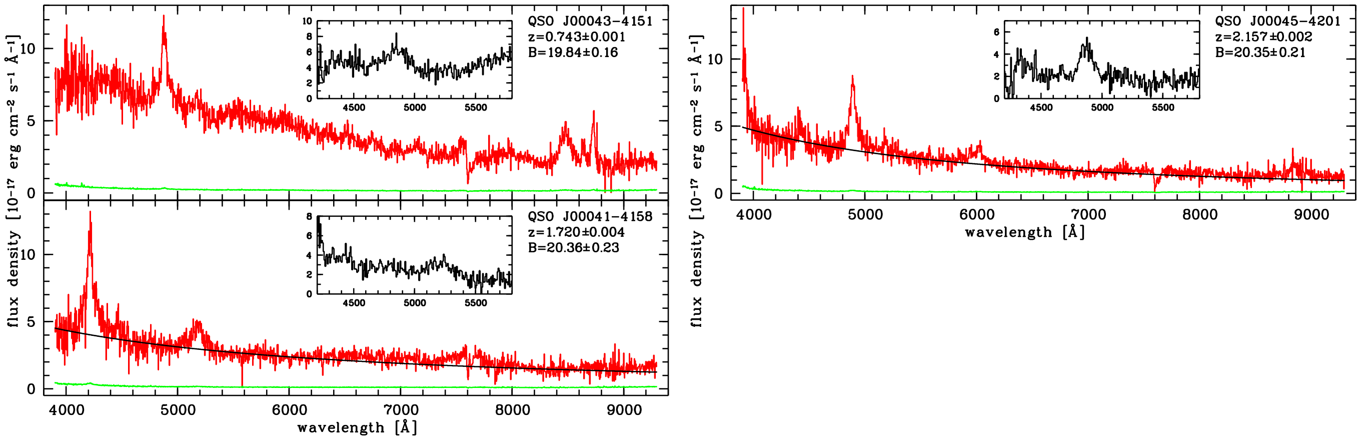

Fig. D.3. The same as Fig. D.1 for the field of Q 0002−422.

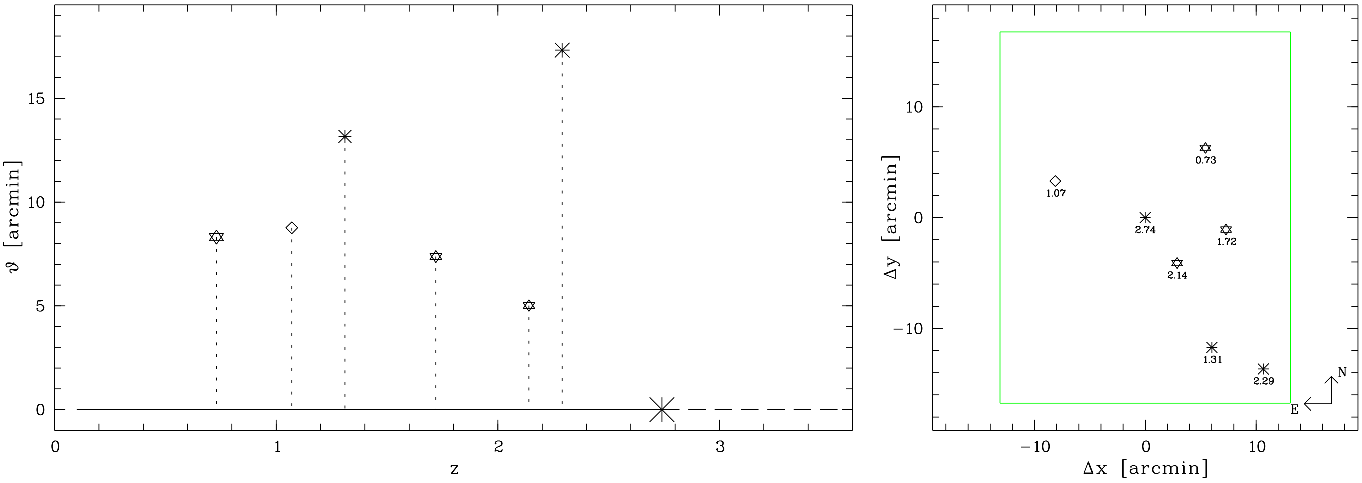

Fig. D.4. The same as Fig. D.2 for the field of Q 0002−422.

Quasars and quasar candidates near H 0055−269

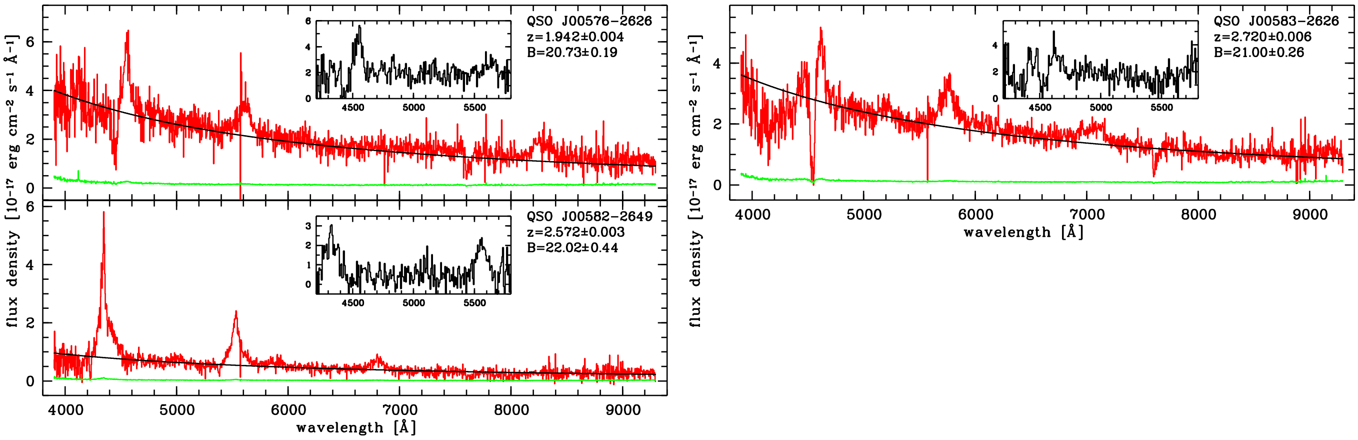

Fig. D.5. The same as Fig. D.1 for the field of H 0055−269.

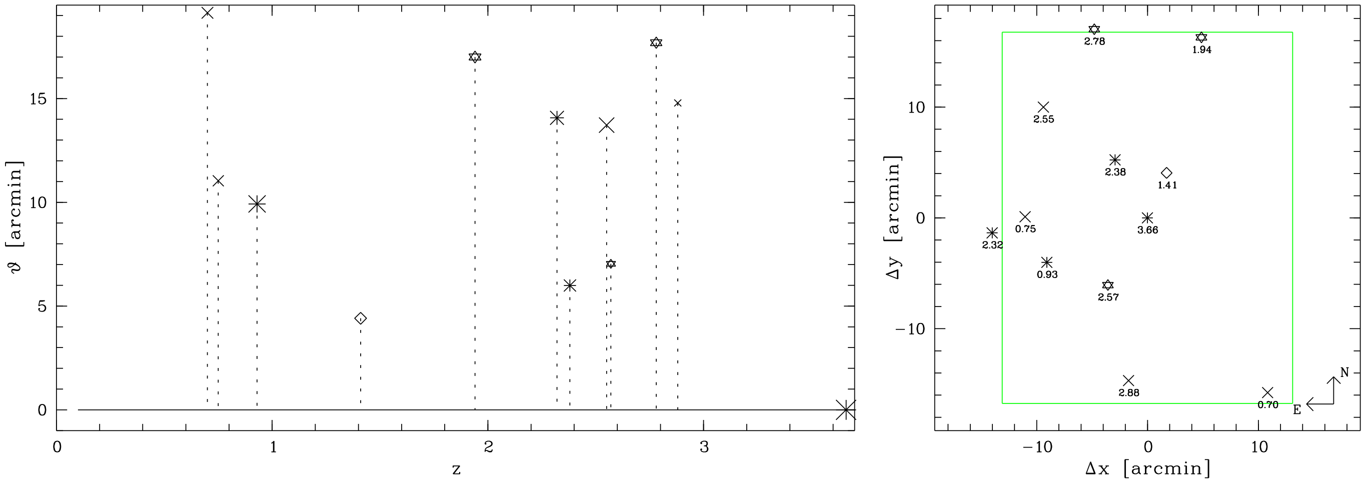

Fig. D.6. The same as Fig. D.2 for the field of H 0055−269.

Quasars and quasar candidates near Q 0302−003

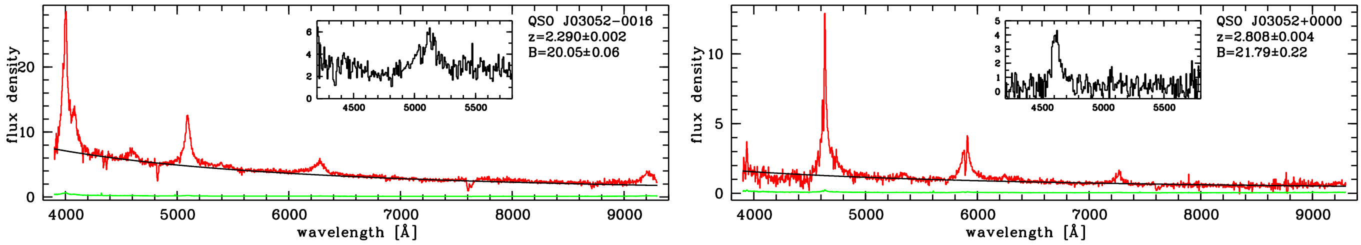

Fig. D.7. The same as Fig. D.1 for the field of Q 0302−003.

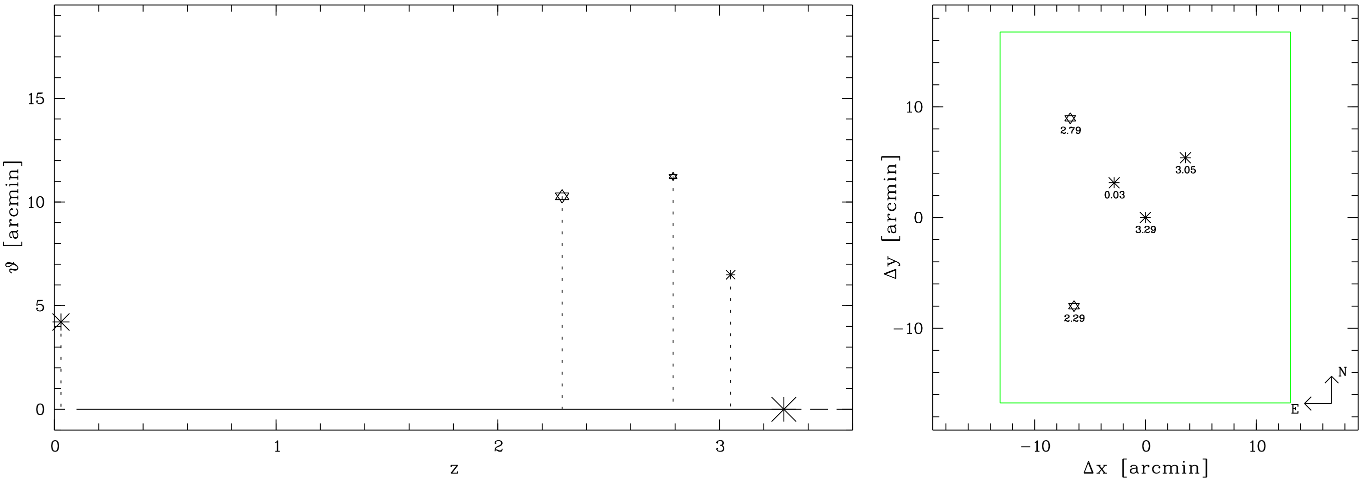

Fig. D.8. The same as Fig. D.2 for the field of Q 0302−003.

Quasars and quasar candidates near Q 0347−383

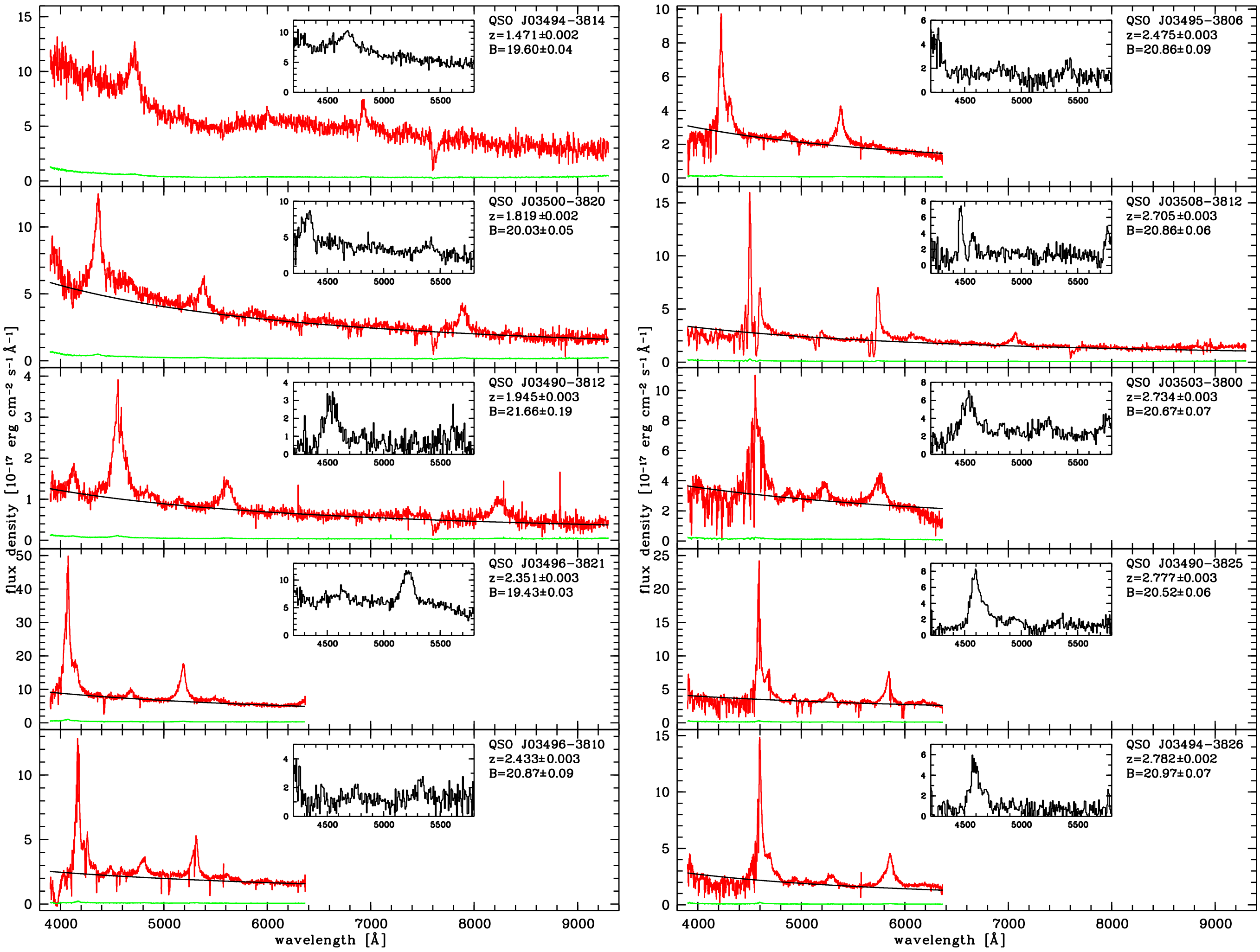

Fig. D.9. The same as Fig. D.1 for the field of Q 0347−383.

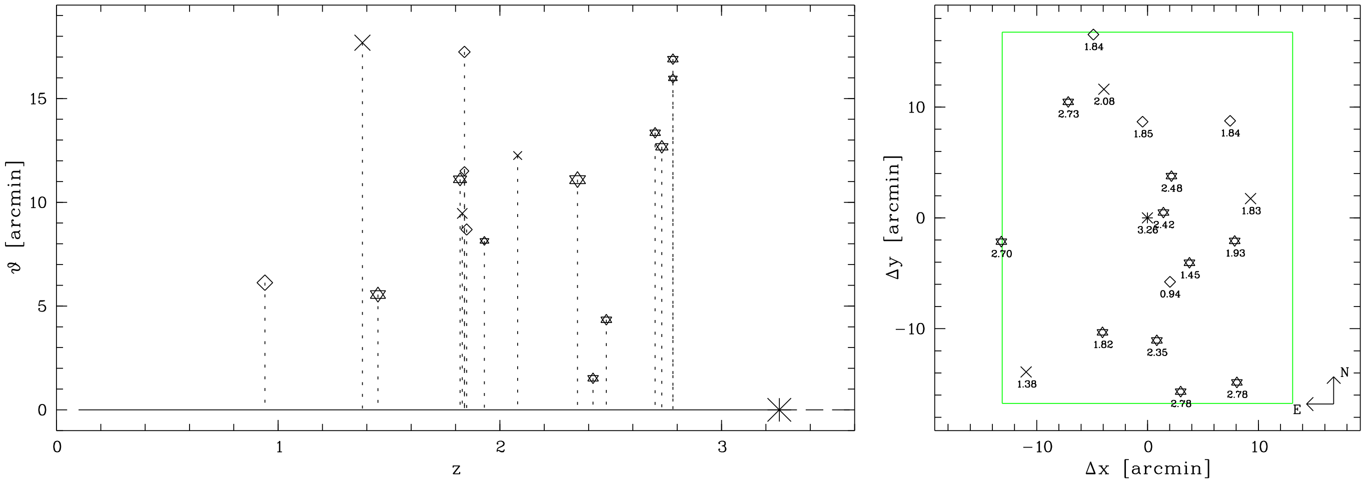

Fig. D.10. The same as Fig. D.2 for the field of Q 0347−383.

Quasars and quasar candidates near CTQ 0247

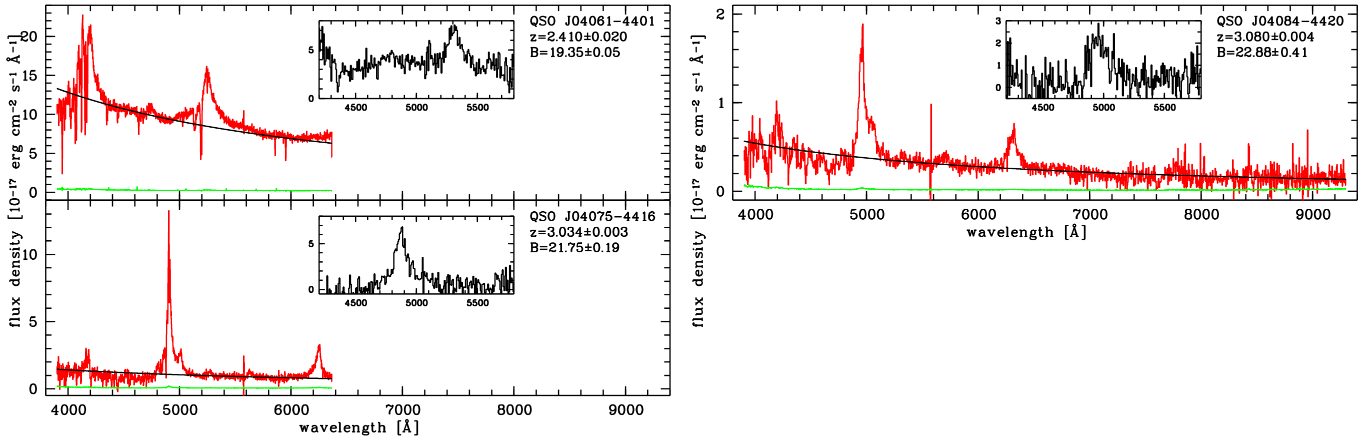

Fig. D.11. The same as Fig. D.1 for the field of CTQ 0247.

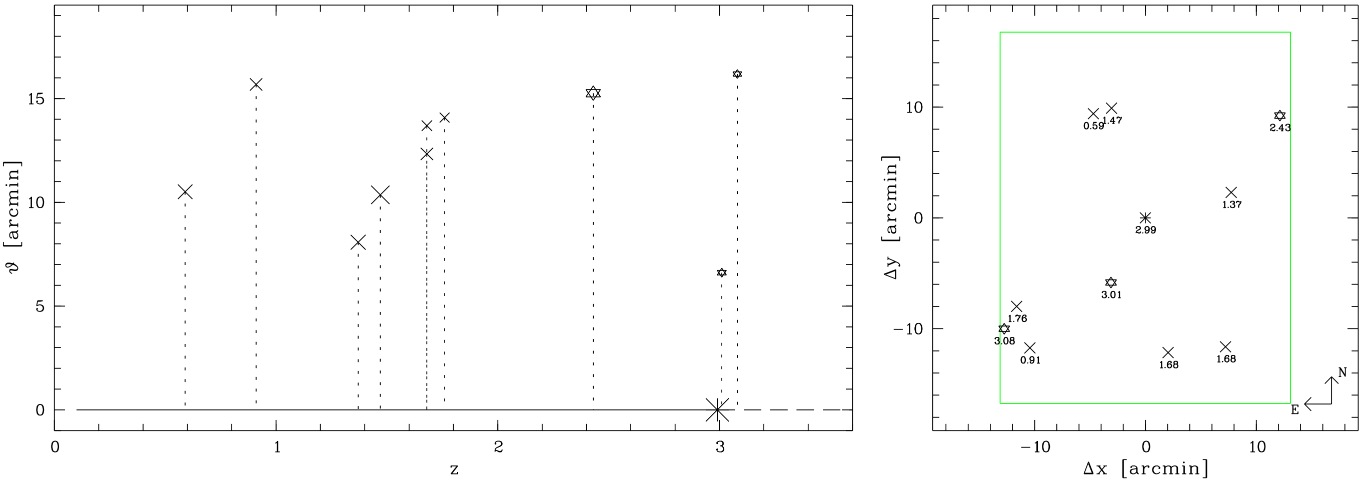

Fig. D.12. The same as Fig. D.2 for the field of CTQ 0247.

Quasars and quasar candidates near Q 0420−388

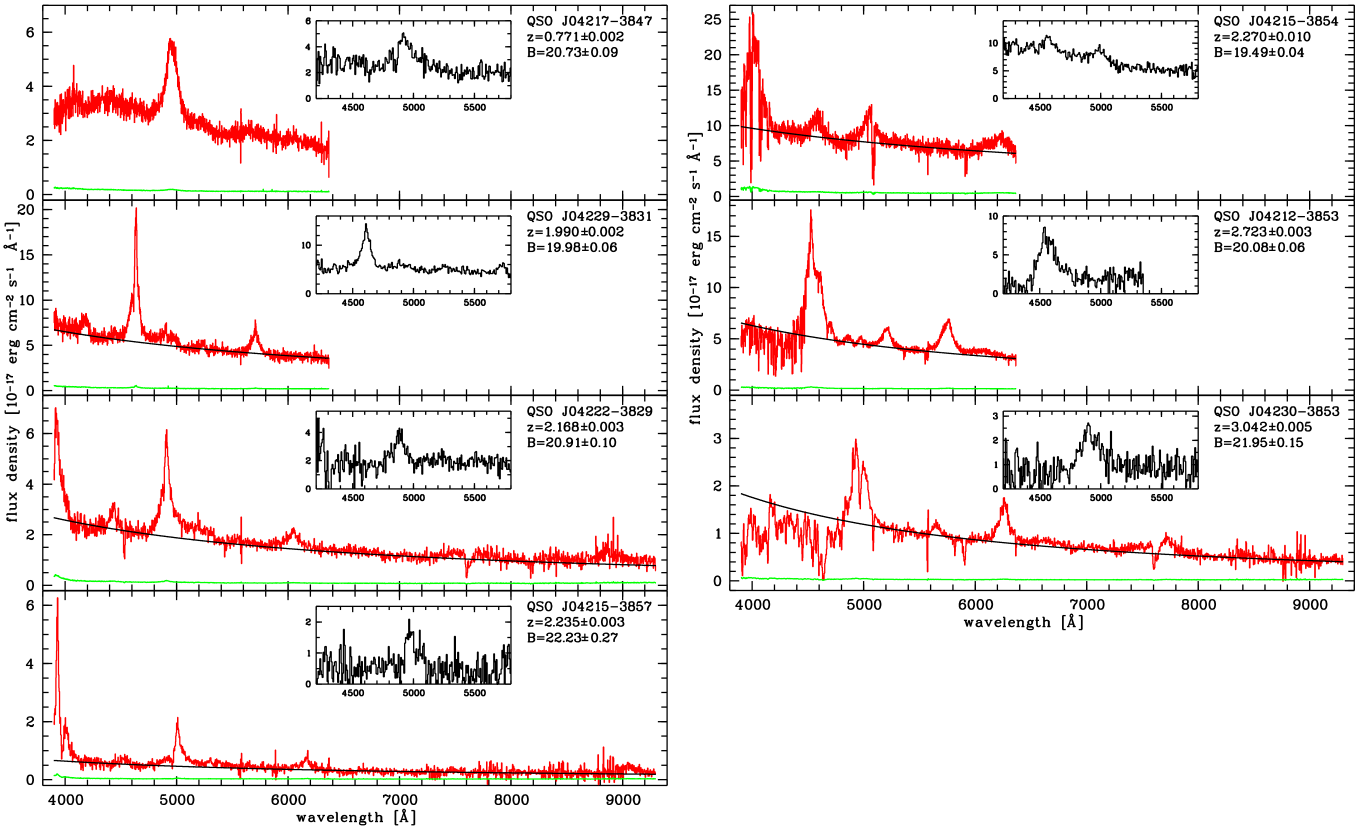

Fig. D.13. The same as Fig. D.1 for the field of Q 0420−388.

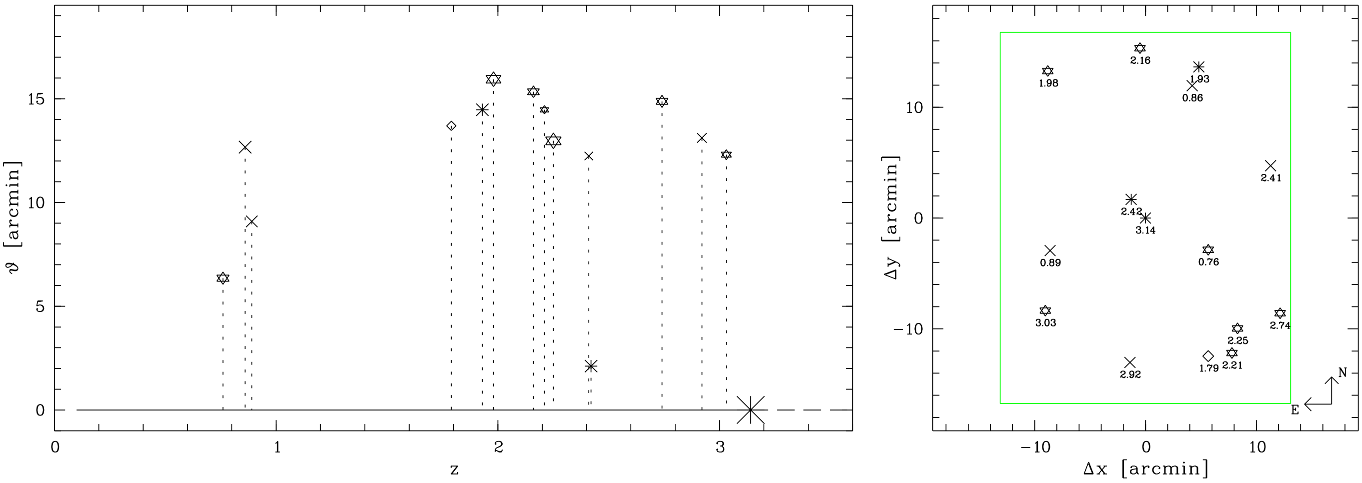

Fig. D.14. The same as Fig. D.2 for the field of Q 0420−388.

Quasars and quasar candidates near HE 0940−1050

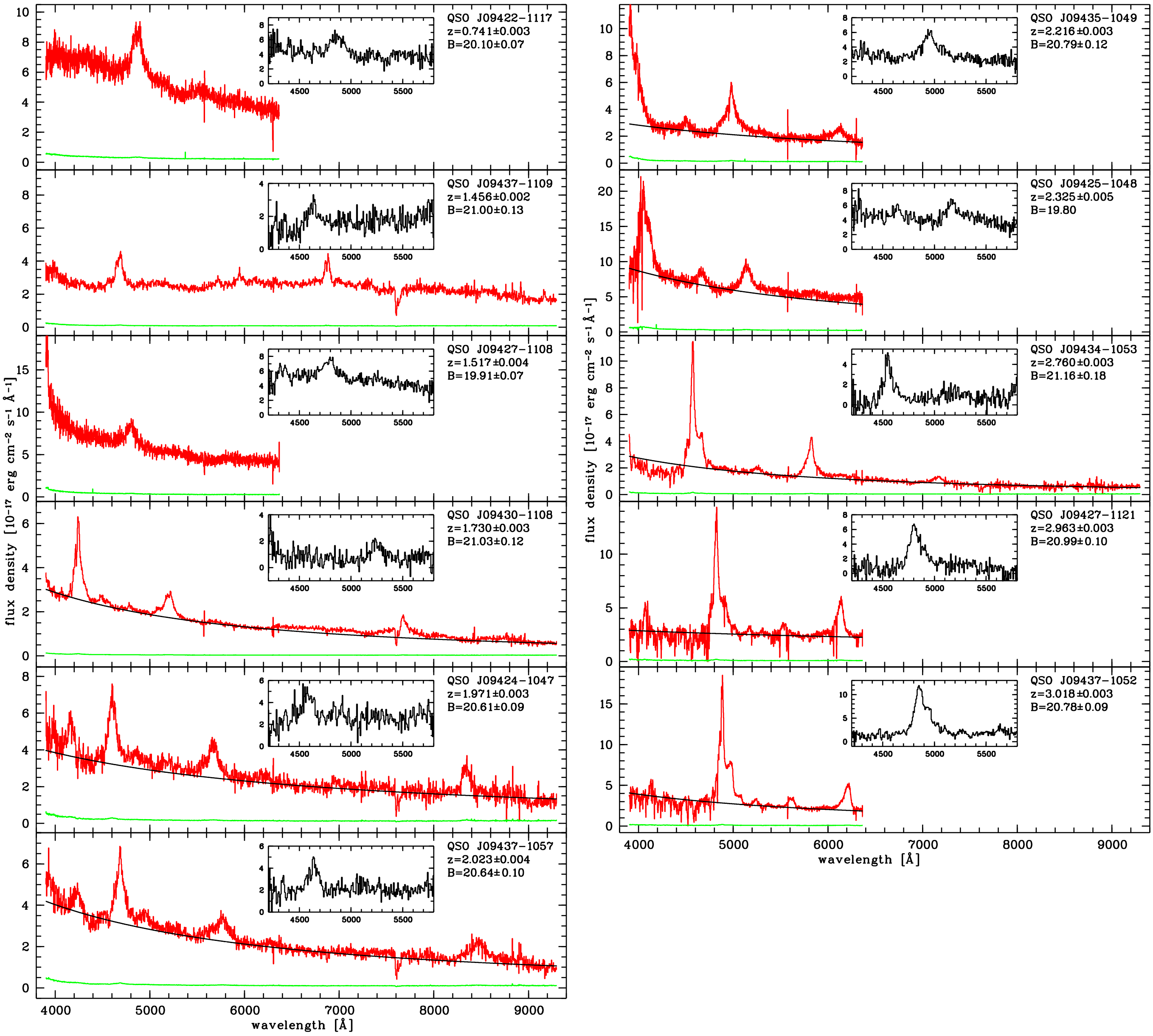

Fig. D.15. The same as Fig. D.1 for the field of HE 0940−1050.

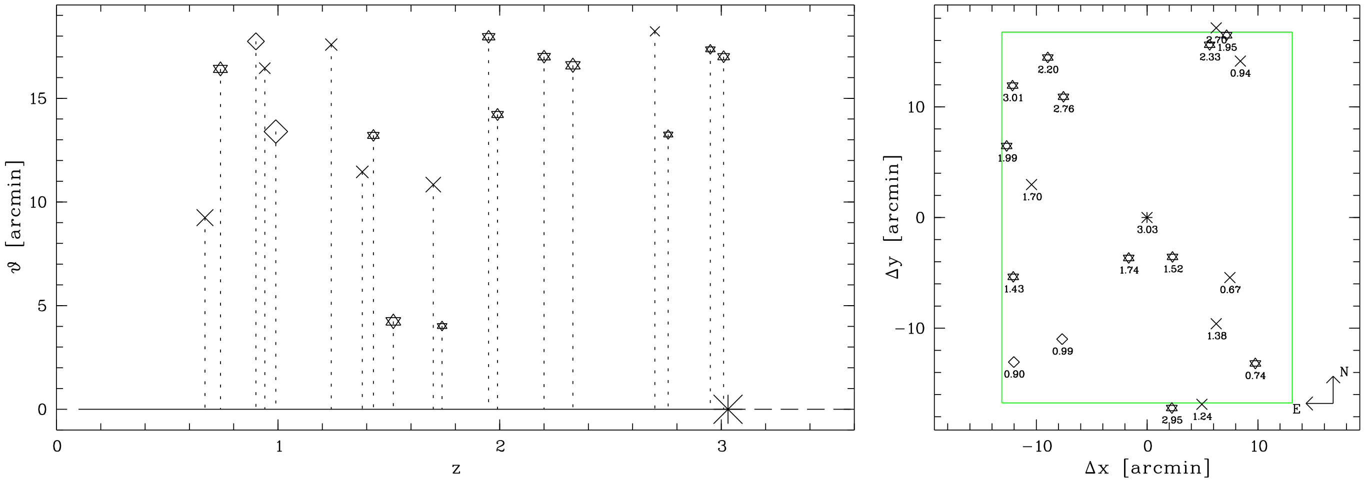

Fig. D.16. The same as Fig. D.2 for the field of HE 0940−1050.

Quasars and quasar candidates near CTQ 0460

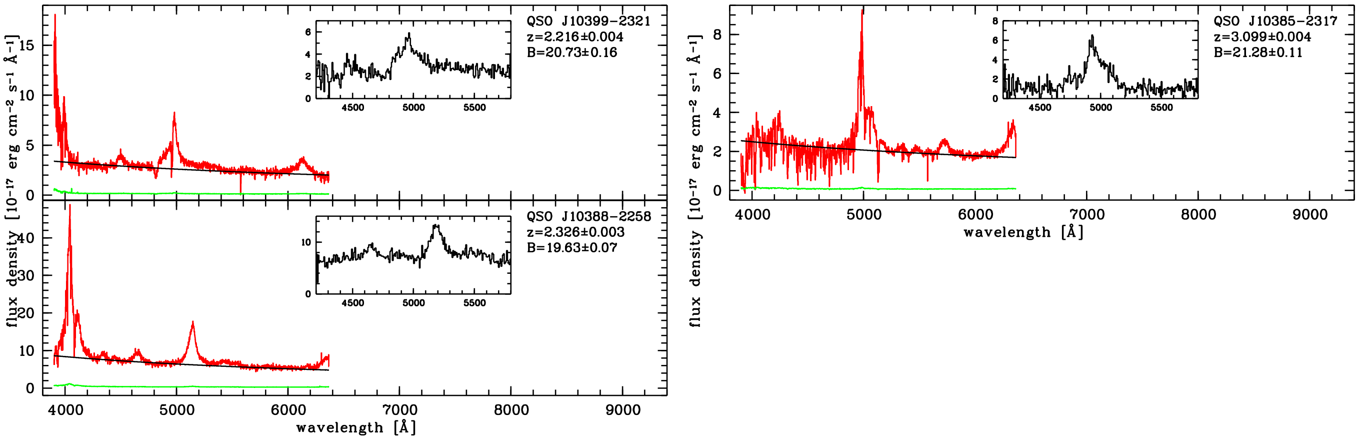

Fig. D.17. The same as Fig. D.1 for the field of CTQ 0460.

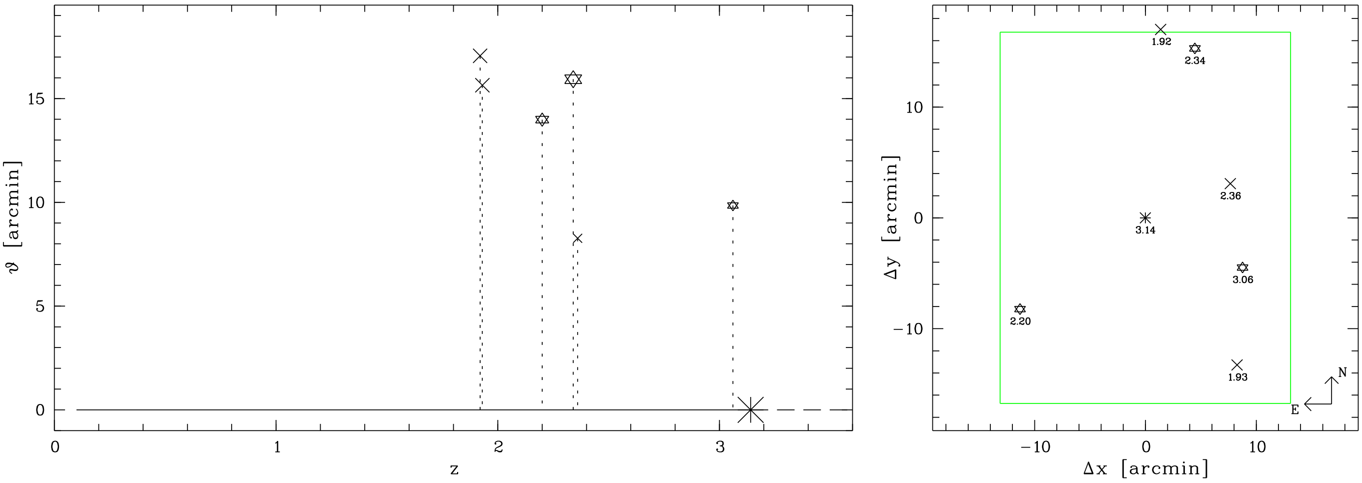

Fig. D.18. The same as Fig. D.2 for the field of CTQ 0460.

Quasars and quasar candidates near BR 1117−1329

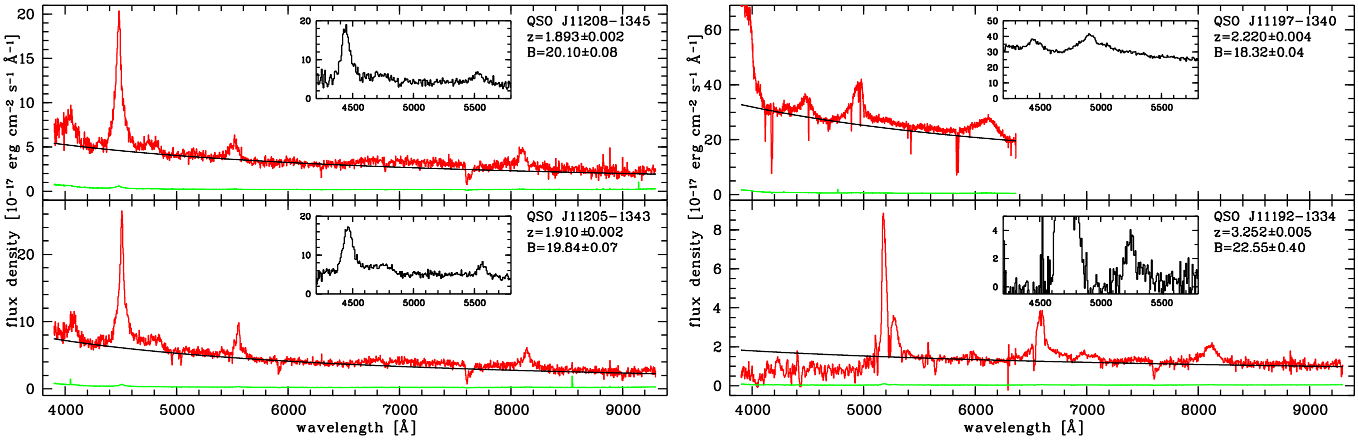

Fig. D.19. The same as Fig. D.1 for the field of BR 1117−1329.

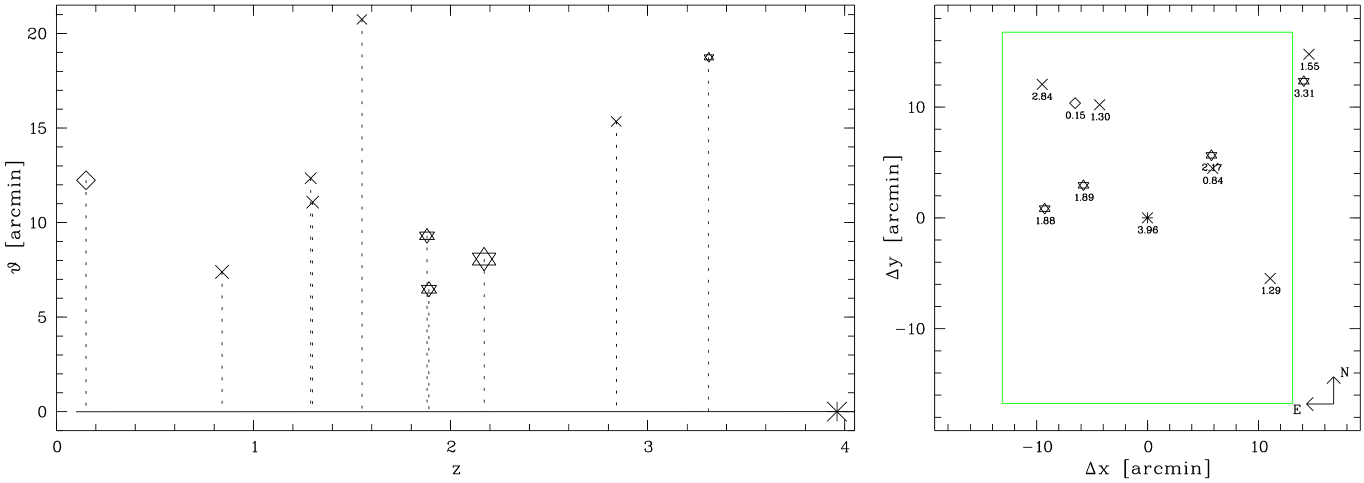

Fig. D.20. The same as Fig. D.2 for the field of BR 1117−1329.

Quasars and quasar candidates near BR 1202−0725

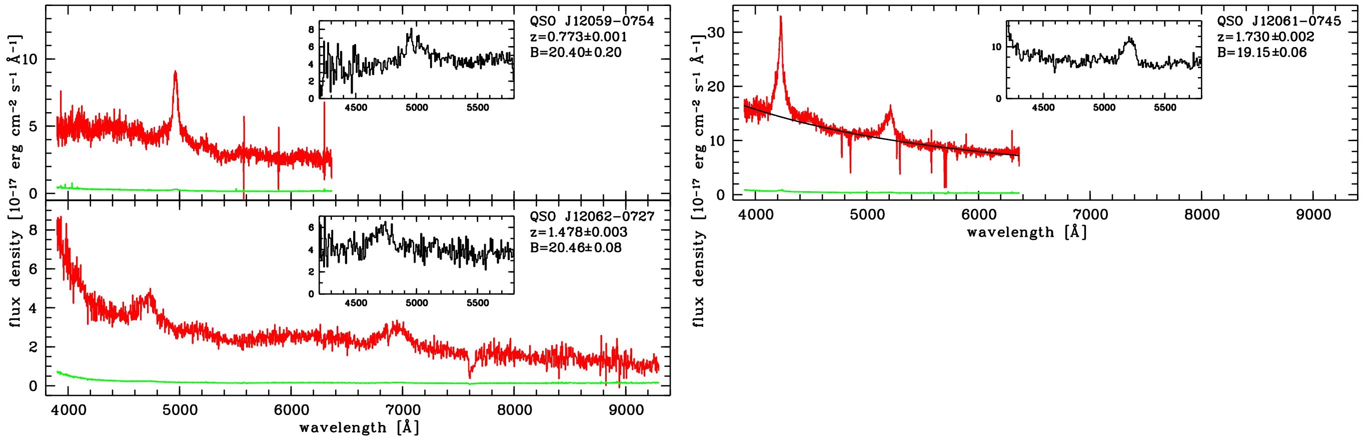

Fig. D.21. The same as Fig. D.1 for the field of BR 1202−0725.

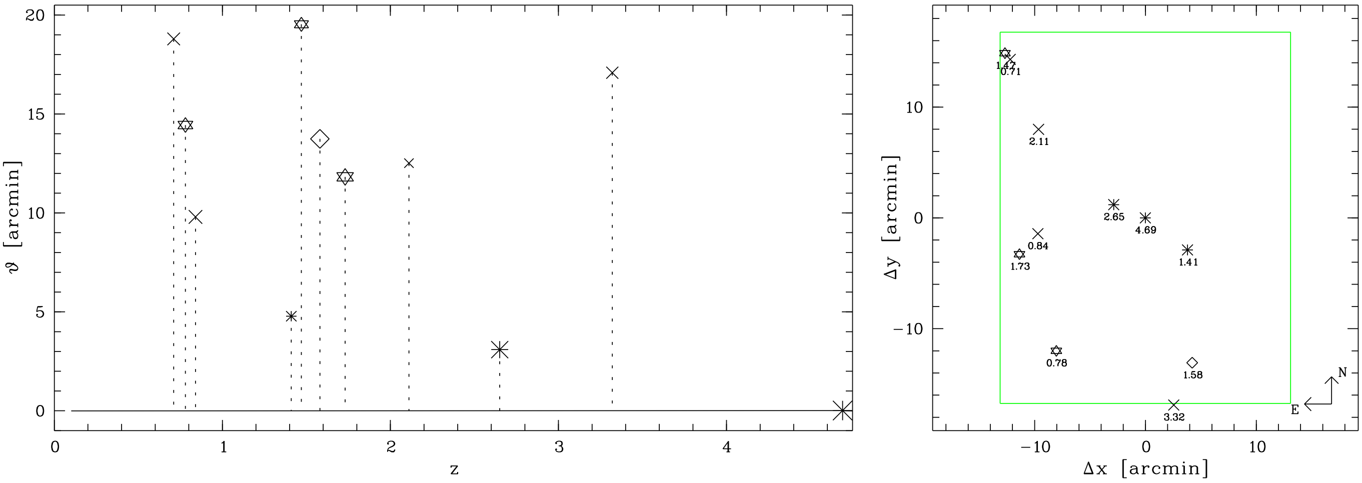

Fig. D.22. The same as Fig. D.2 for the field of BR 1202−0725.

Quasars and quasar candidates near Q 1209+0919

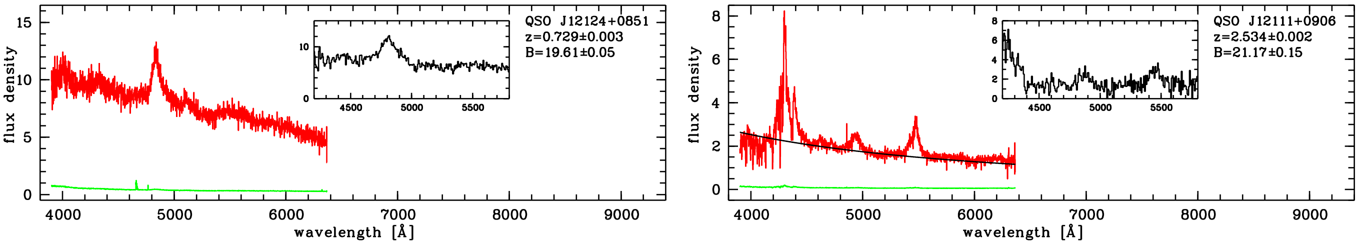

Fig. D.23. The same as Fig. D.1 for the field of Q 1209+0919.

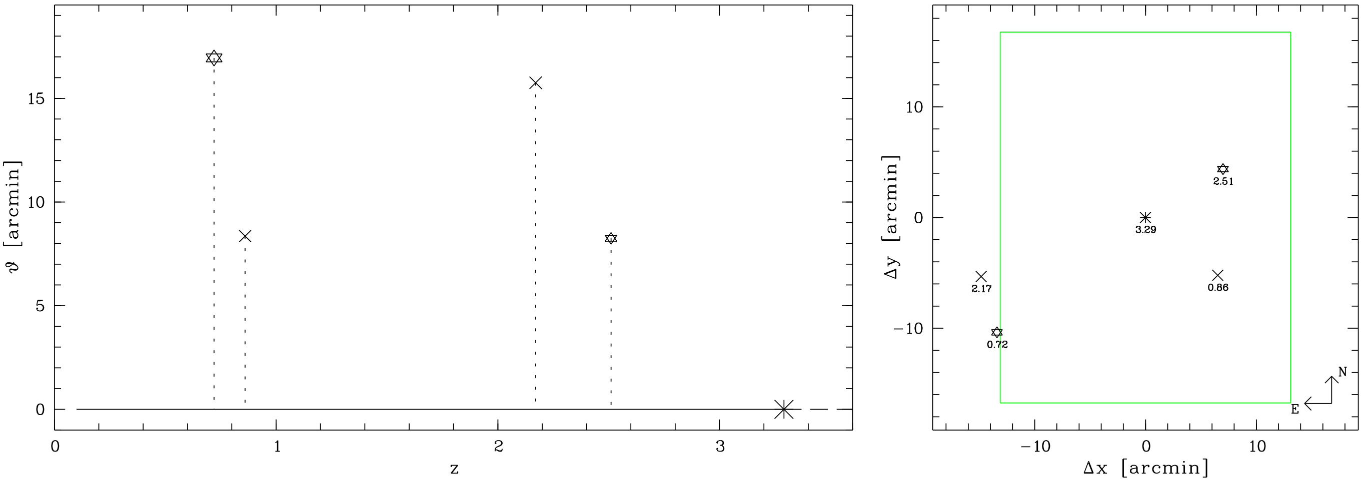

Fig. D.24. The same as Fig. D.2 for the field of Q 1209+0919.

Quasars and quasar candidates near PKS 2126−15

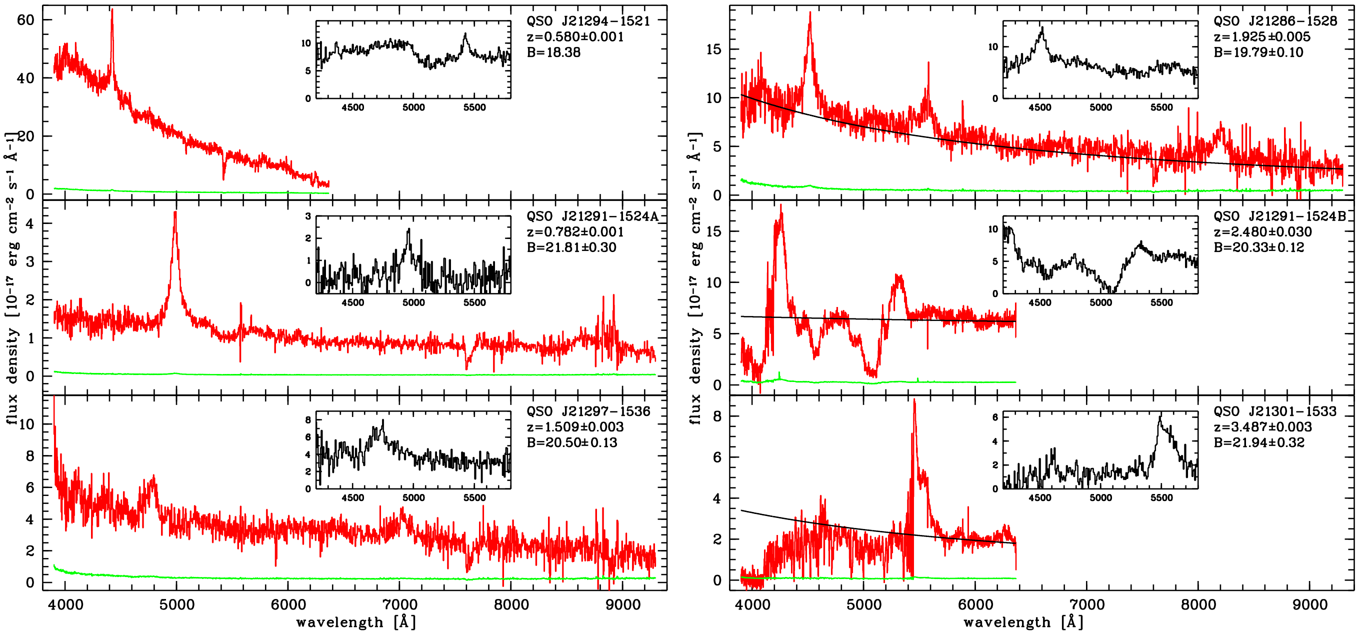

Fig. D.25. The same as Fig. D.1 for the field of PKS 2126−15.

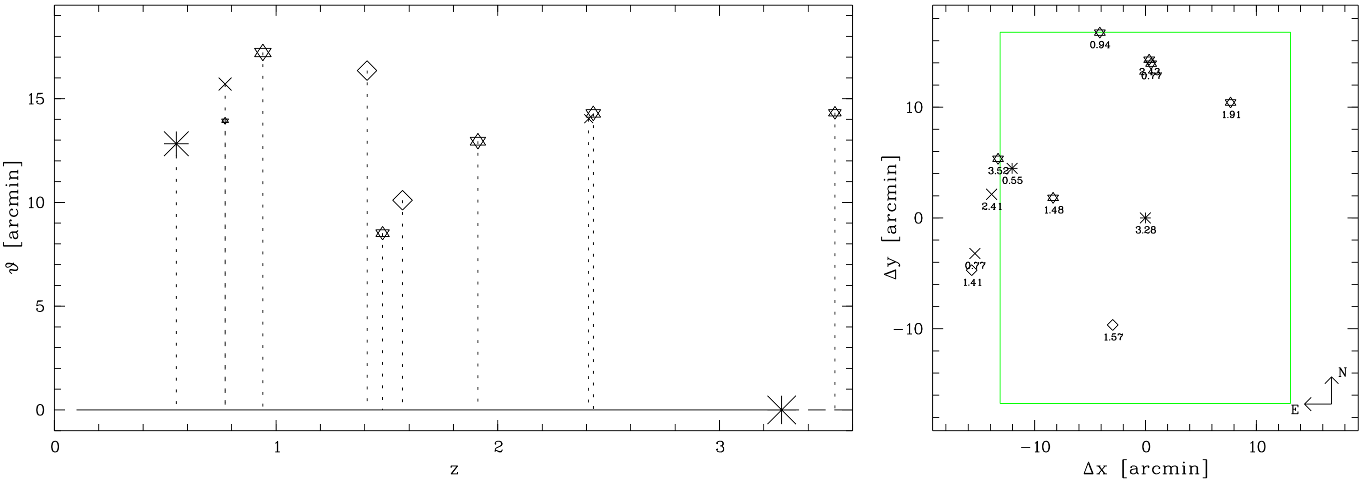

Fig. D.26. The same as Fig. D.2 for the field of PKS 2126−15.

Quasars and quasar candidates near Q 2139−4434

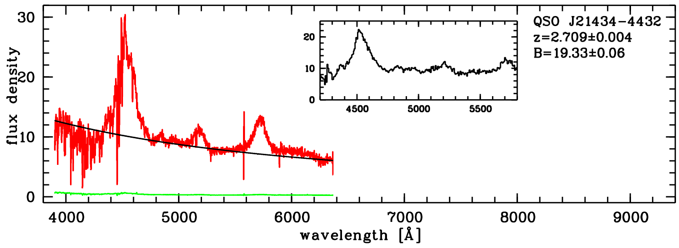

Fig. D.27. The same as Fig. D.1 for the field of Q 2139−4434.

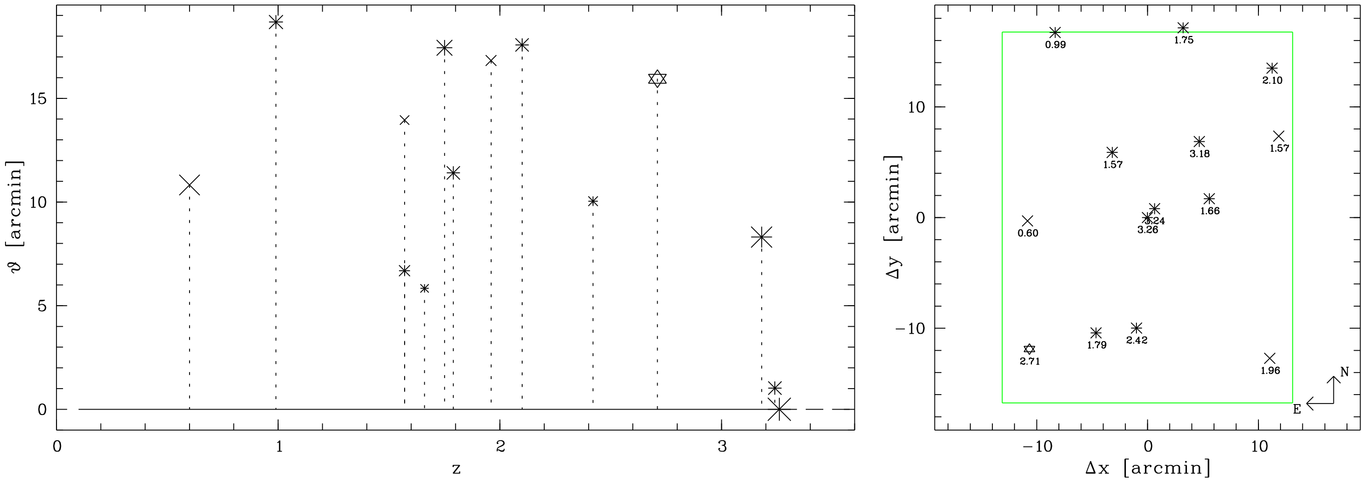

Fig. D.28. The same as Fig. D.2 for the field of Q 2139−4434.

Quasars and quasar candidates near HE 2243−6031

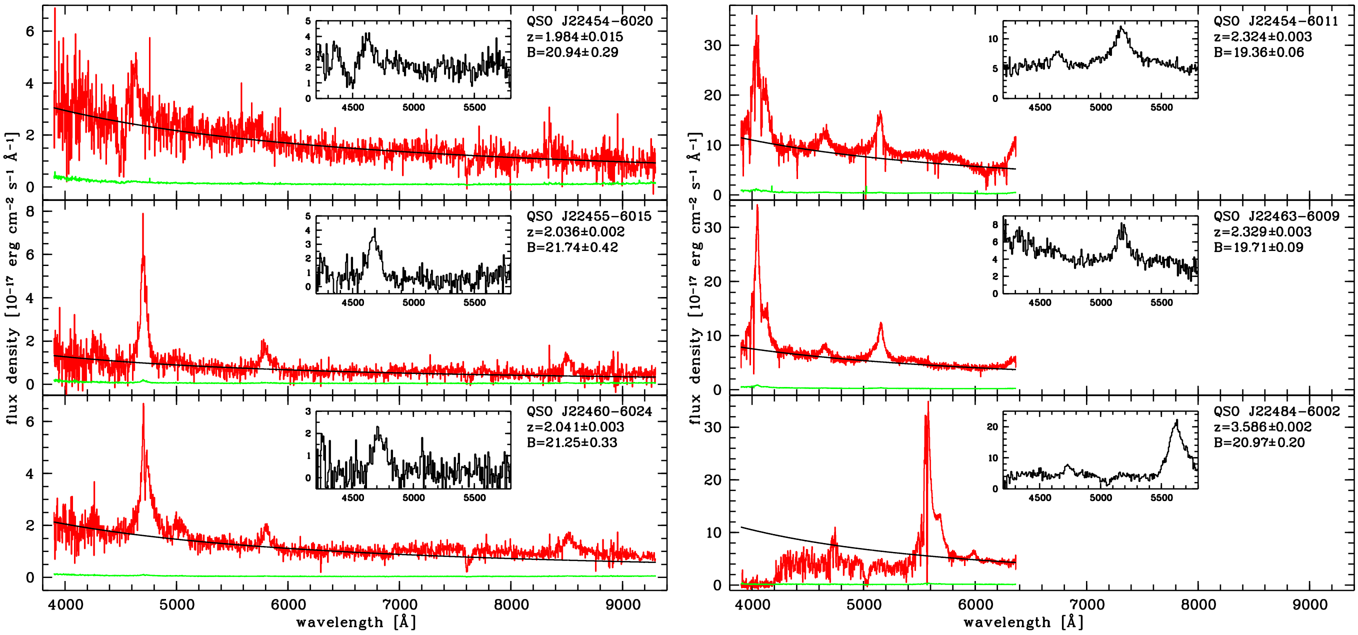

Fig. D.29. The same as Fig. D.1 for the field of HE 2243−6031.

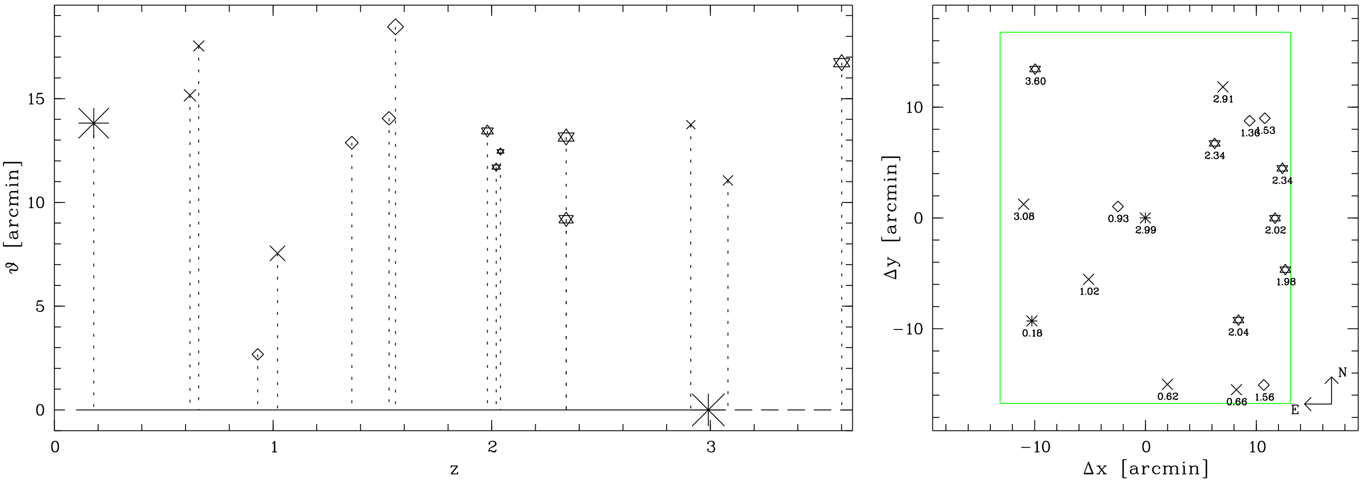

Fig. D.30. The same as Fig. D.2 for the field of HE 2243−6031.

Quasars and quasar candidates near HE 2347−4342

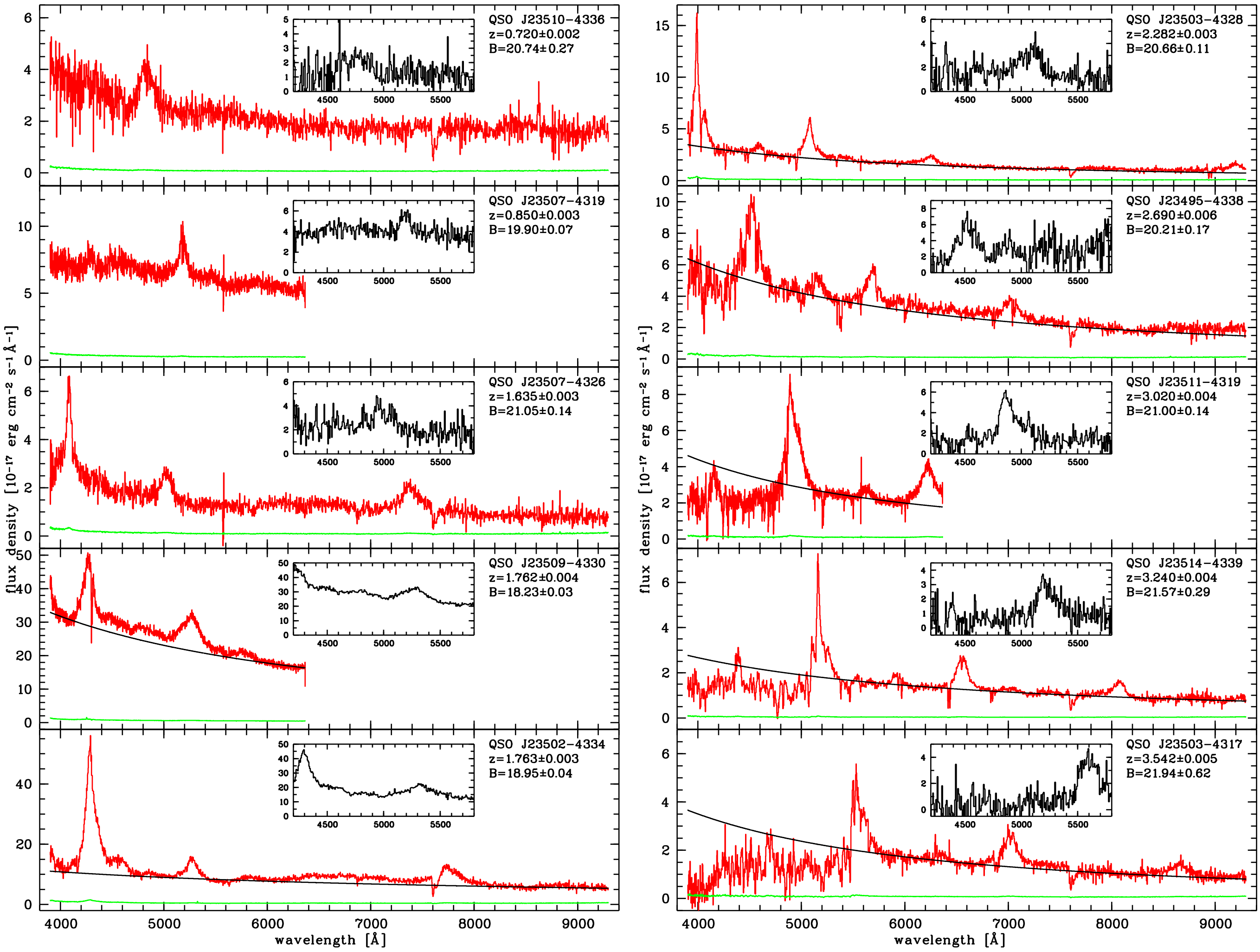

Fig. D.31. The same as Fig. D.1 for the field of HE 2347−4342.

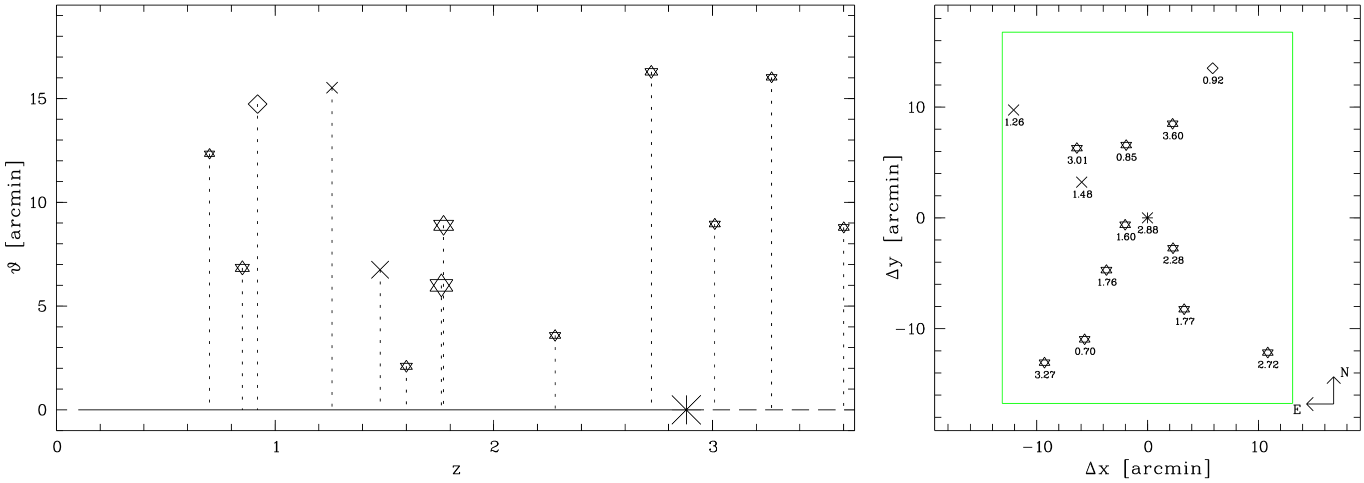

Fig. D.32. The same as Fig. D.2 for the field of HE 2347−4342.

Almost secure quasars and quasar candidates near PKS 0528−250

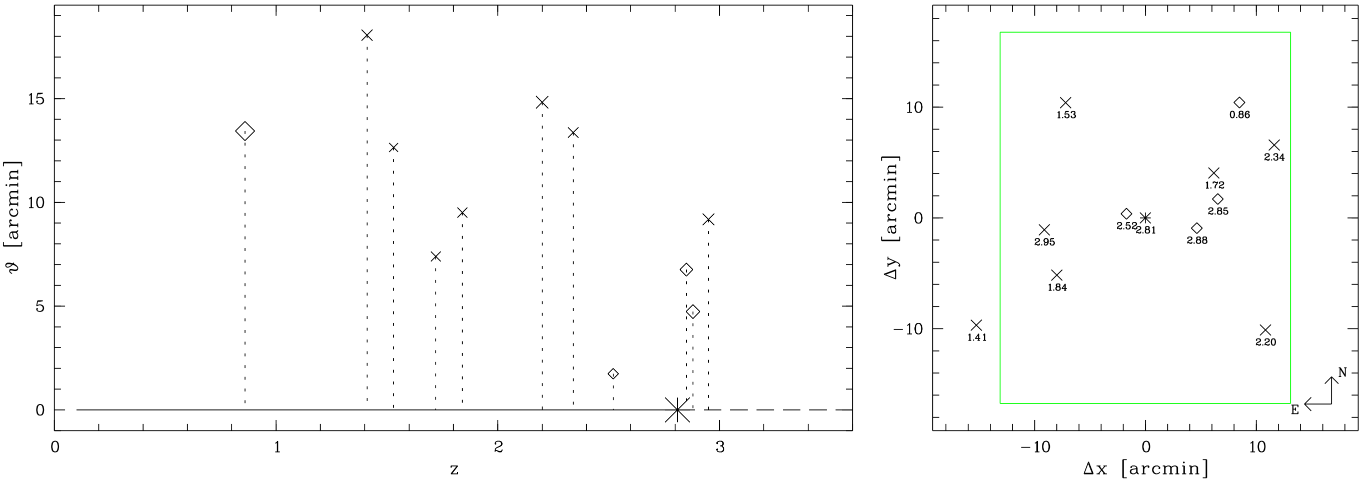

Fig. D.33. *Left:* Angular distribution of quasars and quasar candidates with respect to the central quasar PKS 0528−250 (asterisk) as a function of redshift. This field was not included in the spectroscopic follow-up. Lozenges (crosses) show WFI quasar candidates with secure (estimated) redshifts. Symbol size indicates apparent optical magnitude. *Right:* Quasar distribution on the sky centred on PKS 0528−250 with indicated redshifts. The green/grey rectangle marks the nominal contiguous slitless WFI field of view (26.′2 × 33.′5) without rotating the instrument, for simplicity centred on PKS 0528−250. The actual survey field was offset to the east.

Quasar candidates near Q 1451+123

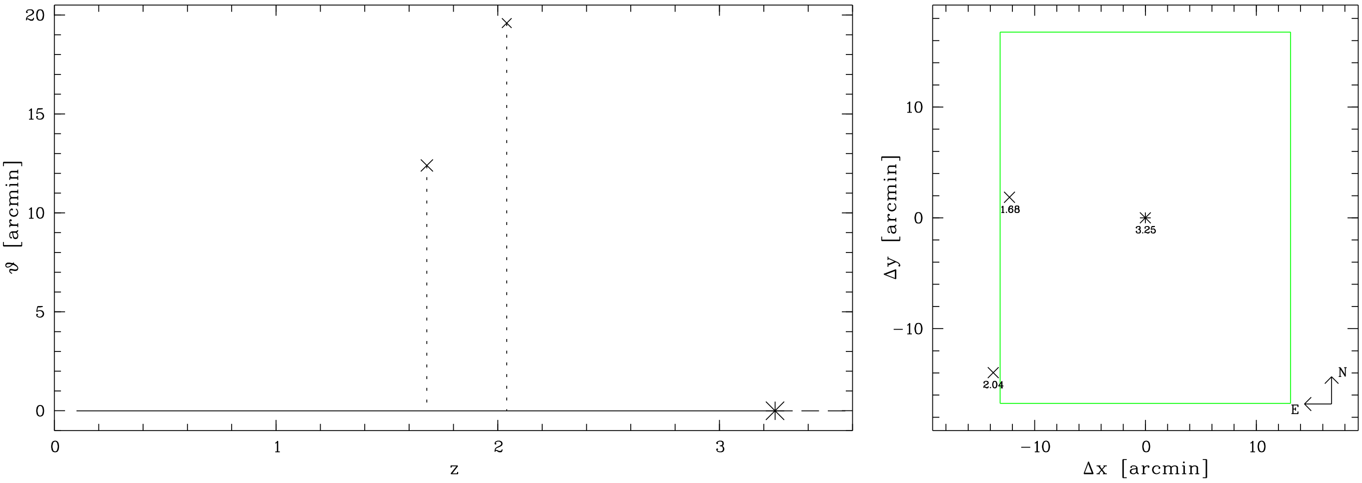

Fig. D.34. *Left:* Angular distribution quasar candidates with respect to the central quasar Q 1451+123 (asterisk) as a function of redshift. Only two low-quality candidates were detected, and none of them was selected for the FORS2 follow-up. *Right:* Quasar distribution on the sky centred on Q 1451+123 with indicated (estimated) redshifts. Again the rectangle marks the nominal contiguous slitless WFI field of view.

Appendix E

Simulations of the He II forest

ABSTRACT

In the published version of Chapter 5 we presented a shortened discussion of the He II forest simulations that were carried out in order to quantify the statistical fluctuations of the spectral shape indicators R and η. We will comment on this in a bit more detail below.

The dependence of the ratio of effective optical depths on the H I absorption

As outlined in Sect. 5.4.2 we simulated 100 Monte Carlo Lyα forests in H I and He II matched to the resolution and quality of the observed spectra. On the adopted redshift scale $\Delta z = 0.005$ we obtained 20000 measurements of R as a function of the considered η and the fluctuating H I absorption, characterised by its normalised value D.

In Fig. 5.5 we did not show the intrinsic variation of the R values around the polynomial fits to $R(D)$ in logarithmic space. We present the fits together with the root-mean-square deviations of R from the polynomial fits in the four panels of Fig. E.1. We see that the R values scatter around the fitted polynomial relation, nevertheless a soft radiation field ($\eta \gtrsim 100$) can be well distinguished from a hard one ($\eta \sim 20$) for $D \lesssim 3$. At high D values the absorption lines are saturated, so that the spectral shape cannot be inferred from the effective optical depths.

Details on the simulated column density ratios

In Chapter 5 we also used 10 Monte Carlo H I forest spectra and their corresponding He II spectra in order to quantify statistical and systematic errors on the η measurements. Again the simulated data closely resembled the actual observed data.

We used AUTOVP (Davé et al. 1997) to fit the mock H I forests automatically. We found that with the standard extraction parameters the AUTOVP fits are generally poor at the high $S/N \sim 100$ of the mock data. In extensive tests we varied the input

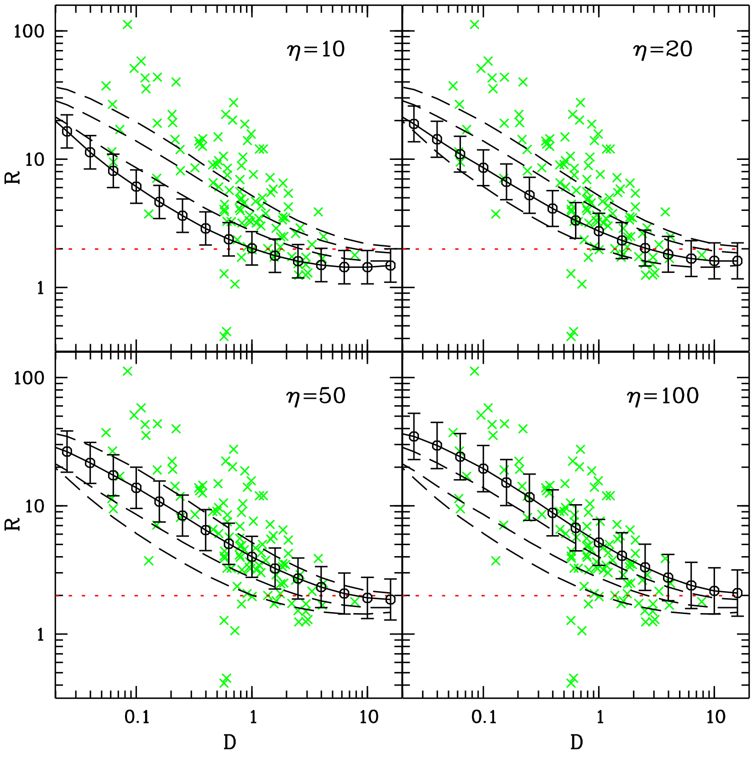

Fig. E.1. Simulated ratio of effective optical depths $R = \tau_{\mathrm{eff,He\,II}}/\tau_{\mathrm{eff,H\,I}}$ as a function of $D = \tau_{\mathrm{eff,H\,I}}/\tau^{\mathrm{exp}}_{\mathrm{eff,H\,I}}$ for different η. For display purposes the 20000 R values per considered η have been binned in $\Delta \log(D) = 0.2$ bins (circles). Error bars indicate the root-mean-square deviation of the simulated R values and the polynomial fit (full line). For comparison each panel shows the other polynomial fits (dashed lines) and the actual R values measured towards HE 2347−4342 (crosses). The horizontal dotted line marks $R = 2$.

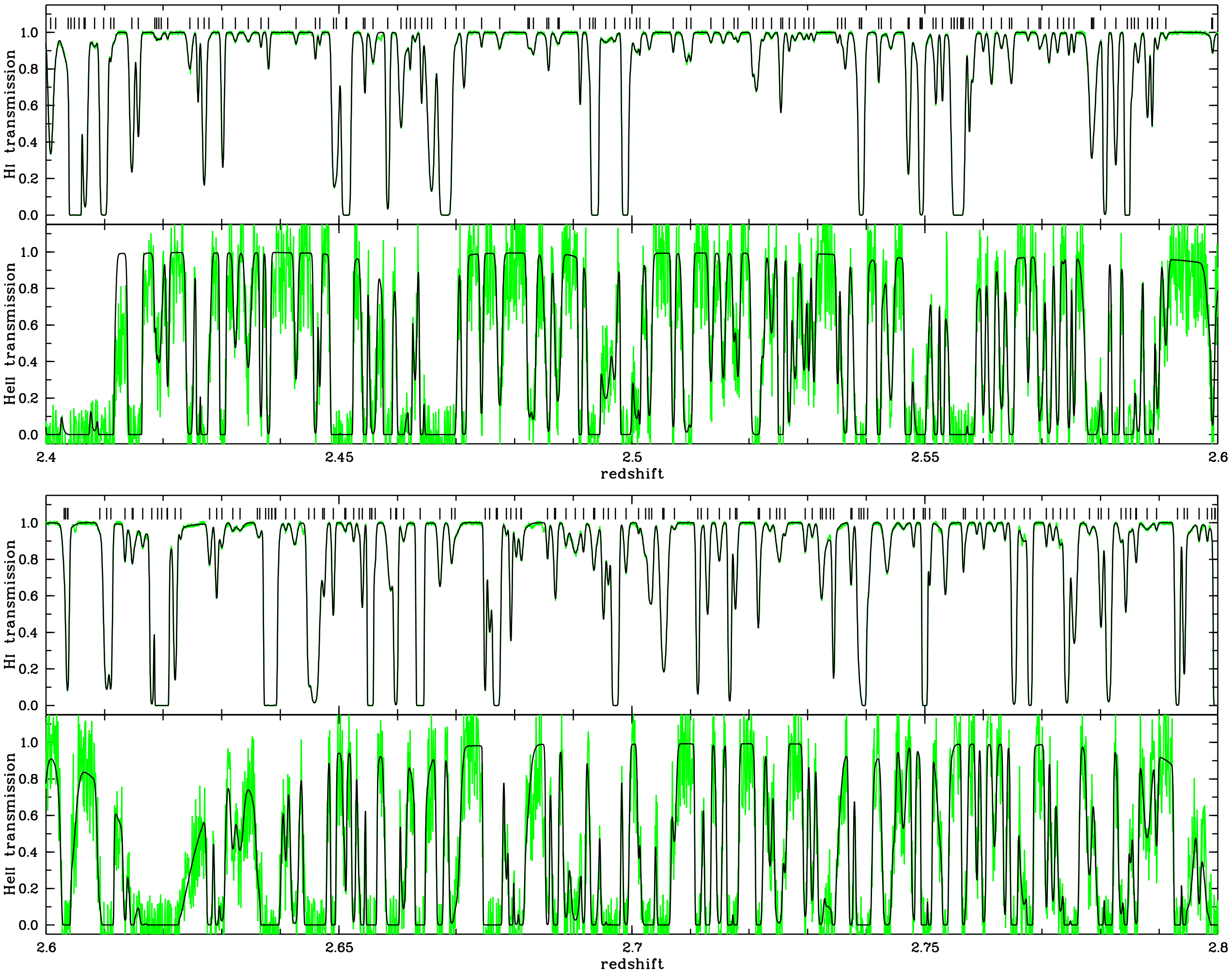

Fig. E.2. A simulated H I forest spectrum and the corresponding He II forest spectrum at $2.4 < z < 2.8$ (green/grey) together with their line fits (black). The simulated H I spectrum has $S/N = 100$ per pixel at $R \sim 45000$, whereas the He II spectrum has $S/N \sim 4$ at $R \sim 20000$, $\eta = 80$ and $b_{\mathrm{He\,II}} = b_{\mathrm{H\,I}}$. Fitted H I lines are marked by vertical dashes.

parameters of AUTOVP until the fits accurately traced the absorption also in blended complexes and only very few weak lines were lost by the fitting routine. After fitting all 10 H I spectra we correlated the 7565 fitted lines with those of the input line list of the Monte Carlo spectra, finding very good agreement in the line parameters ($z, N_{\mathrm{H\,I}}, b_{\mathrm{H\,I}}$).

The simulated He II forest data were generated from the original H I line lists (not the fitted ones) by assuming that both features coincide in redshift with a column density ratio $\eta = 80$. We simulated both pure non-thermal broadening ($b_{\mathrm{He\,II}} = b_{\mathrm{H\,I}}$) and pure thermal broadening ($b_{\mathrm{He\,II}} = 0.5 b_{\mathrm{H\,I}}$). The simulated He II forests were fitted with fixed Doppler parameters and redshifts from the AUTOVP H I line lists assuming pure non-thermal broadening. Only the He II column densities were allowed to vary. The forests were fitted with a downhill-simplex algorithm on spectral regions whose ends reached up to the continuum. However, due to the strong blending in the He II data and the low data quality the χ^2 minimum is not always well defined. Figure E.2 presents a fitted simulated H I spectrum together with its fitted He II spectrum.

The assumption of non-thermal broadening will underestimate the derived η values if the lines are in fact thermally broadened (Fechner & Reimers 2007). The left panel of Fig. E.3 shows the histograms of derived η values. If the assumption of non-thermal broadening is correct η is on average recovered correctly, albeit with a large scatter induced by the low S/N, blending of the He II lines and incorrect H I line parameters in not well deblended line complexes. However, extremely low ($\eta \lesssim 10$) as well as extremely high ($\eta \gtrsim 1000$) values are rather unlikely to occur due to measurement errors. The real data shows more of these extreme values than predicted, indicating that some fluctuations in the shape of the UV background are genuine. A wrong assumption of non-thermal broadening will lead to underestimated η values. Compared to Fechner & Reimers (2007) we increased the statistics for such an analyis by a factor $\gtrsim 10$. The right panel of Fig. E.3 clearly shows that the deviating η values are mainly caused by saturated H I lines, in accord with the results by Fechner & Reimers (2007). If the assumption of non-thermal broadening is correct the η values scatter rather symmetrically in logarithmic space around $\eta = 80$ at all column densities as implied by the η histogram.

References

Davé, R., Hernquist, L., Weinberg, D. H., & Katz, N. 1997, ApJ, 477, 21
Fechner, C. & Reimers, D. 2007, A&A, 461, 847

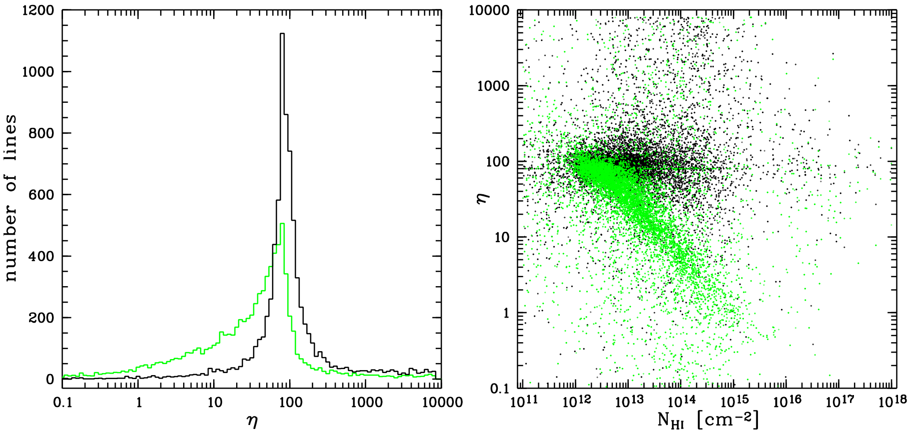

Fig. E.3. Dependence of the derived η values on the assumption of non-thermal broadening. *Left:* Histograms of the fitted η values from the simulated data. The results obtained with the correct (wrong) assumption of non-thermal broadening are shown in black (green/grey). *Right:* Correlation of the fitted η and the H I column density in the same colour coding.

ACKNOWLEDGEMENTS

First, I thank my supervisor Lutz Wisotzki for this great experience in Science. In 2002, he assigned the initial survey project to me as a Diploma Thesis project, when he wrote my name onto an ESO observing proposal. Since then I have been involved in this project, exploiting the large amount of data gathered. Due to his skills in writing good proposals I could travel twice to Chile to go observing, once at La Silla and once at Paranal. I will never forget these experiences I had with Nature during my observing runs with a constantly high level of adrenaline in my venes and a hunting fever to discover quasars. He guided me through this adventure with great care and circumspection. He critically reviewed the manuscripts that I prepared, which improved their clarity and structure. Last but not least, I thank him and Matthias Steinmetz for the conferences I could participate in.

I also thank the ESO staff members who ensured efficient observations with a minimum of overheads and time loss. Especially, I am indebted to Fernando Selman, who knew all the tricks in performing the slitless survey observations, and Poshak Gandhi, who cared a lot to obtain good FORS2 spectra.

I have to thank all those who collaborated with me during these almost four years or shared data and/or software with me. Foremost, I am indebted to Aldo Dall' Aglio for several software programmes he developed for our common purposes. He also kindly reduced the UVES data with great care. Moreover, he was always open for a discussion of the sometimes complex issues of the proximity effect. I thank Cora Fechner for analysing the metal line systems near the foreground quasars towards HE 2347−4342 and providing her carefully obtained He II line list. I am also indebted to Tae-Sun Kim for her additional line list of HE 2347−4342 and invaluable discussions. Thanks go to Gerard Kriss and Wei Zheng for the reduced He II spectrum of HE 2347−4342 and to Peter Jakobsen, who agreed that we can publish the quasars he discovered in his survey.

I thank Ralf Jacob, who showed up in my office from time to time to distract me from working and to enjoy some Indian food in downtown Babelsberg. I also enjoyed the funny long-distance phone calls with my friend Mathias Görlitz lasting up to ∼ 5 hours. Nora Worseck provided the artwork on page 7. I thank my grandparents, Ilse and Michel Worseck, for food, wine and conversations. Finally, I am indebted to my parents, Christiane and Peter Worseck, for their steady assistance along my adventurous path.